UNIVERSITÀ DI PISA

Dipartimento di Fisica

YAP-(S)PET: a small animal PET/SPECT scanner. Performance and applications in oncology, cardiology and neuroscience

PhD Thesis in Applied Physics

of

Antonietta Bartoli

Advisor:

Prof. Alberto Del Guerra

PhD coordinator:

Prof. Francesco Pegoraro

XIX Ciclo (2004-2006) - Settore disciplinare FIS/07

Contents

Chapter 1

Introduction

The term molecular imaging implies the convergence of multiple image-capture techniques, basic cell/molecular biology, chemistry, medicine, pharmacology, medical physics, biomathematics, and bioinformatics into a new imaging paradigm. Moreover, molecular imaging has its roots in nuclear medicine and in many ways is a direct extension of this existing discipline [1].

The origins of nuclear medicine can be traced back to the last years of the 19th century and the discovery of radioactivity by Henry Becquerel (1896) and of radium by Marie Curie (1898).

The biologic foundations for nuclear medicine were laid down between 1910 and 1945. In 1913, Georg de Hevesy developed the principles of the tracer approach and then was the first to apply them to a biologic system in 1923, studying the absorption and translocation of radioactive lead nitrate in plants. The first human study employing radioactive tracers was probably that of Blumgart and Weiss (1927), who injected an aqueous solution of radon intravenously and measured the transit time of the blood from one arm to the other using a cloud chamber as radiation detector.

In 1951, the use of positron emitters and the advantageous imaging properties of these radionuclides were described by Wrenn and coworkers.

In 1958 Hal Anger developed the forerunner of all the modern nuclear medicine single-photon system.

In 1968 Paul Harper and colleagues started to use ^{99m}Tc as imaging tracer. ^{99m}Tc also proved to be very flexible for labeling a wide variety of compounds that could be used to study virtually every organ in the body. Today, ^{99m}Tc is the most widely used radionuclide in nuclear medicine.

The final important development was the mathematics to reconstruct tomographic images from a set of angular views around the patient. This revolutionized the whole field of medical imaging leading to CT, PET, SPECT and MRI. In fact, it was possible to replace the two dimensional representation of the three dimensional radioactivity distribution, with a true three-dimensional representation. This allowed the development of PET by Phelps and coworkers and SPECT by Kuhl and colleagues during the 1970s, and marked the start of modern era of nuclear medicine [2].

By the mid-1990's, a number of groups dedicated to the development of PET technology has realized that the field of small animal PET could provide a fertile area for technological innovation. It was possible to justify the building of PET systems in miniature, in the name of a small animal scanning, at considerably lower cost than would have been incurred by a full-sized tomography [3].

In 2007, Mario Capecchi, Oliver Smithies and Martin Evans received Nobel Laureates in Physiology or Medicine for their discoveries made in the 1980's on "Making Model Mice" The elevation of the humble mouse to become many scientists' experimental animal of choice has been one of the scientific phenomena of the last two decades. Today, genetically-altered mice are an essential component of the experimental toolkit, with thousands of varieties contributing to research in laboratories around the world.

The YAP-(S)PET small animal scanner is part of this environment. It is a specifically built scanner able to perform both PET and SPECT and simultaneous PET/SPECT acquisitions. The scanner was originally developed at the Department of Physics of the Universities of Ferrara and Pisa, Italy. From 2003, fully engineered version of the scanner have been produced and commercialized by the small italian company I.S.E. Ingegneria dei Sistemi Elettronici s.r.l., Pisa, Italy.

This thesis deals with the physical calibration and characterization and with preclinical applications of a new version the YAP-(S)PET originally developed.

Chapter 2 presents an overview of the main characteristics of the emerging molecular imaging and of the small animal systems and its applications in the field.

In chapter 3 the main hardware and software characteristics of the YAP-(S)PET scanner are described in detail. The YAP-(S)PET User Friendly interface and the reconstruction algorithms are widely reported.

Chapter 4 deals with the hardware and software calibration procedures that are necessary periodically and every time a new scanner has been realized. Both PET and SPECT calibration procedures are presented for various head-to-head distances: 100, 125 and 150 mm.

In chapter 5 the performance of the scanner in PET and SPECT modalities are reported. The performance evaluation were performed at various head-to head distances (100, 125 and 150 mm) in order to evaluate the best working point of the YAP-(S)PET scanner.

Chapter 6 illustrates how we were able to implement the possibility to perform simultaneous PET/SPECT acquisitions. The combination of PET and SPECT techniques for small animal studies could offer the unique possibility of developing new and interesting protocols for the investigation of many biological phenomena more effectively than with PET or SPECT modality alone.

Finally, chapter 7 describes some of the imaging studies performed in collaborations with different research groups. The experiments were performed in both PET and SPECT modalities, with different tracers either with mice or rats. All the experiment can be grouped in three main areas corresponding to different medicine branch: oncology, cardiology and neuroscience.

Chapter 2

Molecular imaging and small animals

When Watson and Crick elucidated the double-helical structure of DNA in 1958, they made the greatest discovery of the XX century in the biological sciences. This discovery initiated a time in biology in which biological and physical scientists would strive to unravel the genetic code and its regulated expression, which determines the genotypic basis for the phenotypes of all the cells within the organism. Today, intense exploration is taking place in the biological sciences to determine the patterns of gene expression that encode for normal biological processes, such as replication, migration, signal transduction of cell communication, and the many other functions that cells perform. In addition, belief is growing that most diseases result from altered patterns of gene expression that transition cells to the phenotypes of disease. These alterations in gene expression can result from interactions with the environment, hereditary defects, developmental errors, and aging. As a result, biology is coming together with medicine to design ways to identify these fundamental molecular errors of disease and develop molecular corrections for them. The general name given to this emerging field is molecular medicine [4].

As biology and medicine come together, it is important that imaging also merges with biology to form the technologies referred to as biological or molecular imaging.

Many scientists state that molecular imaging is not a new discipline: nuclear imaging approaches such as positron emission tomography (PET) and single-photon emission computed tomography (SPECT) have been using molecular imaging concepts for more than a decade to visualize the biodistribution of labeled compounds including analyses of receptor occupancy. In these studies image contrast is not governed by the anatomical features of the sample but rather by the local concentration of the radio-labeled reporter compound, i.e., by a molecular property.

Other scientists claim that molecular imaging is a new scientific area merging concepts of molecular biology with noninvasive imaging technologies. This allows the study of biological processes in a noninvasive manner. These concepts go beyond labeling of reporter ligands. They involve the development of a great number of reporter assays that are used to probe specific biological questions. Is the expression of a receptor modified under specific pathological conditions? Does the receptor exert its biological activity. Does it activate its associated signaling cascade? Can these molecular markers be used as early indicators of a pathological transformation? [5]

A precise definition of molecular imaging is an elusive and perhaps not particularly important goal [6]. Rather the term reflects a shift in emphasis and a shift in attitude, moving from the undeniably useful, but largely non-specific, diagnostic imaging approaches that are currently employed in the clinic, to targeting specific genes and proteins that are known to be linked directly or indirectly to human disease.

The emergence of molecular imaging strategies is largely due to recent unprecedented advances in molecular and cell biology techniques, the use of transgenic animal models, availability of newer imaging drugs and probes that are highly specific, and successful development of small-animal imaging instrumentation [1]. This creates the possibility of achieving several important goals in biomedical research:

- to develop noninvasive in vivo imaging methods that reflect specific cellular and molecular processes, for example, gene expression, or more complex molecular interactions such as protein-protein interactions.
- to monitor multiple molecular events near-simultaneously.
- to follow trafficking and targeting of cells.
- to optimize drug and gene therapy.
- to image drug effects at a molecular and cellular level
- to assess disease progression at a molecular pathological level.

- to create the possibility of achieving all of the above goals of imaging in a rapid, reproducible and quantitative manner, so as to be able to monitor time-dependent experimental, developmental, environmental, and therapeutic influences on gene products in the same animal or patient.

2.1 The importance of small animal models in molecular imaging

Molecular imaging in living subjects offers distinct advantages when compared with conventional in vitro and cell culture research techniques in biology.

In contrast to cell and tissue culture, in vivo animal models allow the assessment of phenomena such as tolerances, complementation, and redundancy in biological pathways. Molecular imaging permits both the temporal and the spatial biodistribution of a molecular probe and related biological processes to be determined in a more meaningful manner throughout an intact living subject [1].

Imaging technologies are playing a growing role in animal research, enabling large, expensive laboratory animals to be studied noninvasively and providing the possibility of reducing the number of small laboratory animals required in typical longitudinal studies. As each animal serves as its own individual control, the reproducibility of data from imaging studies may actually be better than that obtained from traditional invasive techniques, although this improvement has yet to be demonstrated unequivocally. Finally, imaging provides a bridge from animal research to human research.

Since the mid 1980s, the effort to understand mammalian biology and the study of disease models have caused the mouse to become the animal of choice. More than 90% of all mammals used worldwide in research in the year 2000 were mice [7]. The rapid rate of reproducibility and short life span of mice aid in keeping down the cost of maintaining colonies and favor them as a molecular biology research vehicle. In addition, most human genes have a related mouse gene, allowing mice to be used as a platform for mimicking many human disease [8]. Furthermore, modern molecular biology contains the technology to “knock-out” or disable genes, and to insert or "knock-in" new ones in order to create many types of transgenic mice. The mouse genome has been the second mammalian genome to be sequenced after the human genome [9].

Molecular imaging of living mice offers distinct advantages when investigating phenotypic abnormalities [1]:

- it eliminates the need to kill such mice as part of their phenotype determination.
- by repetitive imaging it is possible to investigate mutants that are otherwise difficult to interpret with data taken at a single time point.
- it allows concomitant visual and analytical biological phenotyping of animals.
- it allows the researcher to exercise options of multiple imaging strategies (e.g., by using different imaging reporter probes or modalities) in cases in which simple genetic manipulations could result in a very complex phenotype involving a large number of pathways and organs.

Moreover, in vivo mouse imaging as an alternative to killing many animals for histological processing at different time points is also convenient in terms of money. With each transgenic mouse valued in the 200-300 dollars range, the overall costs of conventional post mortem biological assays on many animals can mount substantially. The use of fewer animals in biological assays with molecular imaging would also be more appealing on ethical grounds. In theory, approval for research projects requiring large numbers or many separate cohorts of experimental animals could be obtained more easily [1].

Molecular imaging assays in intact living animals could be of further benefit in resolving biological questions raised by pharmaceutical scientists. Transgenic animals are useful in guiding early drug discovery validating the target protein, evaluating test compounds, determining whether the target is involved in any toxicological effects of test compounds, and testing the efficacy of compounds to ensure that the compounds will act as expected in man [1].

In some disciplines, particularly in neuroscience, the rat also remains an important experimental animal, partly due to the ease of surgical manipulation of the rat brain versus the mouse brain (2 g as opposed to 0.45 g). In addition, there is a large historical knowledge base of both the anatomy and the function of the rat brain, deriving from many decades during which it was the preferred model [10].

2.2 Molecular imaging instrumentation and techniques

Biological discovery has moved at an accelerated pace in recent years, with considerable focus on the transition from in vitro to in vivo models. As such, there has been a greater need to adapt clinical imaging methods for noninvasive assays of biochemical processes. Considerable efforts have been directed in recent years toward the development of noninvasive, high-resolution, small animal in vivo imaging technologies (see figure 2.1). The widespread availability and use of miniaturized imaging systems for rodents are invaluable resources for basic science laboratories. Nonetheless, significant challenges remain to be overcome when attempting to image a 30-g mouse as compared with a 70-kg human, including the size of the subject, the total volume that must be evaluated, the spatial resolution necessary for obtaining meaningful anatomical and/or functional data, and the total time spent on acquiring a set of images [11]. A comparison between human and small animal size can be obtained by figure 2.2.

In small animal research, the primary goal is to obtain as high a signal as possible and to localize the signal as accurately as possible with high temporal resolution and with minimal amount of molecular probe. The ultimate goal is to provide a device that produces a three-dimensional image of anatomical and biological information fused together. The various existing imaging technologies differ for the following main aspects [1]:

- spatial and temporal resolution.

- depth penetration.

- energy used for image generation (ionizing or nonionizing, depending on which component of the electromagnetic radiation spectrum is exploited for image generation).

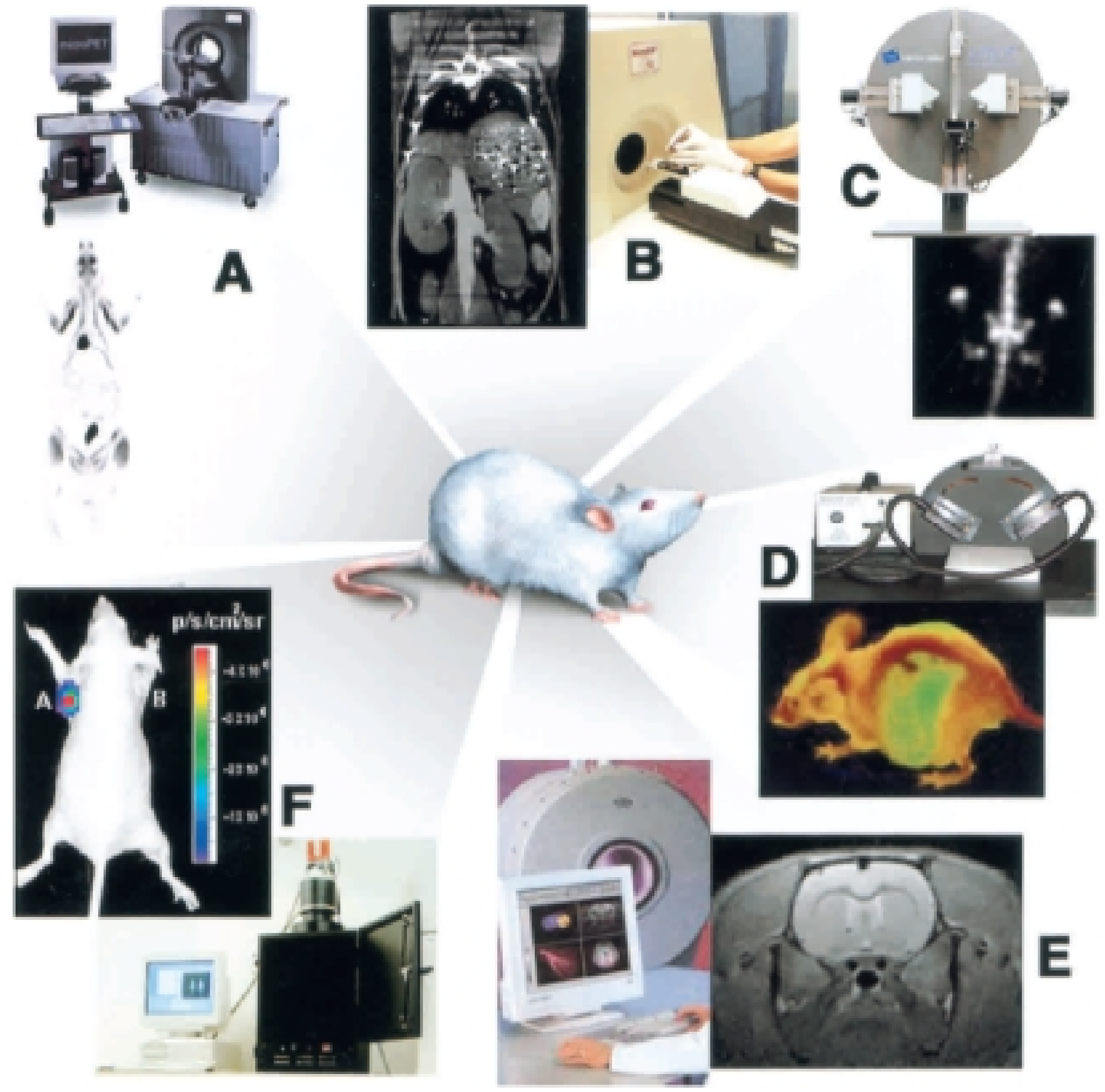

Figure 2.1: Illustrative examples of the variety of images that can be obtained with different imaging modalities. (A) microPET whole-body coronal image of a rat injected with ^{18}FDG, showing uptake of tracer in tissues including muscles, heart, brain, and accumulation in bladder owing to renal clearance. (B) microCT coronal image of a mouse abdomen after injection of intravenous iodinated contrast medium. (C) microSPECT coronal image of a mouse abdomen and pelvis regions after injection of ^{99m}Tc methylene diphosphonate, showing spine, pelvis, tail vertebrae, femurs, and knee joints owing to accumulation of tracer in bone. (D) Optical reflectance fluorescence image of a mouse showing GFP fluorescence from the liver, abdomen, spine, and brain. The mouse contains GFP-expressing tumor cells that have spread to various sites. Images are courtesy of Dr. Hoffman, Anticancer Inc. (E) microMRI coronal T2-weighted image of a mouse brain. (F) Optical bioluminescence image of a mouse with a subcutaneous xenograft expressing Renilla luciferase in the left shoulder region, after tail-vein injection of the substrate coelenterazine. Images were obtained using a cooled CCD camera. The color image of visible light is superimposed on a photographic image of the mouse with a scale in photons per second per square centimeter per steradian (sr) [1].

Figure 2.2: Relative size of a human, rat and mouse brain [12].

- availability of injectable/biocompatible molecular probes
- the respective detection threshold of probes for a given technology.

Table 2.1 outlines some of the general characteristics of the imaging modalities available.

Imaging technique	Spatial resolution	Temporal resolution	Sensitivity (mol/l)	Molecular probe	Amount of probe	Quantitative degree	Advantages	Disadvantages	Cost
PET	1-2 mm	10 s to min	$10^{-11} - 10^{-12}$	radiolabelled direct or indirect	nanograms	+++	high sensitivity; isotope can substitute naturally occurring atoms; translational quantitative studies	PET cyclotron or generator needed	++++
SPECT	1-2 mm	minutes	$10^{-10} - 10^{-11}$	radiolabelled direct or indirect	nanograms	++	many molecular probes available; multiple probes simultaneously	low sensitivity	+++
Optical bioluminescence imaging	3-5 mm	seconds to minutes	not well characterized, possibly $10^{-15} - 10^{-17}$	activable indirect	micrograms to milligrams	+ to ++	high sensitivity quick, easy low cost	low spatial resolution; 2D only	++
Optical fluorescence imaging	2-3 mm	seconds to minutes	$10^{-9} - 10^{-12}$	activable direct or indirect	micrograms	+ to ++	high sensitivity	low spatial resolution	+/++
MRI	25-100 μm	minutes to hours	not well characterized	activable direct or indirect	micrograms to milligrams	+ to ++	high spatial resolution	low sensitivity; long time	++
Ultrasound	50-500 μm	seconds to minutes	not well characterized	limited activable direct or indirect	micrograms to milligrams	+ to ++	real time; low cost	mostly morphological	+

Table 2.1: Characteristics of imaging modalities available in molecular imagign. Temporal resolution refers to the frequency at which the final interpretable version of images can be recorded/captured from the subject once the imaging process is initiated. This relates to the time required to collect enough events to form an image, and to the responsiveness of the imaging system to rates of any change induced by the operator or in the biological system at hand [1].

2.2.1 Radionuclide imaging

The primary advantage of radioactive assays (whether in vivo, ex vivo or in vitro) is their exquisite sensitivity and the ability, with appropriate care, of radiation detection systems to provide quantitative measurements of radioactivity concentrations deep inside tissue. Radiolabelled tracers have a long history of being used to elucidate physiology, metabolic pathways and molecular targets [13], and to provide a high sensitivity tool for molecular imaging studies. A very large number of radiolabelled tracers have been developed to probe specific biological targets and functions [14], and a growing number are moving into clinical use. An important strength is the availability of radionuclides of biologically relevant elements, particularly carbon, allowing contrast agents to be labelled by direct isotopic substitution. This allows small biomolecules (many drugs, receptor ligands etc) to be labelled without changing their biochemical properties. Another powerful approach is to create analog radiotracers, in which deliberate chemical changes are made to a biologically active molecule to isolate specific pathways or cause specific trapping of a radiotracer in cells expressing the target of choice. Analog radiotracers are also designed to allow the use of isotopes of elements that are not found within the molecule of interest, but that have good imaging properties. Larger biomolecules (peptides, antibodies, RNA, synthetic macromolecules) are also readily labelled with a wide range of radionuclides that have excellent properties for imaging. A list of the major radionuclides that are currently being used for in vivo nuclear imaging is provided in table 2.2. A further advantage is that nuclear imaging approaches are readily translated to the clinic, as the majority of the listed radionuclides produce photons with sufficient tissue penetration for studies in man. Disadvantages of nuclear imaging approaches include obvious factors such as the involvement of ionizing radiation, and more subtle factors such as the fact that radioactive decay cannot be controlled, hence there is always non-specific background signal present in an image due to non-specific binding of radiotracers, residual radiotracer in the circulation and routes of excretion [6].

Nuclear imaging techniques include high resolution (<100 μm) ex vivo autoradiographic techniques using film, phosphor storage plates or real time autoradiographic systems [15] and in vivo methods using radionuclides that produce appropriate energy photons (gamma-rays, annihilation photons or characteristic x-rays with energies in the range of 25-511 keV) during decay. The in vivo methods are further broken up into single photon imaging that utilize radionuclides with single or multiple uncorrelated gamma ray emissions and PET in which radionuclides decay by positron emission resulting in two simultaneous annihilation photons emitted back-to-back [2].

The development of higher resolution and higher sensitivity animal PET and SPECT systems is allowing molecular and genomic imaging approaches, traditionally approached by ex vivo autoradiographic methods, to be translated in vivo into animal models of disease [16,17]. Dramatic improvements in image quality have been achieved by using novel detector and collimation approaches, and by exploiting the more favourable environment found in small-animal imaging.

One of the advantages of nuclear imaging, say as, compared to optical imaging, is that the radiation involved is highly penetrating, and so the dependence of the detected signal on the depth at which it is emitted is fairly small. Even without correction for scatter and attenuation, nuclear images within small animals can exhibit fairly high quantitative accuracy in specific circumstances and with the appropriate calibration object [6].

Radionuclide	**Half life**	**Energy of principle photons (keV)**	**Imaging modality**
^{11}C	20.4 mins	511	PET
^{18}F	110 mins	511	PET
^{64}Cu	12.7 h	511	PET
^{99m}Tc	6.02 h	140	SPECT
^{111}In	2.83 days	171, 245	SPECT
^{123}I	13.2 h	159	SPECT
^{124}I	4.18 days	511, 603, 723, 1690	PET
^{125}I	60.1 days	27, 31, 35	SPECT
^{131}I	8.04 days	354	SPECT

Table 2.2: Radionuclides commonly used for in vivo nuclear imaging.

2.2.2 Optical imaging

There has been tremendous growth in the use of optical approaches for in vivo imaging of small laboratory animals. This is in part due to the accessibility of optical approaches, and also in part because of their extremely high sensitivity. Light is both scattered and absorbed in tissues, but there is an absorption minimum corresponding to wavelengths in the approximate range of 700-950 nm [18]. At these wavelengths, the light is still readily scattered but the absorption length is on the order of several centimetres. Thus, light emitted from deep inside a small animal has a reasonable probability of reaching the surface for external detection. Although this light has in general scattered many times when it reaches the surface, some positional information is retained based on the intensity, spatial distribution and spectral distribution of the emitted light [19]. This region of the electromagnetic spectrum is known as the "optical window" because of the more favourable characteristics for imaging through tissue.

At the present time, most studies are based on imaging the intensity of the emitted light at the surface of the animal with straightforward detector systems that are amenable for use in biology labs and have the capability of relatively high throughput. Two distinct contrast mechanisms are being used for molecular and genomic imaging studies: one involving fluorescence [20], and the other involving bioluminescence [21].

In fluorescence imaging, an external light source, either a laser, or a broadband source (e.g., a mercury lamp) with an appropriate low-pass filter, is used to excite fluorescent molecules inside the subject. These fluorescent molecules may be genetically engineered into a mouse, for example by incorporating the gene for a fluorescent protein as a reporter gene. Green Fluorescent Protein (GFP) has been widely used in this manner for cell culture and tissue slice experiments, but is less well suited for in vivo use because of the relatively short excitation (peak $\sim$ 470-490 nm) and emission (peak $\sim$ 510 nm) wavelengths that place it outside the optical window and in a part of the spectrum where there is significant autofluorescence of tissue components. Despite these difficulties, GFP has been used successfully for some in vivo imaging studies [22]. Subsequently, GFP mutants and other fluorescent proteins have been discovered that have excitation and emission spectra better suited to in vivo imaging [23–25]. Another approach to introducing fluorescent molecules into an animal is to use fluorophores (or more recently, fluorescent particles known as quantum dots) as labels on biologically interesting molecules [26]. This is analogous to radionuclide labelling for nuclear imaging, although the approach generally is limited to the labelling of larger biomolecules where the size of the fluorophore does not interfere with the biological activity of the agent. Again, fluorophores that are excited and emit in or close to the optical window are preferred for good penetration depth and large amplitude signals [6]. Table 2.3 provides data on a number of fluorophores that are being used for in vivo studies and an example of a study carried out with a near infrared fluorescence probe is shown in figure 2.3.

Name	**Type of agent**	**Excitation max (nm)**	**Emission max (nm)**	**Extinction coefficient (cm^{-1} M^{-1})**	**Quantum yield**
Cy 5	Fluorophore	649	670	250000	0.28
Cy 5.5	Fluorophore	675	694	190000	0.23
Cy 7	Fluorophore	743	767	200000	0.29
Alexa Fluor 700	Fluorophore	702	723	192000	
Alexa Fluor 750	Fluorophore	749	775	240000	
EGFP	Fluorescent protein	489	508	55000	0.60
DsRed	Fluorescent protein	558	583	57000	0.79
mRFP1	Fluorescent protein	584	607	44000	0.25

Table 2.3: Properties of some fluorophoresa and fluorescent proteins. (Data for DsRed and mRFP1 from [25]. Other data from manufacturers' datasheets [6].)

There are two key advantages to fluorescence imaging. Firstly, many of the fluorophores used have high quantum yields, leading to robust signals when using appropriate illumination and acquisition times. Secondly, as described earlier, the fluorescence emission can be activated by specific biologic molecules or events. This eliminates signal from contrast agent that is circulating and from paths of excretion (a limiting problem for radiotracers), reducing background "noise". This allows very low concentrations (subnanomolar, and with some activatable agents, picomolar or better) of enzymes to be detected. The disadvantage of fluorescence imaging is that there is autofluorescence from tissue that forms a background that ultimately limits detection sensitivity. A second problem is that light has to get into the animal (to excite the fluorescent molecules) and back out again (to reach the detector). Because of the high degree of scattering of both the excitation and emission light, it is not possible to excite and isolate the fluorescence within very small volumes of tissue inside the animal. As a consequence of the strong dependence on depth of both the intensity of the excitation light and the detection of the emission light, quantitative analysis of the images, in all but the very simplest cases of a small point emitter, becomes extremely difficult [6].

Fluorescence imaging can be carried out using conventional CCD cameras. The use of back-illuminated CCDs and cooling, enhances sensitivity and signal-to-noise ratio, but for many studies general purpose scientific CCD cameras are sufficient, because detection sensitivity is limited by autofluorescence rather than by the noise characteristics of the detector. A simple black box and a lens coupled CCD camera connected to a computer can yield acceptable fluorescence images showing the light distribution on the surface of the animal in just a few seconds or minutes [27]. The second approach to in vivo optical imaging involves introducing reporter genes that encode for enzymes (known as luciferases) that can catalyze a light-producing reaction. This process is called bioluminescence and luciferases are found in organisms such as fireflies, glow worms and jellyfish [28]. The most commonly used reporter gene for imaging is the one that encodes for firefly luciferase [29]. This gene is introduced as a reporter gene. Just prior to imaging, animals are injected with the substrate for the enzyme. In the case of the firefly luciferase the substrate is luciferin, a small molecule that rapidly distributes throughout the whole body of the mouse after intravenous or intraperitoneal injection. In cells that are expressing the luciferase reporter gene, the luciferin, in the presence of oxygen and ATP (Adenosintriphospat), is converted to oxyluciferin with the emission of light (peak at 560 nm). The reaction is catalyzed by the luciferase enzyme and does not occur to any significant extent when luciferase is absent. The generation of an optical signal is therefore specific to cells that contain the reporter gene. Mutations of the naturally occurring firefly gene has resulted in a shifting of the emission peak to around 620 nm, with significant amounts of light being emitted in the 550-700 nm range, improving its sensitivity for in vivo imaging studies [21].

The advantage of the bioluminescence approach is that there is no need for external light stimulation. There is no problem, therefore, in depth of penetration of the excitation light as there is with fluorescence, and there is no autofluorescence background to contend with. The disadvantage is that this approach is limited to studying genetically manipulated cells or transgenic mice, or infectious agents such as bacteria and viruses, as the reporter gene has to be introduced to the organism that is to be studied. Also, the bioluminescence signals are typically very weak. These low signals require the use of high quantum efficiency CCDs that are cooled to minimize dark current over the integration time required to obtain an image (typically a few minutes) [6].

The biggest efforts in optical imaging at the present time are devoted to moving from a single image of the light intensity projected at the surface of the animal to tomographic images that provide information on the distribution of the light source in 3D. This involves acquiring data from a small number of views such that the light intensity across the surface of the entire mouse can be mapped.

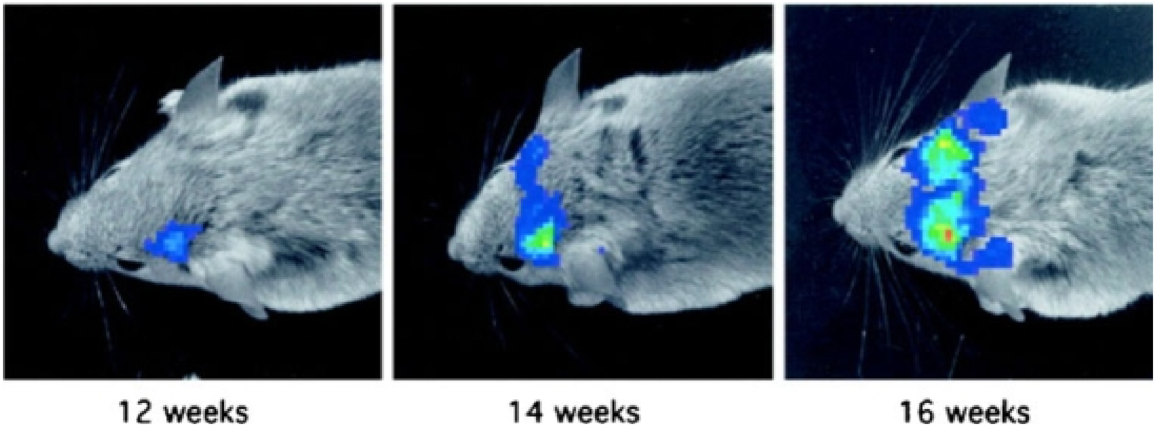

Figure 2.3: In vivo bioluminescence images (in colour) from cancer cells carrying a luciferase reporter gene. These images show the growth of a pituitary tumour over a period of four weeks. The greyscale image is a reflectance light image of the mouse for anatomic reference [6].

2.2.3 Magnetic resonance imaging

Magnetic Resonance Imaging (MRI) is one of the more mature technologies for small-animal imaging. Magnetic resonance microscopy (generally defined as imaging with a resolution of better $\sim$ 100 microns) has been around since the mid 1980s and has found particular applications in neuroscience [30,31] and developmental biology [32]. High-field magnets are introduced in small-bore animal imaging systems several years before they can be achieved for larger bore human applications. Therefore these animal systems serve as important test-beds and catalysts for developing high resolution, high speed and high sensitivity pulse sequences. Most small-animal imaging is currently carried out on horizontal-bore instruments with field strengths between 4.7 T and 9.4 T and bore sizes of 20-40 cm. Research systems with field strengths as high as 11.7 T (40 cm horizontal bore) and 21.1 T (8.9 cm vertical bore) are also being evaluated for small-animal imaging [33]. Higher field strengths are desirable for high-resolution imaging because the signal-to-noise ratio (SNR) is proportional to field strength, and the detected signal is proportional to the tissue volume within a voxel. A reduction in voxel size from $1 \times 1 \times 1$ mm to $0.1 \times 0.1 \times 0.1$ mm therefore results in a 1000-fold reduction in the detected signal.

Since SNR is only linearly proportional to field strength, higher fields only in part make up for the reduced voxel size in high resolution images. Therefore, images at resolutions of tens of microns can only be achieved with very long acquisition times, typically many hours for a whole mouse.

In vivo images of anatomy with a spatial resolution of a few hundred microns can be achieved in several minutes with MRI when combined with appropriate physiologic gating to control cardiac and respiratory motion. Sophisticated physiologic monitoring and forced respiration systems have been developed to allow motion-free in vivo imaging and well controlled physiologic status deep inside a high-field magnet [34]. The good soft-tissue contrast achieved by well-designed pulse sequences has led to MRI becoming the method of choice for following anatomic changes in soft tissue that may be related to a disease course or an intervention. Furthermore, MRI has the ability to measure physiological parameters, including water diffusion and blood oxygenation levels (which leads to the contrast used in functional MRI to study brain activation). The addition of "passive" contrast agents, such as Gd-DTPA, further enhances the utility of MRI, allowing vascular density, permeability and perfusion to be assessed. Another example of a passive agent is the use of Mn^{2+} ions for tract-tracing studies in the brain [35].

Taken together, these MRI methods provide a powerful set of tools for interrogating anatomic and physiologic changes that are a consequence of specific cellular or molecular alterations in living animals. The development of targeted and activatable contrast agents for MRI that offer the prospect of direct molecular imaging.

These agents are based on transition metals or lanthanides that are paramagnetic and change the relaxation time (either T1 or T2) in tissue regions in which they accumulate [36].

One area of active research is into optimal RF coil design for high-field use. Design of better volume coils should improve SNR and allow imaging of an entire animal in significantly shorter times. High-powered imaging gradients with fast switching rates for small-volume imaging have also improved the ability to acquire fast images at higher signal-to-noise, and further improvements in the gradient coils are also likely [6].

2.2.4 X-ray computed tomography

In vivo imaging of small animals with CT has a critical role to play in the evolution of molecular imaging [37, 38]. The conventional anatomic CT with non-specific contrast agents is a relatively straightforward way to obtain high-resolution anatomic information which is often important to analyze molecular imaging studies obtained using other modalities (especially nuclear and optical approaches). MicroCT is also a valuable tool for indirect approaches to molecular imaging [37], for example, imaging changes in vascular density and permeability associated with angiogenesis and anti-angiogenic therapeutics. MicroCT is the method of choice for tracking changes in diseases that affect bone. The high resolution of microCT allows very sensitive detection of bone growth, destruction, remodelling and changes in bone density, and is therefore ideally suited for studying the consequences of diseases such as osteoporosis and rheumatoid arthritis, and for evaluating the effects of therapeutic interventions on the progression of these diseases [6]. MicroCT also has the potential to be used as a fairly high-throughput imaging technique and investigators are considering its use for phenotypic screening in genetically manipulated mice [39].

Some of the specific and continuing challenges in moving from specimen imaging to in vivo imaging have been to reduce the radiation dose, deal with motion artefacts, change the system geometry to allow the animal to be placed horizontally and remain stationary during scanning and to decrease imaging time.

To date, microCT systems have made use of 2D x-ray detectors developed for specimen imaging or digital mammography, and systems generally acquire data in cone-beam geometries. This imaging geometry is relatively simple to implement and the 3D collection makes the most efficient use of the relatively modest x-ray flux that is emitted by the compact microfocus fixed anode x-ray tubes generally employed in these applications [40]. These low-power tubes are supported by compact power supplies and the small x-ray focal spot size offers the potential for very high spatial resolution. At the same time, the anode current (and hence number of x-rays produced) of these compact tubes is limited by the small focal spot size and the fixed anode design when operated continuously for CT acquisition. Typical x-ray tube parameters used in microCT systems are focal spot sizes in the range of 10-100 microns, and tube currents of at most a few mA at an anode voltage of 25-75 kV. Most commonly, tungsten anode tubes are being utilized. For CT imaging, the x-ray tube is generally operated continuously with a shutter to control when x-rays irradiate the object. A resolution of tens of microns is achievable in some microCT systems [6].

2.2.5 Ultrasound

Ultrasound also has been successfully adapted as a tool for small-animal imaging and together with the development of novel echogenic contrast agents promises to add molecular imaging capability in a number of very important areas. Advantages of ultrasound include real-time imaging, portability, low cost, high spatial resolution and the absence of ionizing radiation. One of the key trade-offs in ultrasound is between acoustic frequency, depth of penetration, and spatial resolution. In small-animal models, a depth of penetration of 1-2 cm is generally sufficient, allowing high frequencies on the order of 20-60 MHz to be used. This leads to a spatial resolution in the range of tens of microns [6]. One of the really unique capabilities of ultrasound is in developmental studies [41], particularly pre-natal studies in genetically manipulated mice (see figure 2.4). Genetic manipulations often result in embryonic lethal phenotypes that do not survive to birth, hence the ability to determine phenotypes in utero is extremely important. High-resolution embryonic imaging cannot be performed noninvasively with any other modality at the present time due to fetal motion, which requires very fast acquisition. The real-time nature of ultrasound is also of importance in studying cardiac anatomy and function in rodents, and opens up opportunities for image-guided interventions in animal models.

The capabilities of ultrasound go far beyond anatomic imaging for phenotypic analysis. High frequency Doppler flow mapping enables quantitative measurements of blood flow not only in major vessels, but importantly, also in the microcirculation [42]. Contrast agents are being developed that promise to give ultrasound a major role in molecular imaging and therapeutics [43, 44]. In their simplest form, these contrast agents are small bubbles (typically 1-10 microns in diameter) in which a lipid or albumin shell is filled with a gas such as perfluoropropane. These microbubbles produce very strong ultrasound echoes due to differences in their compressibility and density compared to surrounding biologic tissues. In fact a standard clinical ultrasound system can detect the echo from an individual microbubble, thus in principle, the sensitivity for detection of such contrast agents is extremely high. Microbubbles are already in clinical use, where they are used to detect small vessels and capillary beds by enhancing the signal from the small volume of blood. In addition, microbubbles have interesting non-linear oscillation properties in response to ultrasound radiation. With appropriate acoustic pressure, these bubbles can actually burst. By applying local acoustic pressure to burst the bubbles, the contrast agent can be selectively destroyed within a small volume of tissue. By imaging the return of the signal as blood containing intact contrast agent flows into the region, it is possible to quantify important physiologic parameters such as blood velocity, blood flow and blood volume in the microvasculature. These measurements can be repeated over and over for a single contrast agent injection with high spatial and temporal resolution [6].

2.3 General requirements for molecular imaging

The acquisition of ex vivo information in biomedical research has become relatively easy, because a myriad of specialty reagents, ligands, protocols, and devices have been commercially developed over the past two decades. On the other hand, molecular imaging in living subjects presents more theoretical and practical challenges than in vitro or cell culture detection, primarily because of the need for probes to be

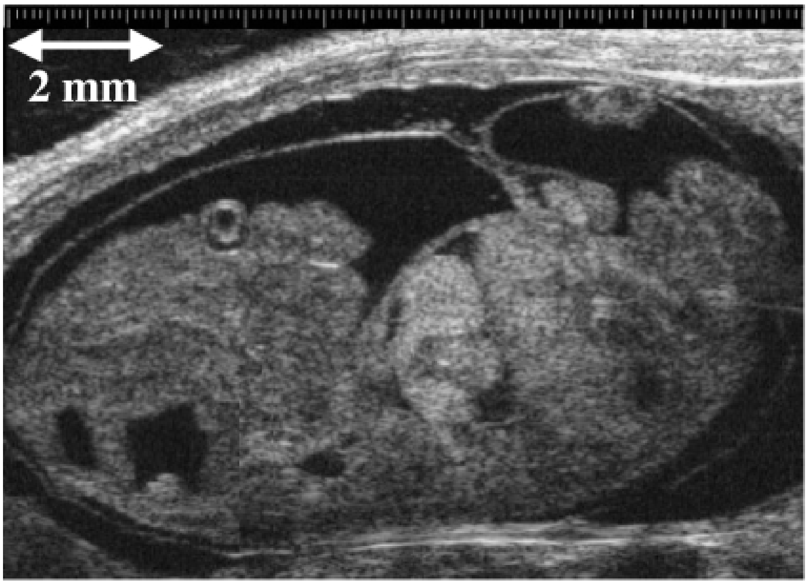

Figure 2.4: High frequency (40 MHz) ultrasound image of a 13.5-day-old mouse embryo. The resolution in this image is better than 100 microns. (Adapted with permission of World Federation of Ultrasound in Medicine and Biology from [45]).

biocompatible, the presence of additional delivery barriers, and the necessity for developing special in vivo amplification strategies [46]. There are several general areas in which considerable research efforts are ongoing [11,27] and will also be necessary in the future to perform in vivo molecular imaging (by seeking answers to the questions in parenthesis) [1]:

- selection of appropriate cellular and subcellular targets to image (what biological process is to be imaged?).
- development of suitable in vivo affinity ligands, that is, molecular imaging probes (what biocompatible chemical/biochemical/ molecular entity can be used in vivo to distinguish that particular biological process and help to generate specific images of that target?).
- delivery of these probes in a manner that efficiently overcomes biological barriers (what are the pharmacokinetic attributes of these probes contributing to successful imaging?).
- amplification strategies able to detect minimal target concentrations, usually in the pico- to nanomolar range (can the imaging signal be amplified?).

- development of imaging systems with high spatial/temporal resolution and sensitivity suitable for small laboratory animals, and that ultimately can be translated to the human patient (what are the imaging modalities and instrumentation available to achieve molecular imaging in living subjects?)

2.4 Specific applications of PET molecular imaging

The use of either of PET or SPECT in small-animal biological research has the advantage that essentially the same methodology can be used in human applications, thereby facilitating translation to the clinic. The classical example of a translational research application in molecular medicine is the introduction of STI- 571 (Gleevec ®), a small molecule designed to alter specific intracellular signalling pathways involved in cell proliferation and apoptosis, which lead to chronic myeloid leukaemia [47]. STI-571 specifically inhibits the oncogenic protein tyrosine kinase breakpoint cluster region (BCR)Abelson (ABL), which is constitutively activated by a chromosomal translocation.

Some PET molecular imaging specific applications are reported.

2.4.1 Glucose metabolism in brain and heart

The probe of excellence in PET studies of metabolism is 2-deoxy-2-[^{18}F]fluoro-D-glucose (FDG). It is transported into cells by the glucose transporter and subsequently converted to the phosphorylated form by hexokinase. FDG-6-phosphate, the product of hexokinase, cannot be further metabolized and is “trapped” inside cells, where its accumulation can be measured in the PET scanner.

In the latest generation of small animal PET systems, the spatial resolution is sufficient ($<$2 mm) to clearly identify structures such as the thalamus, striatum, and cortex subunits are readily and to separate extracerebral activity from cerebral activity in the adult rat. A range of semiquantitative investigations of brain plasticity and conscious brain activation have been performed [48] and a series of fully quantitative longitudinal studies in a traumatic brain injury model, complete with direct comparison to quantitative 2DG autoradiography [49], have also been reported. Even at this resolution, though, there is a problem with brain FDG studies in small rats and mice, due to spillover of activity from the Harderian glands into the cortex. The same spillover problem has been reported in adult rats as well, but with poorer resolution tomographs [50]. Small animal PET scanners are also being employed to measure glucose metabolism and myocardial blood flow (with ^{13}N-ammonia) in rat and mouse heart models of ischemia and infarction. Initial investigations comparing infarct extent [51] and FDG uptake [52] against in vitro measures are promising. The group at Sherbrooke University and Prof. Markus Schwaiger of the Nuklearmedizinische Klinik und Poliklinik der Technischen Universitat Munchen, Munich, Germany have also demonstrated the feasibility of acquiring gated PET images of the rat heart [53, 54].

2.4.2 Dopaminergic system in rat brain

Some of the earliest small animal PET work used a variety of probes to explore the dopaminergic system in the rat brain. Probes that reflect dopamine synthesis (e.g., ^{18}F-fluoro-metatyrosine, ^{18}F-FDOPA), D2 receptor binding (e.g., ^{11}C-raclopride, ^{18}F-fluoroethylspiperone), and dopamine transporter concentration (e.g., ^{11}C-CFT) are available [10]. These probes are accumulated to a high degree in the striata, which are fairly large and well separated in the rat brain. Therefore, successful investigations can be performed even at moderate 3- to 4-mm spatial resolution [55]. This work demonstrated, for example, the ability of PET to quantify D2 receptor in the living rat brain [56], the survival and function of neural transplants [57–59], and the effects of drugs on D1 and D2 receptors [60, 61]. An example from one of these studies is shown in figure 2.5.

2.4.3 Oncology

Some of the best opportunities for small animal PET imaging are in oncology. Studying transplanted primary tumors is often simple since they can be placed away from major organs in the thigh, shoulder, or back of the animal. Under these circumstances, corrections for partial volume are straightforward. In addition, the usual variability between one animal and the next is effectively removed and each animal

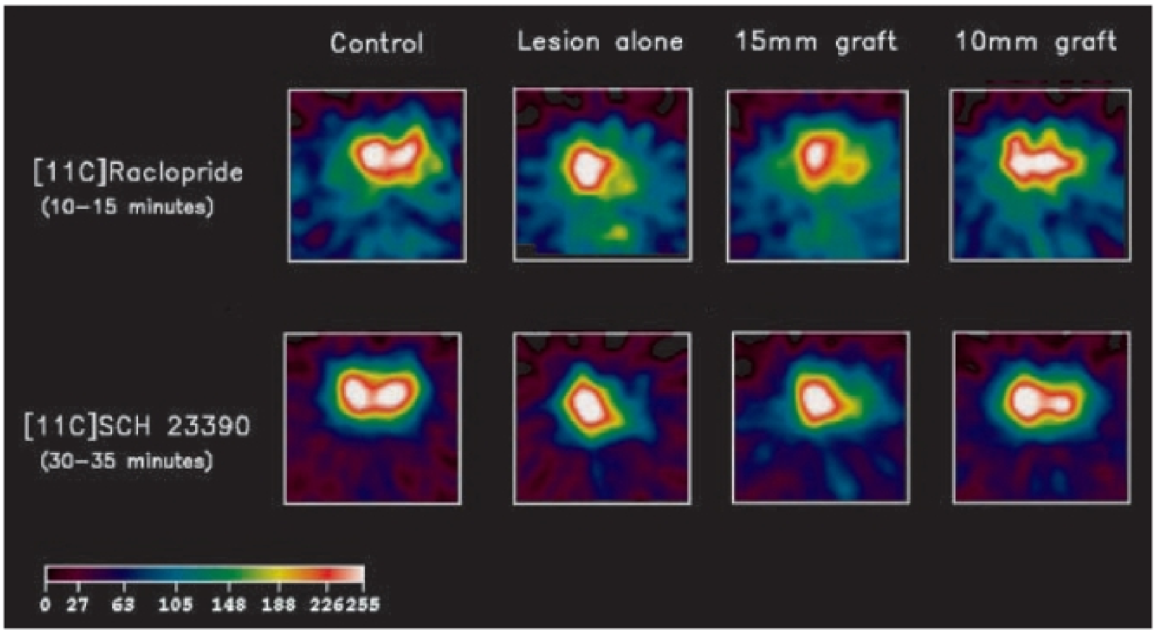

Figure 2.5: Coronal section through rat brains showing D1 and D2 receptor binding following injection of ^{11}C-SCH 23390 and ^{11}C-raclopride respectively. Four different rats are shown: control rat; lesioned rat (unilateral ibotenic acid lesion); lesioned rat following graft of striatal cells from 15-mm crown to rump fetuses; lesioned rat following graft of striatal cells from 10-mm crown to rump fetuses. Rats with grafts were scanned approximately 10 months post surgery. Note: Loss of D1 and D2 binding signal on right side of image following lesion and partial recovery of the signal in the rat that received a striatal graft [10].

can be used as its own control. Furthermore, PET can survey the entire animal and allows the spread of metastatic disease to be observed and monitored [10]. There is a range of PET probes that are of interest in cancer models, including FDG, 3'-deoxy-3'- [^{18}F]fluorothymidine (FLT), a marker of DNA replication and cell proliferation [62], and labeled antibodies and antibody fragments [63]. The power of serial PET investigations as a tool for assessing the time course and localization of antibody fragments is demonstrated in Figure 2.6, which illustrates a mouse imaged using an anti- CEA minibody, a genetically engineered antibody fragment that binds with high affinity to carcinoembryonic antigen [64].

2.4.4 Reporter gene expression imaging

The merger of molecular imaging with molecular biology to create methods to measure reporter gene expression in vivo with PET is an area that has attracted increasing interest. In analogy with the way Green Fluorescent Protein (GFP) is used as a stan-

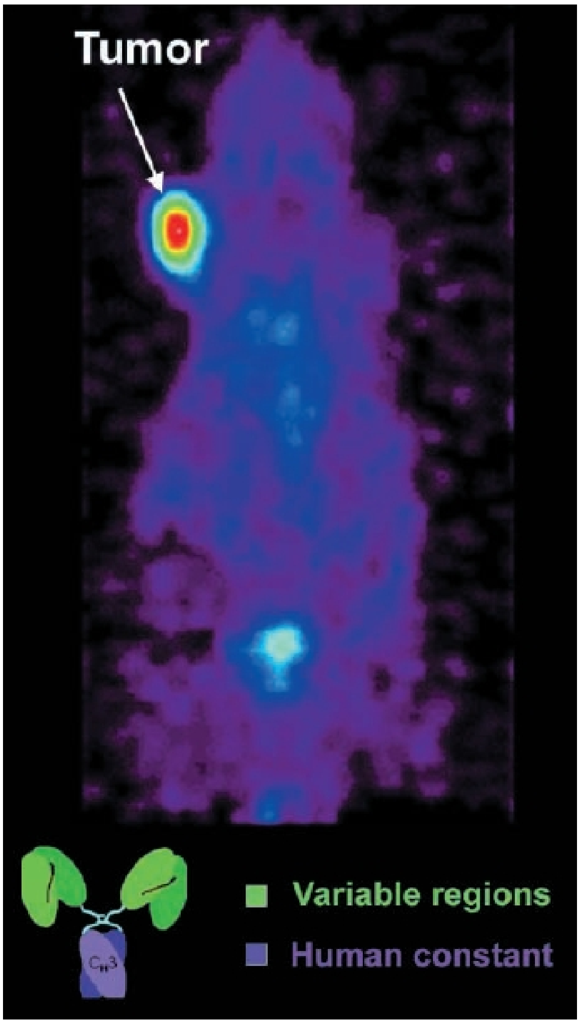

Figure 2.6: Coronal PET image of a mouse injected with a radiolabeled anti-CEA minibody, a genetically engineered antibody fragment that binds with high affinity to carcinoembryonic (CEA) antigen. The minibody was radiolabeled with the positron emitter 124I and used for microPET imaging of LS174T tumor xenograftbearing mice. The mouse shown had a 73-mg tumor on the left shoulder, and was injected with 60 Ci of 124I anti-CEA 18 h before imaging. Note the absence of anatomical landmarks besides the faint mouse outline. The engineered antibody fragment (minibody) is also illustrated [10].

dard reporter gene in molecular biology [65], a PET reporter gene (PRG) expresses a protein that can trap or bind a positron-labeled probe [66–71]. These are called the PET reporter probes. The reporter gene is driven by the same promoter as the gene of interest (the promoter can be thought of as a “switch” that turns the expression of the gene on or off), such that the gene of interest is always expressed along with the reporter gene. The retention of the positron-labeled probe by the protein product of the PRG has been shown to be proportional to the level of reporter gene expression. In turn, this reflects the level of expression of the gene of interest, which has the same promoter or is coupled directly to the PRG (i.e., PRG coupled to a therapy gene) [72]. In this way, the location, magnitude of expression, and time course of expression levels of any gene that is introduced into a mouse can be monitored in vivo. This allows gene therapy protocols to be monitored in vivo, both in animal models and, ultimately, in humans by PET. The same PRG approach can be used in transgenic mice, where every cell in the mouse carries the PRG. In this case, the signal is only detected when the promoter driving the PRG is switched on in the natural location where specific genes are expressed. This now enables endogenous gene expression to be investigated in mice models [73]. Figure 2.7 is an image of a mouse bearing two tumors, each expressing a separate reporter gene, namely the HSV1-tk gene and the dopamine type 2 receptor (D2R) gene. The mouse was injected in two different instances with two different reporter probes, 3-(2'-[^{18}F]fluoroethyl)- spiperone (FESP) and 8-[^{18}F]fluoropenciclovir (FPCV), each probe being specific for one of the gene reporter systems. The image shows clearly the selectivity of the reporter probes in each tumor [74].

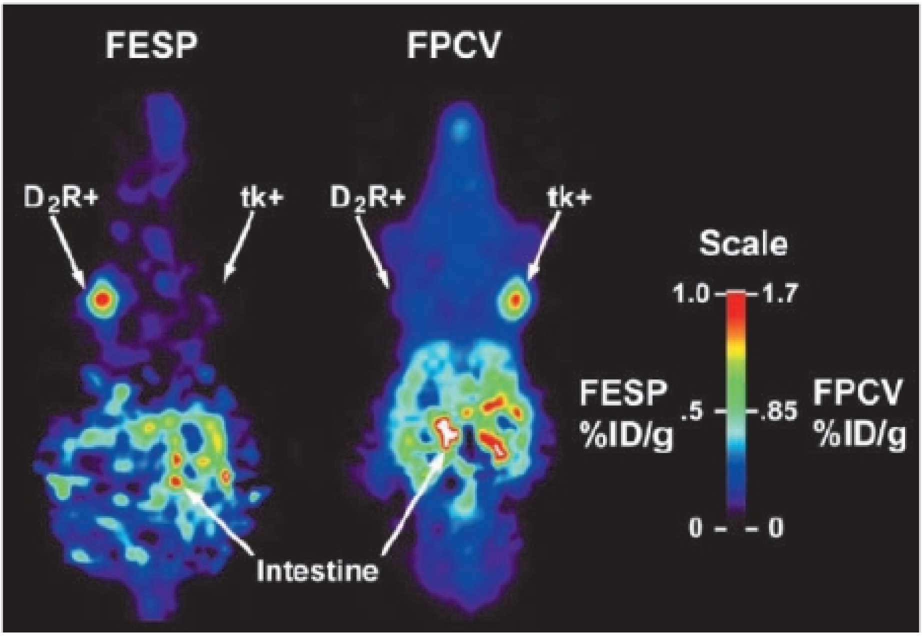

Figure 2.7: Image of a mouse bearing two tumors, each tumor expressing a different reporter gene. The one on the right carries the HSV1-tk reporter gene and the one on the left, the D2R reporter gene. The mouse was injected with two different reporter probes, FESP and FPCV, on two separate days. Each probe was specific for one of the gene reporter systems. The image shows clearly the selectivity of the reporter probes in each tumor. Background activity is seen from routes of clearance of tracer, which are renal and gastrointestinal [10].

Chapter 3

YAP-(S)PET technical characteristics

The YAP-(S)PET is a small animal scanner specifically built to perform PET and SPECT acquisitions. For this reason the scanner uses planar detector rather than the more common cylindrical multiring configuration. Another peculiarity is the utilization of $YAlO_3$:Ce (or YAP:Ce) as scintillator crystal.

The scanner was originally developed ([75, 76]) at the Department of Physics of the Universities of Ferrara and Pisa, Italy. From 2003, fully engineered versions of the scanner have been produced and commercialized by the small italian company I.S.E. Ingegneria dei Sistemi Elettronici s.r.l., Pisa, Italy [77]. At the end of 2003, an engineered version of the tomograph with additional research features has also been realized within a research project at the Center of Excellence AmbiSEN (Ambiente e Sistema Endocrino e Nervoso) of the University of Pisa and installed at the Institute of Clinical Physiology (IFC) of the National Research Council (C.N.R.) within a cooperative research agreement with the Center of Excellence AmbiSEN.

The first versions of the scanner had a detector array composed of a 4 × 4 cm^2 matrix of YAP:Ce of 20 × 20 crystals, each crystal being 2 × 2 mm wide and 25 or 30 mm long (hereafter named "20 × 20" version). The latest version realized during the first half of 2006 has the detection matrices consisting of 27 × 27 elements, with crystals 1.5 × 1.5 mm wide and 20 mm long (hereafter "27 × 27" version). At present, there are only two "27 × 27" version units of the YAP-(S)PET scanner. The research unit is installed at the Institute of Clinical Physiology (IFC) of the National Research Council (C.N.R.) within a cooperative research agreement with the Center of Excellence AmbiSEN of the University of Pisa; while the commercial version has been delivered at the Scientific Institute H. S. Raffaele in Milan, Italy, on July 2006. In this thesis, I discuss the technical characteristics, the calibration procedures and the performance evaluation of the "27 × 27" version of the scanner, and describe animal studies performed with both the "20 × 20" and "27 × 27" version.

3.1 The YAP-(S)PET scanner overview

The scanner is made of four detector heads of pixellated crystals of YAP:Ce. Each matrix consist of 729 (27 × 27) elements of $1.5 \times 1.5 \times 20$ mm^3 glued together, and optically isolated by a 5 μm thick reflective layer. This very thin and efficient reflective layer is applied by the manufacturer (Crytur [78]). The matrix is directly coupled to a position sensitive photomultiplier tube (PS-PMT Hamamatsu R2486, Hamamatsu Photonics, Hamamatsu City, Japan).

The distance between detectors pairs is fixed to 10 cm in the commercial version. In the research unit, the heads can be positioned at different distances ranging from 10 to 20 cm so as to give the possibility of choosing the maximum spatial resolution (larger distance in PET mode and smaller distance in SPECT modality) or maximum sensitivity (smaller distance) configuration (see chapter 5).

The four modules are positioned on a rotating gantry (see figure 3.1) and opposing detectors are in time coincidence when used in PET mode.

The scanner can be switched between PET and SPECT modalities without any change in the detector configuration or in the acquisition system, but simply replacing the tungsten septum (used in PET for shielding the scintillator from the background outside the field-of-view (FOV)) with a high-resolution parallel hole collimator in front of each crystal.

The YAP-(S)PET computing architecture is client/server: the on-site PC (server) that performs data acquisition and motion control can be controlled by a remote PC (client) connected to a local network.

The PC-controlled head rotation allows tomographic acquisition. The scanner is equipped with a laser system and motorized bed for the animal positioning and motion within FOV. The axial motion of the bed can be controlled via a PC software, while the vertical position of the bed can be adjusted manually. There are two bed models available, and both of them have a carbon composition. The flat one (4 cm wide and 50 cm long) is specifically designed for mice holding, while the hollow bed (50 mm in diameter and 50 cm in length) is more suitable for rats (see figure 3.2).

For both PET and SPECT modalities the scanner has an axial and transaxial FOV of 4 cm.

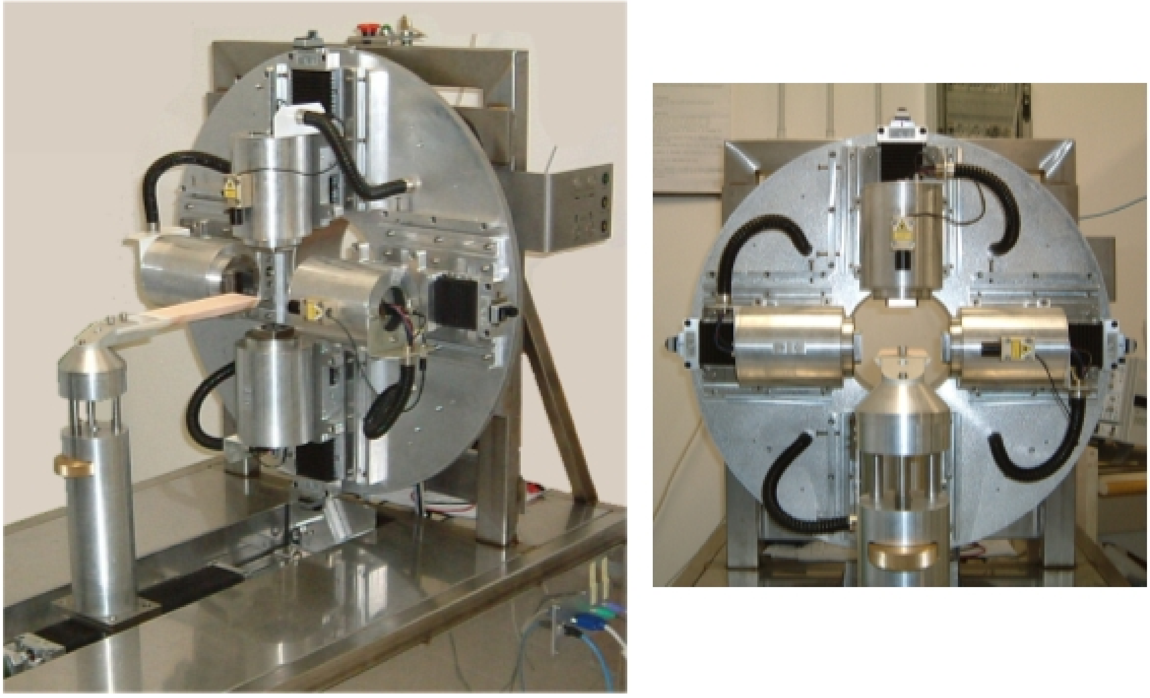

Figure 3.1: Photograph of the YAP-(S)PET scanner (left) and partial view of the four rotating heads (right).

3.2 The main hardware components

3.2.1 Scintillator crystals: YAP:Ce

The ideal detector material for PET systems stops all photons that enter the detector, and provides high spatial, temporal and energy resolution for the recorded event. These parameters could not be optimized simultaneously in one single detector material or geometry; the optimal PET device must be matched to the source geometry and imaging requirements [79].

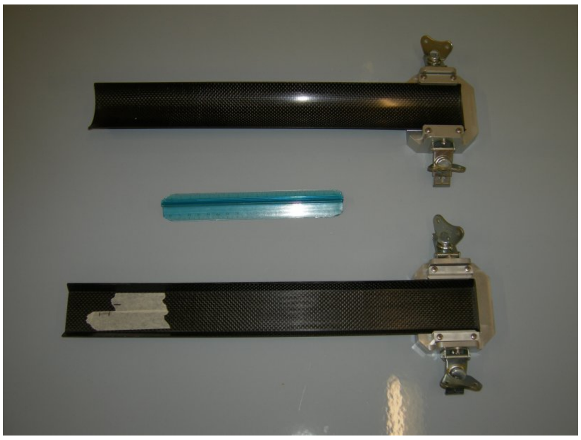

Figure 3.2: Photograph of the two bed models available with the YAP-(S)PET scanner: the flat one (bottom of the figure) for specifically designed for mice holding, and the hollow bed (top) more suitable for rats.

In recent years, there has been considerable research in new PET scintillator materials, especially for high Z materials, to improve the performance of future PET scanners. An important example is LuAP:Ce, with its high Z, high-density, fast decay time and relatively high light yield [80]. In high Z materials, the one gamma mean free path has a shorter extension respect to low Z materials. 90% absorption lengths for 511 KeV photons is about 25 mm in BGO and more than the double in YAP [81]. Moreover, multiple interactions of the incident photon in the detector (such as when the photon undergoes a Compton interaction or a photoelectric interaction with an inner shell electron, with subsequent X-ray emission) are generally closely spaced. All these effects can limit the achievable spatial resolution. In the past [82], low Z plastic detectors have been considered for positron imaging due to the relative low cost. Subsequently, interest has been related to its speed and potential high spatial resolution [79].

Low Z materials have a photoelectric to Compton ratio very low compared to high Z detectors. However, the photon which emerges from the first Compton interaction would travel a large distance from the interaction site. Besides, multiple interactions, especially in thin detectors, will be high improbable. Energy resolution to distinguish true and scattered photons will not be possible, since there is no photopeak. However, locating the site of a photon interaction by using the light produced by a single Compton electron provides low Z detectors the potential for very high spatial resolution. A similar behaviour is expected using a medium-Z scintillator, such as

YAP.

Yttrium Aluminum Perovskite activated by Cerium (YAlO3:Ce or YAP:Ce) is a monocrystal with the structure of perovskite. The crystal is very hard, mechanically and chemically stable, and it is not hygroscopic. Its main features are fast scintillation emission and high light yield that makes this crystal the best compromise for both PET and SPECT applications [76]. Besides, it can be assembled in crystal matrices with small pixels for high spatial resolution maintaining its high light output. Other scintillators, typically used in PET, either do not generate enough light (BGO) for being used at the energy (140 keV) of the main used SPECT radiotracer (^{99m}Tc), are too expensive (GSO) or are intrinsically radioactive producing signals in the relevant energy range (LSO: about 400 cps/cm^3). In table 3.1, the main characteristics of YAP:Ce are summarized and compared with those of other scintillators [83].

Material	**NaI:Tl**	**CsI:Tl**	**BGO**	**GSO:Ce**	**YAP:Ce**	**LSO:Ce**
Z	11/53	55/53	83/32/8	64/14/8	39/13/8	71/14/8
Effective atomic number (511 keV)	51	54	74	60	33	67
Density (g/cm^3)	3.67	4.53	7.13	6.71	5.37	7.42
Index of refraction	1.85	1.80	2.20	1.90	1.95	1.82
Hygroscopic?	yes	slightly	no	no	no	no
Natural radioactivity	no	no	no	no	no	yes
Wavelength of maximum emission (nm)	415	550	480	440	370	420
Decay constant (ns)	230	900	300	30-60 (90%)/ 600	25	12/ 40 (65%)
Radiation length (cm)	2.9	1.86	1.1	1.38	2.7	1.14
Gamma Mean Free Path (511 keV) (cm)	3.05	2.43	1.11	1.43	2.18	1.22
Photoelectric fraction (511 keV)	18%	22%	44%	25%	4.4%	32%
Photoelectric fraction (140 keV)	84%	87%	94%	82.3%	46%	92%
Absolute light yield 300 K (10^3 photons/MeV)	38	52	8-9	9-10	17	27-30

Table 3.1: Basic charactertistics of some scintillator crystals

Due to the low photoelectric/Compton ratio in YAP:Ce (4.4 % at 511 keV), most of the events which contribute to the total absorption peak derive from multiple interactions within the crystal and not from photoelectric absorption. The position of one event is the average value of the coordinates of each interaction weighted by its energy deposition. Hence, the spatial resolution for multiple interactions events deteriorates. Selecting a suitable energy window mostly single Compton events are registered and a higher spatial resolution can be obtained.

Figure 3.3 shows simulated pulse height distributions obtained for different numbers of photon interactions within the YAP:Ce matrix.

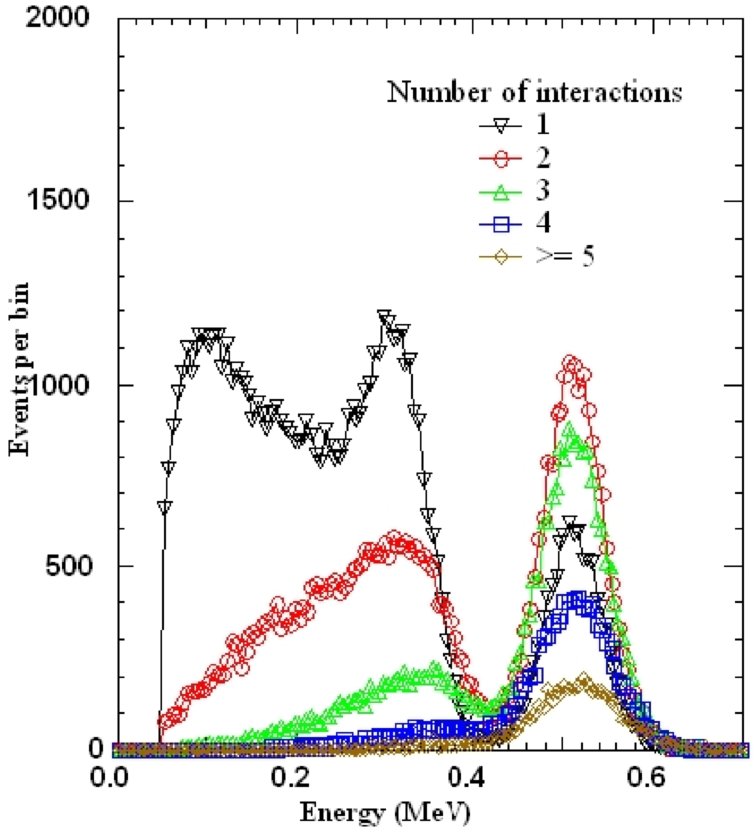

Figure 3.3: Simulated pulse height distributions obtained for different numbers of photon interactions within the YAP:Ce matrix.

It is evident that most of single interaction events have a pulse height below 400 keV, i.e., the valley in the pulse height distribution of Fig. 3.3. In small animal scanners, the scattering from rats or mice is not so important as in clinical scanner, so the single Compton events can be considered "good events". For this reason, YAP:Ce shows better spatial resolution capabilities with respect to high Z scintillators, such as BGO [84]. Since all high Z scintillators have a photofraction below 50% at 511 keV the events under the full energy peak will have a large contribution from multiple Compton scattering in the crystal. These events are usually chosen as the "best" events. In dense medium Z scintillators, like YAP, by selecting only Compton events, even in a crystal whose thickness is one gamma mean free path, a high fraction of these ($\approx 60\%$) will be single interactions, providing, therefore, the correct interaction position. This percentage is more than any photofraction of any scintillator.

In the YAP-(S)PET scanner it is possible to select the energy window in which data for reconstruction are taken. In PET mode, choosing the 50-400 keV window the single Compton events are favoured and a higher spatial resolution reconstruction is obtained. On the other hand, selecting the whole spectrum (50-850 keV) a higher sensitivity is obtained.

Chapter 4 of [85] reports the spatial resolution and the sensitivity for both 50-400 and 50-850 keV energy window. The results clearly show how the spatial resolution improves when using the high spatial resolution energy window (50-400 keV), while there is a significant decrease in sensitivity.

In this thesis, in PET mode we have always used the open energy window 50-850 keV in order to better compare the performance of the new version of the YAP-(S)PET scanner ("27 $\times$ 27" version) with the old one ("20 $\times$ 20" version).

The use of the reduced energy window (140-250 keV) in SPECT mode is justified by a reduction in scatter contribution, as described in [86]. In this article, it is shown how above 140 keV there are about no scatter tails. The test acquisition was performed with a 10 mm diameter cylindrical phantom, filled with ^{99m}Tc and surrounded by a 11 mm thick lucite ring.

Thus, in SPECT mode, in this thesis we have always used the reduced energy window 140-250 keV. There is obviously a reduction in sensitivity, but we gain in spatial resolution: a critical issue in SPECT modality.

3.2.2 Position Sensitive Photomultiplier Tube (PSPMT)

Before the advent of the Position Sensitive Photomultiplier Tube (PSPMT), the task of obtaining 2-dimensional information required the use of an arrangement of multiple

PMTs. This approach was quite expensive and required complex hardware. The R2486 series was the first 3 inch position sensitive PMT developed by Hamamatsu in 1985 [87], and represented a strong technological advancement for gamma ray imaging.

Figure 3.4: Photograph of the R2486 PS-PMT tube by Hamamatsu [88].

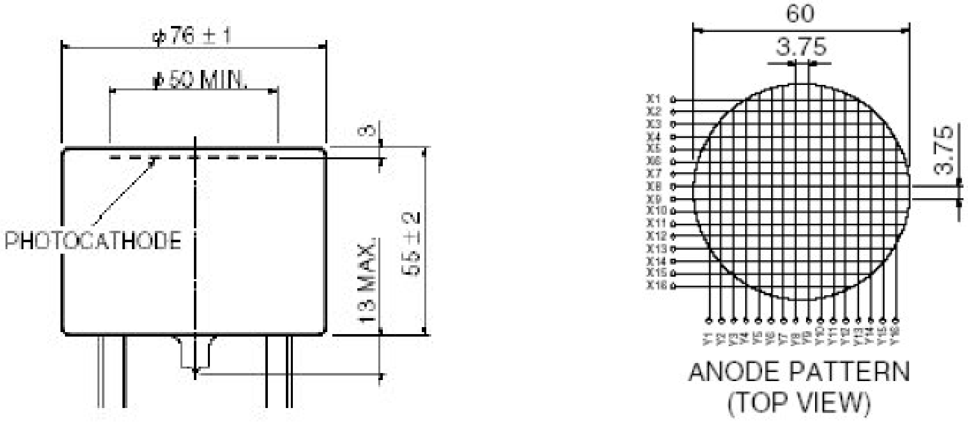

Figure 3.5: Dimensional outline (on the left) and anode pattern (on the right) of the R2486 PSPMT tube by Hamamatsu [88].

The R2486 tube (see figure 3.4) consists of a 3 inch PMT with bi-alkali photocathode, 12-stage coarse mesh dynode structure, and 16×16 anode wires crossing one another in the X and Y directions. The dynode structure consists of two layers: a focusing grid and multiplication bars. The bars are alternatively crossed to obtain multiplication along the X and the Y direction (see figure 3.6). A charge cloud is generated across the 12 dynode stages and finally collected by a crossed wire anode (see figure 3.5). The focusing structure limits the spread of the charge (obtained from a point-like illumination of the photocatode) to 4.3 mm at the last dynode [87], where the charge is back-reflected to the anode wires. The wire pitch is 3.75 mm, thus giving adequate sampling of the charge distribution. The intrinsic spatial resolution of the R2486 tubes ranges between 0.9 mm and 0.12 mm, which improves with increasing charge on the anode. The tube has a circular photo-cathode with an active area of 50 mm in diameter, with respect to an overall diameter of 76 mm. Figure 3.5 shows the dimensional outline and the arrangement of the anode wires. In the standard configuration, the two wire ends of wires in the same direction are connected via a resistive chain. The two ends of each resistive chain (X or Y) produce two charge pulses: $\mathrm{X_a}$ and $\mathrm{X_b}$ (or $\mathrm{Y_a}$ and $\mathrm{Y_b}$) . The final position is then given by the equation:

$$\mathrm{X} = \frac{\mathrm{X_a} - \mathrm{X_b}}{\mathrm{X_a} + \mathrm{X_b}} \tag{3.1}$$

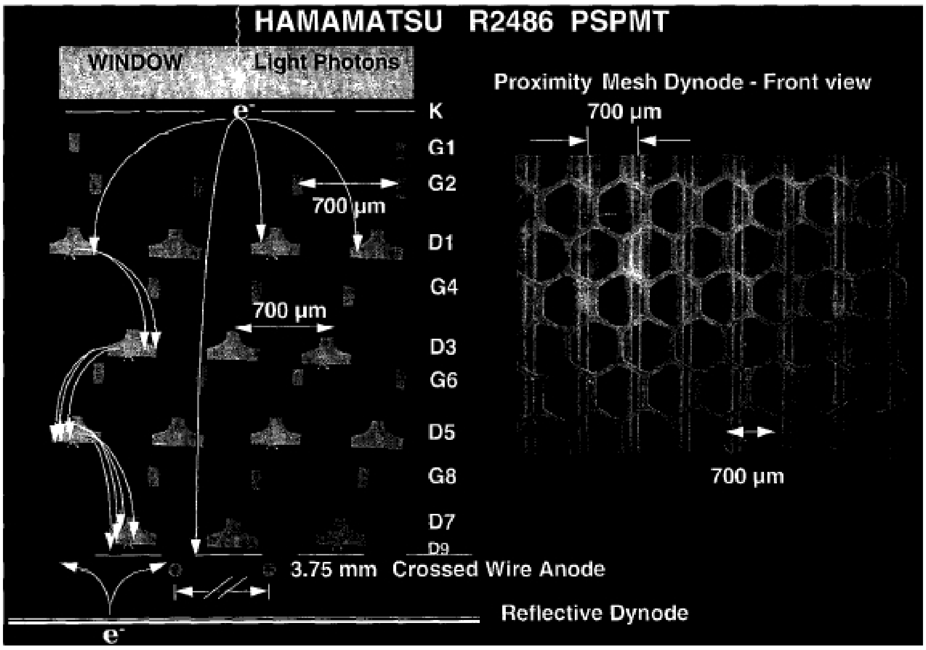

Figure 3.6: Coarse mesh dynode structure. Left: schematic rapresentation of a cross-section of a PSPMT obtained linking digitized images from electronic microscope of dynode cross-section. The figure represents the multiplication process along the X direction where G is the hexagonal grid, D is the bar dynode and K is the bi-alkali photocathode. Right: front view image of the coarse mesh dynode obtained by an optical microscope [89].

The general characteristics of the PSPMT R2486 are reported in table 3.2.

R2486	
Spectral response	300 nm to 600 nm
Wavelength of maximum response	420 nm
Photocatode material	Bialkali
Minimum effective area	50 mm diameter
Window material (thickness)	Borosilicate glass (3.0 ± 0.3 mm)
Dynode structure	Coarse mesh
Number of dynode stages	12
Anode structure	16 (X) + 16 (Y) crossed wires
Max HV	-1300 V
Max gain	5.0×10^5
Signal rise time	5.5 ns

Table 3.2: General characteristics of the Hamamatsu R2486 photomultiplier tube [88].

3.2.3 Electronic read-out

The electronic equipment is mounted on the back of the rotating gantry of the YAP-(S)PET scanner (see figure 3.7). It consists of:

- four High Voltage (HV) units that supply the power to each of the R2486 PSPMTs. The HV value can be set independently for each PSPMT. In the "27 × 27" version of the scanner, PET and SPECT modalities have uncorrelated HV setting (see figure 3.8). It makes possible to better exploit the Analog to Digital Converter (ADC) dynamic range (see section 4.1.1).

- two acquisition boards with dedicated and compact electronic devices for the PSPMTs signal amplification and digitization. Each acquisition board is dedicated to a pair of opposite detectors both in PET and SPECT modalities.

  Each PSPMT has two different type of output signals: the last dynode and the four anodic position signals.

  The last dynode signals are used for fast timing coincidence. The output signal from each PSPMT is amplified by a pre-amplification stage produced by ISEsrl and then sent to the acquisition board for fast timing coincidence. A Constant Fraction Discriminator (CFD) is used for each photomultiplier tube. In PET mode, the logic outputs of the CFDs of opposing detectors are sent to a coincidence module that produces the gate signal for the acquisition of the position signals (see figure 3.9). One of the CFD outputs of each pair of detectors is delayed by 100 ns in order to generate a delayed coincidence window. Events collected in this window are random events and are used to establish the rate of the randoms used for random corrections (see chapter 4). In SPECT mode, the output of each CFD directly generates the gate for the acquisition of the position signals.

The X-Y signals from the PSPMTs are used to determine the energy deposited by the γ-rays and the position of detected events. The four position signals from each PSPMT are processed by a system composed of a peak detector and a peak sensing ADC. The digitization of the signals is enabled by the gate signal.

The digital data are transferrerd to the local PC sever via USB2 connection.

In order to improve the count rate capabilities, at the beginning of 2006 a novel acquisition board has been developed. This new board called FAB (Fast Acquisition Board) (see figure 3.10) includes:

- faster ADCs in order to improve the count rate capabilities;
- a novel electronic pile-up rejection circuitry that allows to improve the image quality. (An application for patent has been filed by ISEsrl for this circuit).
- more on-line counters in order to have a complete control of what is going on during the acquisition.

3.2.4 SPECT collimator

The purpose of a collimator is to form the projection image by permitting gamma-rays photons approching the camera from certain directions to reach the crystals while absorbing most of the other photons. Several kinds of collimator can be found: pinhole, parallel-hole, converging and diverging holes, fan beam and more. The most commonly used collimator is the parallel-hole, particularly for human scanners. In small animal imaging, where one would like a spatial resolution between 1 and 3 mm,

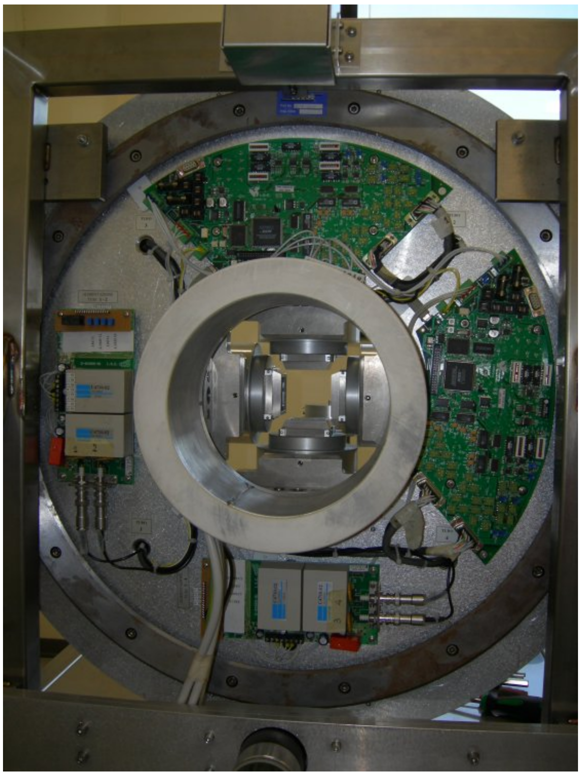

Figure 3.7: Photogtaph of the YAP-(S)PET electronics on the back of the gantry.

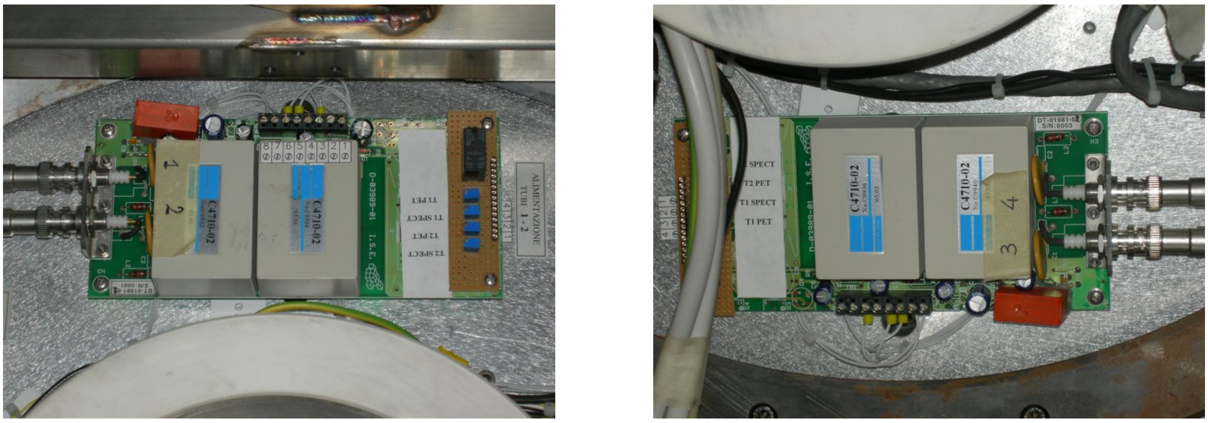

Figure 3.8: The four high-voltage (HV) supplies for each PSPMT of the YAP-(S)PET scanner.

one of the difficulties of this design is to make very small diameter but long collimator holes [90].

In the YAP-(S)PET scanner the collimators can be easily mounted or removed from the detectors head, replacing the tungsten septum used in PET for shielding the scintillators from the background outside the FOV (see figure 3.11). The collimators are made of lead with 0.6 mm hexagonal holes and are 20 mm thick. The septa between holes are 0.15 mm. A particular of the holes of the collimator is shown in

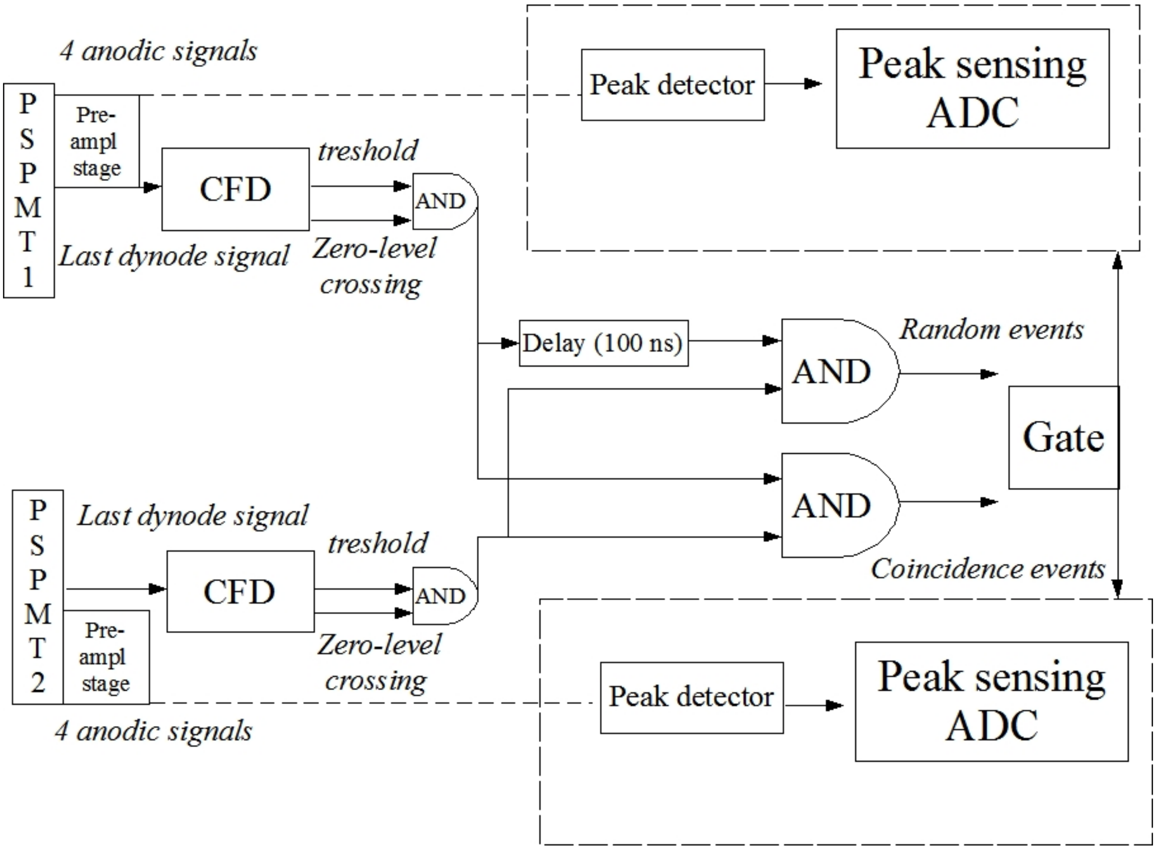

Figure 3.9: Schematic rappresentation of the electronics for the coincidence acquisition of the signals from a pair of opposing detectors.

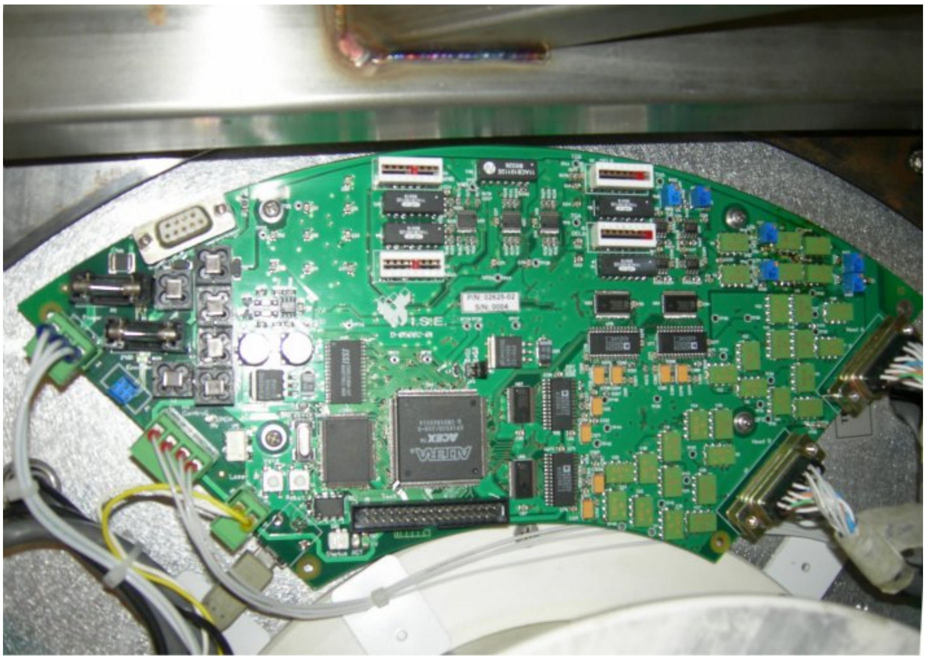

Figure 3.10: The new acquisition board FAB (Fast Acquisition Board) of the YAP-(S)PET scanner.

figure 3.11. The collimator geometrical efficiency g, defined as the fraction of gamma-rays passing through the collimator per gamma-rays emitted by the source toward the collimator, is given by [91] $g \approx [\mathrm{K\ d}^2/\mathrm{L(d+t)}]^2$, where d is the hole diameter, L is the thickness of the collimator, t is the thickness of the intra hole septa and K is a factor depending on the geometry of the holes. In the case of hexagonal holes K=0.26. With d=0.6 mm, t=0.15 mm, and L=20 mm the geometrical efficiency results 4×10^{-5}.

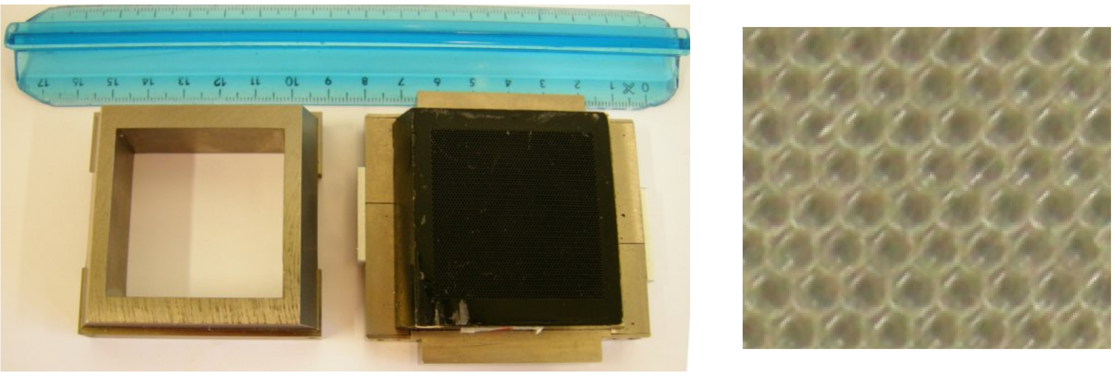

Figure 3.11: PET septum and SPECT collimator (on the left) with zoom of the collimator holes (on the right).

3.3 The software tools

3.3.1 Client/server architecture

The YAP-(S)PET scanner architecture is client/server.

The on-site PC (server) is dedicated to electronic equipment control, data acquisition and motion control.

In the next sections, I will go through a detailed description of the YAP-(S)PET client characteristics. It will help the comprehension of the next chapters.

The YAP-(S)PET client application is characterized by a user-friendly graphic interface. It allows to check and set up all the parameters regarding data acquisition, data analysis and image reconstruction from any remote computer connected via a local network to the server.

The YAP-(S)PET client main panel houses some menus and a command window with four icons (see figure 3.12).

The menus are: File and Operations. The Operations menu contains two groups of commands. The "Operative phase" group includes the same commands of the incons of the command window. The "Server-side operations" menu allows to choose the scanner acquisition mode (PET or SPECT), and to set the distance between the heads of each couple.

Each icon of the command window corresponds to a different command: Acquisition, Analysis, Reconstruction and Display.

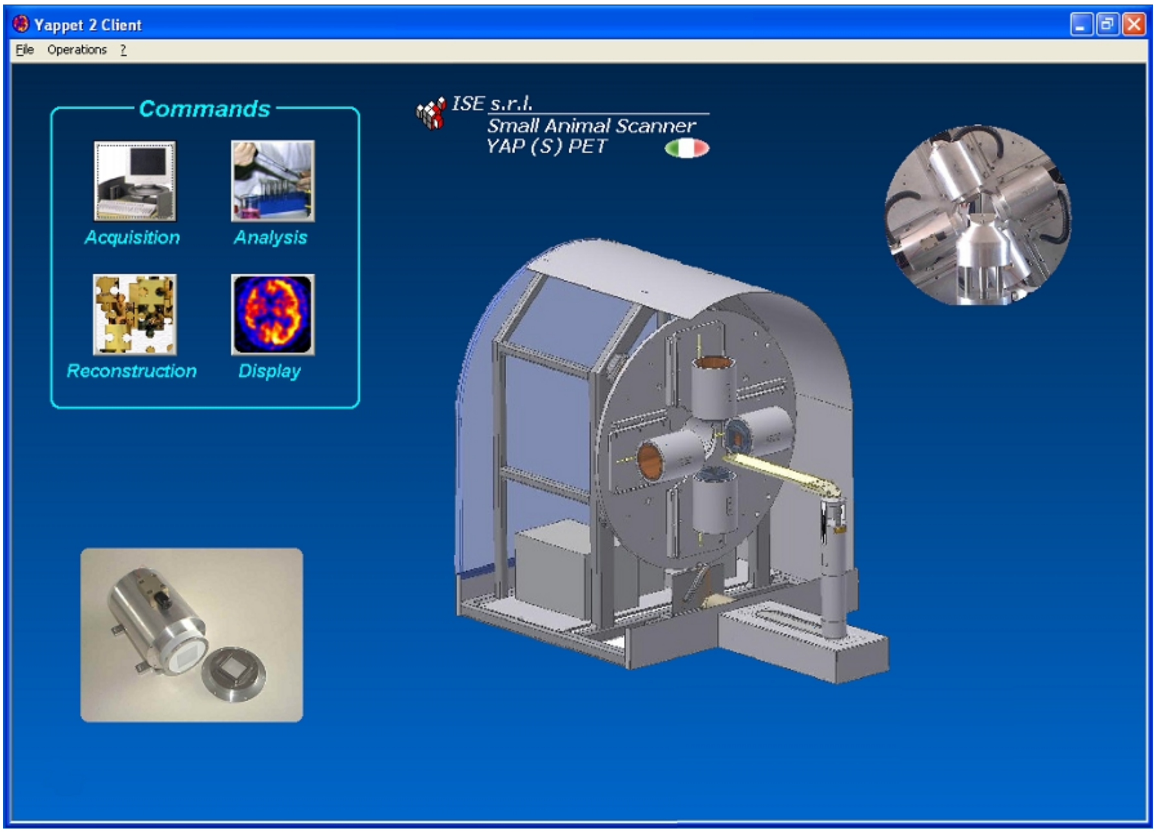

Figure 3.12: Main panel of the YAP-(S)PET client graphic user-friendly interface.

3.3.2 Acquisition

The Acquisition panel (see figure 3.13) allows to set the acquisition parameters. Two different types of acquisitions are possible: Preset Count and Preset Time.

In Preset Count mode, the counting interval ends when a preselected number of events has been acquired.

In Preset Time mode, the counting interval begins when the Start button is pressed and is terminated automatically when the selected counting time has elapsed.

Different parameters can be set for both the acquisition modalities:

- the number of views, ranging from 1 (planar acquisition) to 128. The step is 2^{n}, with n running between 0 and 7.
- in Preset Count mode only, the number of events per view. Actually, the user can set the number of blocks to be acquired per view. Each block contains 63 events, all of them are registered with the same time label with respect to the beginning of the acquisition. The number of blocks ranges from 1 to 10^{8}.
- in Preset Time mode only, the number of acquisitions, the duration (in time) and the delay between an acquisition and the following one. This acquisition mode is particularly suitable for dynamic acquisitions.
- the start and the end angle of gantry rotation. The start angle ranges from 0^{0} to 359^{0}. The end angle can be 90^{0}, 180^{0} or 360^{0}. If the number of views is equal to 1, the start and end angles coincide.
- the bed initial position and the total length to scan. The whole-body acquisitions are performed with the standard protocol of translating the bed through the scanner at discrete, overlapping steps. Each step requires a bed advancement of 20 mm, i.e. half of the FOV dimension. The maximum length to scan is 160 mm, corresponding to 7 bed positions.
- the radioisotope used for the acquisition. This information is used by the Client software to correct acquired data for decay process.
- injection time of the radioisotope. It is an important parameter for tracer kinetic modeling.

Some parameters displayed in the Acquisition panel allow to monitor the progress of the acquisition:

- the total number of the acquired events.
- the remaining time, that is the time remaining to the end of the acquisition. In Preset Count mode, the computation of the remaining time is performed on

the basis of the rate of acquired events and the decay time of the radioisotope used.

- several on-line counters that measure the rate of acquired events by each single head or pair of heads. The displayed rate (cps) are: registered events by each pair of heads; single events acquired by each head; true coincidence registered by each couple of heads; false coincidence acquired by each couple of heads; pile-up events acquired by each head; saturation events registered by each head.
- the number of the current view in the running acquisition and the corresponding gantry angle (in degrees).
- the number of the acquired events in the current view.
- the number of bed positions for whole body studies and the number of acquisition in dynamic studies.

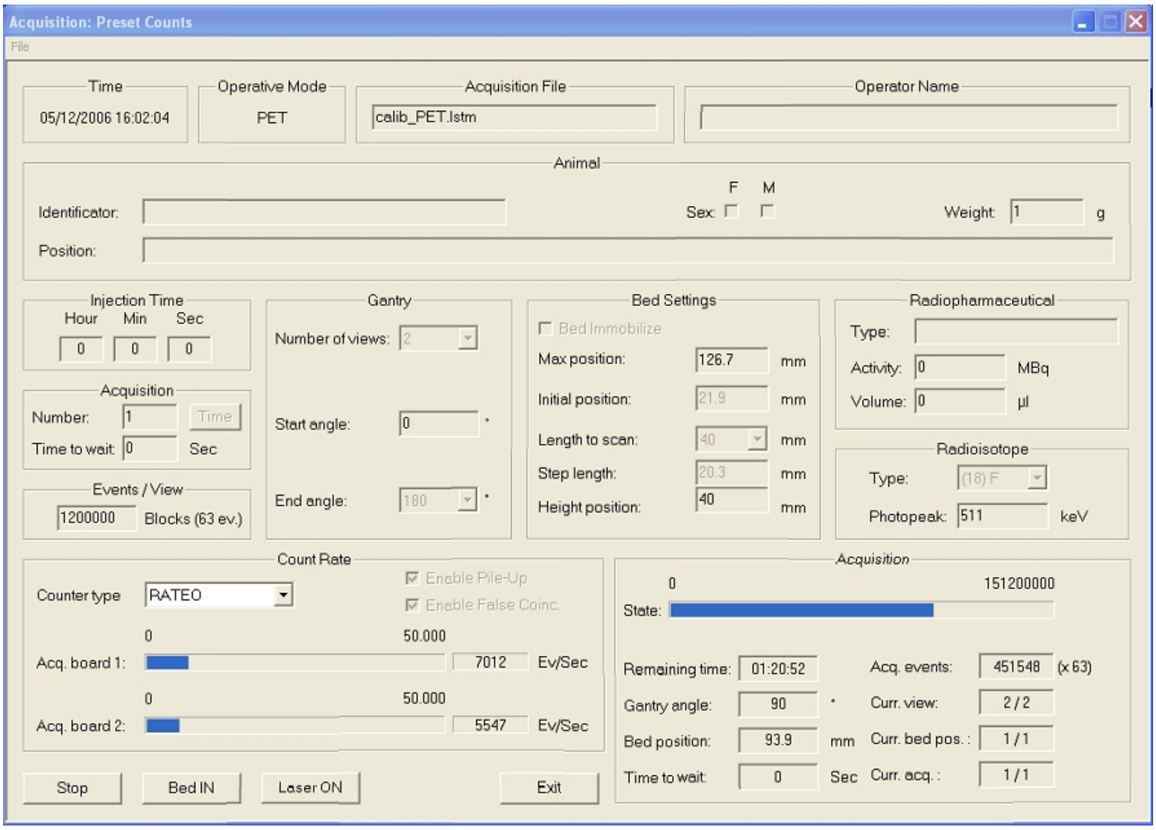

Time: 05/12/2006 16:02:04
Operative Mode: PET
Acquisition File: calib_PET.lstm
Operator Name:
Identificator:
Sex: F ☐ M ☐
Weight: 1 g
Position:
Injection Time: Hour 0 Min 0 Sec 0
Number: 1 Time
Time to wait: 0 Sec
1200000 Blocks (63 ev.)
Number of views: 2
Start angle: 0 °
End angle: 180 °
☐ Bed Immobilize
Max position: 126.7 mm
Initial position: 21.9 mm
Length to scan: 40 mm
Step length: 20.3 mm
Height position: 40 mm
Type:
Activity: 0 MBq
Volume: 0 µl
Type: (18) F
Photopeak: 511 keV
Counter type: RATE0
☑ Enable Pile-Up
☑ Enable False Coinc
Acq. board 1: 0 50.000 7012 Ev/Sec
Acq. board 2: 0 50.000 5547 Ev/Sec
State: 0 151200000
Remaining time: 01:20:52
Gantry angle: 90 °
Bed position: 93.9 mm
Time to wait: 0 Sec
Acq. events: 451548 (x 63)
Curr. view: 2 / 2
Curr. bed pos.: 1 / 1
Curr. acq.: 1 / 1

Figure 3.13: Acquisition panel of the YAP-(S)PET client user interface during a calibration measurement in PET mode.

3.3.3 Analysis

Analysis, as Reconstruction and Display tools, can be accessed by clicking on the corresponding icon in the Acquisition panel (figure 3.12). The selection of the file opens the Yappet File Manager window (see figure 3.14).

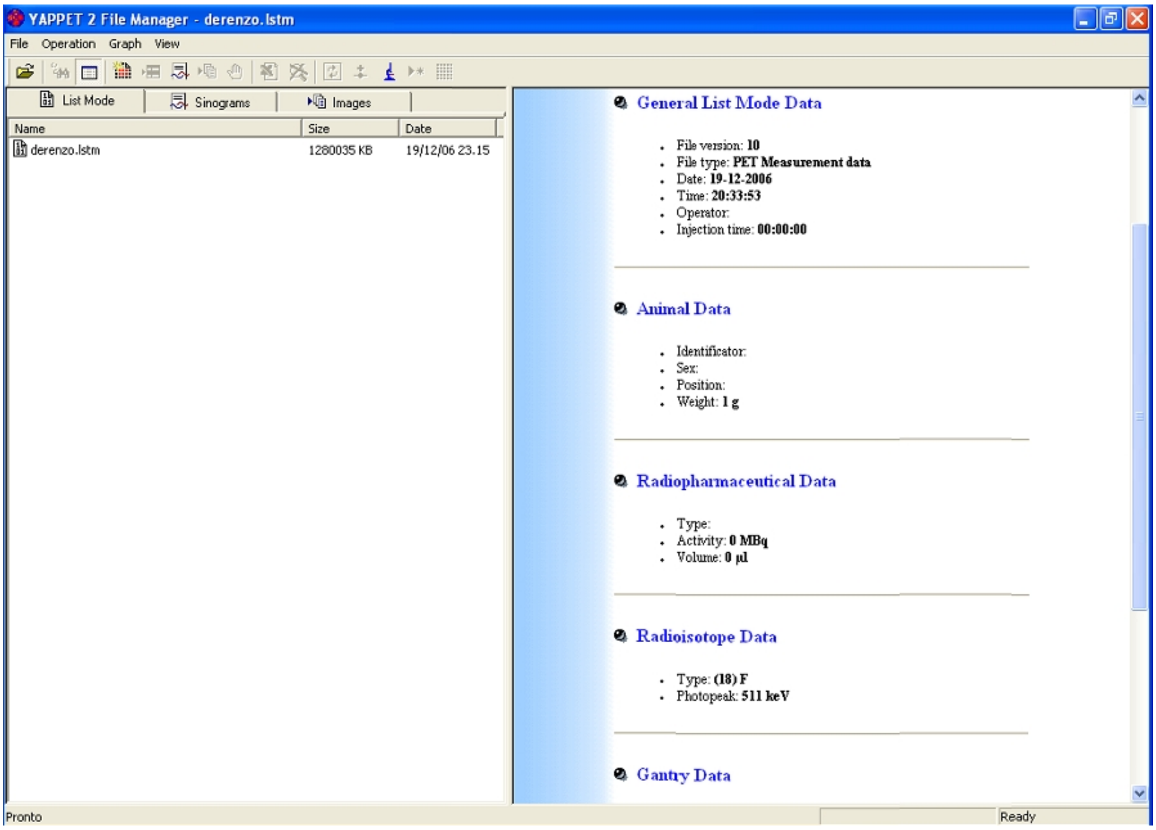

Name	Size	Date
derenzo.lstm	1280035 KB	19/12/06 23.15

General List Mode Data

- File version: **10**
- File type: **PET Measurement data**
- Date: **19-12-2006**
- Time: **20:33:53**
- Operator:
- Injection time: **00:00:00**

Animal Data

- Identificator:
- Sex:
- Position:
- Weight: **1 g**

Radiopharmaceutical Data

- Type:
- Activity: **0 MBq**
- Volume: **0 µl**

Radioisotope Data

- Type: **(18) F**
- Photopeak: **511 keV**

Gantry Data

Figure 3.14: Yappet File Manager window for Analysis, Reconstruction and Display opened from a static acquisition of a the derenzo-like phantom list-mode file.

The Analysis tool concerns the raw data analysis and the sinograms production.

The data are acquired in list-mode binary format and stored in memory in blocks of 64 events. For each pair of γ-rays detected in PET mode, the four position signals from each PSPMT and the related time are registered. In SPECT mode, the detection of a single γ-ray implies the registration of the four position signals of the single PSPMT and the related time.

Two different type of list-mode files can be produced and processed: the **calibration** and **measurement** files.

The **calibration acquisitions** are used in the calibration and maintenance phases of the scanner. The raw analysis that is possible to perform on these files generates:

- the planar image of each YAP:Ce matrix, used for the pixel identification and the generation of a Look Up Table (LUT) of the geometric position of each single crystal.

- the energy spectrum of each single crystal and the sum of them for each head, necessary to perform the energy calibration and to check the proper functionality of the scanner.

- the efficiency corrections used to normalize the yield of the different crystals of each matrix (see chapter 4).

It is possible to choose the raw ADC channel limits for each analysis performed.

Measurement acquisitions refer to all the non calibration acquisitions generally performed. The measurement list-mode files can be processed as calibration acquisition besides allowing the sinogram generation.

The system operates in 3-D data acquisition mode without septa. The collected data can be stored in 2-D (PET and SPECT mode) or 3-D (only PET mode) sinograms.

In 2-D sinograms only data coming from direct planes are processed and the oblique lines of response (LORs) are rejected.

The 3-D sinograms (3-D Positron Volume Imaging o 3-D PVI) take in account both direct and cross-plane detected events, thus storing all the coincidence data acquired by the scanner. Two different approaches are usually used to reconstruct from 3-D coincidence PET data: the rebinning algorithms and the fully 3-D approach of the 3-D reprojection (3-DRP) [92].

The 3-DRP algorithm is a 3D extension of the 2D filtered backprojection (FBP) algorithm and has a very high computational complexity.

This is why at present the YAP-(S)PET Analysis tool implements only rebinning algorithms: single slice rebinning (SSRB or MSRB) and Fourier rebinning (FORE).

A rebinning algorithm is defined as an algorithm which sorts (rebins) the 3-D acquired data into a stack of ordinary 2-D sinograms. These rebinned data are geometrically equivalent to data collected in the conventional 2-D mode and can therefore be reconstructed by applying 2-D reconstruction algorithms (FBP, OSEM) to each slice separately. Unlike standard 2-D sinograms, the rebinned sinograms are less noisy because they employ much more data (the oblique LORs) than those acquired in 2-D mode [93].

In the SSRB or MSRB algorithm, each oblique coincidence line is assumed to have arisen from a parallel plane midway between the axial points of interaction of the two γ-rays in the opposite detectors [94]. Along the central axis of the scanner, this approximation works perfectly. However, it steadly becomes worse with increasing distance from the central axis. This approach yields reasonably acceptable images when the object being imaged takes up a small fraction of the FOV and when the axial acceptance angle (the maximum oblique angle accepted) is small [95]. In the YAP-(S)PET Analysis tool, the SSRB maximum span is fixed to 15 LORs while MSRB accept all the possible inclinations of the LORs.

The FORE techinque relates the 2-D Fourier transform of an oblique sinogram to the 2-D Fourier transform of the direct sinogram of a slice shifted axially by a frequency-dependent offset. Although this is still an approximate method, it yields substantially better results than SSRB, even for large objects and large acceptance angles [96], while retaining much of the advantage in terms of short reconstruction times.

In SPECT mode, each sinogram for each head can be produced besides the sinogram sum. Each sinogram is composed of 27 slices (1.5 mm thickness), has 53 spatial bins (the number of bins used to digitize the radial positions respect to the center of the FOV) and a number of angular bins depending on the number of views of the SPECT acquisition and on the angular rebinning. For example, in a SPECT acquisition of 128 views over 180^0, the number of angular bins will be 128 with angular rebinning or 256 without rebinning (sinogram produced over 180^0 or 360^0 respectively).

In PET mode, the single sinogram is related to the couple of detectors instead of the single head. The sinograms can be produced with both 27 or 53 slices (0.75 mm thickness) in order optimize the axial sampling of the 3D image. The single slice has 53 spatial bins and a number of angular bins depending on the head-to-head distance (see section 3.1) and on the angular rebinning. The angular rebinning is determined on the basis of the minimum detectable angle (δ_{min}). Referring to figure 3.15, the mathemathical expression of δ_{min} is:

$$\tan(\delta_{min}) = \frac{l_{sino}}{2(\mathrm{R} + \mathrm{DOI})} \approx \delta_{min} \tag{3.2}$$

l_{sino} is the spatial sampling, R is half the head-to-head distance and DOI is the most probable interaction depth (in the YAP-(S)PET “27 × 27” version it is set to 8mm).

The approximation is justified up to $l_{sino} \ll \mathrm{R}$. In our case, l_{sino} is 1.5 mm or 0.75 mm and R ranges from 50 to 75 mm. The number of angular bins (N_θ) over 360^0 is obtained by the expression:

$$N_\theta = \frac{\pi}{\delta_{min}} \tag{3.3}$$

If a PET acquisition is performed, i.e., in the configuration with head-to-head distance of 12.5 cm (R=62.5 mm), N_θ will be 148 or 296 according to the sinogram produced with or without angular rebinning.

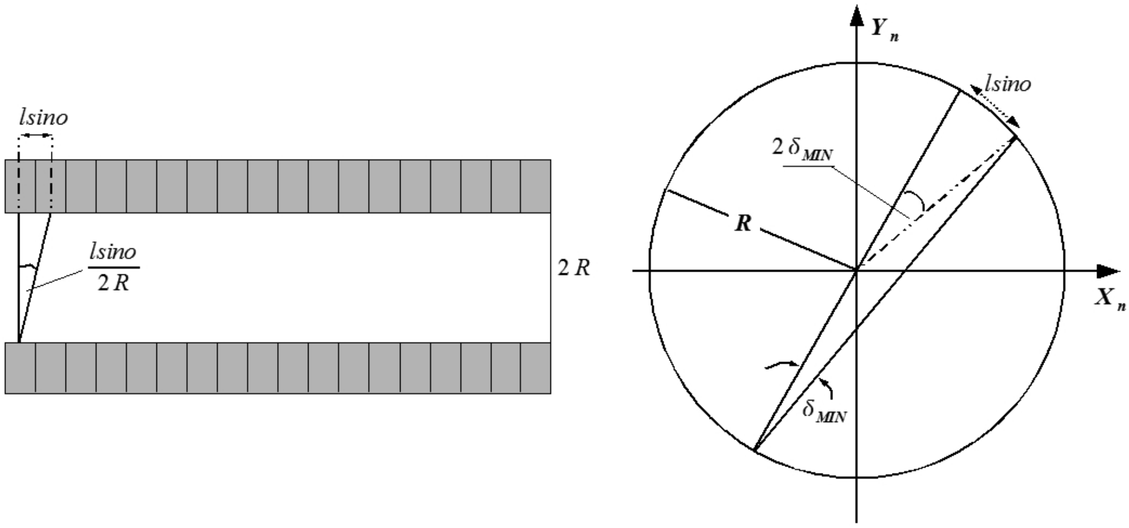

Figure 3.15: Left: Two detectors of a detection couple (PET modality) faced one another. The minimun detectable angle is visualized . Right: Sketch of the geometric configuration for the determination of the number of angular bins.

During each analysis process of both calibration or measurement acquisitions, a log file containing information about the acquisition is created. The log file is structured as a table, whose rows refer to a single view of the acquisition (see figure 3.16). The final row reports the whole contribution of all the views. For each performed scan (dynamic frame or bed position) a table is generated. The columns of each table contain the following information (from left to right of figure 3.16):

- percentage of acquired events effectively used in the analysis.
- percentage of rejected events for energy values.
- percentage of rejected events for ADC values.
- percentage of real events. This percentage is obtained by the number of CFD triggeres. The CFD starts every time a good event arrives. Nevertheless, due to dead time, during the acquisition of one event the electronic equipment can be unable to detect another event. By registering the number of CFD triggers, it is then possible to know the number of real events and to express them as a percentage of the acquired events (obviously this percentage is greater than 100%).
- percentage of random events, available only in PET modality. (See section 3.2.3 for the explanation on the determination of random events).
- percentages of events used by each head (FT in figure 3.16 stands for phototube). These percentages are related to the percentage of acquired events effectively used in the analysis (column Used of figure 3.16).
- duration of the acquistion of the view.

3.3.4 Reconstruction

The goal of image reconstruction is obtain the 3D distribution of the activity in the object that is being scanned, using externally detected radiation. In order to perform tomographic reconstruction, a set of “views” should be acquired at discrete angles around the object, so that each view supplies a 2-D projection of the 3-D activity distribution. As explained before, in the YAP-(S)PET scanner this set of 2-D projections is sorted in a set of 2-D sinograms. The 3-D image is then composed by stacking the slices reconstructed with 2-D methods.

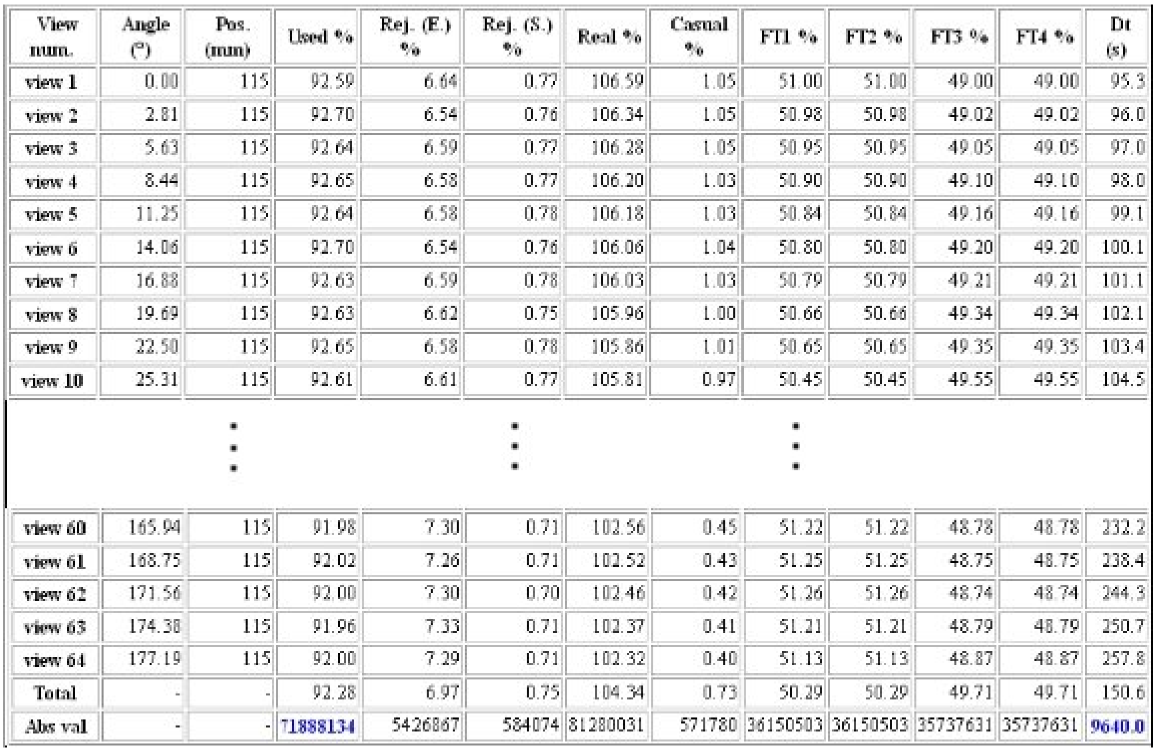

View num.	Angle (°)	Pos. (mm)	Used %	Rej. (E.) %	Rej. (S.) %	Real %	Casual %	FT1 %	FT2 %	FT3 %	FT4 %	Dt (s)
view 1	0.00	115	92.59	6.64	0.77	106.59	1.05	51.00	51.00	49.00	49.00	95.3
view 2	2.81	115	92.70	6.54	0.76	106.34	1.05	50.98	50.98	49.02	49.02	96.0
view 3	5.63	115	92.64	6.59	0.77	106.28	1.05	50.95	50.95	49.05	49.05	97.0
view 4	8.44	115	92.65	6.58	0.77	106.20	1.03	50.90	50.90	49.10	49.10	98.0
view 5	11.25	115	92.64	6.58	0.78	106.18	1.03	50.84	50.84	49.16	49.16	99.1
view 6	14.06	115	92.70	6.54	0.76	106.06	1.04	50.80	50.80	49.20	49.20	100.1
view 7	16.88	115	92.63	6.59	0.78	106.03	1.03	50.79	50.79	49.21	49.21	101.1
view 8	19.69	115	92.63	6.62	0.75	105.96	1.00	50.66	50.66	49.34	49.34	102.1
view 9	22.50	115	92.65	6.58	0.78	105.86	1.01	50.65	50.65	49.35	49.35	103.4
view 10	25.31	115	92.61	6.61	0.77	105.81	0.97	50.45	50.45	49.55	49.55	104.5
		⋮			⋮			⋮				
view 60	165.94	115	91.98	7.30	0.71	102.56	0.45	51.22	51.22	48.78	48.78	232.2
view 61	168.75	115	92.02	7.26	0.71	102.52	0.43	51.25	51.25	48.75	48.75	238.4
view 62	171.56	115	92.00	7.30	0.70	102.46	0.42	51.26	51.26	48.74	48.74	244.3
view 63	174.38	115	91.96	7.33	0.71	102.37	0.41	51.21	51.21	48.79	48.79	250.7
view 64	177.19	115	92.00	7.29	0.71	102.32	0.40	51.13	51.13	48.87	48.87	257.8
Total	-	-	92.28	6.97	0.75	104.34	0.73	50.29	50.29	49.71	49.71	150.6
Abs val	-	-	71888134	5426867	584074	81280031	571780	36150503	36150503	35737631	35737631	9640.0

Figure 3.16: Log file of a static acquisition of a derenzo-like phantom.

In the YAP-(S)PET software, once the acquired data are stored in sinograms (see section 3.3.2), different type of reconstruction can be performed. The **Filtered Back Projection (FBP)**, the **Maximum Likelihood Expectation Maximization (ML−EM)** and the **Ordered Subsets Expectation Maximization (OSEM)**.

The **FBP** is an analytic reconstruction algorithm that uses the central-section theorem. The implementation is based on the following steps [95]:

- compute the 1-D Fourier transform of the first projection angle in the sinogram;
- multiply this by the filter function;
- take the inverse Fourier transform;
- backproject the modified (filtered) projection;
- repeat the procedure for all angles around the object.

The mathematical formulation is:

$$f(x, y) = \frac{1}{N} \sum_{i=1}^{N} p'(x \cos \phi_i + y \sin \phi_i, \phi_i) \tag{3.4}$$

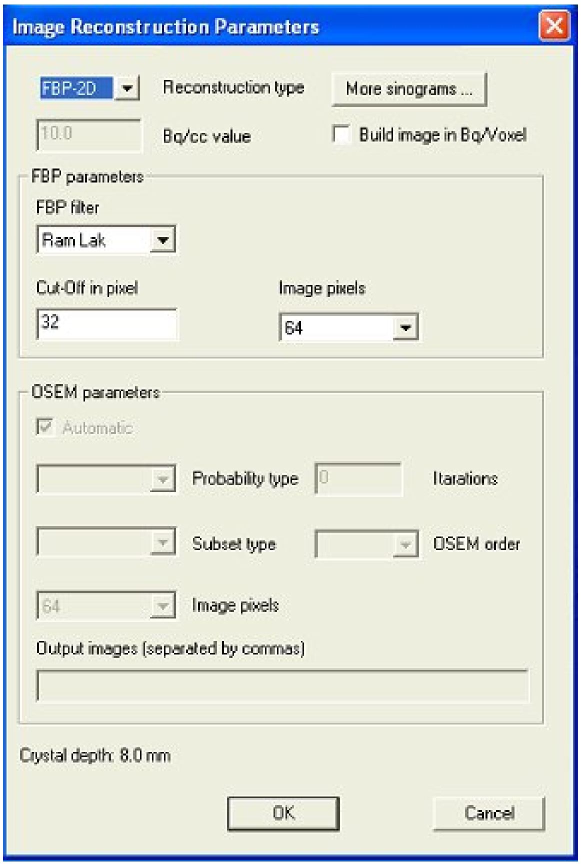

Image Reconstruction Parameters

FBP-2D Reconstruction type

10.0 Bq/cc value

☐ Build image in Bq/Voxel

FBP parameters

FBP filter: Ram Lak

Cut-Off in pixel: 32

Image pixels: 64

OSEM parameters

☑ Automatic

Probability type

Iterations: 0

Subset type

OSEM order

Image pixels: 64

Output images (separated by commas)

Crystal depth: 8.0 mm

Figure 3.17: Image Reconstruction panel with FBP reconstruction selected. The cut-off frequency expressed in pixel actually is expressed in pixel/FOV.

where

$$p\prime(r,\phi) = \frac{1}{2\pi}\mathrm{FT}^{-1}\{\mathrm{FT}[p(r,\phi_i)]\cdot|\nu_r|\} \tag{3.5}$$

FT and FT^{-1} are the direct and inverse Fourier transform, respectively. N is the number of different equally spaced projection angles over which data have been acquired: $p(r,\phi_i)$ is the number of counts in the sinogram element angle ϕ_i and radial offset r, and $f(x,y)$ is the activity distribution. $|\nu|$ is the reconstruction filter, known as Ram-Lak (Ramachandran and Lakshminarayanan [97]) or ramp filter because of its shape in frequency domain (see figure 3.18). It amplifies the high-spatial frequencies with respect to the low-spatial frequencies. The typical 1/r blurring effect introduced by the backprojection is so reversed.

Amplification of the high-spatial frequencies also leads to amplification of high-frequency noise. A typical projection view contains a range of frequencies, with tendency for higher amplitudes at low frequencies and lower amplitudes at higher frequencies. On the contrary, statistical noise (noise related to the finite number of annihilation photon pairs contributing to each element in the profile) has a uniform spectral appearance and contributes equally at all frequencies. Thus, the ramp filter leads to degradation of signal-to-noise ratio (SNR) since higher frequencies are responsible for the finer details (rapidly changing activity, sharp edges, and so on) in a reconstructed images. By modifing the reconstruction filter, it is possible to obtain a trade-off between the SNR and spatial resolution of the reconstructed image. A simple way to do this is to cut off the ramp filter at a frequency $\nu_{cutoff} < \nu_{max}$. Other methods foresee the use of apodizing windows multiplied by the ramp filter, resulting in a reduced magnitude at high frequencies. This filtering avoids a sharp change in the filter at the cut off frequency reducing the chances of introducing artifact into the reconstructed images.

In the YAP-(S)PET Reconstruction tool, the cut-off frequencies value is automatically set to the Nyquist frequency, but it is also possible to select the desidered cut off frequency. In the Image Reconstruction panel (see figure 3.17), the cut off frequency expressed in pixel actually refers to pixel/FOV, that is in the typical frequency expression pixel/mm. Besides the ramp filter, the following types of filter can be choosen: Shepp-Logan [98], Shepp-Logan modified, Hann, Low Pass Cosine and Noise. The mathematical expression of the used filters are:

Ramp: $$H(\nu) = |\nu|$$

Shepp-Logan: $$H(\nu) = \frac{2\ \nu_{cut-off}}{\pi}\ \sin\left(\frac{|\nu|\pi}{2\ \nu_{cut-off}}\right)$$

Shepp-Logan modified: $$H(\nu) = \frac{2\ \nu_{cut-off}}{\pi}\ \sin\left(\frac{|\nu|\pi}{\nu_{cut-off}}\right)$$

Hann: $$H(\nu) = 0.5\ |\nu|\left(1 + \cos\frac{\pi\nu}{\nu_{cut-off}}\right)$$

Low Pass Cosine: $$H(\nu) = |\nu|\cos\left(\frac{|\nu|\pi}{2\ \nu_{cut-off}}\right)$$

Noise: $$H(\nu) = \frac{|\nu|}{0.01 + |\nu|\ ln[\frac{3}{2}\exp(1 + |\nu|^2)]}$$

Figure 3.18 shows the graphs of the filters implented in the YAP-(S)PET Reconstruction tool. The values reported on the y-axis are multiplied by a constant factor [99].

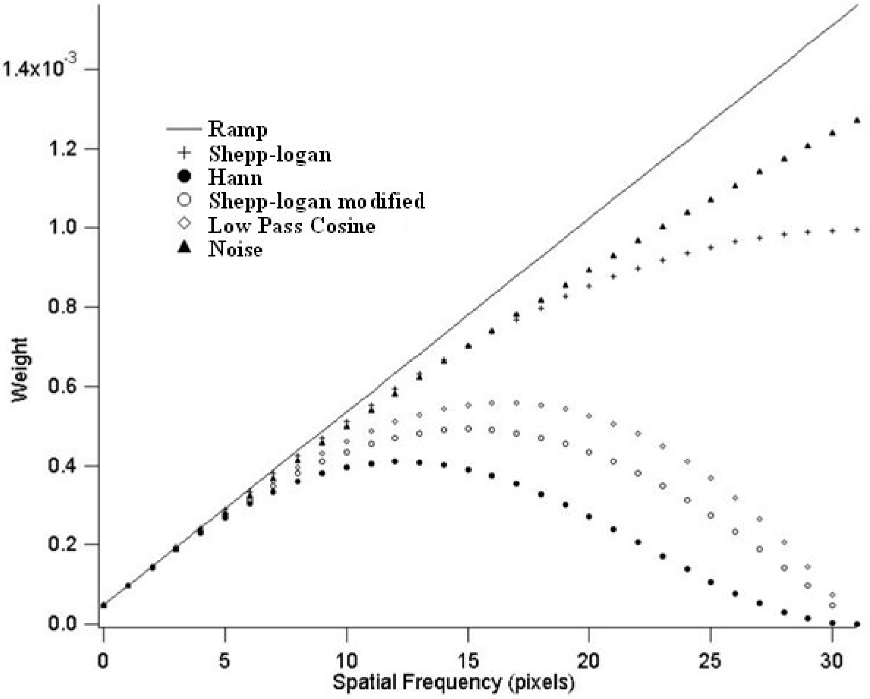

Figure 3.18: Graphs of the filters implemented in the YAP-(S)PET Reconstruction tool for the FBP reconstruction mode. The Spatial frequency expressed in pixel actually refers to pixel/FOV, that is in the typical frequency expression pixel/mm. The values reported on the y-axis (Weight) are multiplied by a constant factor [99].

The FBP algorithm is fast and relative easy to implement, that is why it is the most widely used reconstruction method in nuclear medicine. Nevertheless it does not allow to take in account various physical aspects of the imaging system and data acquisition, such as system geometries, detector properties, scattering evaluation, attenutation correction and so on.

The **Maximum Likelihood Expectation Maximization** algorithm, since its introduction to the field of image reconstruction in 1982 by Shepp and Vardi [100], remains the basis for the most popular statistical reconstruction method and has provided the foundation for many other methods. Likelihood is a general statistical measure that is maximized when the difference between the measured and the estimated projection is minimized. The Expectation Maximization (EM) maximizes likelihood under a Poisson data model. It implicitly treats the projection data as having a Poisson distribution determined by the counting statistics in each projection bin and thus takes into account the statistical noise of the data.

The reconstruction problem can be written as follows:

$$s_j = \sum_{i=1} M_{i,j} a_i \tag{3.6}$$

where a_i is the activity in an image pixel i and s_j is the number of counts in projection element j. The i-index runs on all the FOV pixels, while the j-index covers all the LORs. $M_{i,j}$ is the matrix that provides the probability that gamma rays emitted in the pixel i are detected in the projection element j. This matrix provides the model of the imaging system correlating the positron emission and photon detection. In theory, this matrix should include all the parameters to exactly describe the tomograph: system geometry, detector proprierty, scattering evaluation, attenuation correction, and so on. In ML−EM algorithm implemented in the YAP-(S)PET Reconstruction tool, only the detection geometry is considered. The $M_{i,j}$ elements number is given by the product between the sinogram space and the number of pixels that are used to divide the FOV. Since the $M_{i,j}$ matrix matrix has a size that does not allow storing all the elements, the storage space was drastically reduced by considering both the symmetry and the sparse properties of the probability matrix [101].

The ML−EM algorithm can be written as:

$$a_i^{k+1} = \frac{a_i^k}{\sum_j M_{i,j}} \sum_j \frac{M_{i,j} \cdot s_j}{\sum_i M_{i,j} \cdot a_i^k} \tag{3.7}$$

The meaning of the terms in equation 3.7 can be better explained with reference to figure 3.19 [102]. We start with an initial image guess $\mathbf{a^0}$ that is the entire image set to a costant value. The first step of the ML−EM algorithm (1) foward projects the initial image guess nto the projection domain. Then, (2) these projections are compared with the measured projections, $\mathbf{s}$. This forms a multiplicative correction factor for each projection, which is then (3) backprojected onto the image domain to obtain a correction factor for the initial image estimate. This image domain correction factor is then (4) multiplied by the current image estimate and divided by a weighting term based on the system model to apply the desired strength of each image correction factor. The new image estimate is now reentered in the algorithm as the next image; the algorithm repeats itself while the estimate approaches the maximum likelihood solution. When the estimate projetion data exactly equalize the measured projection data s_j (substituting from equation 3.6):

$$a_i^{k+1} = a_i^k \tag{3.8}$$

and the image does not change any more. This never actually occurs in practice because of noise in the data and approximations in $M_{i,j}$.

As the ML−EM algorithm iteratively guesses an image estimate, the low frequency components of the image appear within the first few iterations. As the Mamimun Likelihood estimate is approached, more and more high frequency definition is resolved in the image, effectively adding more variance to the reconstruction. The convergence rate of ML−EM is image dependent, but usually requires approximately 20-50 iterations to reach an acceptable solution [102].

In ML−EM algorithm implemented in the YAP-(S)PET, it is either possible to freely choose the number of iterations to be performed during the reconstruction or to set the automatic procedure that determine the number of iteration on the basis of an empirical parameter [101].

Due to the possibility to include the detection process in the probabilty matrix $M_{i,j}$, the ML−EM algorithm leads to potentially more accurate images. On the other hand, the reconstruction time is considerably longer than the FBP approach. A number of approximations have been developed to speed up these algorithms.

One of the most popular is the **Ordered Subsets Expectation Maximization (OSEM)** introduced in 1994 by Hudson and Larkin [103]. With OSEM, the projection data are grouped in subsets of projection views. Then, the ML−EM algorithm is applied to the projections in the first subset and the obtained image is used as starting image for the next subset. An iteration of OSEM is then defined as a single pass through all the specified subsets. Further iterations may be performed by passing through the same ordered subsets, using the reconstruction provided by the previous iteration as a starting image. When there is only one subset, OSEM is the same as ML−EM. Even though OSEM resembles ML−EM, this computationally convenient method is not guaranteed to converge to the ML solution. In practice, its convergence is similar to ML−EM and approaches the ML solution roughly B times faster than conventional ML−EM, where B is the number of subsets.

In the YAP-(S)PET Reconstruction tool, it is possible to choose up to six subsets and a maximum of 1000 iterations for both ML−EM and OSEM algorithms. It is also possible to choose the display of the reconstructed image of some of the interemediate itereations, besides the last one.

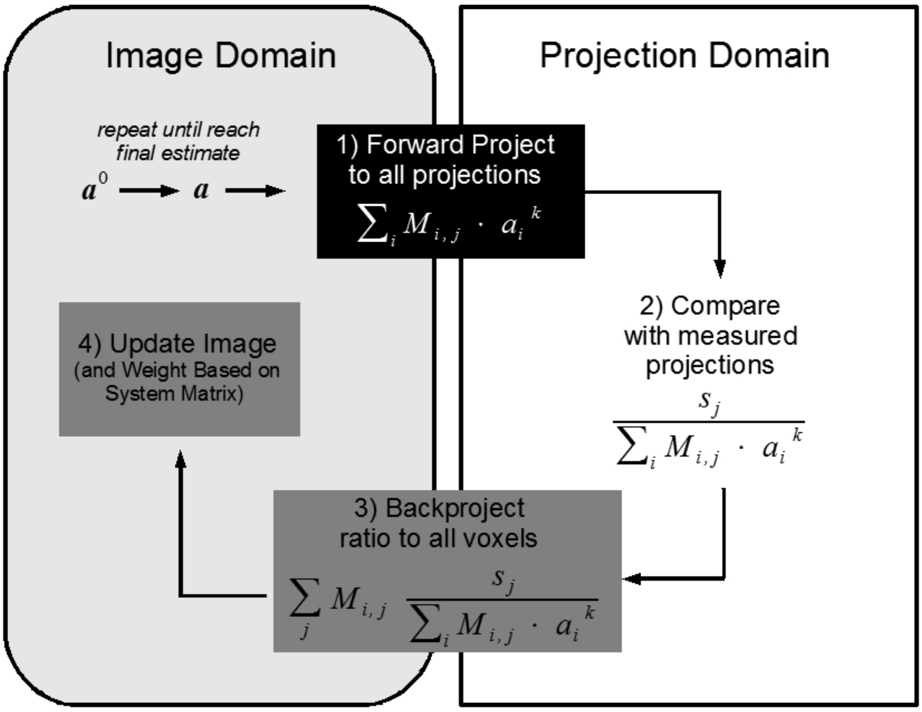

Figure 3.19: Flow diagram of the ML−EM algorithm. Starting with an initial image guess ($\mathbf{a^0}$) in the upper left, the algorithm iteratively chooses new image estimates based on the measured projections, $\mathbf{s}$ [102].

Other reconstruction methods for the YAP-(S)PET scanner are under investigation. In particular, a multi-Ray based system matrix generation for 3-D PET reconstruction [104].

3.3.5 Display

The end result of the Reconstruction process is a 3- D image volume where each individual voxel (volume element) represents the regional tissue radioactivity concentration.

The digital images so produced are saved in a proprietary raw data format (imm).

The matrix size of the transaxial cross-section images can be 64 × 64, 128 × 128 or 256 × 256 corresponding to a pixel dimension of 1.5 mm/2, 1.5 mm/4 or 1.5 mm/8 respectively (1.5 mm is the YAP crystal pitch). The number of slices in the axial dimension can be 27 or 53, corresponding to 1.5 or 0.75 mm sampling, respectively. The pixel depth is 32 bits (4 bytes) and the data are stored in memory with Little-Endian byte order [1]. Image data can also be saved in the DICOM (Digital Imaging and Communications in Medicine [105]) standard format.

The images display and processing can be performed with variuos imaging software provided with the YAP-(S)PET scanner: **ImageJ**, **AMIDE** and **P-MOD** software.

The free and open source **ImageJ** [106] is a public domain Java image processing program inspired by NIH (National Institute of Health [107]) *Image* for the Macintosh. It has been developed by Wayne Rasband at the Research Service Branch, of the NIH, Bethesda, Maryland, USA. It can run virtually on all operating systems since it has been written in Java 1.1. ImageJ is the imaging software embedded in the YAP-(S)PET Analysis and Reconstruction tools and enables to automatically display both sinograms and images.

AMIDE (Amide's a Medical Imaging Data Examiner) [108] is a completely free tool for viewing, analyzing, and registering volumetric medical imaging data sets. It has been developed using GTK+/GNOME, and runs on any system that supports the toolkit (Linux, Windows, Mac OS X with fink, etc.).

PMOD [109] is a proprietary software produced and commercialized by PMOD Technologies Ltd., Zurich, Switzerland. It has been written in Java 2 and is currently offered under Windows, Linux and MacOS X operatin systems. PMOD consists of a set of user-friendly and powerful tools, each corresponding to a major task. Among the main tools, the general kinetic modeling contains a comprehensive set of models for the analysis of time-activity data. The cardiac tool is tailored to assess function in cardiac segments by full kinetic modeling, and to compare the outcome against normal databases. The image fusion tool does not only allow to register images, but also enables the user to explore the calculated functional images in detail.

---

[1] In computing, endianness is the byte ordering in computer memory used to represent data. In the Litte-Endian byte order the least significant byte (LSB) value is at the lowest address. The other bytes follow in increasing order of significance.

Chapter 4

Calibration procedures

Every PET or SPECT scanners needs quality control and calibration procedure to work properly and garantee adequate scanner performance.

Thus, when in the first half of 2006, the new version of YAP-(S)PET scanner with new detection matrices and electronic boards was completed (see chapter 3), new calibration procedures became necessary. These procedures concern both hardware and software issues and are performed on the basis of the calibration procedure developed for the first YAP-(S)PET scanner and described in [85].

The hardware calibrations include both electronics and mechanics settings such as adjustment of PMT gain or precise positioning of the center of rotation (COR). They are performed during the installation and commissioning of the scanner and have to be repeated every time specific hardware upgrade are made on the scanner.

The sotfware calibrations concern definition of crystal and energy maps, and efficiency corrections. Unlike the hardware, the software calibrations must be performed on a regular basis to maintain the scanner performance.

The calibration procedures were performed for 100, 125 and 150 mm head-to-head distance.

4.1 Hardware procedures

Several parameters influence the YAP-(S)PET performance both in PET or SPECT modality. Among these, the more susceptable to variation during a new installation are:

- the High Voltage (HV) of the photomultiplier (PSPMT) tube of each single head.
- the center of rotation of the scanner.

4.1.1 HV settings

The HV value can be indipendently set for each PSPMT (see section 3.2.3).

The optimal regulation is the one that offers the best trade off between a high gain and few saturations of the ADC for the signals of the PSPMT.

PET modality

It is recommended to use a pure positron emitting source (e.g., ^{18}F), since the use of a source that emits also other photons (e.g., ^{22}Na) could alter the evaluation of the saturations. A fraction of saturation events can in fact be generated by the coincidence between a gamma ray of 511 keV and the additional gamma ray (1274 keV for ^{22}Na).

To appropriately take in account possible PSPMT photocatode variations, two different type of acquisitions can be performed:

- a single view acquisition with a planar source that evenly illuminate all the YAP matrix and consequently the whole PSPMT photocatode.
- a tomographic acquisition employing a point or a linear source.

The measurements were performed with a linear source of ^{68}Ge with an activity in the range of 13-16 MBq (500-600 μCi). This source is identical to the source usually employed in clinical PET calibration, but has lower activity. A four view acquisition over 360^0 was performed and at least 12 Mevents were acquired.

The spectra of the four anodic position signals of each PSPMT are generated by the raw analysis of the calibration listmode file (see section 3.3.3). Each spectrum reports the number of counts as a function of the ADC channel (see figure 4.1). Since 12 bits were used to display the ADC channels, the maximum value is 4096.

The saturation of $\mathrm{x_a}$ position signal of head 2 is visible in figure 4.1 (red line). Neverthelss, in this case the HV setting of the head was not modified, since the other position signals use a wide portion of ADC range and do not show significant saturation.

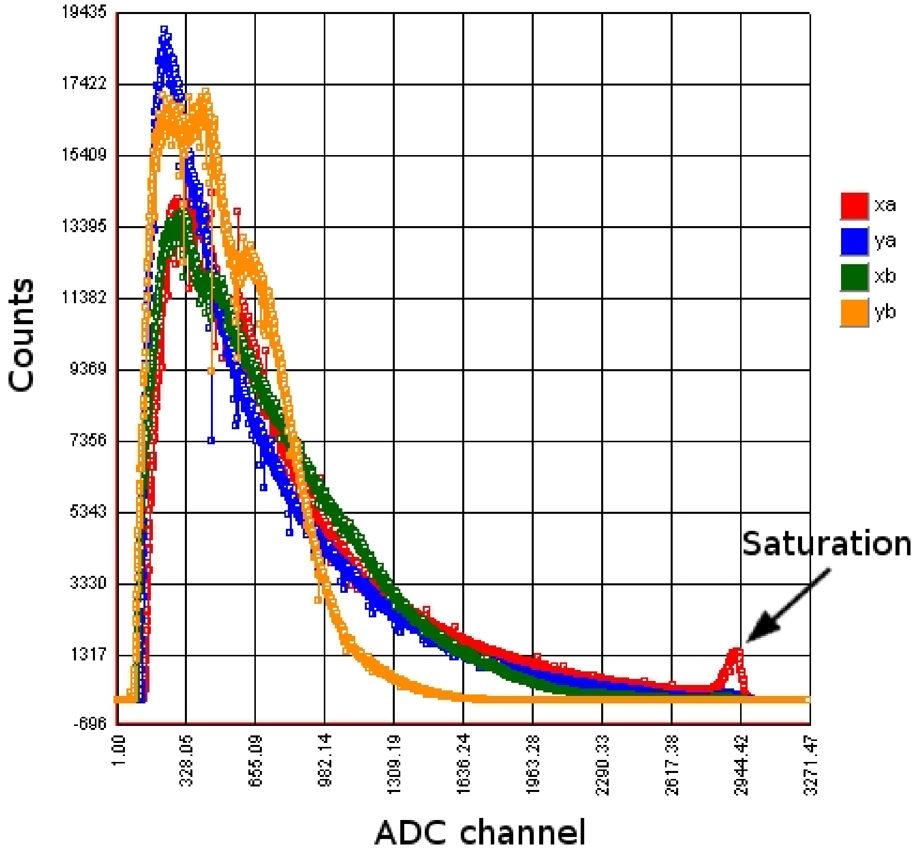

Figure 4.1: Position signals ($\mathrm{x_a}$, $\mathrm{y_a}$, $\mathrm{x_b}$, $\mathrm{y_a}$) spectra of head 2. $\mathrm{x_a}$ spectrum shows a saturation.

On the contrary, when spectra such as the one represented by the cyan line in figure 4.2 take place, a HV regulation is necessary. Figure 4.2 represents the histogram obtained by the sum of the four anodic position signals, the cyan line is related to the head 4 of the YAP-(S)PET scanner.

Since the single and summed anodic position signals histograms, figure 4.1 and 4.2, respectively, give information about saturation and gain of the PSPMT, they are very helpful for HV setting and control.

SPECT modality

The SPECT procedures for HV setting are performed in the same way as in PET mode, so no further details will be provided.

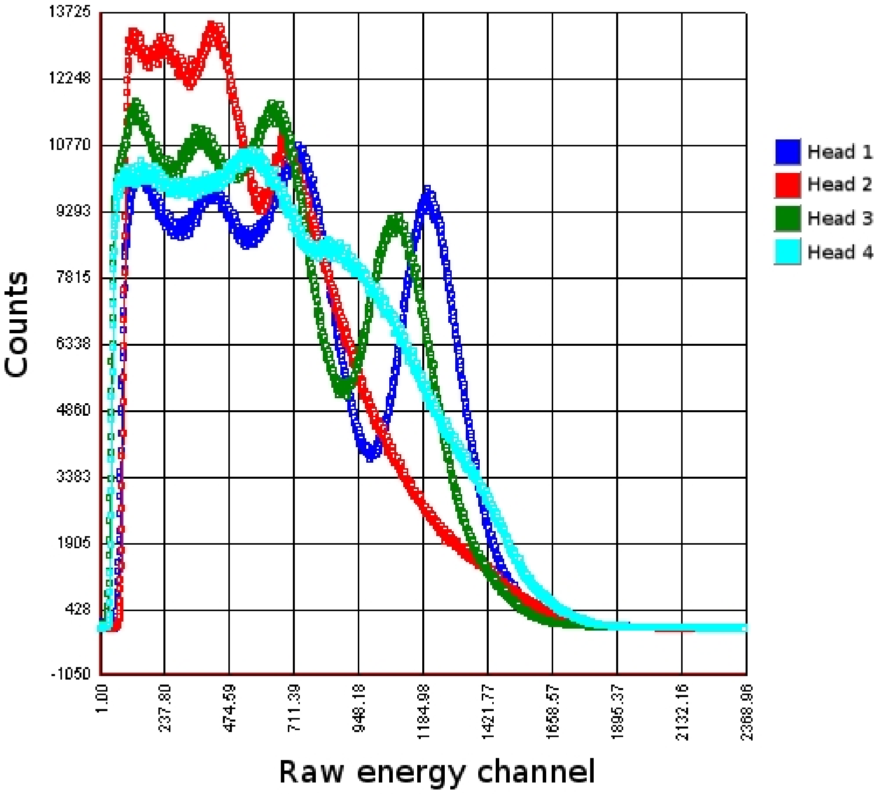

Figure 4.2: Raw energy spectra for each heads.

However, it is worthwhile to note that now the used source must be single gamma emitting.

As for PET modality, two different type of acquisitions can be performed to take in account possible PSPMT photocatode variations: single view acquisition with a planar source or tomographic acquisition with linear source. We performed the acquisition with a glass capillary (of 44.7 μl volume, inner 0.8 mm, outer diameter 1.2 mm, respectively) filled with 111 MBq (3 mCi) of ^{99m}Tc. A 4 views acquisition over 360^0 was performed and at least 3 Mevents were acquired.

4.1.2 Center of rotation

In the reconstruction of images from projections it is assumed that the image matrix, representing the activity distribution in a section, has a constant relationship to the data acquisition matrix (detector matrix). In other words, it is critical that the mechanical center of rotation coincides with the center of rotation (COR) defined for the projection data used for reconstruction. The non-perfect alignment between detector and image matrix for different angles of data acquisition, means that the COR is moving during the acquisition. It causes blurring in the reconstructed image, resulting in a loss of spatial resolution.

Since it is extremely difficult to make a mechanically or rotationally perfect gantry, measure of misalignment and hardware or software corrections must be performed. Software corrections are usually adopted by manufacturers to take into account the detectors misalignment respect to the real rotation center. The YAP-(S)PET software correction procedure is still under evaluation, so at the moment the COR corrections are performed with an hardware procedure. It consists in mechanical corrections realized with the help of “Johnson blocks”, a series of calibration blocks.

In PET mode, the COR misalignment is related to the shift between the center of rotation and the axis joining a pair of detectors: no information about the absolute shift of the single head can be obtained. The SPECT COR misalignments produce more image degradation with respect to PET acquisitions, and in severe case lead to generation of ring or annular artifacts. For these reasons, the COR misalignment is evaluated in SPECT modality and then checked in PET mode.

SPECT modality

The simplest way to measure the COR misalignment is to perform an acquisition over 360^0 of an off-axis point or line source [110]. The amplitude of the sine wave of the sinogram is the distance of the point source from the center of rotation. The advantage of using a line source is the capability of measuring the center of rotation for each axial slice at the same time.

We performed the acquisition with a glass capillary (44.7 μl volume, inner diameter 0.8 mm, outer 1.2 mm) filled with 111 MBq (3 mCi) of ^{99m}Tc. A 128 views acquisition over 360^0 was performed and at least 3 Mevents were acquired. The capillary was filled for a length at least equal to the FOV transaxial dimension (4cm) and placed off-axis parallel to the axial direction.

The collected data were sorted in 2-D sinograms and a 140-250 keV energy window was used. In order to produce correct sinograms, software corrections must be performed on the acquired data. The center of rotation measurement is then performed after software correction procedures (see section 4.2).

The 2-D sinograms are produced for each head and without angular rebinning, so for an acquisition of 128 over 360^0 each sinogram has 128 angular bins (see section 3.3.3).

Once the sinograms for each head are produced, the YAP-(S)PET software tool "Center calculator dialog" (see figure **??**) allows to fit each slice of the sinogram with a sinusoid and to estimate the COR offset. The function used to fit each slice of the sinogram is:

$$\mathrm{s}(\theta_{\mathrm{bin}}) = \mathrm{A}_0 + \mathrm{A} \cdot \sin\left(\frac{2\pi}{\mathrm{N}_\theta} \cdot \theta_{\mathrm{bin}} + \phi\right) \tag{4.1}$$

where s is the radial coordinate of the sinogram, θ_{bin} is the angular bin in the slice, N_θ is the number of angular bins (see equation 3.3), ϕ is the phase.

Since the produced sinograms have 27 spatial bins (running between 0 and 26), the A_0 value for a good center of rotation alignment is 13.

For each head and for each slice of the sinogram the shift from the right COR value (Δ_{COR}) is shown by the tab nearby the gray square indicating the number of the head in figure 4.3. The average COR error in the direction perpendicular to the axis joining a couple of detectors in the transaxial plane, is given by the following relation:

$$\mathrm{E}_{\mathrm{err\ COR}} = \frac{1}{\mathrm{N_s}} \sum_{i=1}^{\mathrm{N_s}} \Delta_{\mathrm{COR}} \tag{4.2}$$

where $\mathrm{N_s}$ is the number of axial slices of the sinogram.

Besides COR misalignment due to mechanical shift of the axes of rotation, also both local and global deviations of the parallel holes with respect to the perpendicular direction to the detector surface may affect the center of rotation [110]. In order to separate the two contributions, two acquisitions of the COR were performed. The second one with the collimators rotated of 180^0 respect to the their axis (forth to back rotation). If there are variations in collimator hole angle, the COR shift error ($\Delta_{\mathrm{COR},180^0}$) assumes the same abosolute value but with opposite sign of Δ_{COR}. On the contrary, Δ_{COR} and $\Delta_{\mathrm{COR},180^0}$ assume different values. The head shift (Δ) is obtained by averaging the value of the two COR offset.

In this way the contribution of the collimator misalignment is bypassed. The head shift so evaluated is corrected mechanically with “Johnson blocks” by moving up or down the head.

If Δ offset of a head is under 1/10 of mm, we do not apply any corrections to the center of rotation.

Due to COR variability caused by the collimator holes angle, the SPECT corrections to the center of rotation can not be appropriate for PET purposes. Once adjusted the COR in SPECT mode, it is then necessary to repeat the measurements in PET modality.

PET modality

The acquisition was performed with the same ^{68}Ge linear source employed in HV setting (see section 4.1.1) placed about 1 cm off axis. A 128 views acquisition over 360^0 was performed and at least 15 Mevents were acquired.

The collected data were sorted in 3-D MSRB sinograms without angular rebinning and a 50-850 keV energy window was used. The COR offset is obtained by fitting the sinogram of each couple with a sinusoid function (see equation 4.1 and figure 4.3).

In PET modality, the offset gives only the distance between the center of rotation and the axis joining a couple of detectors: no infomation about the absolute shift of the single head can be obtained.

If the offset of a couple of detectors is under 1-2/10 of mm, we do not apply any corrections to the center of roataion.

4.2 Software procedures

The software calibration procedures consists essentially of three procedures:

- Pixel identification
- Energy correction
- Efficiency corrections

These procedures must be perfomed for both PET and SPECT modalities and were realized through the planar source acquisistion described in the next section.

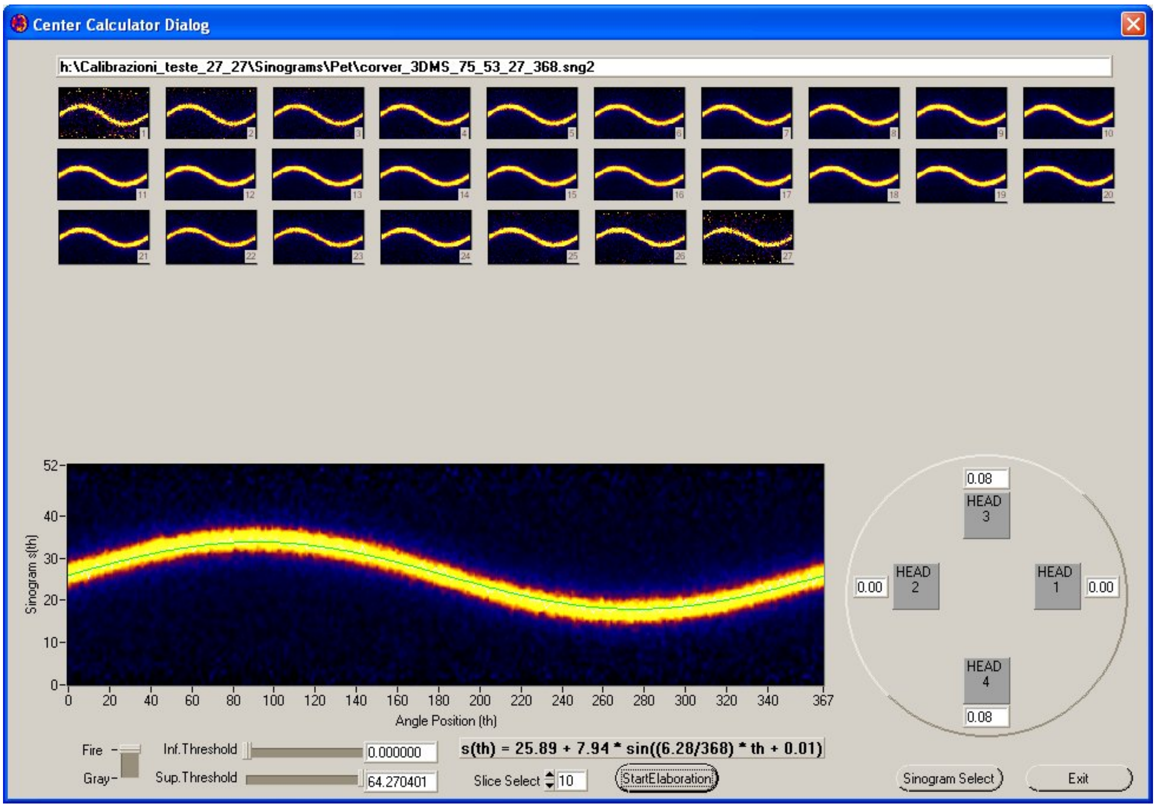

h:\Calibrazioni_teste_27_27\Sinograms\Pet\corver_3DMS_75_53_27_368.sng2

Inf.Threshold 0.000000

Sup.Threshold 64.270401

s(th) = 25.89 + 7.94 * sin((6.28/368) * th + 0.01)

Slice Select 10

Figure 4.3: PET 2-D sinogram produced without angular rebinnig for the head pair 3-4. The measured pair of heads is + 0.08 mm.

4.2.1 Pixel identification

To correctly determine the lines of flight (LORs) of the detected photons, it is necessary to identify the YAP crystal array pixels in which the interaction takes place. The identification procedure associates each interacting photon (“event”), detected in the crystal that faces the center of the tomograph, to the geometric center of the YAP crystal in which the interaction has occured. A Cartesian coordinates system (x,y) is used.

In both PET and SPECT modalities a uniformly filled planar source is used to evenly illuminate each detector matrix.

PET modality

The planar source was filled with about 11 MBq ($\sim$ 300 μCi) of a solution of ^{18}F and placed in the center of the FOV (see figure 4.4) in order to obtain a flood field illumination for each head of the couple of coincidence detectors. An acquisition of 2 views over 180^0 is performed. Since the accuracy of the calibration measurement is determined by a good acquisition statistics, 100-200 Mevents were acquired.

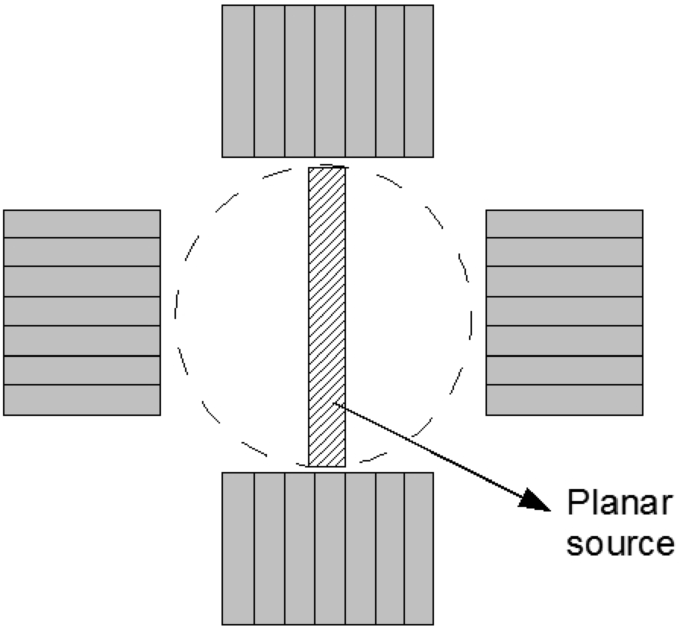

Figure 4.4: Sketch of the positiong of the planar source used to perform PET or SPECT Pixel Identification procedure.

The acquired data of each head are organized by the YAP-(S)PET software tool "Pixel Identification Panel" in a 2-D histogram image based on the calculated x,y positions (see figure 4.5).

Due to the position non linearity determined by the photocatode nonuniformity and gain variation of the mesh dynodes, the image is not uniform. The data are clustered in small localized areas corresponding to individual crystal elements and there is a small amount of overlap. Nevertheless, the separation between the center of the crystals is enough to allow each x,y location assignment in the Cartesian coordinate system by a Look Up Table (LUT). The single crystal identification and spatial assignment is performed by the "Pixel Identification" software tool through the following operations:

- automatically finds the center of each crystal and allows a manual operation when the automatic procedure fails (see figure 4.5).

- progressively enumerates (from top to bottom and from left to right for each row) each crystal of the YAP matrix (see figure 4.6).

- uses a numeric algorithm (the Manhattan algorithm) to calculate the distance between the centers of two contiguous crystals.

- defines a geometric region around the center of each crystal and assignes to the center of the crystal all the events inside this region (see figure 4.6).

The crystal position matrices so determined are saved in binary files in both YAP-(S)PET client and server applications (see section 3.3.1), and are used in all the subsequent acquisitions until a new pixel identification procedure is performed.

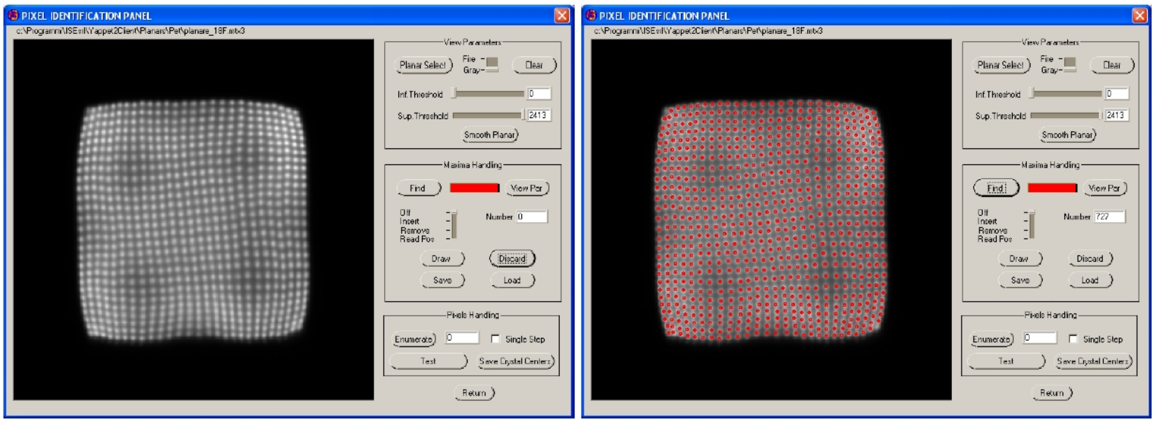

(a) (b)

Figure 4.5: PET mode images. (a) 2-D histogram image based on the calculated x,y positions of the events detected by head 3 in PET mode. (b) Automatically identification of the center of each crystal in the 2-D histogram image.

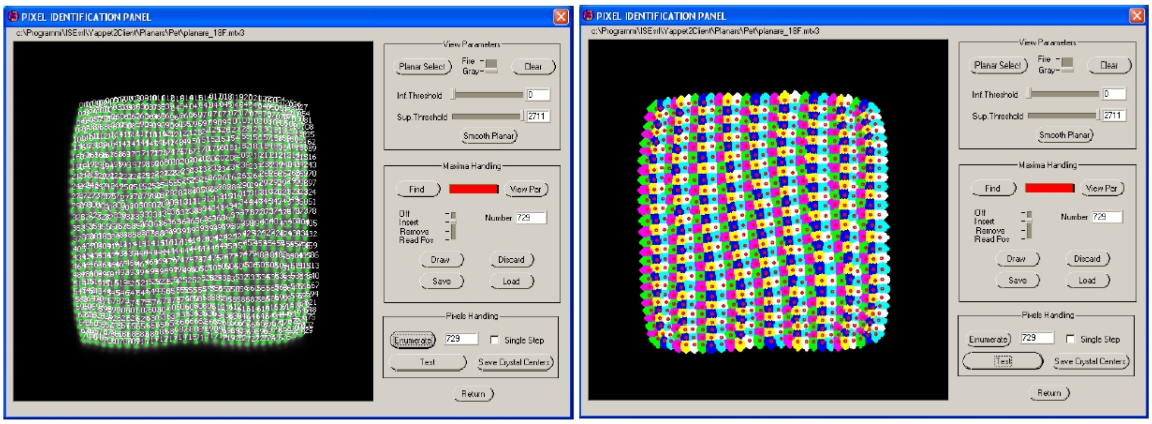

(a) (b)

Figure 4.6: (a) Enumeration of the center of each crystal in the 2-D histogram image. (b) Geometric region around the center of each crystal of the 2-D histogram image. All the events inside this region are assigned to the center of the crystal.

SPECT modality

The SPECT pixel identification procedure is performed in the same way as in PET mode; further details are given and only the difference with respect to PET modality are highlighted.

The planar source was filled with 185 MBq ($\sim$ 5 mCi) of a solution of ^{99m}Tc and placed at the center of the FOV in order to flood illuminate each single head. An acquisition of 4 views over 360^0 is performed and at least 120 Mevents are acquired. Figure 4.7 shows the image obtained by the even illumination of the detector matrix 1 (a) and the same image with the the center of each crystals automatically found by the software tool (b).

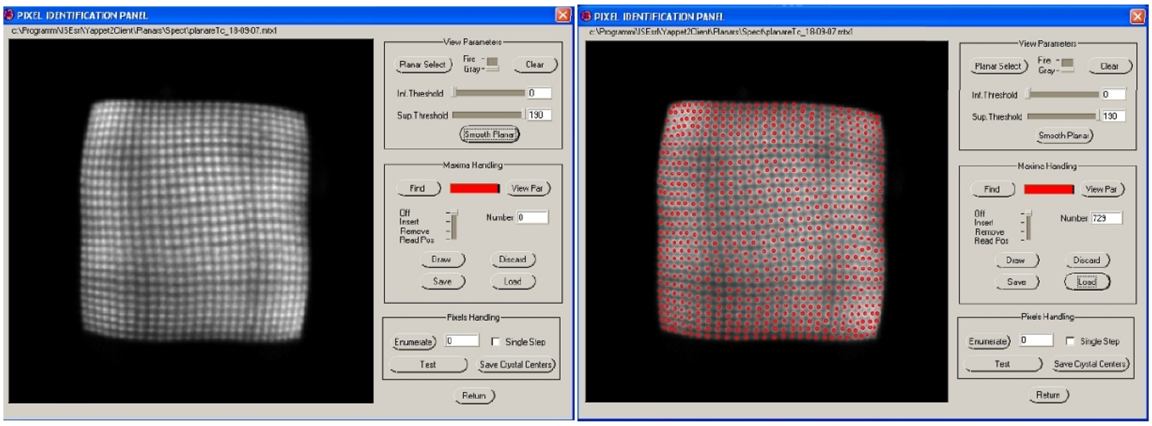

c:\Programmi\ISEst\Yappet2Client\Planars\Spect\planareTc_18-09-07.mtx1

Inf. Threshold 0
Sup.Threshold 190
Number 0

c:\Programmi\ISEst\Yappet2Client\Planars\Spect\planareTc_18-09-07.mtx1

Inf. Threshold 0
Sup.Threshold 190
Number 729

(a) (b)

Figure 4.7: SPECT mode images. (a) 2-D histogram image based on the calculated x,y positions of the events detected by head 3 in PET mode. (b) Automatically identification of the center of each crystal in the 2-D histogram image.

4.2.2 Energy corrections

Once the matrix of the center of the crystals is imported into the listmode file of the planar source acquisition, an energy spectrum of each crystal can be produced by the YAP-(S)PET software. The spectra are reported as a function of the channels (see figure 4.8). Then an energy-channel calibration is necessary.

PET modality

The YAP-(S)PET software tool, "Energy correction panel", automatically perform a gaussian fit on each spectrum of detector matrix crystals (729 per each detector matrix) to find out the photopeak channel value. If the automatic fit fails, manual tuning is possible. The energy-channel calibration factor is then obtained by the ratio between the energy and channel value of the photopeak. For positron emitters, the energy value is 511 KeV. Since the calibration is performed per each spectrum, a correction matrix is obtained. Typical corrections value as obtained for head 3 of the YAP-(S)PET scanner are presented in figure 4.9. This procedure allows to remove the difference in energy response among the crystals of the detector matrix and the different zones of the photocatode. It is then possible to produce a summed energy spectrum for each detector head (see figure 4.10).

The energy correction matrices, as crystal position matrices, are saved in binary files in both YAP-(S)PET client and server application and used in all the subsequent acquisitions until a new calibration procedure is performed.

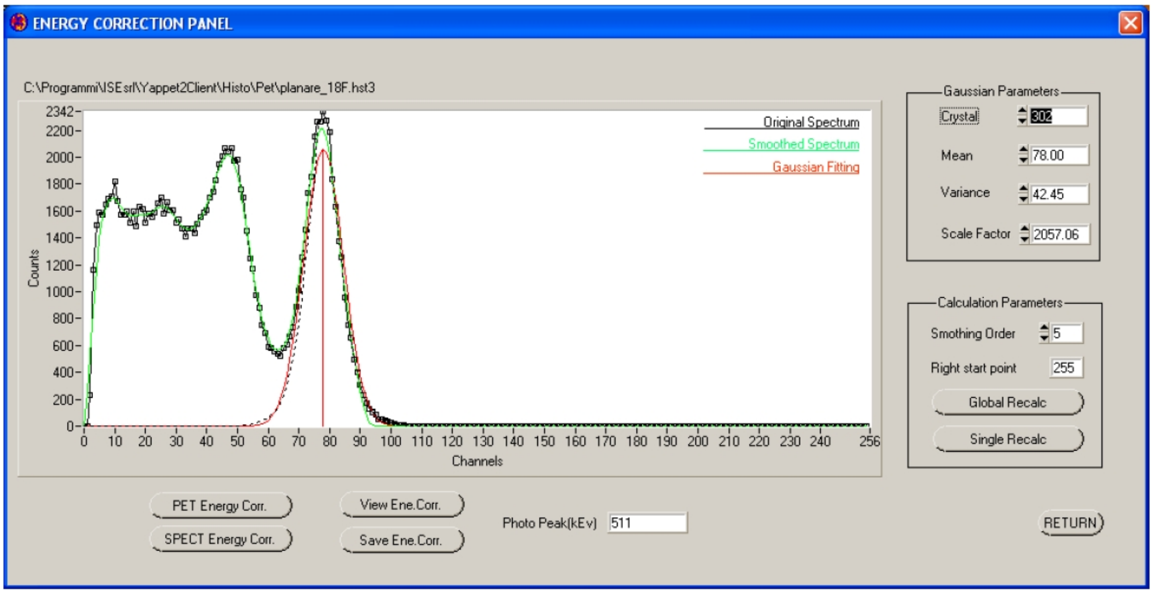

ENERGY CORRECTION PANEL

C:\Programmi\ISEsrl\Yappet2Client\Histo\Pet\planare_18F.hst3

Gaussian Parameters
Crystal 302
Mean 78.00
Variance 42.45
Scale Factor 2057.06

Calculation Parameters
Smothing Order 5
Right start point 255

Photo Peak(kEv) 511

Figure 4.8: A typical PET spectrum of a of a single crystal of the head 3. The red line represents the gaussian fit of the photopeak.

SPECT modality

The SPECT energy calibration is performed as in PET mode.

It is worthwhile to note that each single gamma emitter has a peculariar photopeak energy value, i.e., for ^{99m}Tc it is 140 keV. If radionuclides different than ^{99m}Tc are used, a specific energy calibration procedure must be perfomed.

Figure 4.11 reports the summed calibrated energy spectrum for head 1 of the scanner.

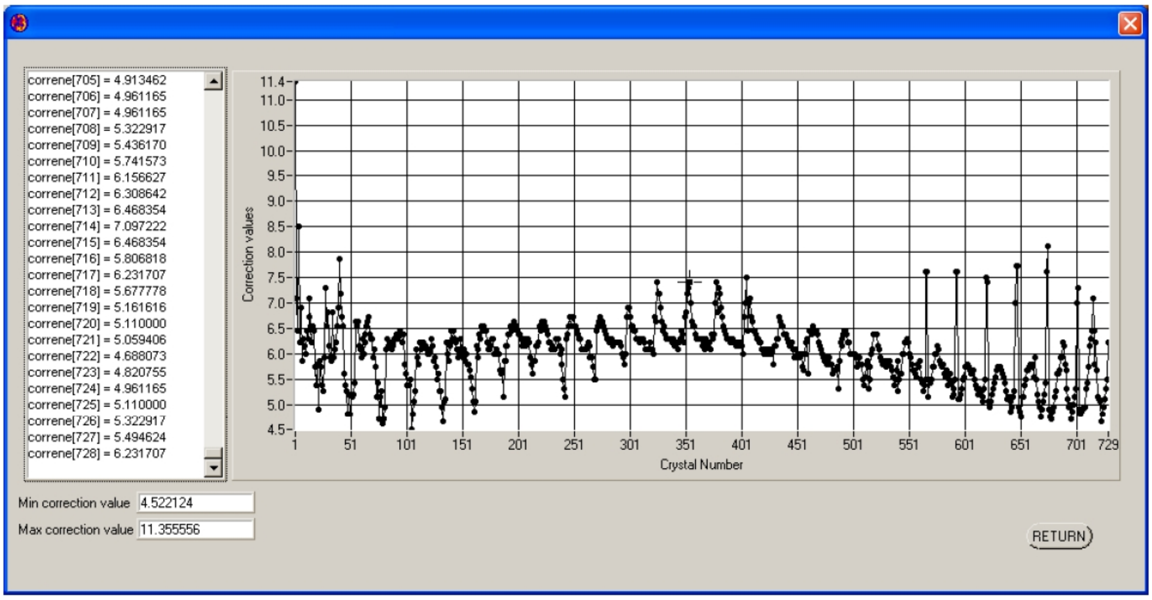

```
correne[705] = 4.913462
correne[706] = 4.961165
correne[707] = 4.961165
correne[708] = 5.322917
correne[709] = 5.436170
correne[710] = 5.741573
correne[711] = 6.156627
correne[712] = 6.308642
correne[713] = 6.468354
correne[714] = 7.097222
correne[715] = 6.468354
correne[716] = 5.806818
correne[717] = 6.231707
correne[718] = 5.677778
correne[719] = 5.161616
correne[720] = 5.110000
correne[721] = 5.059406
correne[722] = 4.688073
correne[723] = 4.820755
correne[724] = 4.961165
correne[725] = 5.110000
correne[726] = 5.322917
correne[727] = 5.494624
correne[728] = 6.231707
```

Min correction value 4.522124

Max correction value 11.355556

Figure 4.9: Examples of energy correction coefficients obtained ofr head 3 in PET mode.

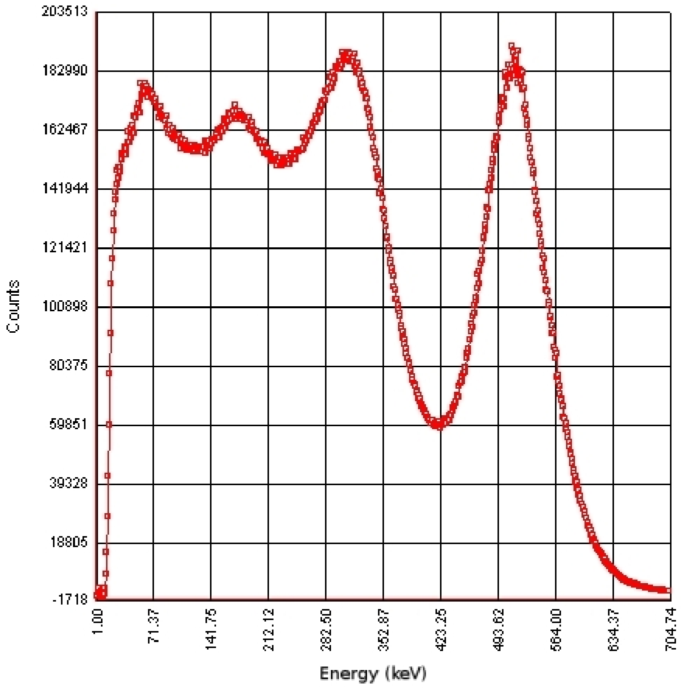

Figure 4.10: Summed energy spectra for head 3 in PET mode.

4.2.3 Efficiency corrections

Efficiency calibrations are necessary to normalize the differing responses of individual crystals. The corrections are performed both in PET and SPECT modalities.

PET modality

In PET mode, the differences among crystals responses are mainly due to photo-

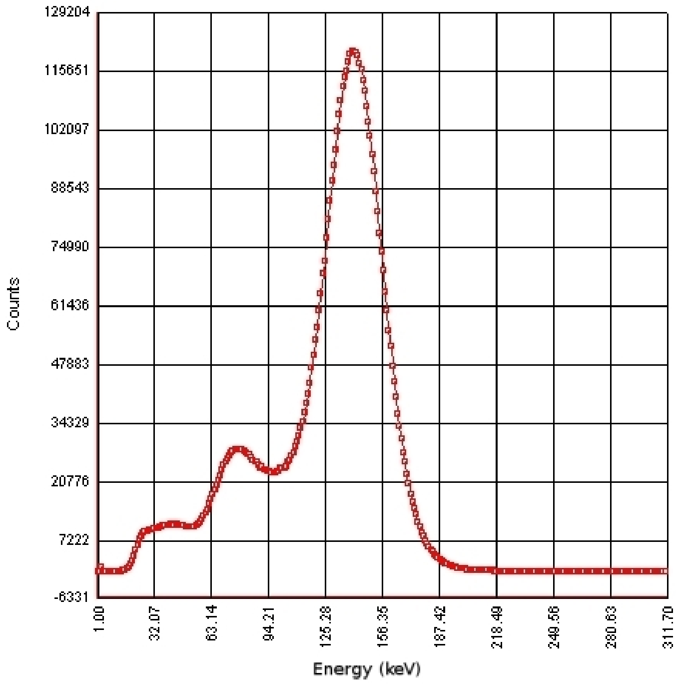

Figure 4.11: Summed energy spectra for head 1 in SPECT mode.

catode nonuniformity and different dimension of the crystals [111].

Even if less important than in SPECT modality, PET efficiency corrections are essential in producing artefact-free images [112].

The efficiency corrections are applied LOR per LOR. The most straightforward way to obtain a full set of normalization coefficients is to perform an acquisition with an uniformly filled planar source, where every possible LOR is illuminated by the same coincidence source [112].

We employed the planar source and performed the acquisition described in section 4.2.1. For each angular view, only the events detected in that geometric configuration are considered. At the end of the acquisition two identical views, one for couple of detectors, are obtained. After having corrected the data for the source decay during one view and the other, it is possible to obtain the efficiency corrections. The efficiency factor ($\varepsilon_{\mathrm{i,j}}$) for the coincidence LOR between a given pair of detectors is then estimated as the ratio between the number of coincidences measured in that LOR during the planar acquisition ($C_{\mathrm{i,j}}$), and the number of coincidences which would have been measured if the sensitivities of the detectors were uniform. This latter is estimated as the mean number of coincidences detected, averaged over all active

LORs [113].

$$\varepsilon_{\mathrm{i,j}} = \frac{\mathrm{C_{i,j}}}{\sum_{\mathrm{i,j}} \mathrm{C_{i,j}}} \cdot 729^2 \tag{4.3}$$

where 729 is the number of YAP crystals in each detector matrix (see section 3.1).

The normalization factors ($\mathrm{P_{i,j}}$) that are then used to correct the phantoms or animals acquisitions are proportional to the inverse of the counts recorded in any given LOR.

$$\mathrm{P_{i,j}} = \frac{1}{\varepsilon_{\mathrm{i,j}}} \tag{4.4}$$

SPECT modality

In SPECT mode, the different response of the crystals can be due to the following issues:

- the crystal - collimator coupling, that can be more or less favourable in terms of portion of the crystal covered by the collimator septum.
- nonuniformity of the photocatode.
- the different dimension of the crystals.

As for the PET mode, the efficiency corrections were obtained by performing an acquisition with an uniformly filled planar source. Four angular views over 360^0 were performed (see section 4.2.1) and for each view only the events detected in the head at the right the planar source were considered. Four identical views, one for each head, were obtained. After the correction for the source decay during the different views, it is possible to obtain the global correction coefficients of the four heads.

Chapter 5

Performance evaluation

To objectively compare the performance of different emission scanners (PET or SPECT) guidelines must be developed on how certain parameters (such as spatial resolution and sensitivity) should be evaluated and presented. National Electric Manufacturers Association (NEMA) is the organization that provides standardization procedures. For clinical PET scanners, NEMA NU2-1994 [114] and the subsequent NEMA NU2-2001 [115] are the reference documents. NEMA NU1-1994 [116] is the reference standard for clinical SPECT scanners.

Since there is no overall accepted evaluation standard for small animal PET imaging systems, the practice followed by several groups ([117–123]) consists of rescaling the performance characteristics evaluation reported for clinical PET scanners [115].

Recently, NEMA has created a task force, Animal PET Scanner Standard Task Force [124], in order to standardize the measurements to carry out the performance evaluation of small animal PET scanners. The aim of this work finds its roots in several motivations: the increasing number of dedicated small animal systems, the growing interest in small animal PET scanners and the impossibility in applying a part of clinical NEMA standards [125]. The latest version of the draft documents for the task force working on the proposal for a new small animal PET standard to be submitted to NEMA has been updated on June 22nd, 2007 [126].

In this chapter, the PET performance of the YAP-(S)PET scanner have been evaluated following the standards proposed by the PET NEMA task force for small animal scanners [127], [128]. Since the lack of small animal SPECT performance standardization, the SPECT performance of YAP-(S)PET scanner has been evaluated by rescaling the clinical SPECT NEMA reference standards NU1-1994 [116].

For both PET and SPECT modalities, the performance were evaluated at different head-to-head distances (see section 3.1): in particularly 10, 12.5 and 15 cm.

5.1 PET modality performance

5.1.1 Spatial resolution

The reconstructed image spatial resolution for PET scanners can be nicely described in terms of FWHM by the empirical formula of Moses and Derenzo [129]:

$$\mathrm{FWHM} = a\sqrt{(d/2)^2 + b^2 + r^2 + (0.0022D)^2 + p^2} \tag{5.1}$$

where d is the detector size, b the position decoding accuracy, r the positron range, D the detector distance, used here to describe the annihilation photon non-collinearity ($0.5\ D\tan 0.25^0 = 0.0022\ D$), and p the parallax error.

The factor $1.1 < a < 1.3$ depends on the algorithm used to reconstruct the image and typically takes a value of 1.2 when using FBP with a ramp filter.

The first two terms under the square root form what is referred to as the intrinsic detector resolution consisting of the geometric and decoding resolution factors.

The positron range in tissue has an "inverse cusp" like distribution consisting of a narrow spike and long exponential tails. Whereas the actual FWHM is very small [130], the effective FWHM taking into account the broadening due to the entire range distribution (r=2.35 rms) provides a more realistic estimate of the image blurring resulting from positron range. For ^{18}F (one of the most common positron emitters) the FWHM is 0.13 mm, while the effective FWHM (r=2.35 rms) is 0.54 mm.

The contribution from non-collinearity to resolution is significant (2.1 mm) in clinical whole-body scanner having a diameter D$\approx$80 cm, but is almost negligible ($\leq$ 0.33 mm) in a small animal scanner with D $\leq$ 15 cm.

Assuming that the positron range and annihilation photon non-collinearity can be minimized by using radioisotopes with low energy positrons such as ^{18}F and a small detector distance, the image resolution degradation would still amount to about 0.7 mm for a parallax error around zero. With reference to equation (5.1):

$$\mathrm{FWHM} = a\sqrt{(0.54)^2 + (0.0022 \times 150)^2 + p^2} \approx 0.7mm \qquad (5.2)$$

Since the parallax error can no completely be avoided, the achievable intrinsic detector resolution will always exceed 0.7 mm.

Figure 5.1 [131] reports the effects of non-collinearity and positron range as a function of crystal size for several small animal scanners. It shows that the positioning accuracy, and so the spatial resolution, scales down with the size of individual crystals.

On the basis of this assumption and on the results of performed simulation [132], in the 27 × 27 version of the YAP-(S)PET scanner 3 (YAP-(S)PET II) the crystal pitch was reduced from 2.0 down to 1.5 mm.

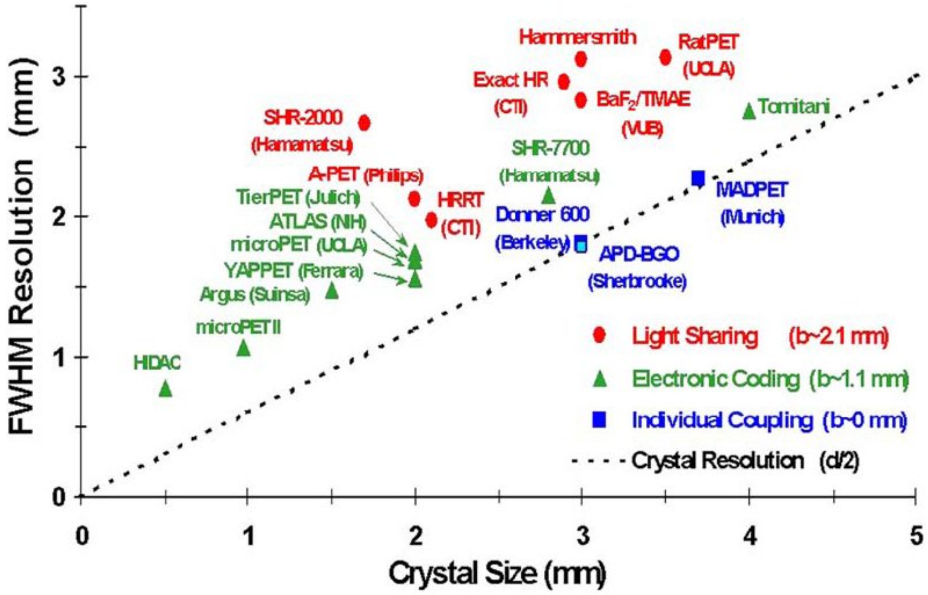

Figure 5.1: Intrinsic spatial resolution of several existing tomographs as a function of detector size. Data have been labeled according to the type of position decoding scheme used to identify the crystal of interaction [131].

In accordance with the NEMA Animal PET Scanner Standard Task Force draft documents [126], the spatial resolution measurements have been performed by imaging point sources in some scatter media, and then reconstructing images with no smoothing or apodization. Although this does not represent the condition of imaging a subject in which there is significant tissue scatter, or where a limited number of acquired events require the use of a smooth reconstruction filter, the measured spatial resolution provides a reproducible comparison among scanners, indicating the highest achievable performance for a given mode of acquisition. The purpose of this measurement is to characterize the widths of the reconstructed image point spread functions (PSF) of compact radioactive sources. The width of the spread function is defined by its FWHM.

The spatial resolution was measured with a ^{22}Na point-like source of 1 mm in diameter, embedded in the geometrical center of a lucite support measuring 23.5 mm × 11 mm and 2 mm in height (see figure 5.2). The activity of the source was 370 kBq (10 μCi) on May 23rd 2001 ($t_{1/2}$= 2.61 y). The average range of the ^{22}Na positrons in this support is similar to the average range of the ^{18}F positrons in water because both isotopes have similar average emission energy ($E_{^{22}Na}$ = 216 keV, $E_{^{18}F}$ = 250 keV). As a result, one can safely assume that the ^{22}Na source size was dominated by its physical dimensions.

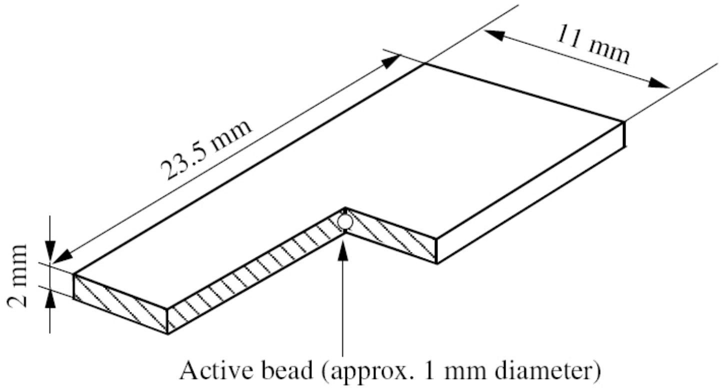

Figure 5.2: Sketch of the ^{22}Na point-like source used for spatial resolution and sensitivity measurements. The source has been provided by Campo Verde srl.

Experimental procedure

The spatial resolution measurements were performed by fixing the ^{22}Na source parallel to the axis of the YAP-(S)PET scanner, and located at the at various radial offsets along the x axis in the transaxial plane: 5, 10, 15 mm (see figure 5.6).

The measurements were repeated for 100, 125, 150 mm head-to-head distances. The acquisitions were performed over 180^0 with 128 views. At least four hundred thousand counts have been acquired in each source positions and for each head-to-head distance.

Data analysis

The collected data were processed via 3-D MSRB sinograms (see section 3.3.3) and then reconstructed with FBP algorithm with ramp filter with cut off at the Nyquist frequency. A wide-open energy window 50-850 keV was used.

Three components of the spatial resolution were measured: the radial and tangential in the transaxial plane, and the axial component along the axis of the scanner (see figure 5.3). The spatial resolution of the point source response function (PSF) in all three directions was determined by taking profiles through the image volume in three orthogonal directions, through the peak of the distribution.

In order to measure the width of the PSF as accurately as can practically be achieved, its FWHM should span at least five pixels (see NEMA proposal for small animal PET scanners [126]). The pixel size should be made no more than one-fifth of the expected FWHM in the transverse dimensions during reconstruction. For this reason, a matrix size of 128 × 128 pixels have been used for the transaxial cross-section of the reconstructed image (0.38 mm for an expected resolution of about 2 mm).

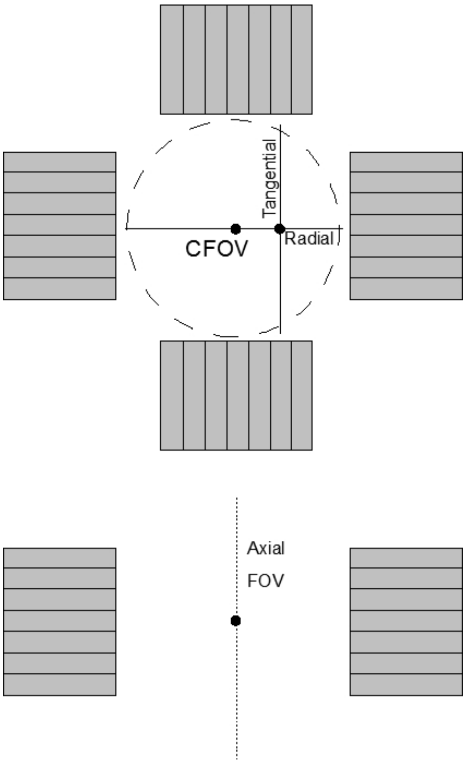

Figure 5.3: Illustration of the radial, tangential and axial component of the measured spatial resolution.

Each FWHM was determined by linear interpolation between adjacent pixels at half of the maximum value of the response function (see figure 5.4). The maximum value was determined by a parabolic fit using the peak point and its two nearest neighboring points respectively. Values were then converted to distance in millimeters by multiplication with the pixel size. The dimension of the source (1 mm in diameter) was not subtracted from the obtained FWHM.

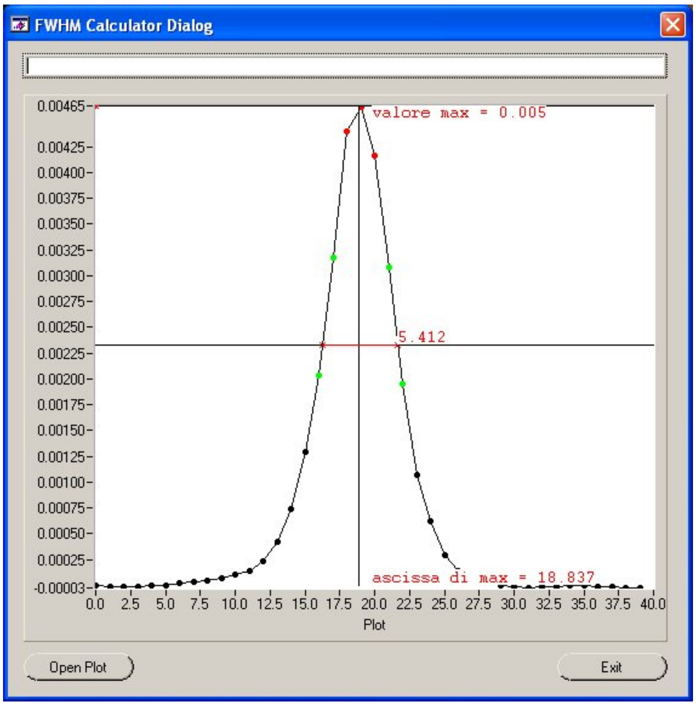

Figure 5.4: Plot of the point source response function (PSF) for the ^{22}Na point source.

Results

Radial ($\mathrm{R_{FWHM}}$), tangential ($\mathrm{T_{FWHM}}$) and axial ($\mathrm{A_{FWHM}}$) FWHM resolutions are reported in figure 5.5 for each radial source position in the FOV (5, 10 and 15 mm) and for each head-to-head distance (100, 125 and 150 mm). The data are reported in table 5.1.

Radial, tangential and axial spatial resolution have the same trend across the FOV for all three head-to-head distances (figure 5.5 (a), (b) and (c)).

The radial spatial resolution shows a little improvement as the radial offset increases, while the tangetial spatial resolution increases slowly approaching the edge of the FOV.

The axial resolution degrades as the source radial offset exceeds 5 mm. This is due to the rebinning method (MSRB, see section 3.3.3) used during the sinograms production.

As can be easily seen from the 15 mm radial offset, the axial degradation is more pronounced at shorter head-to head distance: 4.6 mm at 100 mm with respect to 3.9 at 150 mm. This trend can be explained by the wider acceptance angle (more significant parallax error) offered by closer detectors configuration. The parallax error, infact, manifests itself as a degradation of the axial spatial resolution for off-center sources because of obliquely incident gamma rays that can penetrate the crystals adjacent to that of incidence, thus modifying the real LOR.

Head-to-head distance (mm)	**Position (mm)**	**Radial$_{\mathbf{FWHM}}$**	**Tangential$_{\mathbf{FWHM}}$**	**Axial$_{\mathbf{FWHM}}$**
100	0	2.13	2.31	1.92
	5	2.00	2.43	2.48
	10	1.82	2.81	3.63
	15	1.81	3.00	4.63
125	0	2.04	2.32	1.87
	5	1.93	2.21	2.30
	10	1.81	2.54	3.44
	15	1.74	2.71	4.39
150	0	1.96	2.18	1.87
	5	2.08	2.10	2.17
	10	1.77	2.31	3.03
	15	1.91	2.45	3.92

Table 5.1: Image spatial resolution in radial, tangential and axial directions as a function of the source radial position and the detectors distance. A 50-850 keV energy window was used.

5.1.2 Sensitivity

The sensitivity of a positron emission tomograph is expressed as the rate (expressed in counts per second) of true coincidence events detected for a given source strength.

Two different protocols were followed to evaluate the absolute system sensitivity:

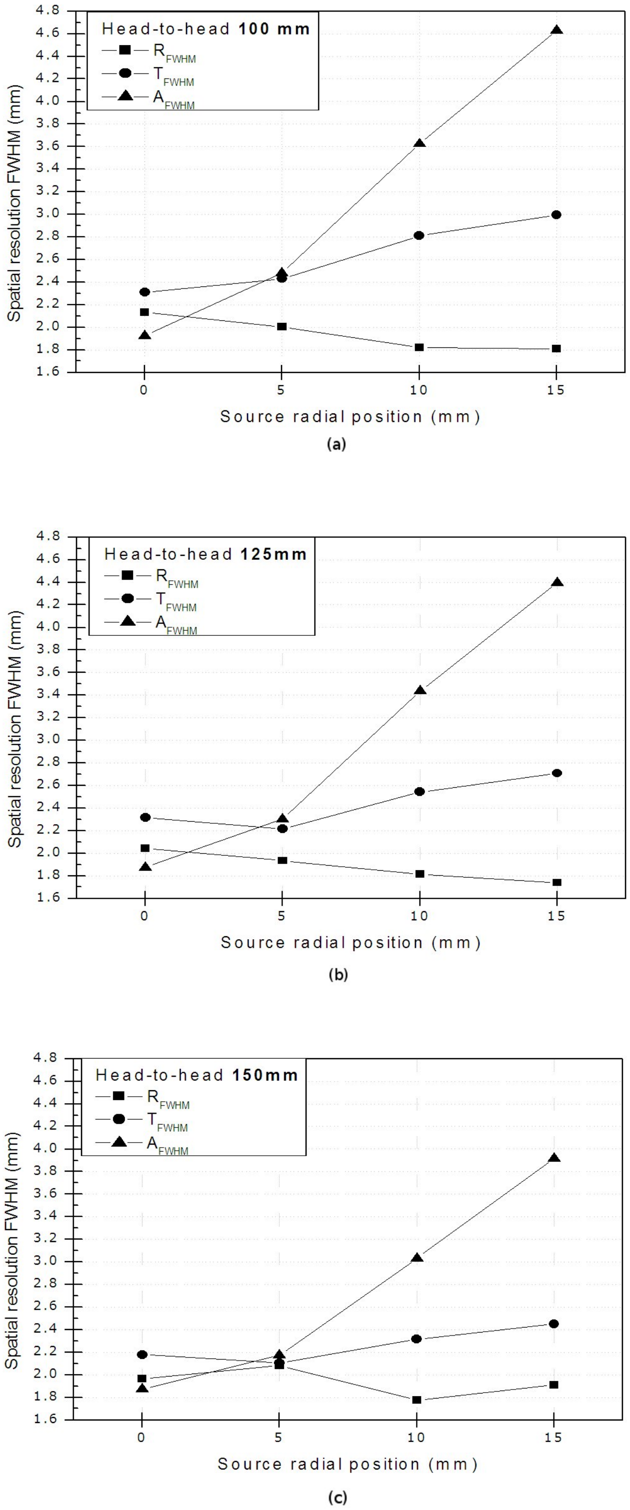

Figure 5.5: Radial (R_{FWHM}), tangential (T_{FWHM}) and axial (A_{FWHM}) FWHM resolutions for each radial position of the ^{22}Na point source in the FOV (5, 10 and 15 mm) and for each head-to-head distance: (a) 100, (b) 125 and (c) 150 mm. A 50-850 keV energy window was used.

a-) the one described in the NEMA NU2-2001 [115] and rescaled for small animal imaging that employs a ^{22}Na point source;

b-) the procedure reported in the NEMA proposal for small animal PET scanners [126], in which a tube filled with known amount of activity is placed inside a series of sleeve with increasing thickness.

a-) ^{22}Na point source

Experimental procedure

We used the same ^{22}Na point source employed for the spatial resolution measurement (activity source 370 kBq – 10 μCi – on May 23rd 2001, $t_{1/2}$= 2.61 y).

Although ^{22}Na has an additional 1275 keV gamma ray emission, the effect on the sensitivity measurement is in the percentage order. In fact, at the center of the FOV, even considering that the detection efficiency of a 1275 keV gamma ray is the same as for the 511 keV, and using no energy discrimination, the relative probability of such a false coincidence (i.e., P(1275/511)/P(511/511)) is less than 1.5% [120].

The transaxial sensitivity was characterized by positioning the ^{22}Na point source at various radial offsets along the x and y axis: 5, 10, 15 and 20 mm.

The axial sensitivity was evaluated for the source placed at the center of the FOV and at 5, 10, 15 and 20 mm of axial offset (see figure 5.6).

Both the axial and transaxial sensitivity measurements were performed for 100, 125, 150 mm head-to-head distances.

The acquisitions were performed over 180^0 with 128 views. At least hundred and half thousand counts have been acquired in each source positions and for each head-to-head distance.

To better investigate the sensitivity trend towards the head-to-head distance, we performed several acquisitions at various head-to-head distances (ranging from 100 to 150 mm at fine steps) with the source place at the center of the FOV.

Data analysis

The number of detected coincidences (C_j) and the acquisition time ($T_{acq,j}$) were registered for source position and for each head-to-head distance in order to obtain the counting rate (R_j) in counts per second (cps).

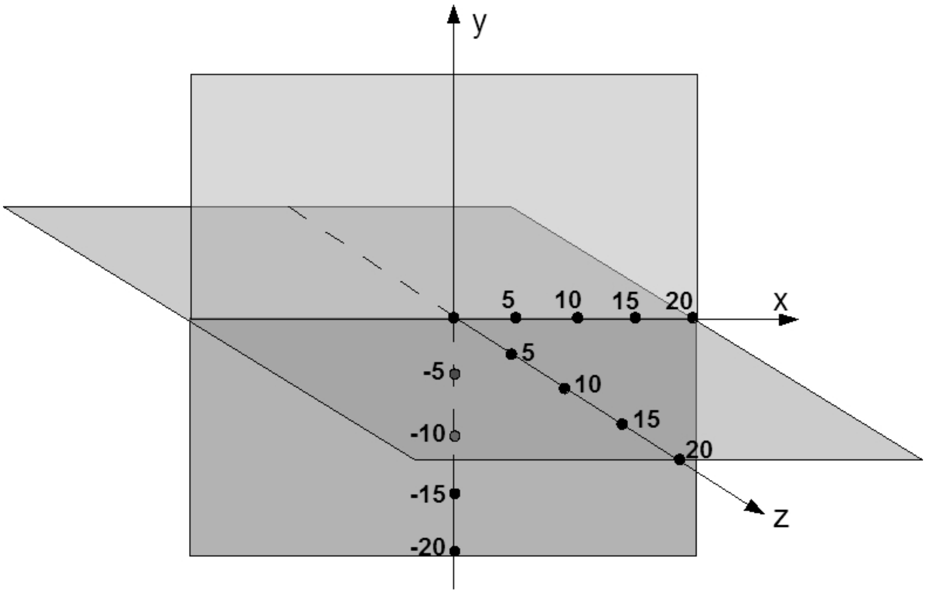

Figure 5.6: Illustration of the positioning of the ^{22}Na point source to measure the absolute system sensitivity using a rescaled version of the protocol described in in the NEMA NU2-2001 [115].

$$R_j = \frac{C_j}{T_{acq,j}} \tag{5.3}$$

C_j and $T_{acq,j}$ were obtained by the final row of the column “Used%” and “Dt(s)” of the YAP-(S)PET log file, respectively (see section 3.3.3).

A wide-open energy window 50-850 keV was used and the measured random counts (final row of the column “Casual%” the YAP-(S)PET log file (see section 3.3.3)) were subtracted from the data.

Results

The transaxial and axial sensitivity at different position in the FOV for 100, 125 and 150 mm head-to-head distances are reported in figure 5.7. The data are reported in table 5.2.

The transaxial sensitivity shows approximatively the same trend for both x and y FOV axis source position. Only towards the edge of the FOV (radial offset 20 mm) the y component is slightly better that the x one for 100 and 125 mm head-to-head distances. Due to rotation invariance the x and y radial distance should show exactly the same trend. The small difference at the edge of the FOV for closer detectors distance can be explained with a major scatter contribution along the x component

FOV axis	**Source position (mm)**	**Head-to-head distance (mm)**		
		100	**125**	**150**
	0	2.94	2.02	1.49
x	5	2.68	1.93	1.33
	10	2.23	1.53	1.11
	15	1.77	1.20	0.86
	20	1.33	0.90	0.65
y	5	2.71	1.86	1.35
	10	2.25	1.54	1.12
	15	1.79	1.22	0.89
	20	1.61	1.08	0.64
z	5	2.27	1.54	1.11
	10	1.61	1.05	0.75
	15	0.86	0.55	0.38
	20	0.26	0.14	0.09

Table 5.2: Sensitivity values (%) for each radial and tangential position of the ^{22}Na point source in the FOV (5, 10, 15 and 20 mm) and for each head-to-head distance: 100, 125 and 150 mm. A 50-850 keV energy window was used.

due to the source shape (see figure 5.2), i.e., a parallelepiped.

Both transaxial and axial sensitivity have a maximum at the center of the FOV (CFOV) and decrease moving towards the edge of the FOV. For the axial sensitivity the decrease is almost linear in accordance with the triangular shape typical of sensitivity profile in the axial direction of the 3-D PET acquisition [95]. At the axial extreme of the FOV, the sensitivity is equivalent to the 2-D data acquisitions.

The maximum sensitivity value is 2.94% (29.4 cps/kBq or 1088 cps/μCi), registered at the CFOV for the closest head-to-head distance (100 mm). The CFOV sensitivity decreases down to 1.5% (about 50%) at the largest distance (150 mm).

In figure 5.8 the sensitivity at the center of the FOV is reported as a function of the head-to-head distance. Due to the reduced solid angle coverage, the sensitivity decreases by raising the detectors separation.

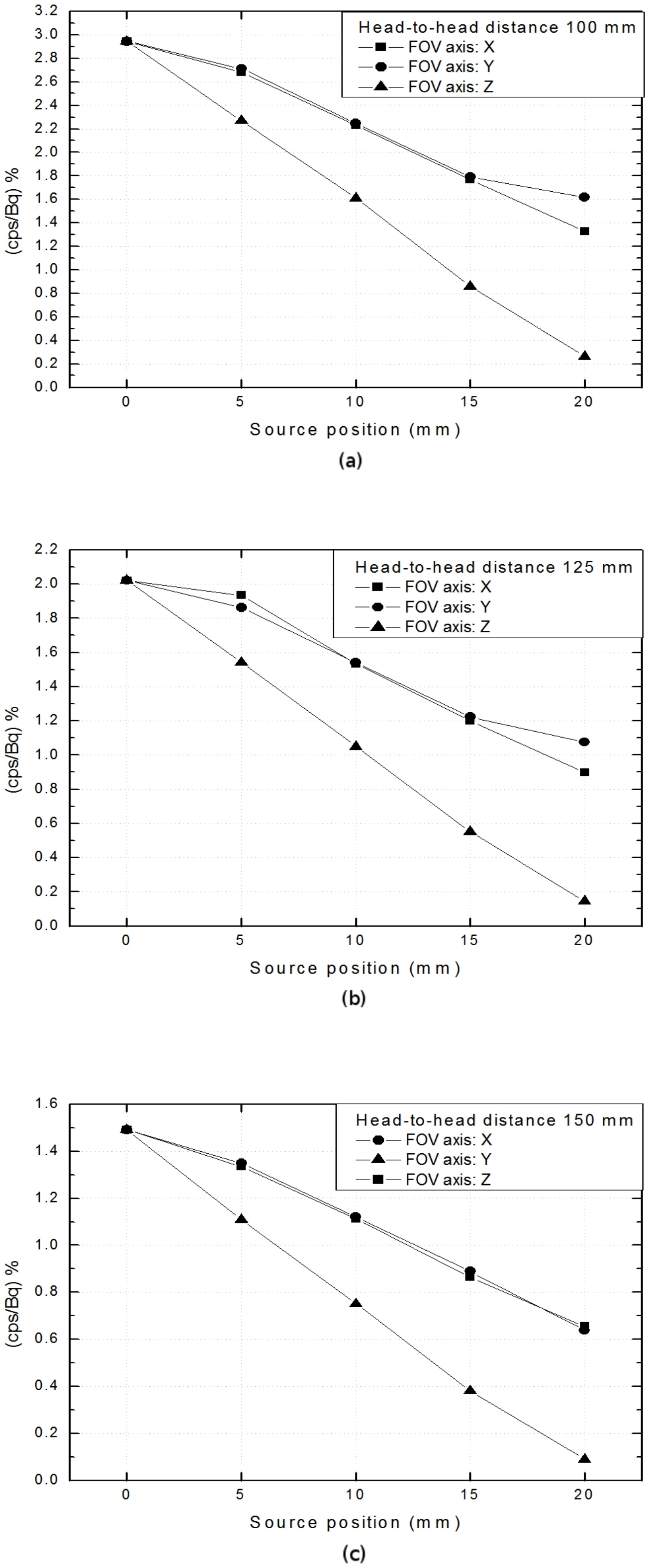

Figure 5.7: Sensitivity values (cps/Bq)% for each radial and tangential position of the ^{22}Na point source in the FOV (5, 10, 15 and 20 mm) and for each head-to-head distance: (a) 100, (b) 125 and (c) 150 mm. A 50-850 keV energy window was used.

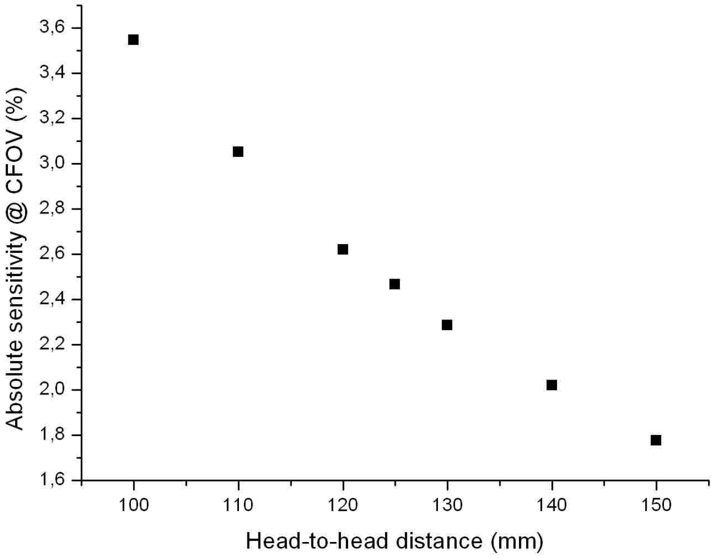

Figure 5.8: Sensitivity values (%) at the center of the FOV as a function of the head-to-head distance. A 50-850 keV energy window was used.

b-) Linear source and NEMA phantom

Experimental procedure

Since the emitted positrons annihilate in matter, to create pairs of gamma rays a significant amount of material must surround the linear source to ensure annihilation. This surrounding material also attenuates the gamma rays, so it is not possible to measure sensitivity without interference from attenuation. To obtain at an attenuation free measurement, successive measurements are made with a uniform line source surrounded by known absorbers. From these measurements, the sensitivity with no absorber can be extrapolated. This measurement technique is based on the work described in [133].

The test equipment required for this measurement is the sensitivity phantom (see figure 5.9) elaborated by the Animal PET Scanner Standard Task Force [124]. The actual sizes and thicknesses of the metal tubes are not critical, nor is the material, but the wall thicknesses must be known precisely, and all tubes must be made of the same material. As reporter in the NEMA proposal [126], we used metal tube of 2.5 mm thickness each. The dimension of the inner and outer diameter are reported in table 5.3.

Tube number	**Inside Diameter (mm)**	**Outside Diameter (mm)**
1	3.9	6.4
2	7.0	9.5
3	10.2	12.7
4	13.4	15.9
5	16.6	19.1

Table 5.3: Inside and Outside diameter of the different metal tubes of the sensitivity phantom described in the NEMA proposal for small animal PET scanners [126].

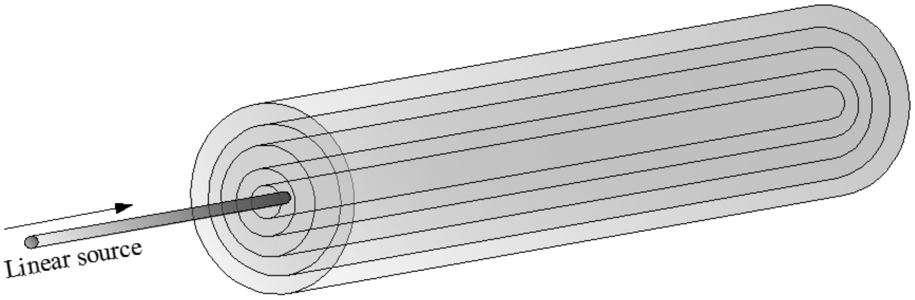

Figure 5.9: Sketch of the sensitivity phantom used for the sensitivity evaluation described in NEMA proposal for small animal PET scanners [126].

A linear source in a plastic tube filled with about 13 MBq (350 μCi) of ^{18}F was placed inside the smallest of the metal tubes described in table 5.3, and the whole system was suspended in the center of the transaxial field of view, aligned with the axis of the scanner. The counting rate was measured in this position, and then the other metal tubes were added, one at a time, and the counting rate measured for each set of metal tubes.

The acquisitions were performed over 180^0 with 128 views and repeated for 100, 125, 150 mm head-to-head distances.

The amount of radioactivity used is low enough so that the counting losses are less than one percent and the random event rate due to the test source activity is less than 5% of the trues rate. At least 8 Mevents were acquired in each source positions and for each head-to-head distance.

Data analysis

The number of coincidences detected (C_j) and the acquisition time ($T_{acq,j}$) were registered for each sleeve and for each head-to-head distance, in order to obtain the counting rate (R_j) in counts per second (cps).

$$\mathrm{R_j} = \frac{\mathrm{C}_j}{\mathrm{T}_{acq,j}} \tag{5.4}$$

The measured random counts were subtracted from the data.

The initial radioactivity at the beginning $\mathrm{T_0}$ of an acquisition was found using the activity A_{cal} as recorded in the dose calibrator at time T_{cal} according to the following equation:

$$\mathrm{A_0} = \mathrm{A}_{cal} \exp\left(\frac{\mathrm{T}_{cal} - \mathrm{T_0}}{\mathrm{T}_{1/2}}\, ln2\right) \tag{5.5}$$

where $\mathrm{T}_{1/2}$ is the half-life of the radioisotope (109.8 min for ^{18}F).

The average radioactivity for a particular acquisition (A_{ave}) was found using the activity $\mathrm{A_0}$ at the beginning of the acquisition (5.5), the half-life of the radionuclide $\mathrm{T}_{1/2}$ and the duration of the acquisition T_{acq}, according to the equation:

$$\mathrm{A}_{ave} = \frac{\mathrm{A_0}}{ln2}\left(\frac{\mathrm{T}_{1/2}}{\mathrm{T}_{acq}}\right)\left\{1 - \exp\left(\frac{-\mathrm{T}_{acq}}{\mathrm{T}_{1/2}}\, ln2\right)\right\} \tag{5.6}$$

The activity presents in the FOV was calculated with the relation:

$$\mathrm{A_{FOV}} = \frac{\mathrm{A}_{ave}}{\mathrm{L}} * \mathrm{D_{FOV}} \tag{5.7}$$

where L is the length of the plastic tube filled with ^{18}F (in our case about 5 mm) and $\mathrm{D_{FOV}}$ is the dimension of the FOV expressed in cm, i.e., 4 cm for the YAP-(S)PET scanner (see chapter 3).

Results

The system sensitivity (S_j) was evaluated as the ratio between the counting rate R_j (5.4) and the activity in the FOV, $\mathrm{A_{FOV}}$ (5.7).

$$\mathrm{S_j} = \frac{\mathrm{R}_j}{\mathrm{A}_{FOV}} \tag{5.8}$$

For each head-to-head distance, a graph of the system sensitivity S_j versus the accumulated sleeve wall thickness used in the measurement j (X_j) were produced (see figure 5.10.

The sensitivity with no attenuation was extrapolated by fitting the data with the

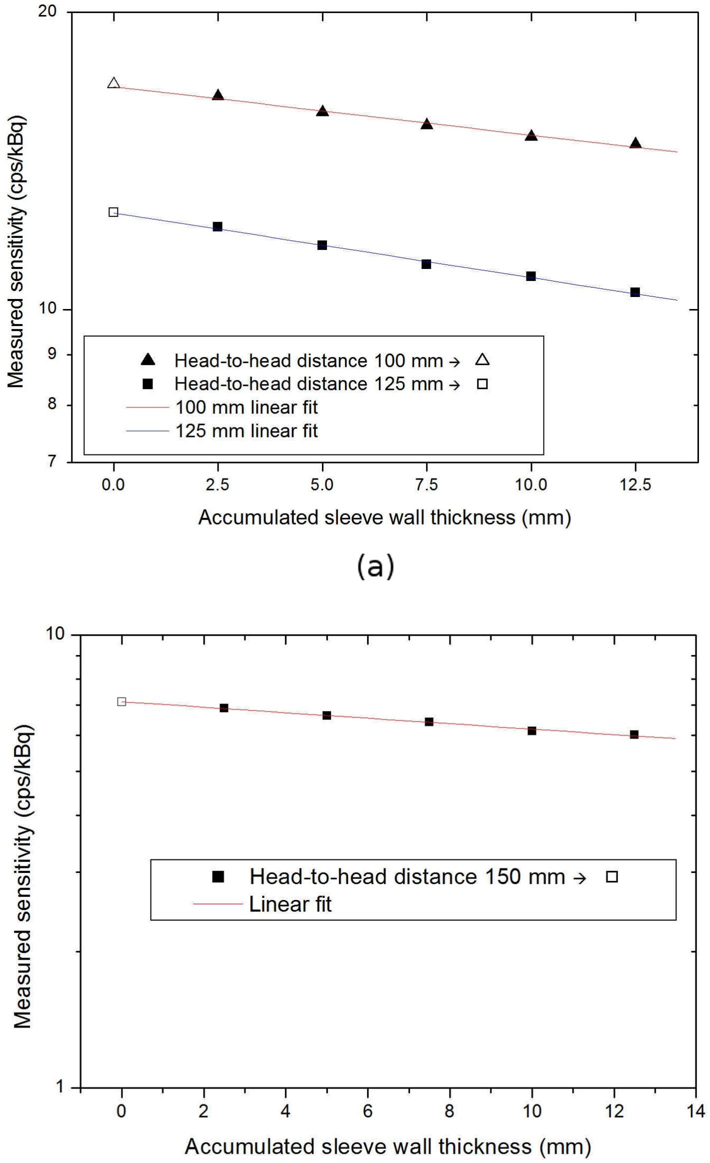

(a)

(b)

Figure 5.10: Sensitivity values (cps/kBq) as a function of the accumulated sleeves of the metal tubes of the sensitivity NEMA phantom [126]. The sensitivity was evaluated for (a) 100, 125 and (c) 150 mm head-to-head distance. The y values are represented in log scale. A 50-850 keV energy window was used.

following equation:

$$\mathrm{S_j} = \mathrm{S_0}\,\exp\left(-2 \cdot \mu \cdot \mathrm{X}_j\right) \qquad (5.9)$$

where the unknowns are the attenuation coefficient μ and the sensitivity with no attenuation $\mathrm{S_0}$.

To simplify the fit, we reported $\log\left(\mathrm{S}_j\right)$ vs. X_j and used a linear fit to determine

S_0.

The S_0 values obtained for different head-to-head distance are reported in table 5.4.

As expected, the sensitivity increase as the head-to-head distance is reduced. It is due to the greater solid angle covered by the detectors when the heads are nearer. The difference between the sensitivity at 150 mm and 100 mm is greater than 50%, increasing from 0.7% to 1.7%.

Head-to-head distance (mm)	**S_0 (cps/kBq)**
100	17.0
125	12.5
150	7.0

Table 5.4: Sensitivity values (cps/kBq) at the center of the FOV for different head-to-head distance (100, 125 and 150 mm) evaluated according the the procedure reported in the NEMA proposal for small animal PET scanners [126]. A 50-850 keV energy window was used.

5.1.3 Scatter fraction

The scatter fraction is a measure of the contamination of the data from scattered photons.

The scattering of the gamma rays emitted by the annihilation of positrons within the object before being detected results in wrong located coincidence events.

The scatter fraction (SF) is defined as the dimensionless ratio of scattered coincidence events to the total events (sum of scattered and true coincidence events) measured at low count rate to minimize random coincidences and dead time.

The phantoms suggested by the NEMA Animal PET Scanner Standard Task Force [124] for SF have sizes related to typical animals used in the laboratory.

The YAP-(S)PET is a scanner dedicated to the imaging of small animals, particularly rats and mice. In the SF measurements, we concentrate on the evaluation of SF for the mouse-like phantom.

The mouse-like phantom (see figure 5.12) is made of a solid right circular cylinder composed of high density polyethylene (density 0.96 g/cm^3) 7 cm long and 2.5 cm of diameter. A cylindrical hole (3.2 mm diameter) is drilled parallel to the central axis at the radial distance of 1 cm.

The test phantom line source insert is a clear flexible tubing with a fillable section 1 cm shorter than the cylindrical phantom with an inner diameter of 2.1 mm and an outside diameter of 4.2 mm. Once filled with a known quantity of activity, the linear source is threaded through the hole in the mouse-like phantom.

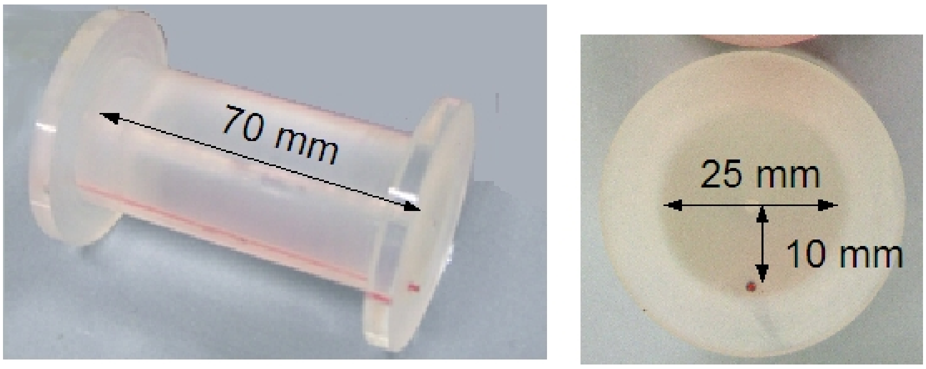

Figure 5.11: Photos of the NEMA mouse-like phantom [126] used for scatter fraction and NEC measurements.

Experimental procedure

A line source of 5 cm filled with about 600 kBq ($\sim$ 16 μCi) of ^{18}F was inserted in the cylindrical hole of the mouse-like phantom such that the region of activity coincides with the central 5 cm length of the phantom. The phantom was then centered in the transverse and axial plane of the FOV, but rotated so that the line source insert was positioned nearest to the animal bed (see figure 5.11).

The acquisitions were performed over 64^0 with 128 views and repeated for 100, 125, 150 mm head-to-head distances. A wide-open energy window 50-850 keV was used.

The amount of radioactivity was chosen low enough to guarantee a random rates less than 1% of true rate. In this case, the contribution of random events can be considered negligible, and the total events can be assumed to consist only of true and scattered counts. At least eight hundred counts were acquired for each head-to-head distance.

Data analysis

The collected data were sorted in 3-D MSRB sinograms (see section 3.3.3). A

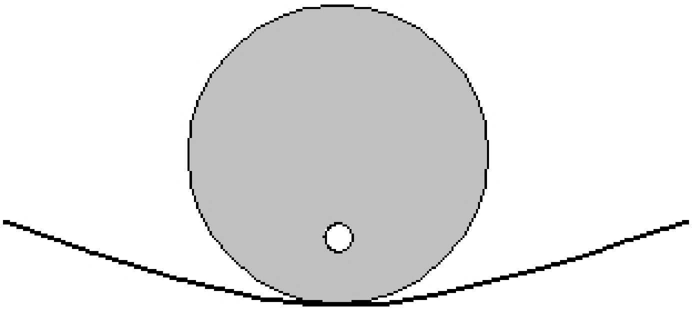

Figure 5.12: Sketch of the positiong of the mouse-phantom used for scatter fraction and NEC measurements.

wide-open energy window 50-850 keV was used.

All pixels in the sinogram located farther than 8 mm from the edges of the phantom were set to zero. In other words, only the data within a band 1.6 cm wider than the phantom were kept in the analysis. Since the FOV of the YAP-(S)PET scanner spans over 4 cm in both axial and transaxial dimensions, we did not discard any data.

For each projection angle a within the sinogram, (i.e. 148 for no angular rebinning sinograms for a head-to-head distance of 12.5 cm) (see section 3.3.3), the location of the center of the line source response was determined by finding the pixel having the greatest value. Each projection was shifted so that the pixel containing the maximum value was aligned with the central pixel of the sinogram. After alignment, a sum projection was produced so that a pixel in the sum projection was the sum of the pixels in each angular projection having the same radial offset as the pixel in the sum projection.

$$C(r) = \sum_{a} C(r - r_{max}(a)), \phi) \tag{5.10}$$

where

- r is the number of bin in a projection. We have chosen a number of projection bins double of the number of spatial bins in the sinogram (53, see chapter 4).
- ϕ is the angular bin in the sinogram (i.e. 148 for no angular rebinning sinograms for a head-to-head distance of 12.5 cm) (see section 3.3.3).
- $r_{max}(a)$ refers to the location of the maximum value in projection ϕ.

The counts C_L and C_R, the left and right pixel intensities at the edges of a 14 mm wide strip at the center of the sinogram, are obtained from the sum projection (see figure 5.13). Linear interpolation was employed to find the pixel intensities at ± 7 mm from the central pixel of the projection. Referring to figure 5.13), the 14 mm wide strip spans from bin 45 to bin 63 for a total of 19 bins. The counts C_L are obtained by summing all pixels from bin zero up to bin 44. The counts C_R are obtained by summing all pixels from bin 64 up to bin 106. The average of the two pixel intensities C_L and C_R was multiplied by the number of pixels between the edges of the 14 mm wide strip, and the product added to the counts in the pixels outside the strip, to yield the number of random plus scatter counts C_{r+s} (area highlighted in yellow in figure 5.13).

$$C_{r+s} = \text{counts } C_L + \text{counts } C_R + (\text{counts at bin } 45 + \text{counts } C_R + (\text{counts at bin } 63) \cdot 19/2) \tag{5.11}$$

The total event count C_{TOT} is the sum of all pixels in the sum projection (yellow and red areas in figure 5.13).

The average activity A_{ave} during the acquisition was calculated with equation (5.6).

Since we performed an acquisition in which the contribution of random events can be considered negligible (less that 1% of true rates), it is assumed that C_{r+s} has a negligible number of random counts and consists only of scatter counts, and likewise, C_{TOT} consists only of true and scatter counts.

The system scatter fraction SF is then computed as the ratio of C_{r+s} to C_{TOT}.

$$SF = \frac{C_{r+s}}{C_{TOT}} \tag{5.12}$$

Results

The SF values obtained for the mouse-sized phantom for different head-to-head distances are reported in table 5.5.

As expected, the SF is higher for closer head-to-head configuration (100 mm) due to greater solid angle covered by the detectors.

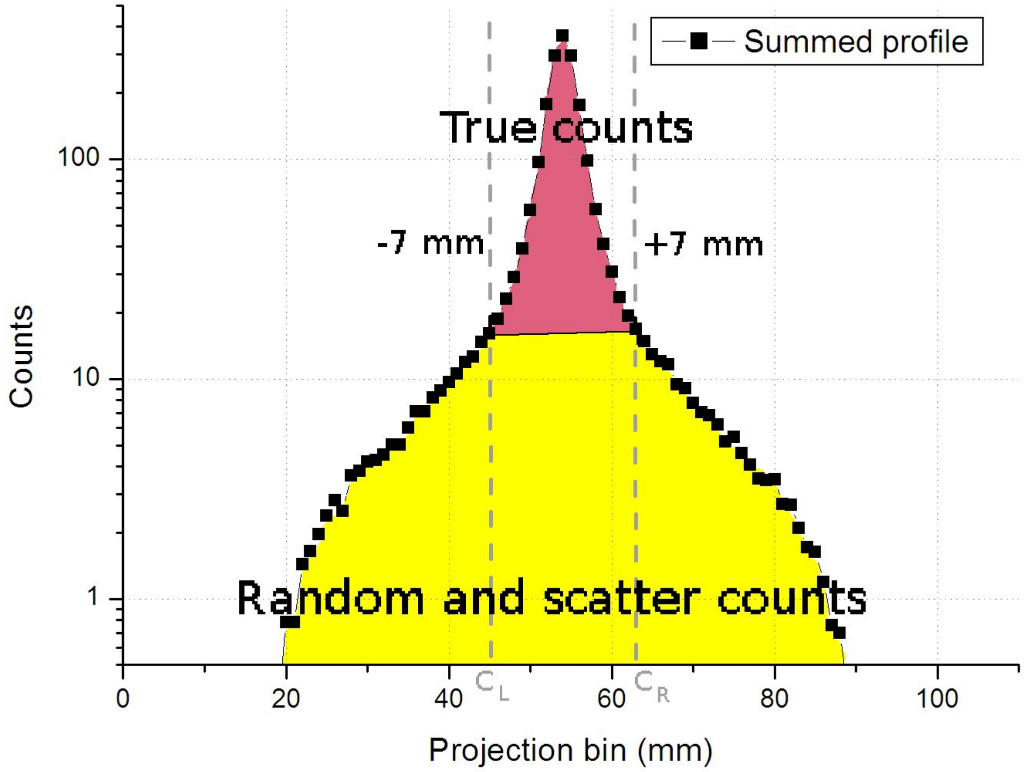

Figure 5.13: Aligned and summed projections of the sinograms produced by the scatter fraction acquisition. The scatter events (yellow) are estimated by fitting the projection tails up to ± 7 mm from the center of the summed projection profile. A 50-850 keV energy window was used.

Head-to-head distance (mm)	**SF (%)**
100	27
125	24
150	22

Table 5.5: Scatter fraction values (%) for different head-to-head distances: 100, 125 and 150 mm. A 50-850 keV energy window was used.

It is important to note that the SF takes into account the scattering events occurred both in object and detectors.

In order to evaluate the scatter in the object, it would be necessary to perform the scatter fraction measurement by a dual-acquisition method [134, 135]. This method consists in performing an acquisition with the line source inserted in the phantom and an acquisition with the same line source suspended in air. The difference between the scatter fraction in the phantom and the scatter fraction in air provides the scatter in the object.

In [135], it is shown that for a Lucite phantom of 4 cm in diameter and 4 cm in length with a ^{18}F line source inserted in a 2 mm hole drilled along its axial direction at its center, the scatter fraction is 33%. The scatter fraction of the line source alone is 26%. Then, the scatter contribution due to the Lucite phantom is only 7% and the scatter fraction of the line source alone (26%) gives an estimate of the scatter due to the scanner geometry and to the multiple interaction within the crystals.

At present time, no scatter correction is performed on the YAP-(S)PET data, but in the multi-Ray 3-D PET reconstruction tool under evaluation (see section 3.3.4) the crystal scatter is taken into account by means of Monte Carlo simulations [104].

5.1.4 Count rate performance

The measurements of count losses and random rates express the ability of a positron emission tomograph to measure highly radioactive sources with accuracy.

Noise equivalent count (NEC) rate, which incorporates the noise effects of subtracting the randoms and scatter count components, provide a direct link between image signal-to-noise ratio and the scatter, randoms and trues coincidence count rates [136]. The measurements of noise equivalent count rates is based on the work described in [136].

The purpose of these measurements is to evaluate the effects of system dead-time and the generation of random events at several levels of source activity.

Experimental procedure

We employed the same phantom used for SF measurements (see section 5.1.3).

The line source of 5 cm was now filled with about 150 MBq ($\sim$ 4 mCi) of ^{18}F and inserted in the cylindrical hole of the mouse-like phantom such that the region of activity coincides with the central 5 cm length of the phantom.

The acquisitions were performed over 180^0 with 64 views and repeated for 100, 125, 150 mm head-to-head distances. A wide-open energy window 50-850 keV was used.

The amount of radioactivity was chosen high enough in order to provide appreciable scanner dead time. Regular measurements were then taken while the activity in the phantom decays over several half-lives. Overall, 23 acquisitions were performed.

Data were acquired at intervals more frequent than half the radionuclide half-life $T_{1/2}$. The durations of the individual acquisitions, $T_{acq,j}$, was less than one fourth of T1/2. At least eight hundred counts were acquired for each head-to-head distance. A decrease in the ratio of the random event rate to the true event rate accompanies the activity decay, till the random rates are less than 1% of true rates.

Data analysis

For each acquisition j the noise equivalent count rate $R_{NEC,j}$ is computed as follows:

$$R_{NEC,j} = \frac{R_{t,j}^2}{R_{TOT,j}} \tag{5.13}$$

where $R_{t,j}$, $R_{s,j}$ and $R_{r,j}$ are the true, the scattering and the randoms event rate of the j-th acquisition, respectively.

The various rates were calculated with the following equations:

Total event rate: $R_{TOT,j} = \frac{C_{TOT,j}}{T_{acq,j}}$

True event rate: $R_{t,j} = R_{TOT} \cdot (1 - SF)$

Random event rate: $R_{r,j} = R_{TOT} - \frac{R_{t,j}}{(1 - SF)}$

Scatter event rate: $R_{s,j} = R_{t,j} \cdot \frac{SF}{(1 - SF)}$

$C_{TOT,j}$ and $T_{acq,j}$ were obtained by the final row of the column “Used%” and “Dt(s)” of the YAP-(S)PET log file, respectively (see section 3.3.3).

In the other rates equation, SF is the scatter fraction value as obtained with equation 5.12.

The previous rates were evaluated for each of the 23 acquisitions performed. It was thus possible to study the noise equivalent count rate, true, random, scatter and total event count rate as a function of average effective radioactivity concentration in the FOV. The activity in the FOV was evaluated with equation 5.7. The concentration was obtained by dividing A_{FOV} by the volume V of phantom used (see figure 5.11). For the cylindrical mouse-like phantom the volume is 34.36 cm^3.

A wide-open energy window 50-850 keV was used.

Results

Figure 5.14 reports total (R_{TOT}), random (R_r), true (R_t), scatter (R_s) and noise equivalent count rate (R_{NEC}) as a function of the average effective radioctivity concentration in the FOV.

The total, true, scatter and NEC count rate present the same trend for all the head-to-head distances. An initial approximately linear increase increasing with activity that leads to the peak of the count rate and the subsequent slow count rate decrease for higher activity, when saturation effects occur.

As can clearly be seen from figure 5.14 (a),(b) and (c), the activity at which true and NEC count rate reach the peak increases with increasing head-to-head distance. This effect is mainly determined by the reduced sensitivity due to the reduced solid angle coverage with raising detectors separation (see section 5.1.2). Table 5.6 reports the R_t and R_{NEC} peak values and the activity concentration at which they are reached for 100, 125 and 150 mm head-to-head distance. For both true and NEC count rate, the peak is higher and is reached at lower activity concentration for closer detectors configuration. This is in agreement with the increase in sensitivity and coincidence rate at closer head-to-head distance.

The NEC trend for 100, 125 and 150 mm head-to-head distance is best highlighted in figure 5.15. Moving from 100 to 150 mm head-to-head distance the R_{NEC} peak pass from 38.4 kcps at 370 kBq/ml ($\sim$ 400 μCi or 11 MBq in the phantom) to 39.4 kcps at 730 kBq/ml ($\sim$ 900 μCi or 24 MBq in the phantom). These data are important for in vivo studies, since the NEC peak gives indication about the maximum injectable activity for good working conditions.

For each head-to-head distance, the random contribution presents a three phases trend throughout the activity concentration span. A significant increase with increasing activity up to an activity concentration a bit higher that the value at which R_t and R_{NEC} peaks occur, a sort of plateau and a slow decrease at higher activity due to saturation effects. For 150 mm head-to-head distance the decrease at higher activity is slower with respect to 100 mm distance because of a reduced effect of saturation.

For 100 mm head-to-head distance, the scatter peak reaches a higher value (23 kcps at 370 kBq/ml) with respect to 150 mm (17 kcps at 730 kBq/ml) due the greater solid angle covered by the detectors.

Head-to-head distance (mm)	**Peak (kcps) @ activity concentration (kBq/mL)**
100	$R_t = 60.5$ @ 370
	$R_{NEC} = 38.4$ @ 370
125	$R_t = 58.8$ @ 530
	$R_{NEC} = 39.0$ @ 430
150	$R_t = 59.0$ @ 730
	$R_{NEC} = 39.2$ @ 730

Table 5.6: The R_t and R_{NEC} peak values and the activity concentration at which they are reached for 100, 125 and 150 mm head-to-head distance. A 50-850 keV energy window was used.

5.1.5 Partial volume effect

One of the main difficulties in the ROI (Region Of Interest) or VOI (Volume Of Interest) analysis in in vivo studies 7 is to accurately determine the activity concentration in regions or volumes of dimensions comparable with the resolution of PET scanner. This is of particular importance in the quantitative characterization of small lesions or structures.

Due to PET systems finite spatial resolution, the radiation emitted from infinitely small point source will be smeared out and will appear as a finite-size blob in the reconstructed image. This is known as the **partial volume effect, (PVE)** [137]. This effect occurs for structures that have dimensions of about 2 × FWHM the spatial resolution of the scanner or smaller. Since the spatial resolution of the YAP-(S)PET scanner is about 2 mm (see section 5.1.1), the radioactivity presents in objects with dimensions of 4 mm or smaller will be underestimated. The degree of underestimation is a function of both object size and system reconstructed image resolution, and is characterized by the recovery coefficient (RC) defined as the ratio between the measured and the true activity concentration in the ROI:

$$\mathrm{RC} = \frac{\text{Measured peak activity concentration}}{\text{True activity concentration}} \tag{5.14}$$

If the recovery coefficient can be determined, it is possible to correct reconstructed

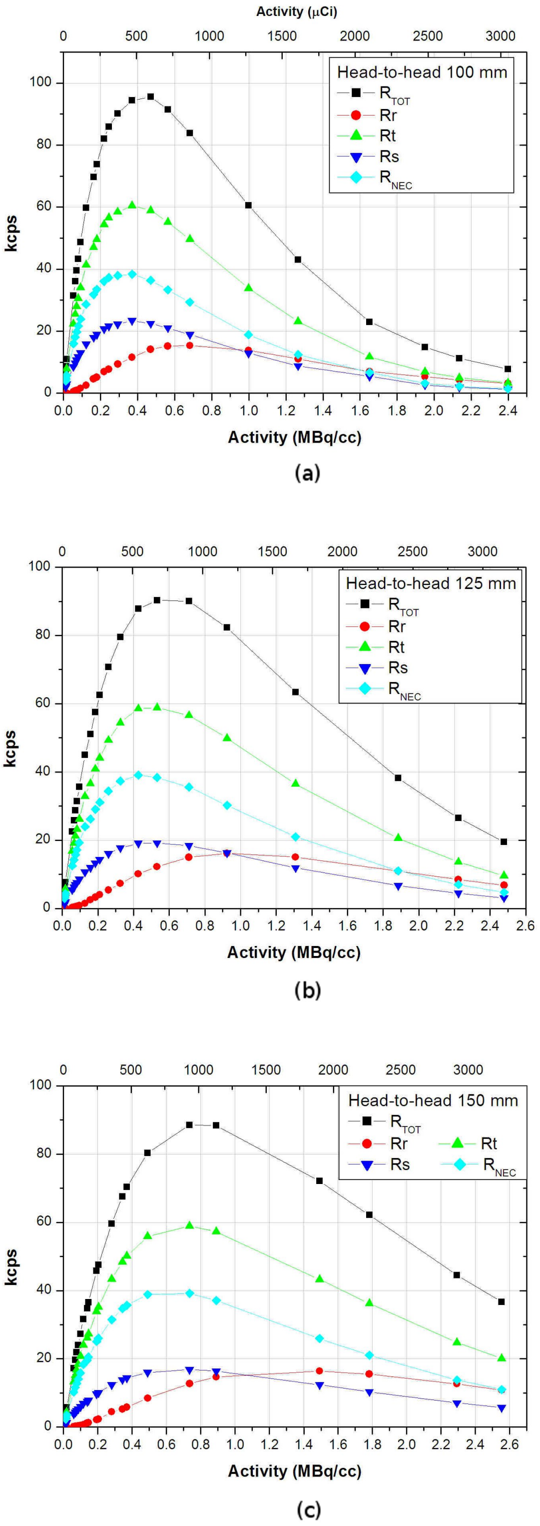

(a)

(b)

(c)

Figure 5.14: Total (R_{TOT}), random (R_r), true (R_t), scatter (R_s) and noise equivalent count rate (R_{NEC}) as a function of the average effective radioctivity concentration in the FOV. The measurements are reported for different head-to-head distances: (a) 100 mm, (b) 125 mm and (c) 150 mm. A 50-850 keV energy window was used.

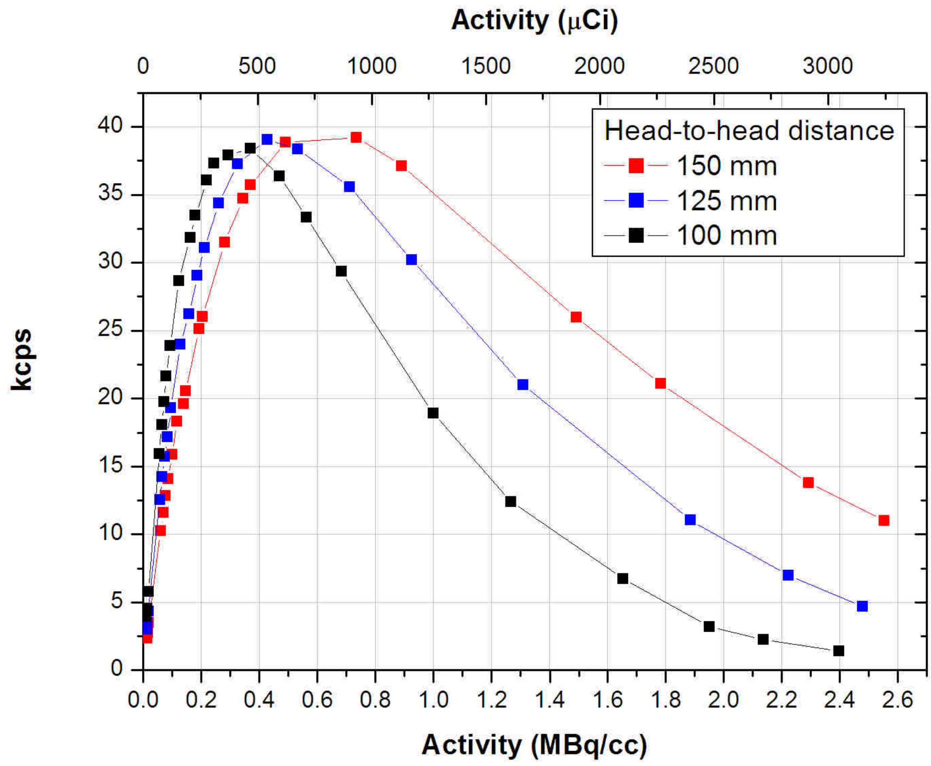

Figure 5.15: The NEC trend measured for the mouse-like phantom at 100, 125 and 150 mm head-to-head distance. A 50-850 keV energy window was used.

images for partial volume effects.

Experimental procedure

To evaluate the RC for different dimensions object size, we used the Image Quality (IQ) phantom described in [126] for image quality evaluations (see section 5.1.7). In fact, due to the physical limitations in producing hot spheres in non-zero background with physical walls much smaller than the spatial resolution of the imaging systems, we used the fillable rods of different diameters in cold solid background of the IQ phantom (see figure 5.19).

The rods have radii of 1, 2, 3, 4 and 5 mm and were filled with the same activity concentration, about 7.5 μCi/mL (0.20 MBq/mL) of ^{18}F. A wide-open energy window 50-850 keV was used and FBP reconstruction with ramp filter with cut off at the Nyquist frequency was used.

Data analysis

The recovery coefficients were calculated by considering, for each rod, the maximum value or the mean value of a ROI having the same size of the physical dimensions of the rod. The RC are then reported as a function of the rod size.

Results

The RC curve for 100 and 125 mm head-to-head distances are reported in figure 5.16. In panel (b) the recovery coefficient calculated as the maximum value (red circles) and the mean value of a ROI having the same size of the physical dimensions of the rod (black squares) are represented.

For 4 mm rod, that is object size about $\simeq 2 \times$ FWHM the spatial resolution of the scanner, the activity concentration underestimation is about 20% for 100 head-to-head distances and less than 15% for 125 mm. The better quantification at wider detectors distance is due to lower acceptance angle, thus less parallax error and better spatial resolution (see section 5.1.1).

The comparison of the RC curves for maximum or mean value of a ROI having the same size of the physical dimensions of the rod (see panel (b) of figure 5.16) highlight that if the size of region is identical to the object size, the underestimation of activity concentration is increased. Particularly, the rods with diameters of 2, 3 and 4 mm shows a quantification error about 40% greater when considering the mean value of the ROI.

5.1.6 Attenuation corrections

At 511 keV, a relatively high probability exists that one or both annihilation photons will interact in the subject, predominantly through Compton interactions. The results of these interactions are the removal or attenuation of primarly photons from a given LOR and the potential detection of scattered photons in a different LOR.

The erroneous identification of the LOR degrades the spatial resolution and makes more difficult the quantitive evaluation. Thus, attenuation corrections methods have been developed.

Correction means correcting each LOR for the fraction of events that were attenuated from that LOR.

Attenuation of the signal from a given LOR can be corrected either by a direct measurement or using a mathematical model or a combination of the two.

At present time, no attenuation correction is performed on the YAP-(S)PET data,

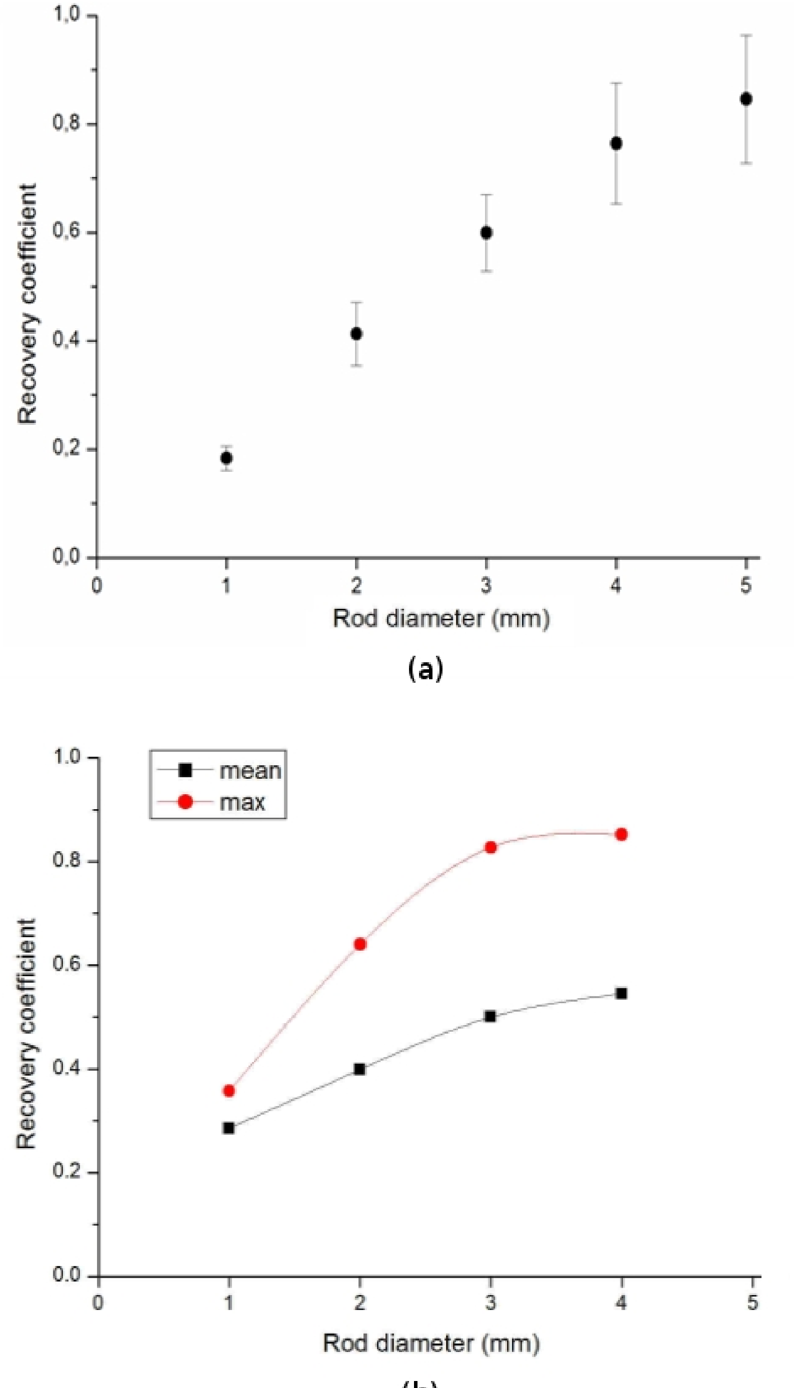

(a)

(b)

Figure 5.16: (a) Calculated recovery coefficients for the 1, 2, 3, 4 and 5 mm rods of the NEMA Image Quality phantom [126] and for 100 mm head-to-head distance. (b) Effect of the region of interest dimensions on Recovery Coefficient calculated for 1, 2, 3 and 4 rods of the NEMA Image Quality phantom [126], for 125 mm head-to-head distance. A 50-850 keV energy window was used.

but in the multi-Ray 3-D PET reconstruction tool under evaluation (see section 3.3.4) a mathematical model for the attenutation corrections has been implemented. The model assumes that the outline of the object being imaged can be approximated with a geometrical shape as a cilinder. Furthermore, the attenuation coefficient within this object is assumed to be constant.

Considering a circular section of the cilinder and a point source located at an unknown depth x (see figure 5.17), if D is the diameter, the probability that the annihilation photon 1 will escape the object is:

$$\mathrm{p1} = \frac{\mathrm{I(x)}}{\mathrm{I(0)}} = \exp(-\mu \cdot \mathrm{x}) \tag{5.15}$$

In the same way, the probability that annihilation photon 2 will escape is:

$$\mathrm{p2} = \frac{\mathrm{I(D-x)}}{\mathrm{I(0)}} = \exp(-\mu \cdot (\mathrm{D}-\mathrm{x})) \tag{5.16}$$

The probability that both annihilation photons will escape the object is the product of the individual probabilities:

$$\mathrm{p1} \cdot \mathrm{p2} = \exp(-\mu \cdot \mathrm{x}) \cdot \exp(-\mu \cdot (\mathrm{D}-\mathrm{x})) = \exp(-\mu \cdot \mathrm{D}) \tag{5.17}$$

The attenuation correction factors, $\mathrm{c_{ij}}$, that need to be applied to the emission data for the LOR joining two coincidence detectors ij is the reciprocal of the combined probability:

$$\mathrm{c_{ij}} = \exp(\mu \cdot \mathrm{D_{ij}}). \tag{5.18}$$

The coefficients $\mathrm{c_{ij}}$ applied in the standard ML-EM algorithm used in the multi-Ray 3-D PET reconstruction is a moltiplication coefficients in equation 3.7):

$$a_i^{k+1} = \frac{a_i^k}{\sum_j \mathrm{c_{ij}} \cdot \mathrm{M_{i,j}}} \sum_j \frac{M_{i,j} \cdot s_j}{\sum_i M_{i,j} \cdot a_i^k} \tag{5.19}$$

The attenuation correction method implemented in the multi-Ray 3-D PET reconstruction can in principle be applied to previous data. It is then necessary to fit a circle to the outline of the subject imaged on each individual transaxial slice. From these circle, the attenutation corrections are calcualted and applied to the raw data, which are reconstructed again. However, due to the approximation of the shape of the object and the assumption of a uniform coefficient, the method tends to underestimate the attenutation.

In order to estiamte the entity of attenuation inside the rat brain, we have calculated the attenuation correction of photons of 511 keV produced inside a circular water object with a diameter of 3 cm. The mass attenuation coefficient μ/ρ for 511 keV photons in water is 0.0958 cm^2/g, with water density ρ= 1 g/cm^3. So the combined probability p1 $\cdot$ p2 is about 0.75, that indicate that attenuation effects decrease the intensity of emitted radiation of about 25%.

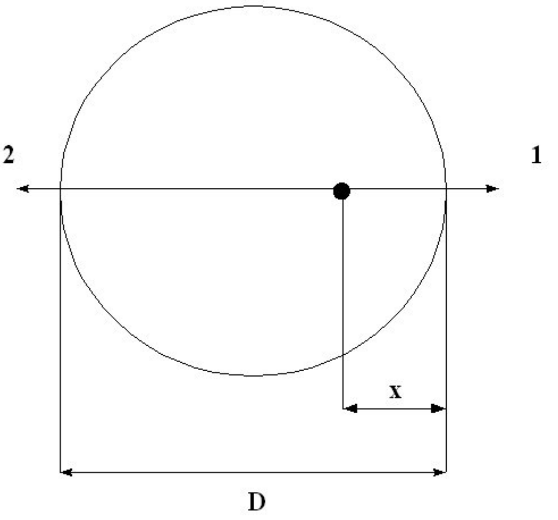

Figure 5.17: Sketch of a transaxial section of the uniform cilinder employed in the mathematical model used for attenuation corrections.

5.1.7 Phantoms studies

Three phantoms were imaged to test the imaging capability of the YAP-(S)PET scanner in PET modality:

- **a-)** a miniature version of a Derenzo-like phantom ([138]).
- **b-)** the Image Quality proposed by the Animal PET Scanner Standard Task Force [124] for image quality evaluations.
- **c-)** the mini Defrise phantom.

a-) The mini Derenzo-like phantom is a hot-rods phantom. It is a solid plexiglas cylinder 38 mm in diameter and 37 mm in height, divided in sectors of rods with the same diameter (see figure 5.18). The phantom used has 5 sectors with rods diameters of 3.0, 2.5, 2.0, 1.5 and 1.2 mm, respectively. The center-to-center distance between adjacent rods is twice the rod diameter.

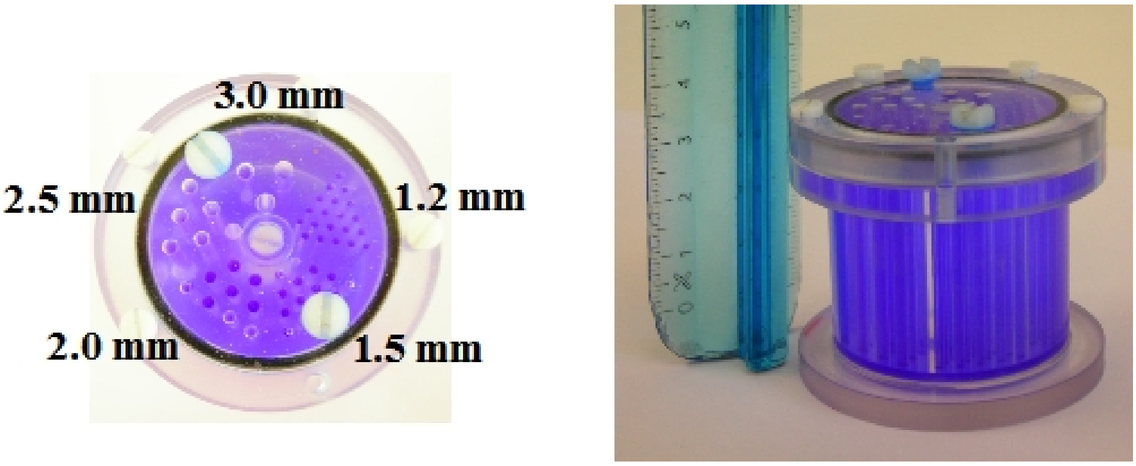

Figure 5.18: Top and full body photos of the Derenzo-like phantom.

b-) The Image Quality is a plexiglas cylinder (see figure 5.19). It consists of three parts:

- a main fillable chamber with 30 mm diameter and 30 mm in length in the central part.
- a lid that is attached to the large uniform region of the phantom, containing two cold region chambers. The chambers are composed of hollow fillable cylinders 15 mm in length and 8 mm of internal diameter (10 mm external diameter and 1 mm wall thickness).
- a 20 mm solid final part with 5 fillable rods drilled through (at 7 mm from the center) with radii of 1, 2, 3, 4, and 5 mm.

c-) The Defrise phantom is a hot/cold disks phantom. Is is a hollow plexiglas cylinder of 38 mm in diameter and 38 mm in height containing 5 plexiglas disk with 3 mm thickness (see figure 5.20). Once filled with radioactive solution, it presents alternate cold (plexiglass disks) and hot regions.

Experimental procedure

All the phantoms were filled with a solution of ^{18}F.

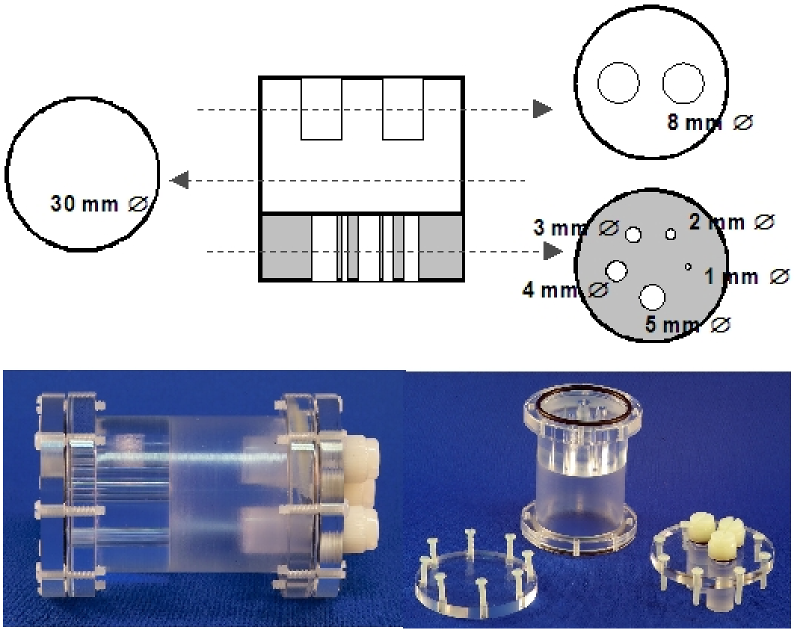

Figure 5.19: Sketch and photo of the Image Quality NEMA phantom [126].

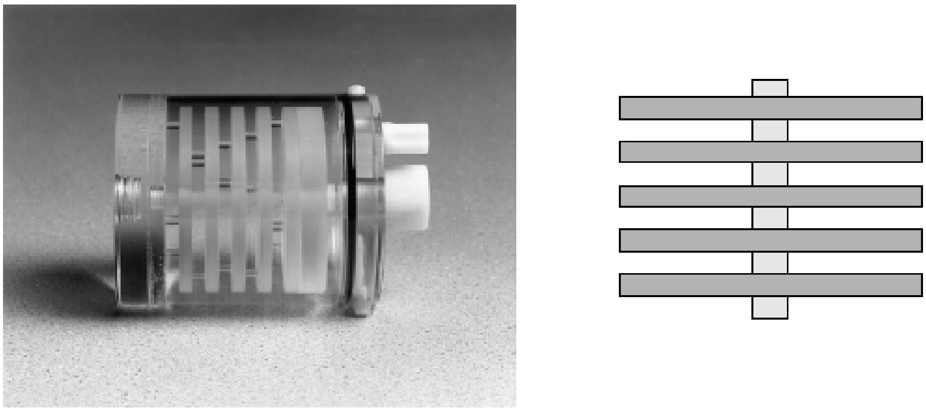

Figure 5.20: Sketch and photo of the Defrise phantom.

Since the spatial resolution performance are comparable at 100, 125 and 150 mm (see section 5.1.1), while the sensitivity decreases with incresing head-to-head distance (see section 5.1.2), the phantom studies were performed only at 100 and 125 mm.

The evaluation performance results highlighted that the best compromise between spatial resolution and sensitivity is obtained whit a head-to-head distance of 100 cm. Due to reduced working space at 100, the best compromise between scanner performance and animal experiments is to fix the head-to-head distance at 100 mm for mice studies and 125 mm for rats studies.

a-) The Derenzo phantom was filled with about 8 MBq ($\sim$ 300 μCi) of ^{18}F and placed at the center of the FOV with the rods axis parallel to the scanner axis. A 128 views over 180^0 acquisition was performed for 100 and 125 mm head-to-head distances. About 120 Mevents were acquired.

b-) The Image Quality was filled with about 16 MBq ($\sim$ 600 μCi) of ^{18}F and placed in the FOV such that its main axis is aligned with the longitudinal axis of the tomograph. A preset time acquisition of 40 minutes over 180^0 with 128 views was performed for 100 and 125 mm head-to-head distances.

c-) The mini Defrise phantom was filled with about 11 MBq ($\sim$ 600 μCi) of ^{18}F, centered in the transverse FOV and oriented along the body axis of the scanner. A 128 views over 180^0 acquisition was performed for 100 and 125 mm head-to-head distances. About 1 Gevents were acquired.

Data analysis

The collected data were processed via 3-D MSRB sinograms (see section 3.3.3) and then reconstructed with FBP algorithm (with ramp filter with cut off at the Nyquist frequency) or EM algorithm. A 128 × 128 reconstructed image matrix was chosen (pixel dimension 1.5 mm/4, about 0.38 mm). In the axial dimension the sampling step was 1.5 mm (27 slices) for Derenzo and Image Quality phantom and 0.75 mm (53 slices) for the Defrise phantom. The thinner sampling in the axial direction for the Defrise phantom was chosen to better evaluate the YAP-(S)PET axial spatial resolution. A wide-open energy window 50-850 keV was used.

Results

a-) Figure 5.21 shows the FBP (ramp filter at the Nyquist frequency) reconstructed transaxial section of the Derenzo phantom for 100 and 125 head-to-head distances. The slice thickness is 19.5 mm (13 slices summed). The 1.5 mm hot rods can be distinguished for both head-to-head distances, while the 1.2 mm rods start to be resolved only for wider detectors distance.

Figure 5.22 reports the transaxial section of the Derenzo phantom for four central slices (a) and for 13 summed slices (b) obtained with EM reconstruction algorithm. The profile of the last series of 1.5 mm and 1.2 mm rods are also reported.

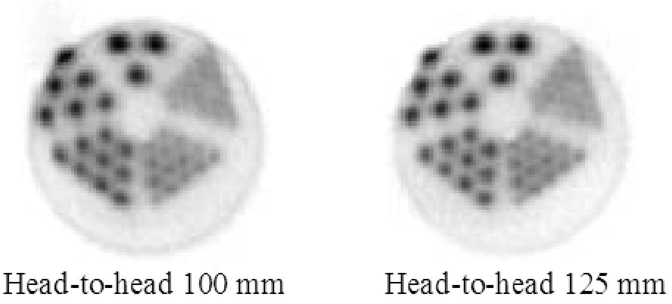

Figure 5.21: Transaxial sections of the Derenzo-like pahtnom for 100 and 125 mm head-to-head distances. FBP reconstruction algorithm with ramp filter with cut off at the Nyquist frequency was used.

b-) Figure 5.23 reports the FBP (ramp filter at the Nyquist frequency) transaxial section of the 5 fillable rods and the two cold region chambers, in addition to a coronal section of 4 cm portion centered on the uniform region. Due to partial volume effects (see section 5.1.5), the 1 mm radii hot rod is not resolvable neither for 100 nor 125 mm head-to-head distance, and the 3 and 4 mm rods show a lower activity concentration.

In figure 5.24 coronal and transaxial sections of the Image Quality phantom acquired at 100 head-to-head distance and reconstructed with EM algorithm are reported. The 1 mm radii hot rod is barely distinguishable.

c-) In figure 5.25 two coronal sections of the Defrise phantom for 100 and 125 mm head-to-head distance are represented. The slice thickness is about 4 mm (5 slices summed, 0.75 mm each). Due to the lower axial degradation for wider detectors distance (5.1.1), the alternate cold and hot regions is better defined for 125 head-to-head distance.

5.2 SPECT modality performance

5.2.1 Spatial resolution

As for PET systems, the spatial resolution is commonly quantified from the FWHM of point or line spread response function. It depends on the intrinsic capabilities of the scintillation detectors, the geometrical properties of the collimator, the scattered radiation and the septal penetration [2]. In terms of the FWHM of the point spread function (PSF) or Line Spread Function(LSF), the most important factors are the

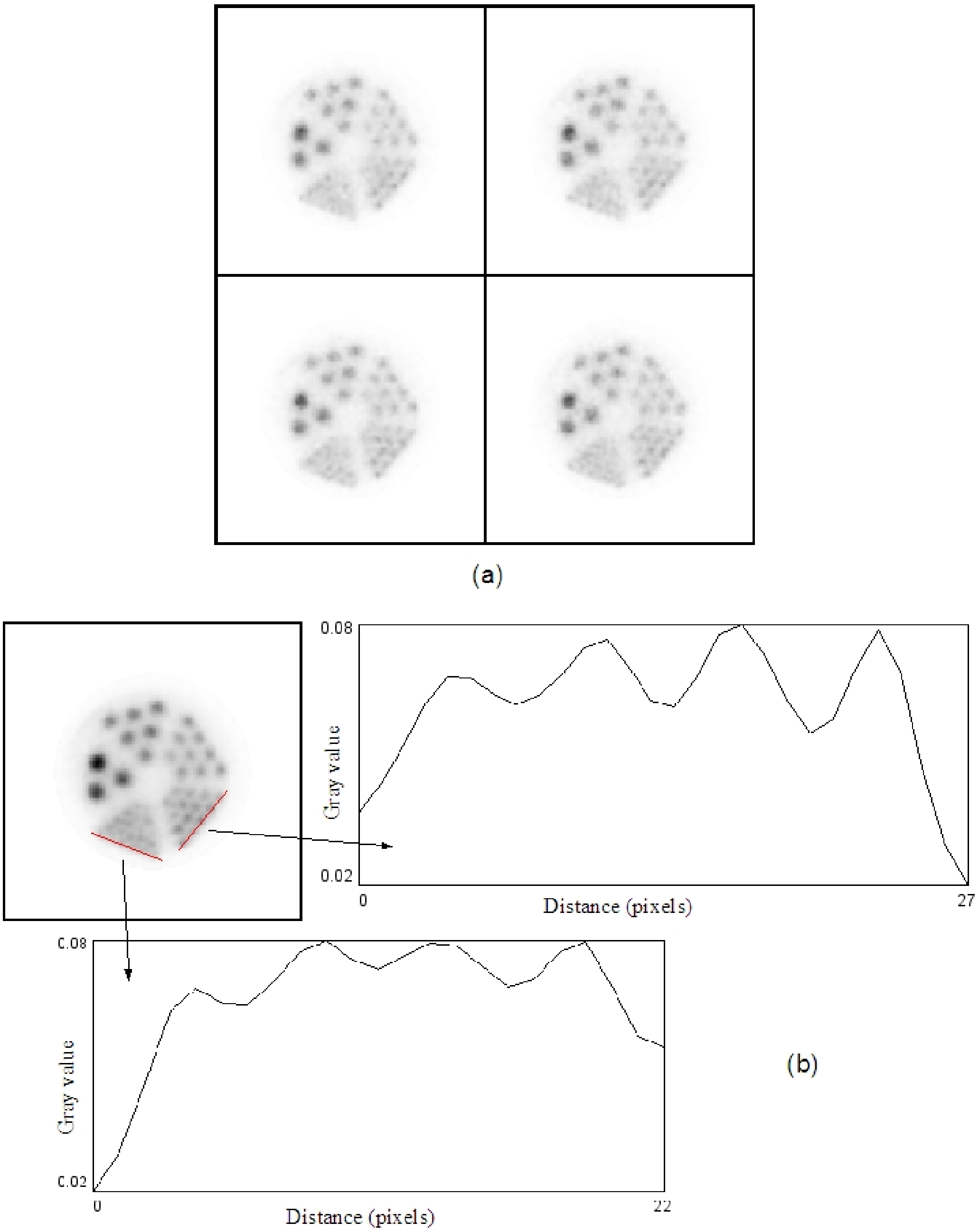

Figure 5.22: Transaxial section of the Derenzo-like phantom for four central slices (a) and for 13 summed slices (b) obtained with EM reconstruction algorithm. The profile of the last series of 1.5 mm and 1.2 mm rods are also reported. The measurements have been performed at 100 mm head-to-head distance.

intrinsic resolution R_{int} of the detector and electronics, and the collimator resolution R_{coll}. The combined effect of these two factors is to produce the system resolution R_{sys} that is somewhat worse than either one alone. System resolution R_{sys} (FWHM) is so determined by the relation:

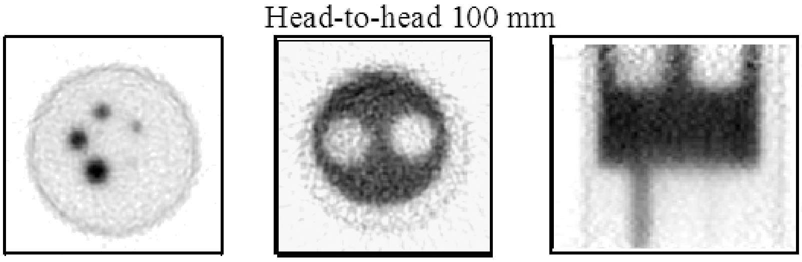
Head-to-head 100 mm

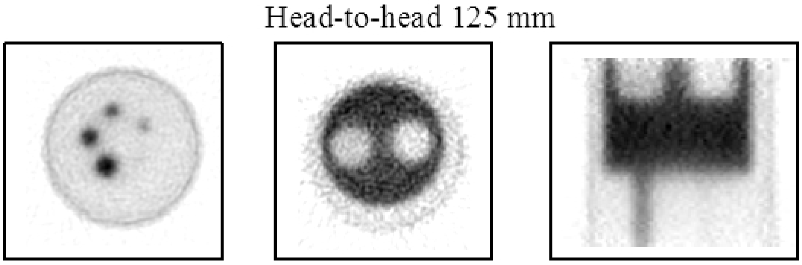
Head-to-head 125 mm

Figure 5.23: Transaxial section of the 5 fillable rods and the two cold region chambers, in addition to a coronal section of 4 cm portion centered on the uniform region of the NEMA Image Quality phantom. The FBP reconstruction algorithm with ramp filter with cut off at the Nyquist frequency was used. The measurements were performed at 100 and 125 head-to-head distances.

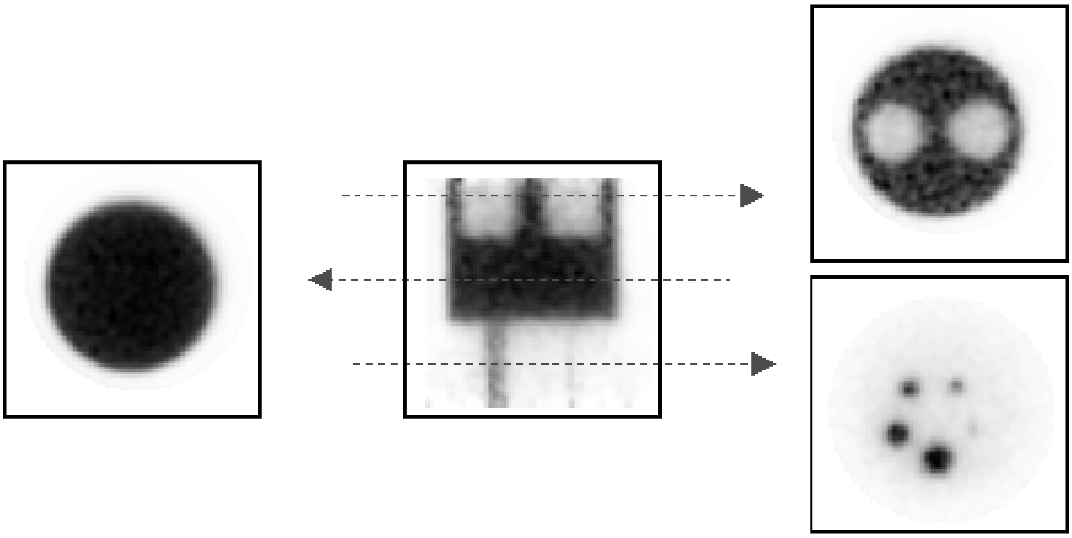

Figure 5.24: Coronal and transaxial sections of the NEMA Image Quality phantom acquired at 100 head-to-head distance and reconstructed with EM algorithm.

$$\mathrm{R}_{sys} = \sqrt{(\mathrm{R}_{int})^2 + (\mathrm{R}_{coll})^2} \tag{5.20}$$

The spatial resolution of a parallel-hole collimator can be approximated by the expression [91]:

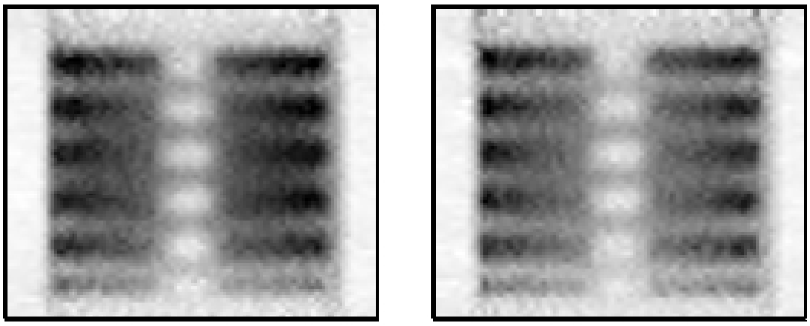

Head-to-head 100 mm Head-to-head 125 mm

Figure 5.25: Coronal sections of the Defrise phantom for 100 and 125 mm head-to-head distance. The slice thickness is about 4 mm (5 slices summed, 0.75 mm each).

$$\mathrm{R}_{coll} = d + D\frac{d}{L} \tag{5.21}$$

where d and L are the diameter and the length of the holes of the collimator, respectively. D is the object - collimator distance. The parallel-hole collimator of the YAP-(S)PET scanner has d=0.6 mm and L=20 mm (see section 3.2.4), so R_{coll} will range between 2.1 mm (for 10 mm head-to-head distance and the source placed at the CFOV) to 2.7 mm (for 150 mm head-to-head distance with the source at the CFOV).

The procedures followed for the spatial resolution measurement are based on those defined by the clinical SPECT NEMA reference standards NU1-1994 [116] and on the report number 52 of American Association of Physicists in Medicine (AAPM) [139].

Experimental procedure

The measurements were performed with a glass capillar with inner and outer diameter of 0.8 and 1.2 mm, respectively. The capillar was filled with 111 MBq (about 3 mCi) of ^{99m}Tc and positioned parallel to the FOV longitudinal axis with 1 cm radial offset. The measurements were repeated for 100, 125, 150 mm head-to-head distances.

The acquisitions were performed over 180^0 with 128 views. At least four hundred thousand counts were acquired for each head-to-head distance.

Data analysis

The collected data were processed via 2-D sinograms (see section 3.3.3) and then reconstructed with FBP algorithm with ramp filter with cut off at the Nyquist frequency. A 140-250 keV energy window was used.

The radial and tangential spatial resolution components in the transaxial plane were measured. The spatial resolution was determined by drawing a profile along the radial and tangential direction through the hottest pixel in the reconstructed image and calculating the FWHM by linear interpolation.

Since the reconstruction matrix size can affect the spatial resolution, we have chosen a pixel dimension that could provide a FWHM as accurately as can practically be achieved. A 128 × 128 pixels matrix have been used for the transaxial cross-sections.

Results

The radial (R_{FWHM}) and tangential (T_{FWHM}) FWHM resolutions at 1 cm radial offset and for 100, 125 and 150 mm head-to-head distances are reported in figure 5.26. Table 5.7 reports the radial spatial resolution at the different head-to-head distances.

Head-to-head distance (mm)	**Radial$_{FWHM}$ (mm)**
100	2.94
125	3.17
150	3.38

Table 5.7: Radial (R_{FWHM}) FWHM resolutions at the center of the FOV for each head-to-head distance: 100, 125 and 150 mm.

Since collimator resolution R_{coll} depends on source-to-collimator distance (see equation 5.21), also the system resolution depends on this parameter. This effect explains the spatial resolution degration at wider detectors distance. Moving from 100 to 150 head-to-head distance R_{FWHM} show a degradation higher than 10%, passing from 2.94 to 3.38 mm.

5.2.2 Sensitivity

The sensitivity of a SPECT scanner is measured as the number of detected counts per unit time per unit source activity for a specified energy window and geometry of measurement.

$$\text{Sensitivity(cps/MBq)} = \frac{\text{counts}}{\text{time(sec)} \times \text{sourceactivity(MBq)}} \tag{5.22}$$

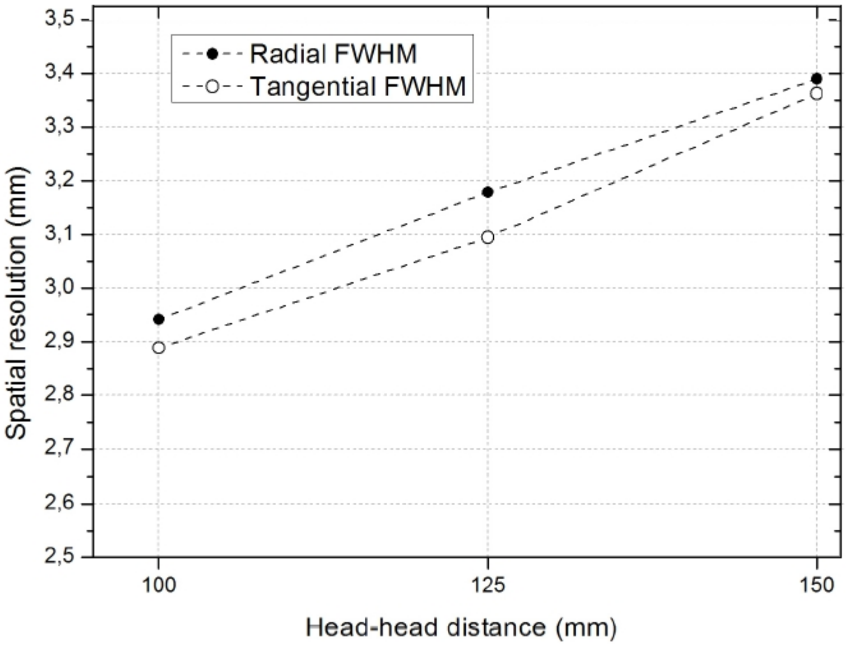

Figure 5.26: Radial and tangential spatial resolutions at the center of the FOV for each head-to-head distance: 100, 125 and 150 mm. A 140-250 keV energy window was used.

Experimental procedure

The system sensitivity measurements were performed with the same glass capillar filled with ^{99m}Tc employed for the spatial resolution measurements. The activity was measured with a calibrated well-counter. The uncertainity on the activity was about 10%. The activity was low enough so that dead time data loss is negligible.

The acquisitions were performed over 180^0 with 128 views. At least four hundred thousand counts have been acquired. The sensitivity was evaluated only for 100 mm head-to-head distance since the spatial resolution significantly degrades as the head-to-head distance is increased (see section 5.2.1).

Data analysis

The number of counts (C) and the acquisition time (T_{acq}) registered to obtain the counting rate ($R=C/T_{acq}$) in counts per second (cps), were obtained by the final row of the column “Used%” and “Dt(s)” of the YAP-(S)PET log file, respectively (see section 3.3.3). A 140-250 keV energy window was used.

Results

In the energy window 140-250 keV, the system sensitivity is 37 cps/MBq (3.7×10^{-3}%).

5.2.3 Phantoms studies

To test the imaging capability of the YAP-(S)PET scanner in SPECT modality we performed acquisitions with both Derenzo and Image Quality phantom. These phantoms are the same used for phantom studies in PET modality, and their characteristics can be found in section 5.1.7.

Experimental procedure

All the phantoms were filled with a solution of ^{99m}Tc.

a-) Derenzo phantom

The Derenzo phantom was filled with about 150 MBq ($\sim$ 4 mCi) of ^{99m}Tc and placed at the center of the FOV with the rods axis parallel to the scanner axis. A 128 views over 360^0 acquisition was performed for 100 head-to-head distance. More than 90 Mevents were acquired.

b-) Image quality phantom

The Image Quality was filled with about 170 MBq ($\sim$ 5 mCi) of ^{99m}Tc and placed in the FOV so that the axis of its main cylindrical compartment is aligned with the longitudinal axis of the tomograph. A 128 views over 180^0 acquisition was performed for 125 head-to-head distance. To obtain a high statistic image 160 Mevents were acquired in about 4 hours and half acquisition.

Data analysis

The collected data were processed via 2-D sinograms (see section 3.3.3).

Image reconstruction was performed with FBP algorithm with ramp filter with cut off at the Nyquist frequency for Derenzo phantom and with EM with collimator model [99] and 50 iterations for IQ phantom. A 128 $\times$ 128 transaxial image matrix (pixel dimension about 0.38 mm) with 27 axial slices (1.5 mm) was chosen for both Derenzo and Image Quality phantom. A 140-250 keV energy window was used.

Results

a-) Figure 5.27 (a) and (b) reports the transaxial section of the Derenzo phantom for four central slices and for 5 summed slices, respectively, obtained with FBP (ramp filter at the Nyquist frequency) algorithm. The profile of the last series of 3.0, 2.5, 2.0, and 1.5 mm hot rods are reported. The 1.5 mm is barely distinguishable, while the 1.2 mm is completely unresolved.

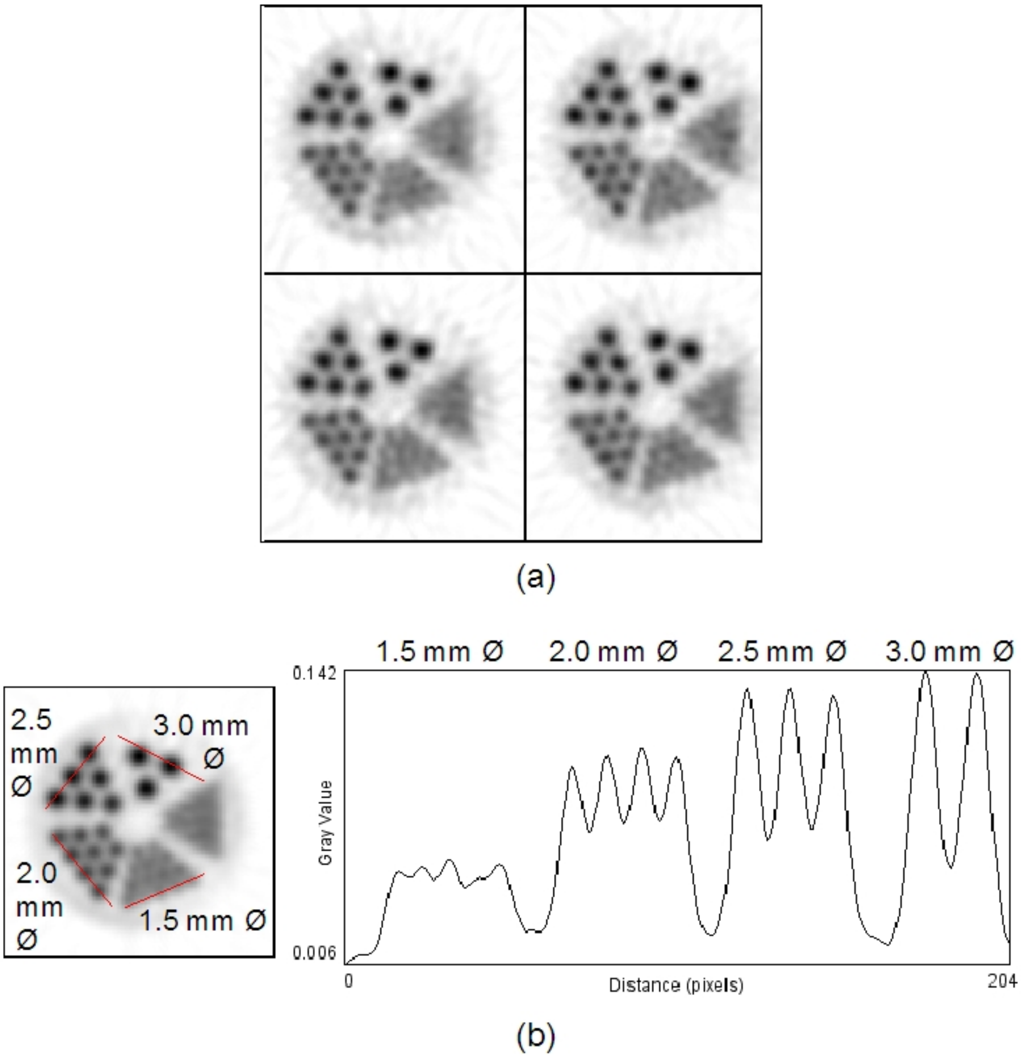

Figure 5.27: (a) Transaxial sections of the Derenzo phantom for four central slices. (b) Transaxial section of the Derenzo phantom for 5 summed slices.

b-) Figure 5.28 (a) shows all the 27 transaxial slices of the IQ phantom reconstructed with EM algorithm with collimator model and 50 iterations. The transaxial sections of the uniform hot region show several non-uniformities highlighted by concentric ring or "bull's eye" artifacts [140]. These artifacts are determined by spatial non-uniformities in the detectors or by local sensitivity variations (see chapter 4). The radius of the ring artifacts is equal to the distance of non uniform pixels from the center of rotation of the scanner.

Figure 5.28 (b) reports the summed slices of the transaxial section of the two

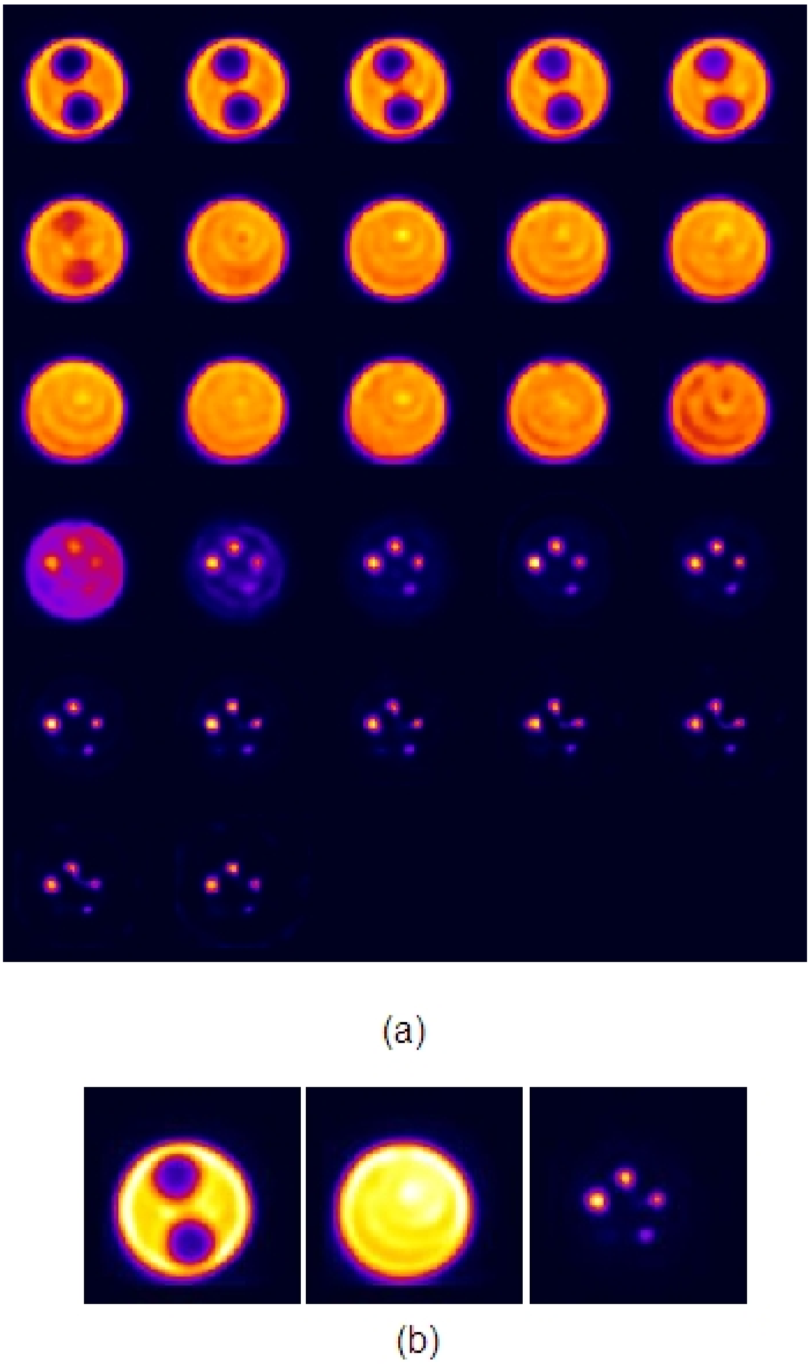

Figure 5.28: (a) All the 27 transaxial slices of the NEMA Image Quality phantom reconstructed with EM algorithm with collimator model and 50 iterations. (b) Summed slices of the transaxial section of the two cold region chambers, of the central hot uniform region and of the 5 fillable rods of the NEMA Image quality phantom.

cold region chambers, of the central hot uniform region and of the 5 fillable rods. The 1 mm radii hot rod is hardly distinguishable. The profiles through the hot rods are reported in figure 5.29. Due to partial volume effect (same effect described in section 5.1.5 for PET modality), the activity concentration in the center of rod highly decreases as the source becomes smaller. The activity concentration of 1 mm hot rod is underestimated by about 95%.

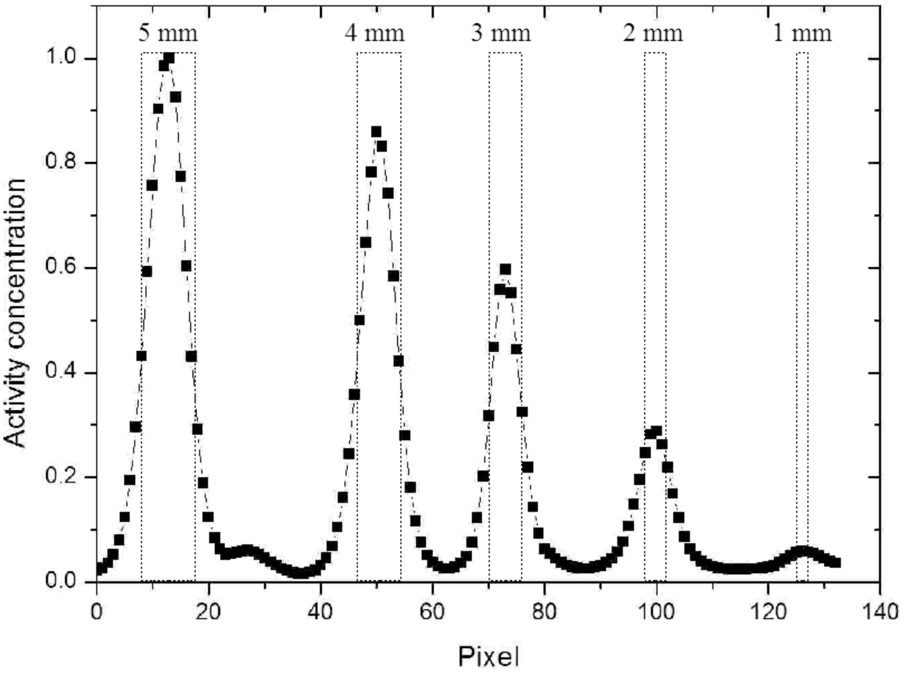

Figure 5.29: The profiles through the 1, 2, 3, 4, and 5 hot rods of the NEMA Image Qualuty phantom.

Chapter 6

Simultaneous PET/SPECT imaging

In the last decade, various research groups have shown a growing interest in developing PET/SPECT systems able to perform combined PET and SPECT acquisitions in one single device [76, 141–144].

Exploiting the YAP-(S)PET scanner intrinsic capability of performing both PET and SPECT imaging [120], we have implemented the capability of performing simultaneous PET/SPECT acquisitions with the new version of the YAP-(S)PET scanner, the "27 × 27" version (see chapter 3).

6.1 Simultaneous PET/SPECT data imaging architecture

The peculiar YAP-(S)PET scanner architecture (four detector heads mounted on the same gantry, see chapter 3) and the use of the same detector for PET and SPECT modalities (YAP) provide the capability to perform simultaneous PET/SPECT acquisitions.

Referring to figure 6.1: the opposing heads 1 and 2 are equipped with the collimators and independently acquire single events (SPECT mode), while the other pair 3-4 detects coincident events (PET mode). In order to reduce the background produced by the Compton scattering of 511 keV gamma rays, each SPECT head (1 and 2) is set in anticoincidence with the opposing one.

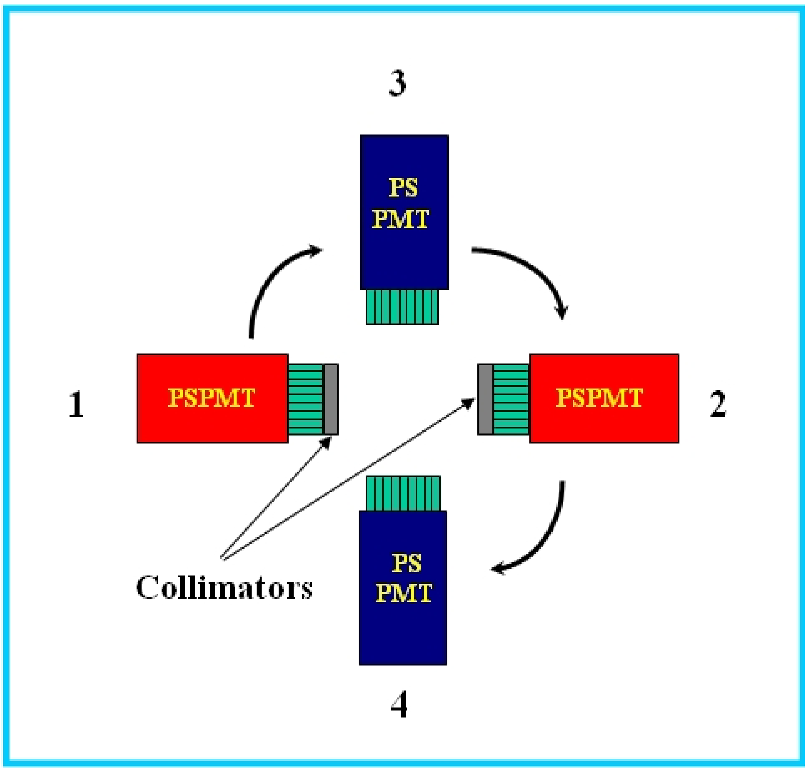

Figure 6.1: Scheme of the layout used for combined PET/SPECT acquisitions. Head 1 and 2 (red ones) works in SPECT mode, while the couple 3-4 (blue heads) acquires events in PET modality.

6.2 Data analysis

Data analysis is performed in two steps. In the first step, we process the data acquired in PET mode, then we analyze the SPECT data.

Since the thickness of the collimators (2 cm) is optimized to stop low energy gamma rays, particularly the 140 keV gamma rays of ^{99m}Tc, the high energy radiation (511 keV) passes or scatters through the collimator. The events detected by the SPECT heads during the simultaneous PET/SPECT acquisition are mainly due (about 95%) to scattered gamma rays produced by the interaction of 511 keV gamma rays with the lead collimators. This scattered radiation generates significant artifacts in the reconstructed images. Hence, it is necessary to perform a subtraction procedure to clean up the SPECT data.

On the contrary, the events detected by the PET pair (3-4) are only slightly influenced by the random coincidences produced by the a 511 keV photons originated by the positron annihilation and a single gamma emitted by the ^{99m}Tc decay (140 keV). For a 10:1 ^{99m}Tc/^{18}F activity ratio, the random coincidences are about 5%. Thus, the data acquired by the PET pair 3-4 do not need heavy clean up procedures for SPECT heads 1 and 2. Two techniques were adopted to reduce the incidence of ^{99m}Tc on PET coincidence imaging:

- an hardware procedure consisting in placing a lead layer of about 2 mm in front of the scintillator of the heads used for the PET acquisition
- a software procedure based on selecting only the coincidence events registered in an energy window excluding all the possible contamination from ^{99m}Tc. The energy window used is 200-850 keV. It is worthwhile to note that this energy window start at a energy higher that the ^{99m}Tc photo-peak energy window (125-180 keV).

Since the two procedures provide comparable results, usually we adopted the software procedure. Neverthelss, in animal studies we preferred to adopt the hardware procedure in order to further reduce the scattered radiation.

The PET data (pair 3-4) are sorted in 3-DMS sinograms, while the SPECT data (heads 1 and 2) are stored in 2-D sinograms. The reconstruction has been performed both with FBP or EM algorithms.

The two produced images are then fused using the PMOD image data analysis software [109]. At the end of the procedure, we obtain an image that correspond to the simultaneous PET/SPECT acquisition.

6.2.1 Subtraction procedure

The subtraction procedure we have elaborated is based on multi-energy window method [95] and relies on the following approximation. The background events produced by the 511 keV gamma rays scattered radiation that are detected in the energy region of ^{99m}Tc photo-peak (140 keV) are a fraction (f) of the events registered in an energy window close to the photo-peak but containing only scattered events. In order to determine the fraction f, before the simultaneous PET/SPECT acquisition we performed an acquisition that provides an evaluation of the background produced by the scattered 511 keV photons acquired in SPECT mode (see Fig. 6.2).

We used a cylindrical phantom (2.5 cm in diameter, 5.6 cm in height) filled with a known quantity of ^{18}F and acquired data in SPECT mode with the collimators mounted on the heads 1 and 2. The energy window containing the ^{99m}Tc photo-peak spreads out one σ at left and two σ at the right of the photo-peak (125-180 keV). The energy window close to the photo-peak but containing only Compton events extends from 220 to 280 keV. The fraction f is given by the ratio between the SPECT sinogram produced in the 125-180 keV energy window (SA_{BG} of Fig. 6.2) and the sinogram (still SPECT) generated in the 220-280 keV energy window (SB_{BG} of Fig. 6.2). For a more accurate evaluation, the SPECT sinograms ratio is performed independently for each head (1 and 2), slice by slice and pixel by pixel. A better statistics is gained averaging out on the angular coordinates the pixel by pixel ratio for each slice.

The corrected sinogram (Pk_{SA}), used for image reconstruction (in SPECT mode) of the data acquired in simultaneous PET/SPECT mode, is obtained by subtracting the scattered background due to 511 keV photons from the image sinogram evaluated in the same photo-peak energy window (125-180 keV) used to produce SA_{BG}.

Referring to figure 6.2, the corrected sinogram Pk_{SA} has the following expression:

$$\mathrm{PK_{SA} = SA - BG_{SA} = SA - f \cdot SB} \tag{6.1}$$

with

$$\mathrm{f = SA_{BG}/SB_{BG}} \tag{6.2}$$

6.2.2 How simultaneous PET/SPECT affects single mode PET and SPECT acquisitions

Since the simultaneous PET/SPECT modality is realized by performing the acquisition with a couple of heads in PET mode and the other two heads in SPECT mode (see section 6.1), the performance of each single modality are degraded: particularly, the sensitivity and a little bit the spatial resolution.

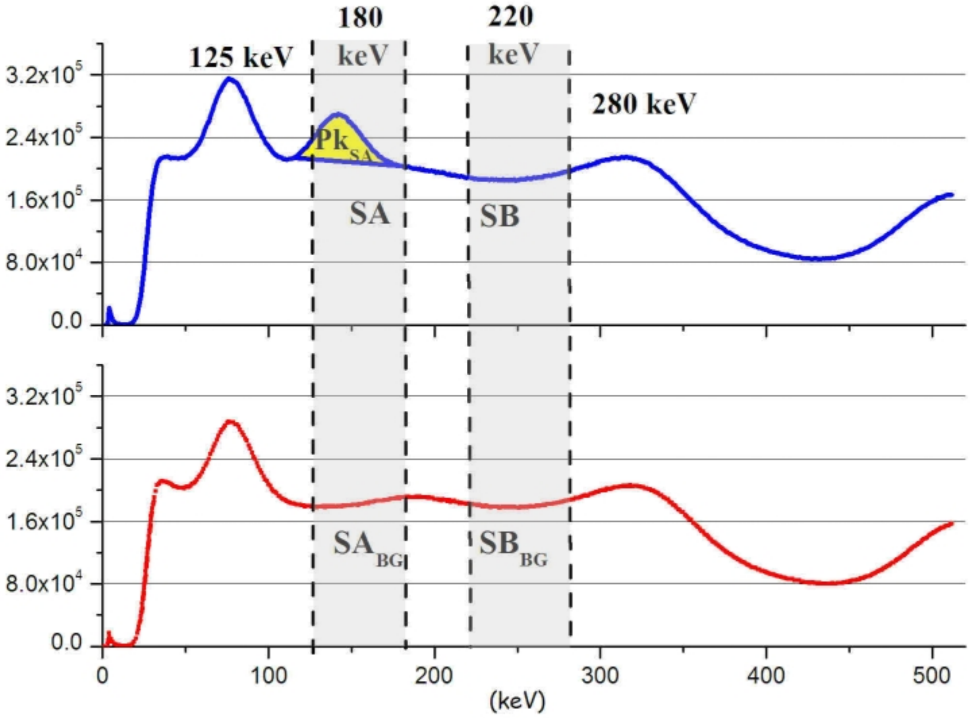

Figure 6.2: Top (blue line): energy spectrum of a simultaneous PET/SPECT acquisition with ^{99m}Tc as SPECT radiotracer and ^{18}F-FDG as PET radiopharmaceutical. Bottom (red line): energy spectrum of ^{18}F-FDG performed in SPECT mode with the collimators. Both spectra refer to head 1 of the YAP-(S)PET scanner.

- **SENSITIVITY**

  As a first evaluation, the sensitivity of each modality (PET or SPECT) can be estimated to be about the half of the sensitivity of each single mode. In fact, in the simultaneous acquisition only half of the scanner detectors are used: one couple in PET and two heads in SPECT.

PET modality

To evaluate the difference in sensitivity between the PET mode in the simultaneous acquisition (a couple of detector) and the full PET modality (two couples of detector), we used a glass capillary (inner diameter of 0.8 and outer diameter 1.2 mm) filled with 177.6 kBq (4.8 μCi) of ^{18}F and placed 10 mm off-axis. We placed the capillary not in the CFOV in order to obtain an average value. In fact, in sections 5.1.1 and 5.1.2 it is shown how resolution and sensitivity change with the source position. Since for animal studies, especially mice, we used a 100 mm head-to-head distance, the measurements were performed with the scanner in this configuration.

The acquisitions were performed over 180^0 with 128 views and at least one and a half million counts have been acquired.

The sensitivity was evaluated with the ^{22}Na point source procedure (see section 5.1.2).

Table 6.1 compares the sensitivities among the full PET modality (two couple of detectors) in the energy window 50-850 keV and the PET mode in the simultaneous PET/SPECT acquisition. The sensitivities of the two different techniques used to reduce the incidence of ^{99m}Tc on PET coincidence (see section 6.2) are reported. In the hardware procedure the usual 50-850 keV energy window was used. In the simultaneous PET/SPECT acquisition, the PET sensitivity is reduced of about 76% using an energy window of 200-850 keV and no lead shields, and more than 80% using an open energy window (50-850 keV) and 2 mm thick lead layers in front of the detectors.

The high reduction in sensitivity with the open energy window and the lead shields leads to prefer the software procedure to clean-up the PET data. We used the lead shields only for animal studies with high activity concentrantion in the FOV.

Modality	**Sensitivity (%)**
Full PET 2 couples 50-850 keV	1.71
PET/SPECT 1 couple without Pb 200-850 keV	0.40
PET/SPECT 1 couple with Pb 50-850 keV	0.33

Table 6.1: Comparison of the sensitivity for the full PET modality and the PET mode in simultaneous PET/SPECT acquisition.

SPECT modality

In SPECT mode, the difference in sensitivity between the simultaneous acquisition (only two detectors) and the full SPECT modality (all the four detectors), was evaluated by using a glass capillary (inner diameter of 0.8 and outer diameter 1.2 mm) filled with a 20.15 MBq (544 μCi) of ^{99m}Tc and placed at 10 mm from the CFOV.

The acquisitions were performed over 180^0 with 128 views and at least one and half million counts have been acquired.

The sensitivity was evaluated according to the procedure described in section 5.2.2.

The SPECT sensitivity in the simultaneous PET/SPECT acquisition is closely connected to the ^{99m}Tc/^{18}F activity ratios. In fact, the SPECT sensitivity in the 125-180 keV energy window after the subtraction procedure ranges bewteen 40% and 10% of the sensitivity of the full SPECT sensitivity (four heads and 140-250 keV) by changing the ^{99m}Tc/^{18}F activity ratios between 34 to 10.

- **SPATIAL RESOLUTION**

The spatial resolution would in principle not be affected in similtaneous acquisitions. Nevertheless, the necessity of the subtraction procedure in SPECT mode and the use of lead shields or a reduced energy window in PET mode lead to a small degradation of the spatial resolution.

PET modality

The spatial resolution evaluation was deduced by the acquisition used for the sensitivity evaluation.

Since we used a capillary, we have evaluated just the radial ($\mathrm{R_{FWHM}}$) and tangential ($\mathrm{T_{FWHM}}$) FWHM resolutions.

The obtained value are reported in table 6.2. Both the radial and tangential spatial resolution of the reduced energy window (200-850 keV) are a little bit worse than the values obtained for the full PET acquisition (two couples). On the contrary, the spatial resolution with the lead shield is even slightly better than the spatial resolution of the full PET acquisition. This effect can be explained with the removal of scattering due to the attenuation produced by the 2 mm lead layer in front of the detector. By using the attenutation law ($\mathrm{I(x) = I_0 \exp(-\mu \cdot x)}$), we obtained an attenuation ($\mathrm{1 - I(x)/I_0}$) of about

25% for 511 keV photons and more tha 50% for photons of 300 keV and lower energies.

SPECT modality

The spatial resolution evaluation was obtained from the same acquisition used for the sensitivity evaluation. As in PET modality, we evaluated only the radial and tangential FWHM resolutions. For both the radial and tangential spatial resolution we have a degradation of about 20%. This is mainly due to the subtraction procedure.

Modality	**Radial$_{\mathbf{FWHM}}$ (mm)**	**Tangential$_{\mathbf{FWHM}}$ (mm)**
Full PET 2 couples 50-850 keV	2.62	2.68
PET/SPECT 1 couple without Pb 200-850 keV	2.64	2.72
PET/SPECT 1 couple with Pb 50-850 keV	2.58	2.61

Table 6.2: Comparison of the radial (R_{FWHM}) and tangential (T_{FWHM}) FWHM resolutions for the full PET modality and the PET mode in simultaneous PET/SPECT acquisition.

6.3 Phantom imaging

The simultaneous PET/SPECT imaging capabilities were evaluated performing several acquisitions with different phantoms and various ^{99m}Tc/^{18}F activity ratios.

The phantoms employed are:

A-) capillaries.

B-) syringes for insuline (0.5 mm diameter).

C-) Image quality phantom (see section 5.1.7).

The ^{99m}Tc/^{18}F activity ratios range between 5 and 50:1.

All the acquisitions were performed for a 125 mm head-to-head distance, in order to exploit the best compromise between spatial resolution and sensitivity of both PET and SPECT modalities (see chapter 5).

A-) Two glass capillaries with inner and outer diameter of 0.8 and 1.2 mm were used. A capillary was filled with 370 kBq (10 μCi) of ^{18}F and the other one with 18.5 MBq (about 500 μCi) of ^{99m}Tc (^{99m}Tc/^{18}F activity ratio 50:1). The capillaries were placed parallel to the longitudinal YAP-(S)PET scanner axis at about 1 cm far from the central axis of the scanner. A simultaneous acquisition of about 30 minutes over 180^0 with 128 views was performed. The data were reconstructed with EM algorithm with 50 iterations. In SPECT mode EM algorithm with collimator model was used [99]. The transaxial and coronal sections are reported in figure 6.3.

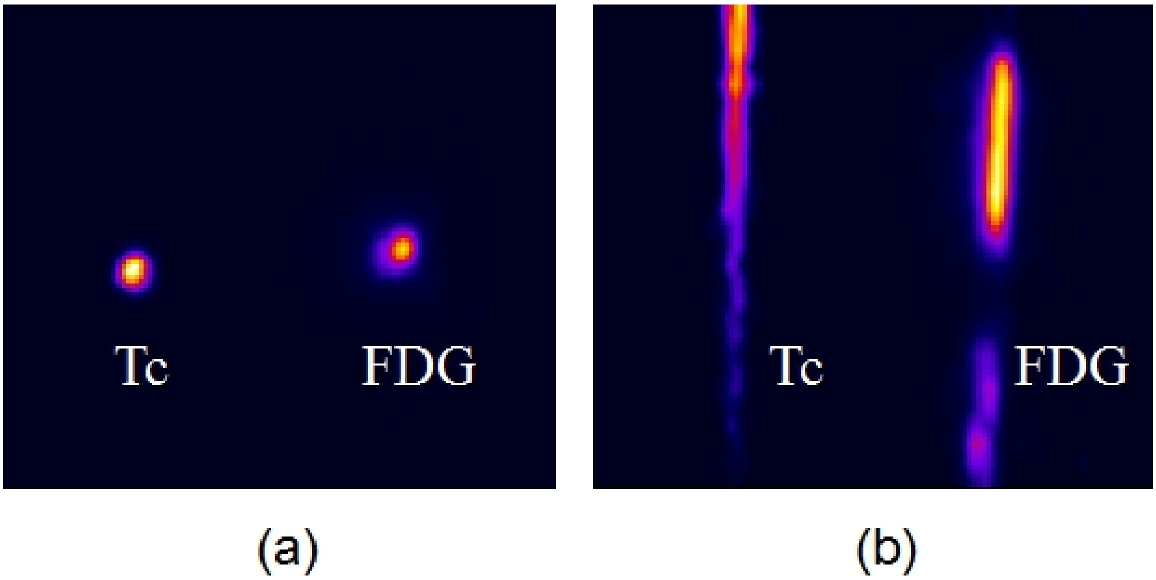

Figure 6.3: Transaxial (a) and coronal (b) section of a simultaneous PET/SPECT acquisition of two capillaries. The left one was filled with 18.5 MBq (about 500 μCi) of ^{99m}Tc, while the right with 370 kBq (10 μCi) of ^{18}F (^{99m}Tc/^{18}F activity ratio 50:1).

B-) Figure 6.4 shows the simultaneous acquisition of two syringes for insulin (5 mm inner diameter). The syringes were placed parallel to the longitudinal axis of the scanner. The syringe on the left was filled with 16.3 MBq (70 μCi) of ^{99m}Tc, while the syringe on the right was filled with 630 kBq (about 17 μCi) of ^{18}F (SPECT/PET radiotracers ratio 10:1).

In order to evaluate the more appropriate ^{99m}Tc/^{18}F activity ratio, various PET/SPECT simultaneous syringes acquisition were performed. The SPECT/PET radiotracers ra-

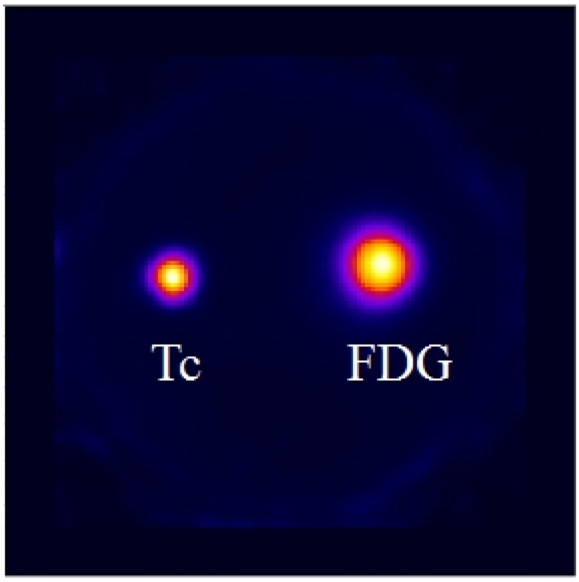

Figure 6.4: Transaxial image of a simultaneous PET/SPECT acquisition of two syringes for insulin: the left one filled 16.3 MBq (70 μCi) of ^{99m}Tc and the right one with 630 kBq (about 17 μCi) of ^{18}F (SPECT/PET radiotracers ratio 10:1).

tio ranged between 5:1 to 50:1. Four different acquisitions were performed. Referring to figure 6.5, the syringe on the right was filled with ^{99m}Tc, while the one on the left with ^{18}F, and the activity ratio are as follow:

(a) 141 MBq (3.80 μCi) of ^{99m}Tc and with 30 MBq (about 800 μCi) of ^{18}F, for a SPECT/PET radiotracers ratio 5:1.

(b) 100 MBq (2.70 μCi) of ^{99m}Tc and 10 MBq (about 260 μCi) of ^{18}F: SPECT/PET radiotracers ratio 10:1.

(c) 63 MBq (1.70 μCi) of ^{99m}Tc and 2.10 MBq (about 60 μCi) of ^{18}F, for a SPECT/PET radiotracers ratio $\sim$ 30:1.

(d) 51 MBq (1.30 μCi) of ^{99m}Tc and 0.96 MBq (about 26 μCi) of ^{18}F, for a SPECT/PET radiotracers ratio 50:1.

Figure 6.5 reports the transaxial slices of three central sections of the two syringes. A qualitatively evaluation shows that the 50:1 ^{99m}Tc/^{18}F supplies the best results. The activity ratio more suitable for animal studies in order to maintain the tracer principle [145] is of the order of 30:1. Since the images quality of SPET/CT radiotracers 30:1 is acceptable, we assumed that 30:1 is the best compromise between image quality and tracer principle.

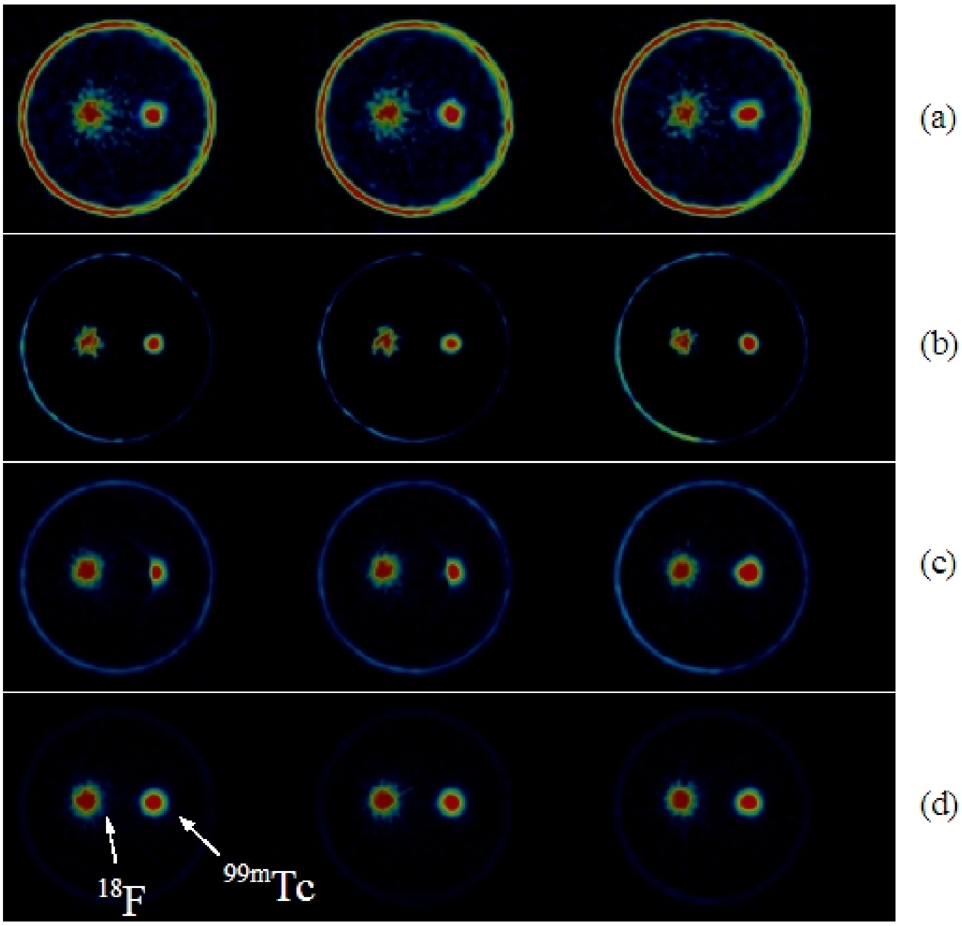

Figure 6.5: Transaxial images of a simultaneous PET/SPECT acquisition of two syringes for insulin. the syringe on the right was filled with ^{99m}Tc, while the one on the left with ^{18}F, and the activity ratio are as follow: (a) 141 MBq (3.80 μCi) of ^{99m}Tc and with 30 MBq (about 800 μCi) of ^{18}F, for a SPECT/PET radiotracers ratio 5:1. (b)100 MBq (2.70 μCi) of ^{99m}Tc and 10 MBq (about 260 μCi) of ^{18}F: SPECT/PET radiotracers ratio 10:1. (c) 63 MBq (1.70 μCi) of ^{99m}Tc and 2.10 MBq (about 60 μCi) of ^{18}F, for a SPECT/PET radiotracers ratio $\sim$ 30:1. (d) 51 MBq (1.30 μCi) of ^{99m}Tc and 0.96 MBq (about 26 μCi) of ^{18}F, for a SPECT/PET radiotracers ratio 50:1.

C-) The NEMA Image Quality (IQ) phantom (see section 5.1.7) was used to exploit the simultaneous PET/SPECT imaging capabilities of objects having shape and dimensions comparable with small animal used for preclinical experiments, particularly mice. The whole IQ phantom, except the two 8 mm diameter hollow chambers, was filled with 133 MBq (about 3.6 mCi) of ^{99m}Tc. The hollow chambers were filled with 6.6 MBq ($\sim$ about 180 μ Ci) of ^{18}F. The SPECT/PET radiotracers ratio was 28:1, quite close to the best compromise between image quality and tracer principle (see syringes experiments reported in **B-)**). The IQ is placed in the FOV such that the axis of its main cylindrical compartment is aligned with the longitudinal axis of the tomograph. The SPECT data were reconstructed with EM algorithm with collimator model [99], while PET data were reconstructed with FBP algorithm with ramp filter with cut off at the Nyquist frequency. Figure 6.6 represents all the transaxial sections of the IQ for both PET and SPECT tracers of the PET/SPECT simultaneous acquisitions.

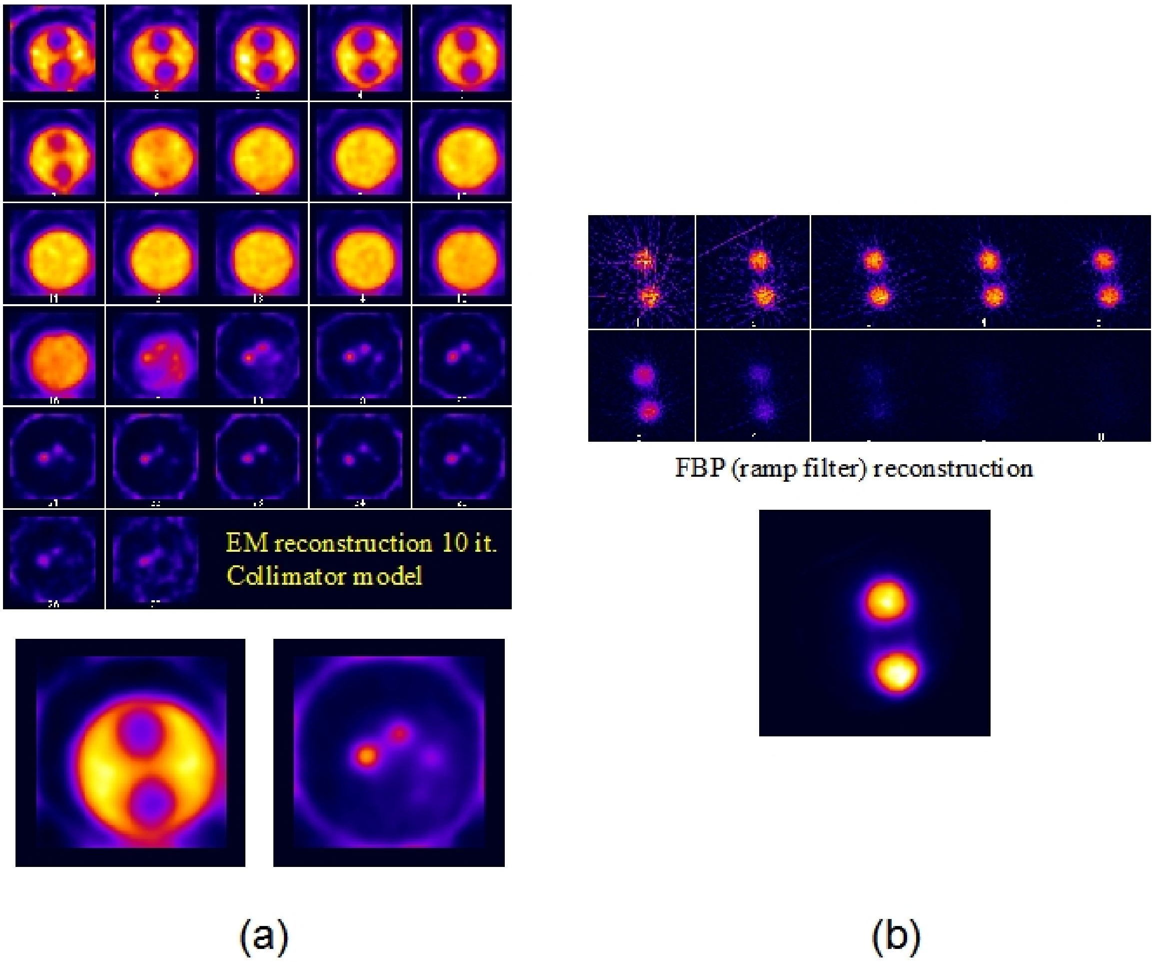

Figure 6.6: Transaxial sections of a simultaneous PET/SPECT acquisition of the NEMA Image Quality phantom. (a) SPECT image obtained filling the whole IQ phantom, except the two 8 mm diameter hollow chambers, was filled with 133 MBq (about 3.6 mCi) of ^{99m}Tc. Top: all 27 transaxial sections. Bottom: summed slices of the uniform region conatining the hollow chambers filled with ^{18}F and of the rods regions of the IQ. (b) PET images obtained filling the hollow chambers with 6.6 MBq ($\sim$ about 180 μ Ci) of ^{18}F. Top: all the transaxial slices containg the hollow chambers. Bottom: sum of all the slices containg the hollow chambers.

6.4 Animal imaging

In order to evaluate the feasibility of simultaneous PET/SPECT acquisition on living subject injected with SPECT and PET tracers at the same time, we performed a study in a male healthy mouse. The aim of the study was to investigate the system capability to image the mouse heart.

260 MBq (about 7 mCi) of ^{99m}Tc-sestamibi (see section 7.4) and 12.70 ($\sim$ 340 μCi) of ^{18}F-FDG were injected via tail vein. Before the tracers injection, the mouse was injected with 5 ml of glucosate at 5% 10-15 in order to have a better ^{18}F-FDG uptake. After an uptake time of 45 minutes, the mouse was anesthetized with intraperitoneal injection of a mix of ketamine (60 mg/kg and 4.4 mg/kg) and fenobarbital (50 mg/kg) and placed on the flat bed. About one and half hour of simultaneous acquisition was performed. In order to reduce the random 511 -140 keV random coincidences (see section 6.2), a lead layer of about 2 mm was placed in contact of the heads used for the PET acquisition. The data were reconstructed with EM algorithm with 50 iterations. In SPECT mode EM algorithm with collimator model was used [99]. Figure 6.7 shows the transaxial, coronal and sagittal sections of the images obtained by the SPECT heads 1 and 2 (first row), the PET pair 3-4 (central row) and the fusion (final row) realized by the fusion of the two images. The PMOD software [109] was used for fusion.

The images is quite blurred and difficult to understand. It is due to the very small dimensions of mouse heart (some millimeters) and to heavy effect of partial volume and spillover.

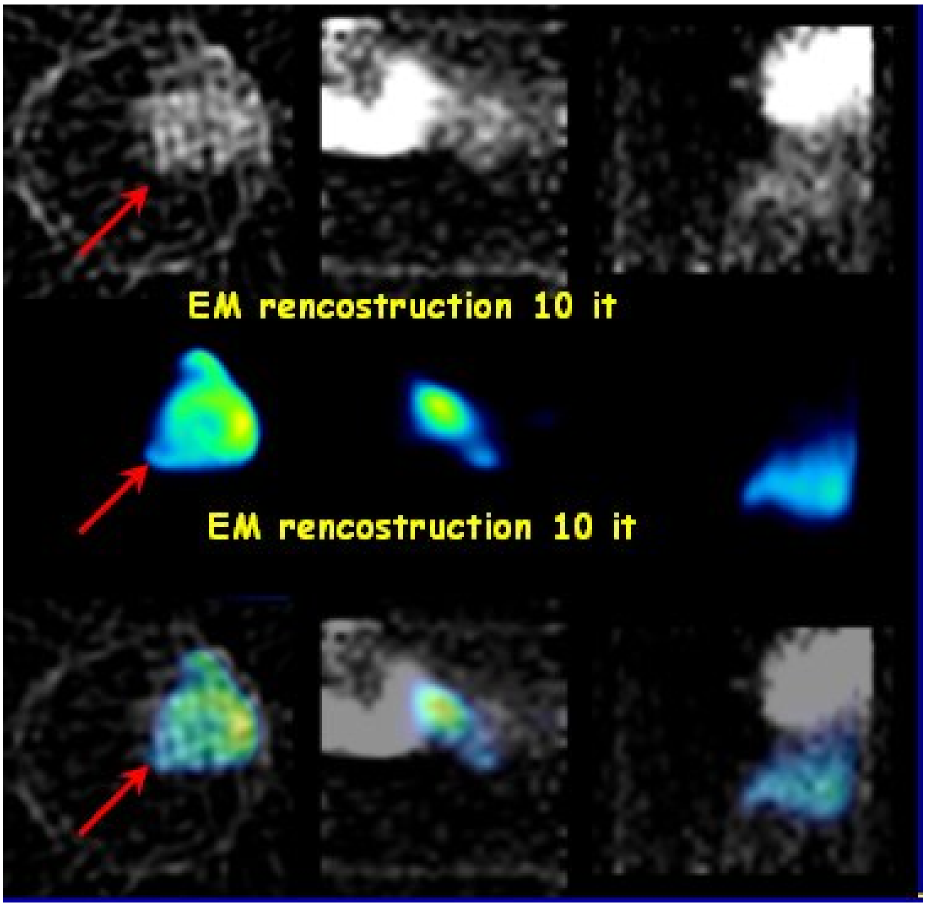

Figure 6.7: Transaxial (left column), sagittal (central column) and coronal (right column) of the simultaneous PET/SPECT acquisition of a male healthy mouse. Top row: SPECT images. 260 MBq (about 7 mCi) of ^{99m}Tc-sestamibi injected. Central row: PET images. 12.70 ($\sim$ 340 μCi) of ^{18}F-FDG were injected via tail vein. Bottom row: Fusion of the two previous images realized with Pmod software [109]. The uptake time before the simultaneous acquisition was 45 minutes and the acquisition time one and half hour. Both PET and SPECT images were obtained with a EM reconstruction algorithm with 10 iterations.

Chapter 7

YAP-(S)PET small animal studies

Since the new version of the YAP-(S)PET scanner (the “27 × 27” version) with improvements in both hardware and software (see chapter 3) has been completed during the first half of 2006, the majority part of the animal studies reported in this thesis were performed with the first 20 × 20 version of the YAP-(S)PET scanner.

Different animal models and various isotopes and tracers have been used in the experiments performed in collaborations with the different research groups. In these thesis only some of these studies are reported in order to point out the YAP-(S)PET imaging capabilities, particularly in neuropharmacology, psychiatry and oncology. Other studies performed in collaboration with various European research groups can be found in [146, 147].

Recently, a collaboration projection aimed to evaluate a rat model of ischemia and reperfusion has been started. Preliminary results of this studies performed with the new 27 × 27 version of the YAP-(S)PET scanner are reported.

7.1 Brain’s glucose metabolism

The brain is metabolically one of the most active organs in the body. In adult humans, for example, in whom the brain comprises only 2% of body weight, the brain alone accounts for approximately 20% of the total body basal oxygen consumption and maintains a steady rate of energy expenditure of at least 20 watts [148].

Brain’s glucose metabolism is one of the most powerful tools to investigate tumors and brain disorders such as Alzheimer or Parkinson.

The study presented here was performed in collaboration with the Endocrinology and Metabolic Disease Department of the University of Pisa using the YAP-(S)PET scanner installed at the IFC institute of the CNR in Pisa. The aim of the collaboration project is to understand the relation between hypothyroidism and cognitive or psychiatric disturbance. Up to now, the experimental results are under study by medical doctors. In this thesis, an image regarding healthy male rat is reported in order to show the capability of the YAP-(S)PET scanner to visualize the different brain structures. (see figure 7.1).

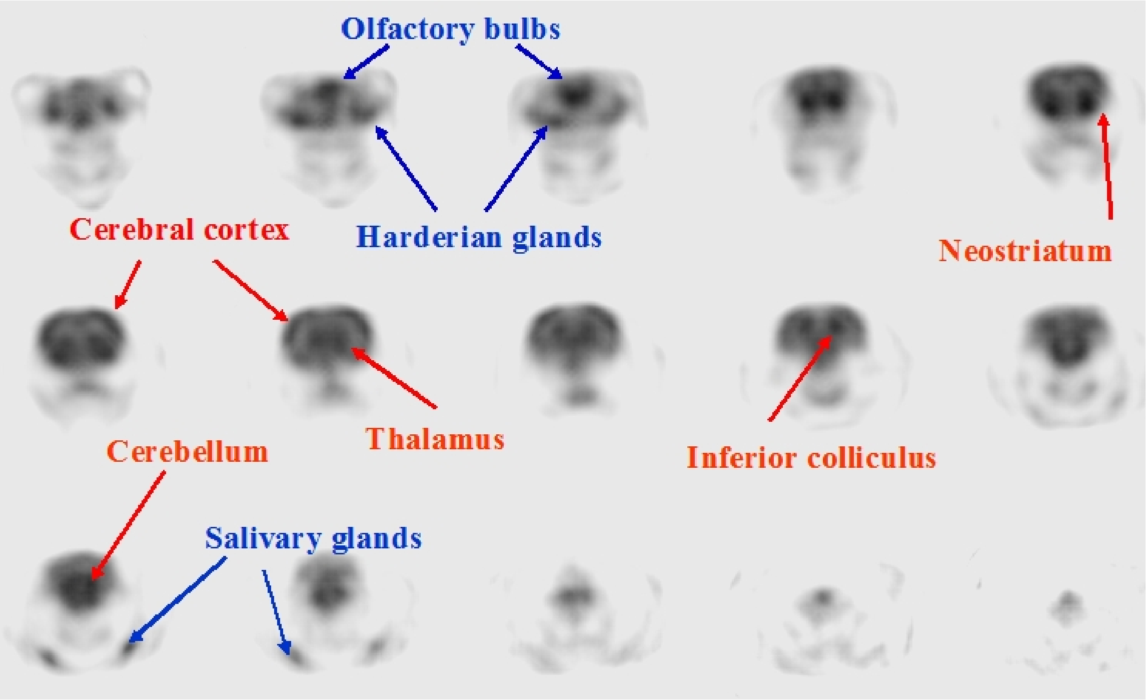

Figure 7.1: Transaxial (coronal) section ($0.5 \times 0.5 \times 2$ mm voxel size), of a rat brain injected with 37 MBq of ^{18}F-FDG and acquired for 45 minutes, after 30 minutes of uptake. The images are arranged from rostral (upper left) to caudal (lower right). The right hemisphere of the animal is represented on the right hand side of the figure, and the dorsal aspect corresponds to the top of the figure. EM algorithm with 30 iterations was used for image reconstruction.

The rat was injected with 37 MBq ($\sim$ 1 mCi) of ^{18}F-FDG and acquired for 45 minutes after 30 minutes of uptake. Figure 7.1 shows how cerebral activity can be clearly distinguished from extracerebral activity. More specifically, activity in the Harderian glands is clearly distinct from brain activity. Within the brain, principal brain structures such as cortex, thalamus and striatum are well resolved [149].

7.2 Receptors studies

Dopamine neurotransmitters affects brain processes that control movement, emotional response, and ability to experience pleasure and pain. Regulation of dopamine plays a crucial role in certain brain diseases, e.g. Parkinson's disease and schizophrenia. Some drugs are known as dopamine agonists. These drugs bind to dopamine receptors in place of dopamine and directly stimulate those receptors. Some dopamine agonists are currently used to treat Parkinson's disease. In contrast to dopamine agonists, dopamine antagonists are drugs that bind but do not stimulate dopamine receptors. Antagonists can prevent or reverse the actions of dopamine by keeping dopamine away from attaching to receptors. Dopamine antagonists are traditionally used to treat schizophrenia and related mental disorders. A person with schizophrenia may have an overactive dopamine system. Dopamine antagonists can help regulate this system by “turning down” dopamine activity [150].

Studies on the binding of various radiolabeled dopamine neurotransmitter analogues in order to visualize dopamine D2/D3 receptor availabilities were performed in both PET and SPECT modality using rats and mice.

The PET studies were performed within a collaboration project with the Vita-Salute San Raffaele University, Milan, group leader Dr. R. M. Moresco.

The SPECT studies were realized in collaborations with the University of Pisa, Nuclear Medicine Department, group leader Prof. G. Mariani.

7.2.1 PET studies: ^{11}C-Raclopride, rat model of Huntington's disease

Huntington's disease (HD) results from genetically programmed degeneration of neurons in certain areas of the brain. This degeneration causes uncontrolled movements, loss of intellectual faculties, and emotional disturbance. HD is a familial disease, passed from parent to child through a mutation in the normal gene. HD can be identified in individuals by genetic testing and, when present, is associated with a phenotypic penetrance of nearly 100 % (i.e., if you have the mutate gene, you get the disease) by the time the patient's fifth decade is reached [95]. The presymptomatic detection of metabolic abnormalities has specifically been shown for HD disease using PET. Abnormalities are identified by PET with FDG about 7 years before symptoms emerge [151]. In contrast, there are generally no structural abnormalities evident on CT on MRI scan preclinically or even during the symptomatic stages. PET scanning thus offers a non-invasive yet sensitive method to detect the disease when actual pathologic changes in the brain become functionally manifest at the neuronal level.

A preclinical model of Huntington's disease was studied within a collaboration project with the Vita-Salute San Raffaele University, Milan, group leader Dr. R. M. Moresco.

This model which consists in the intrastriatal administration of an excitotoxin, the quinolinic acid (QA), produces neurochemical changes that approximate Huntington's disease including the degenerations of intrinsic striatal neurons, reactive gliosis and microglia activation [152–155].

The aim of the experiment is the quantitative evaluation of the neuronal loss in lesioned and unlesioned striatum [156]. Male albino CD rats (225-250 g; Charles River, Italy) were used for the study. QA solution was prepared dissolving 50.2 mg of acid (Sigma-Aldrich, Milan, Italy) in 0.6 ml of 1 M sodium hydroxide and 0.4 ml of PBS solution (0.1 M, pH 7.4) to obtain a final concentration of 300 nmol/μl. Rats were anesthetized by intraperitoneal injection (50 mg/kg) of pentobarbital and placed on a stereotaxic frame (Narashige, Japan). The scalp was cleaned with an iodine solution, incised on the midline and two holes were made in the skull at the appropriate stereotaxic location using a micro-drill. Unilateral intrastriatal administration (left side) of 0.7 μl of QA solution (210 nmol) was performed using a 5 μl Hamilton syringe; contralateral injection (right side) of 0.7 μl of PBS 0.1 M was used as internal control. Either QA or solvent were infused into striatum at a rate of approximately 0.5 μl/min. The stereotaxic coordinates of the target site were AP = +1.5, L = +2.6, V = -7.0mm from the Bregma, according to the atlas of [157]. After the injection, the needle was left in place for additional 5 min, and then slowly withdrawn. At the end of the surgery, the wound was closed with metallic clips, and the rats were located in their cage [158].

The PET studies were performed ^{11}C-Raclopride and repeated at different times from the striatum lesion induction. Since ^{11}C-Raclopride is a radiotracer that selectively binds to D2 receptors presents on the intrastriatal GABA neurons, it is suitable to provide information about neuronal losses in the lesioned striatum. The rats were injected with no more than 7.4 MBq ($\sim$ 200 μCi) of ^{11}C-Raclopride and acquired for 10 minutes after 30 minutes of uptake. The acquisitions were performed over 90^0 with 64 views. A wide-open energy window 50-850 keV was used and images were reconstructed with EM algorithm.

Figure 7.2 shows the transaxial sections of the PET acquisition at different times after striatum lesion induction. It is evident how the ^{11}C-Raclopride radiotracer selectively binds to D2 receptors accumulating in the striata. It is interesting to note that the bind is maximum in the unlesioned striatum and progressively gets lower in the lesioned striatum (left side). As described in [159, 160], the neuronal loss in lesioned striatum is already significant within 8 days from QA injection and increases when time from lesion increases.

Quantitative analysis can be found in [156].

7.2.2 SPECT studies: ^{123}I-FP-CIT, binding in a new model for Parkinson's disease

The dopamine D2 receptors have been evaluated on mice with the ^{123}I-DaTSCAN tracer. ^{123}I-DaTSCAN is a radiotracer commonly used in clinical trial. It is indicated for detecting loss of functional dopaminergic neuron terminals in the striatum of patients with clinically uncertain Parkinsonian Syndromes, in order to help differentiate Essential Tremor from Parkinsonian Syndromes.

We have performed static acquisitions of healthy male mice in order to determine the YAP-(S)PET capability to resolve the mouse striatum. The mice striata are, in fact, tiny brain region with less than 20 mm^3 in volume.

The mice were intravenously injected with 11 MBq ($\sim$ 300 μCi) of ^{123}I-DaTSCAN and scanned for six hours, after an uptake time of 6 hours. Figure 7.3 shows transaxial sections of the SPECT acquisition of a mouse injected with ^{123}I-DaTSCAN. The striata are the two hot spots in the seventh image starting from upper left and going from left to right. The image is not very clear and there is a rough ring corresponding

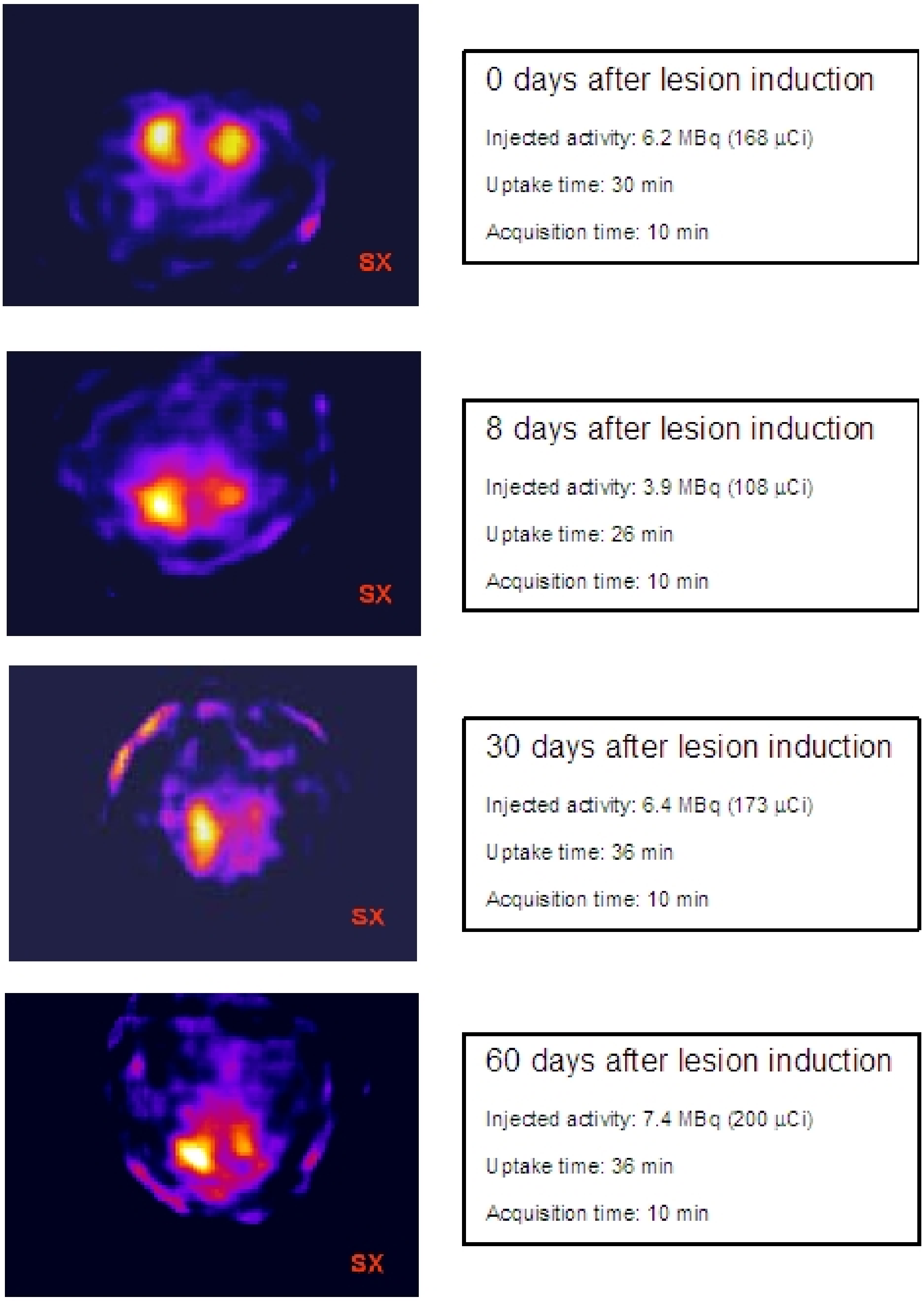

0 days after lesion induction

Injected activity: 6.2 MBq (168 µCi)

Uptake time: 30 min

Acquisition time: 10 min

8 days after lesion induction

Injected activity: 3.9 MBq (108 µCi)

Uptake time: 26 min

Acquisition time: 10 min

30 days after lesion induction

Injected activity: 6.4 MBq (173 µCi)

Uptake time: 36 min

Acquisition time: 10 min

60 days after lesion induction

Injected activity: 7.4 MBq (200 µCi)

Uptake time: 36 min

Acquisition time: 10 min

Figure 7.2: Transaxial sections of the ^{11}C-Raclopride PET acquisitions of a rat model of Huntington's disease at different times after striatum lesion induction (0, 8, 30 and 60 days). It is evident how the ^{11}C-Raclopride radiotracer selectively binds to D2 receptors accumulating in the striata. The bind is maximum in the unlesioned striatum and progressively gets lower in the lesioned striatum (left side).

to the FOV edge. This is due to the thickness of YAP-(S)PET scanner collimators. In contrast to ^{99m}Tc imaging, the thickness of the collimators (2 cm, see section 3.1) is not enough to stop the small percent (1-2%) of high energy radiation (around 520 keV) emitted by ^{123}I, whose Compton interaction in the crystals produces a nearly uniform background below the photopeak region of the 159 keV gamma-lines. It was therefore necessary to elaborate a subtraction procedure [146].

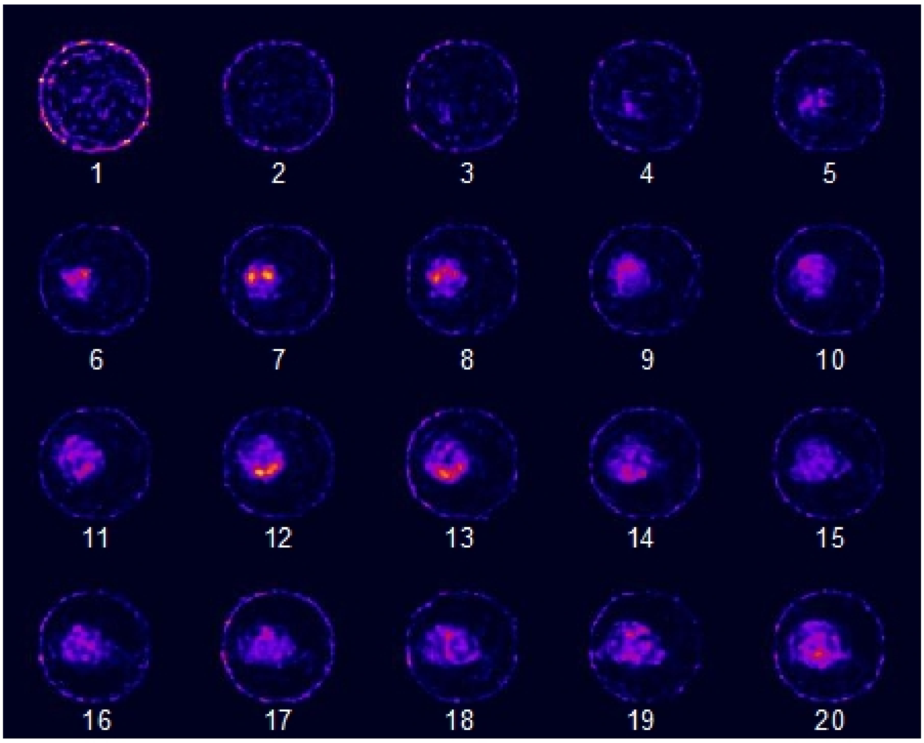

Figure 7.3: Transaxial (coronal) section (0.5 × 0.5 × 2 mm voxel size), of a mouse brain injected with 11 MBq of ^{123}I-DaTSCAN and acquired for 6 hours, after 6 hours of uptake. The images are arranged from rostral (upper left) to caudal (lower right). The right hemisphere of the animal is represented on the right hand side of the figure, and the dorsal aspect corresponds to the top of the figure. EM algorithm with 30 iterations was used for image reconstruction.

7.3 Oncologic studies

The biological alterations of tumor cells goes back to more than 80 years ago, when the German biochemist Otto Warburg and colleagues published their observations on the metabolism of cancer cells [161]. A decade before, Flexner and Jobling [162] studied the metabolism of tumor cells in a rat model and have found that the glycolitic rates of tumors were 124 times greater than the glycolitic action of blood. From these and other observations, they concluded that the metabolism of rat tumor cells is predominantly one of glicolysis. They subsequently confirmed these finding in a variety of human cancer cells and uncovered that benign tumors also exhibited increased glycolitic activity but to a much smaller degree than malignant tumors.

Traditionally, the diagnostic tools for diagnosing, staging and restaging of patients with cancer relied on anatomic imaging with computed tomography, magnetic resonance and ultrasound. Nevertheless, these techniques can not reliably discriminate between benign and malignant tumors. Since their introduction, emission computed tomography, and particularly PET have been used to investigate oncologic diseases. The most extensively used positron-emitting tracer in oncological evaluation has been FDG (glucose analogue 2-deoxy-2-[^{18}F]fluoro-D-glucose) [163].

Studies on rats and mice models of tumors were performed in both PET and SPECT modalities.

The PET studies were performed within a collaboration project with the C.N.R. (Centro Nazionale delle Ricerche) Institute of Clinical Physiology, Pisa, group leader Dr. Piero Salvadori.

The SPECT studies were realized in collaboration with the University of Pisa, Nuclear Medicine Department, group leader Prof. G. Mariani.

7.3.1 PET studies: ^{18}F-FDG, human glioma implantation in rat brain

Gliomas are the most common of primary human brain tumors [164]. About 50% of gliomas and 20% of all brain tumors are glioblastomas. They represent the second death cause among cerebral disease after stroke. Diffuse gliomas are therapeutically vexing: their infiltrative (diffuse) growth pattern essentially prevents surgical cure, and the majority of these gliomas are resistant to standard chemotherapeutic and radiotherapeutic approaches.

In 1951, Sweet [165] first suggested that Neutron Capture Therapy (NCT) might be useful for the treatment of brain tumors, and in particular, the treatment of the most highly malignant and therapeutically persistent of all brain tumors, glioblastoma multiforme (GBM). Boron neutron capture therapy (BNCT) is based on the nuclear reaction that occurs when ^{10}B, a nonradioactive constituent of natural elemental boron, absorbs thermal neutrons (<0.025 eV) and undergoes instantaneous nuclear fission to produce high energy alpha particles and recoiling ^{10}Li nuclei (see equation 7.2).

$$^{10}\mathrm{B} +^{1} \mathrm{n}_{\mathrm{thermal}}(0.025\ \mathrm{eV}) \rightarrow^{7} \mathrm{Li}^{3+} +^{4} \mathrm{He}^{2+} + 2.79\ \mathrm{MeV}_{\ (\mathrm{kinetic\ E})} \quad (6\%)$$

$$\begin{aligned} ^{10}\mathrm{B} +^{1} \mathrm{n}_{\mathrm{thermal}}(0.025\ \mathrm{eV}) \rightarrow^{7} \mathrm{Li}^{3+} +^{4} \mathrm{He}^{2+} + \gamma\ (0.48\ \mathrm{MeV}) + \\ +2.79\ \mathrm{MeV}_{\ (\mathrm{kinetic\ E})} \quad (94\%) \end{aligned} \tag{7.1}$$

These heavy particles have pathlengths of approximately 5-9 μm and deposit their energy within cells ^{10}B containing. If a sufficient amount of ^{10}B (20-40 parts per million or ppm) can be delivered, and enough thermal neutrons (fluence @ 10^{13} n. cm^{-2}) reach the treatment volume, then selective destruction of tumor cells can occur as a result of the ^{10}B (n,α) ^{10}Li capture reaction. Clinical failures of BNCT for patients with brain tumors in the United States in the 1950's [166,167] and early 1960's [168] were due to a lack of boron compounds with the requisite selectivity, as well as thermal neutron beams that were incapable of depositing adequate fluence at depths greater than a few centimeters. As a result of this, efforts have been made to synthesize boron compounds that had more desirable biological and biochemical properties, and to develop higher energy epithermal neutron beams that had greater tissue penetrating properties. After the promising results obtained in 1991 by the Japanese research group leaded by Hatanaka [169], new BNCT therapy clinical trials started again in USA [170], Japan [171] and Europe [172–174].

A preclinical model for BNCT therapy has been realized within the collaboration project with Institute of Clinical Physiology of the C.N.R. in Pisa. F98 glioma cells [175] were intracerebral implanted in a Wistar male rats. F98 glioma tumor has an infiltrative pattern of growth within the brain, is very weakly immunogenic, and an intracerebral inoculum of as few as ten cells invariably killed all animals. These characteristics closely resemble those of human glioblastoma, and for this reason we have found it to be a particularly good tumor model for our studies on BNCT [175]. The implantation methodology and the tumor-neuronal tissue ratio were evaluated through YAP-(S)PET acquisitions performed with ^{18}F-FDG.

A group of 7 rats (male Wistar, 190-250 g) composed of 4 implanted rats and 3 control animals has been evaluated. The control animals have been exposed to the same implantation methodology without F98 glioma cells inoculation. The animals were anesthetized with intraperitoneal injection of chloral hydrate (400 mg/kg), placed on hollow bed (see section 3.1) and positioned with the brain in the FOV. The ^{18}F-FDG was introduced with a bolus injection in the femoral vein. The mean injected dose was 54 MBq (about 1.5 mCi). The uptake time was 45 minutes and the acquisition time 60 minutes. The acquisitions were performed over 180^0 with 128 views. A wide-open energy window 50-850 keV was used and images were reconstructed with EM algorithm. After the YAP-(S)PET acquisition, the animals were euthanized with anesthetic overdose and the brain was extracted. Tumors and surrounding normal brain tissues were treated following conventional preparative histological protocols to fixation and subsequent criosectioning. Coloration with hematoxylin/eosin was performed.

Figure 7.4 (a) shows the transaxial section of one the rat bearing F98 glioma: the tumor is the blacker spot clearly visible in the central line. Figure 7.4 (b) reports the comparison with an istological section. The agreement is quiet good.

Table 7.1 reports the tumor-neuronal tissue ratio for three of F98 glioma implanted rats. The tumor captation ratio ranges between 1.5 and 2.

Further details can be found in [176].

F98 glioma bearing rat	**Transaxial section**	**Tumor-neuronal tissue ratio**
Ratto291004	Slice 11	1.973
	Slice 12	2.096
	Slice 13	1.943
	Mean ± σ	2.00 ± 0.08
Ratto251004	Slice 11	1.652
	Slice 12	1.494
	Slice 13	1.319
	Mean ± σ	1.49 ± 0.17

Table 7.1: Tumor-neuronal tissue ratio for three of F98 glioma implanted rats.

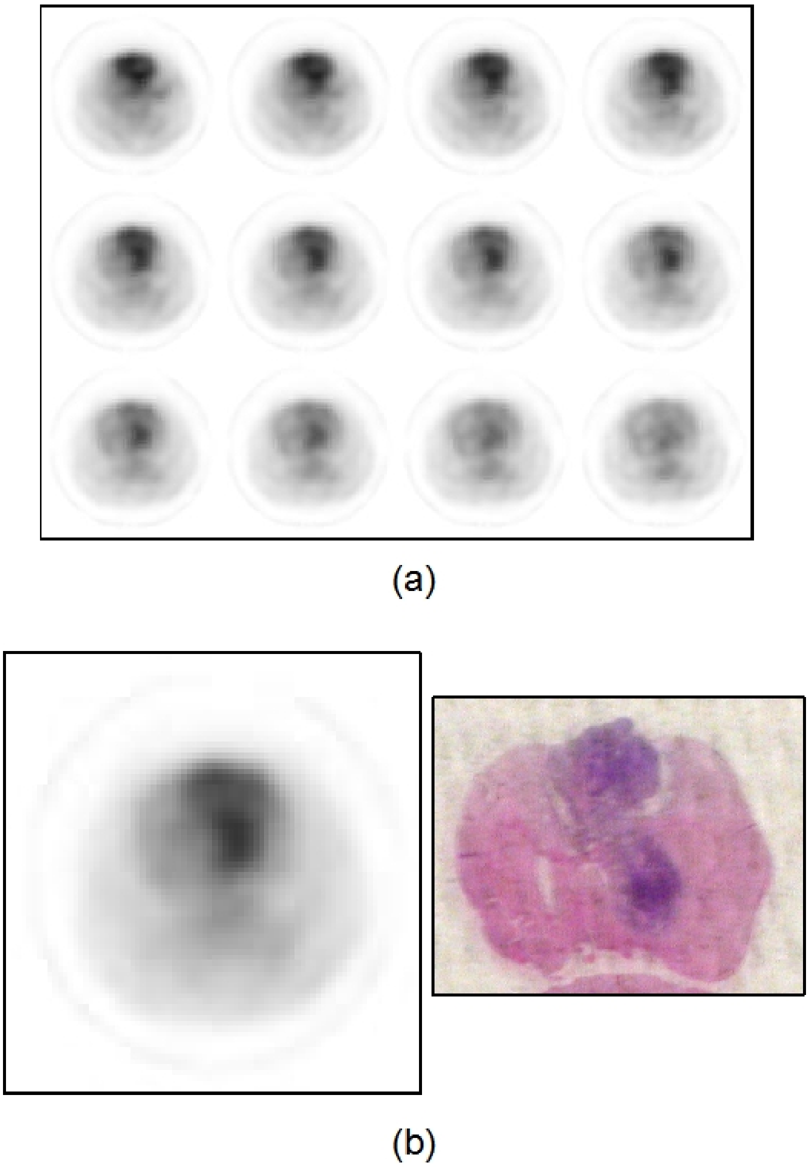

Figure 7.4: (a) The transaxial section of one the rat bearing F98 glioma: the tumor is the blacker spot clearly visible in the central line. (b) Comparison between a transaxial image of the rat bearing F98 glioma obtained with the YAP-(S)PET scanner and an istological section.

7.3.2 SPECT studies: ^{99m}Tc-Annexin V mice model of breast cancer

Breast cancer represents the most common tumor in women with the highest incidence being recorded in western Europe and the USA. During the last two decades, several favorable factors have considerably decreased breast cancer mortality. These factors include early diagnosis, development of new therapeutic strategies, and more reliable monitoring after primary treatment. In general, early disease management includes surgery and adjuvant therapy, combining hormonal therapy, chemotherapy and radiotherapy. Chemotherapy is associated with side effects: nausea, vomiting, alopecia, and hematologic toxicity with the risk of subsequent infections, neurotoxicity (e.g., taxanes), or cardiotoxicity (e.g., anthracyclines). Therefore, in order to avoid ineffective treatment together with unnecessary side effects, a molecular tool to assess the early response to treatment would be very helpful. This line of thought is the basis for the experiments performed in collaboration with the Nuclear Medicine Department of the University of Pisa. These experiments aim at evaluating the degree of apoptosis occurring in tumor tissue as the result of anti-cancer treatment.

Programmed cell death or apoptosis is an essential process for normal development and function of tissue. Tissue homeostasis is achieved by a tight regulation of proliferation, differentiation, and apoptosis. Dysregulation of apoptosis is associated with a variety of diseases, either leading to excessive cell proliferation, e.g., in malignancies, or increased cell death as found in neurodegeneration, tissue ischemia, immunological disorders (e.g., transplant rejection), and autoimmune diseases [5].

The apoptotic signaling cascade is schematically depicted in figure 7.5.

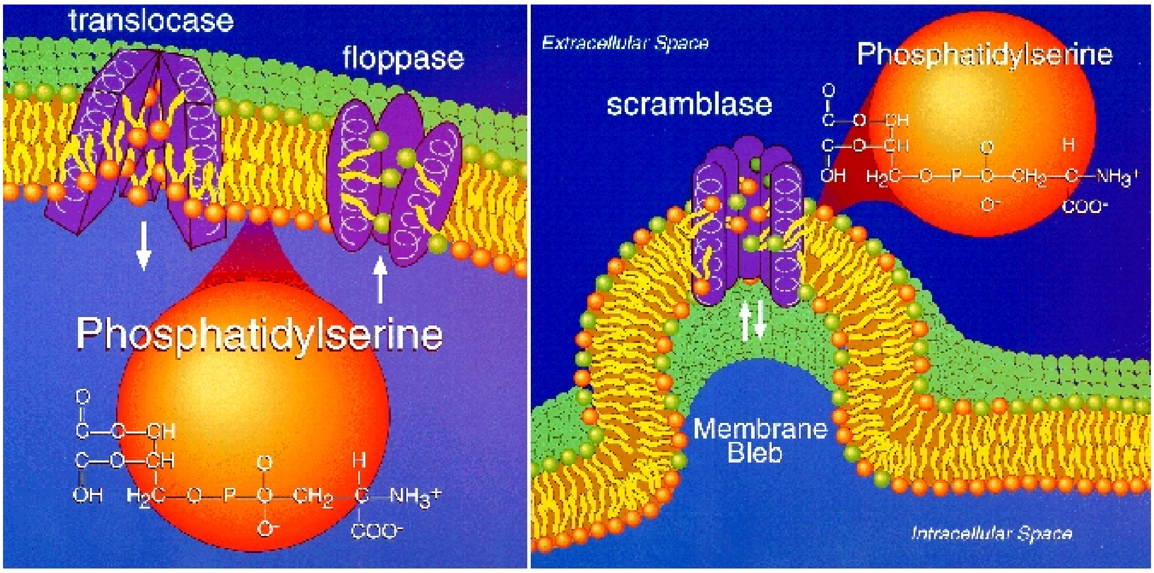

Figure 7.5: Apoptosis Expression of the phosphatidylserine. On the left: normal membrane translocase and floppase activity. On the right: translocase and floppase inactivated, scramblase activated. .

Apoptosis induces characteristic histomorphological changes including cell shrinkage, DNA fragmentation (laddering), nuclear condensation, and membrane-enclosed apoptotic body formation. However, histological analyses require sampling of biopsy material, a severe limitation for a method to be used for clinical diagnosis. Hence, noninvasive methods to assess apoptosis are highly desired and several approaches are currently under development.

Cells undergoing apoptosis redistribute aminophospholipidis that normally are localized at the cytoplasmatic leaflet of the cell membrane to the outer (extracellular) leaflet [177]. These extracellular aminophospholipidis, primarily phosphatidylserine are recognized by phagocytotic cell prompting a signal for cell removal [177–179]. The presence of apoptotic cells is a transient event with a limited time window between the induction of the apoptotic cascade and cell death/removal.

Externalized phosphatidyl-serine moieties are recognized by annexin-V [180, 181], a human protein of molecular weight 36 kDa, to which it binds with high affinity ($\mathrm{p}K_\mathrm{d}$ = 8.15-10). Labeling of the macromolecule Annexin V with radioligands, MRI contrast agents, or fluorescent dyes constitutes an attractive approach for *in vivo* imaging of apoptotic cells. A distinct advantage of using annexin-V as targeting moiety is the fact that its molecular target is located at the extracellular membrane leaflet; hence, no cell penetrating reporter constructs are required. An additional features of Annexin V is its rapid clearance from circulation by the renal system providing a high contrast between the target-specific signal and the nonspecific background.

Blankenberg and co-workers [182] have used the bifunctional linker hydrazinonicotinamide (HYNIC) that forms stable bounds to lysine residues of polypeptides/proteins and conjugates metallic centers such as ^{99m}Tc.

The aim of the experiments was to evaluate drug-induced apoptosis signal after a single dose of chemotherapy. For this purpose, we used mice with spontaneous breast cancer and studied the accumulation pattern of ^{99m}Tc-Annexin V over time after the administration of Paclitaxel (Taxol®). This chemotherapy agent was selected because it is effective in this mouse model used and is often used in patients with breast cancer.

The RIII female mouse represents a model of genetically modified breast cancer induced by a virus (RIII virus, murine mammary tumor virus, MuMTV) which is transmitted from mother to daughter through breast feeding. The effect of Taxol was evaluated at different time points after the drug administration (1, 3, 6 and 24 hours), trying to understand when the highest uptake of ^{99m}Tc-Annexin V, as indicator of Taxol induced apoptosis, occurs.

Human Annexin V, provided by Theseus Imaging Corporation (Boston USA), was produced by expression in Escherichia coli [183]. The recombinant protein was radiolabeled with 740-1110 MBq (about 20-30 mCi) of freshly eluted ^{99m}Tc from a 6 Gb generator (Amersham GE HealthCare, UK) after derivatization with hydrazinonicotinamide (HYNIC) (^{99m}Tc-Annexin V; specific activity, 3.0 MBq/μg protein). Specific activity was 10 to 15 MBq/μg protein (depending on desired activity) with a radiopurity of 85-90 % determined with Sephadex G25 column chromatography instant thin layer chromatography using saline solution as a solvent.

The animals were treated with a single dose of Taxol (0.02 mg/g, about 6mg/animal) administered through intravenous (i.v.) injection in one of the caudal veins. After 1, 3, 6 and 24 hours from Taxol administration, the radioligand was injected i.v. (via tail vein), at the dose of about 37-55 MBq ($\sim$ 1, 1.5 mCi) of ^{99m}Tc-Annexin V (corresponding to about 3.5 μg protein) per mouse. One hour after radiotracer injection the animals were anaesthetized with intraperitoneal injection of a mix of ketamine (60 mg/kg and 4.4 mg/kg) and fenobarbital (50 mg/kg). Once placed on the flat bed (see section 3.1), multiple bed positions were acquired in order to perform a whole body scan. Figure 7.6 and 7.7 highlight ^{99m}Tc-Annexin V uptake in breast cancer sites. The images are visualized with Pmod software [109] and the blue cross-axises are positioned on the tumor signal. These results have been confirmed by phosphor image system (Cyclone Storage Phosphor System, Packard). The maximum uptake has been registered at 3 hours from Taxol administration [184].

7.4 Cardiology studies of a rat model of ischemia and reperfusion

Ischemia is the condition suffered by tissues and organs when deprived of blood flow, mostly the effects of inadequate nutrient and oxygen. Reperfusion injury refers to the tissue damage inflicted when blood flow is restored after an ischemic period. Ischemia

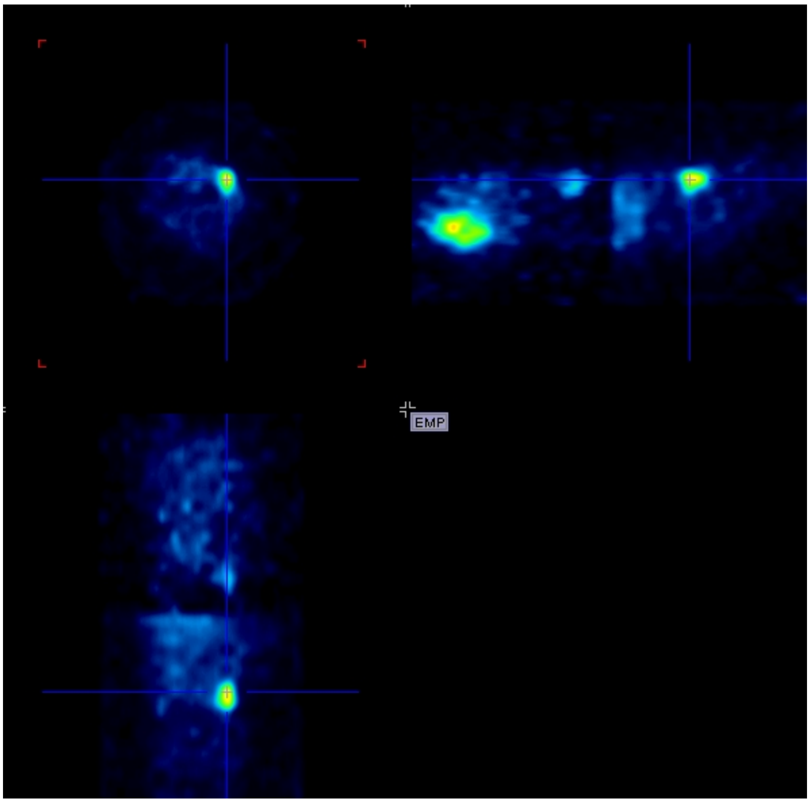

Figure 7.6: Transaxial (top left), coronal (bottom left) and sagittal (top right) section of RIII female mouse PET scans performed with ^{99m}Tc-Annexin V. The uptake in breast cancer sites is highlighted by the blue cross-axises. The images are visualized with Pmod software [109].

and reperfusion can cause serious brain damage in stroke or cardiac arrest.

There is increasing evidence that cell death after myocardial ischemia and reperfusion may begin as apoptosis rather than necrosis [185, 186].

Investigation of the biodistribution and dosimetry of various forms of radiolabeled annexin in humans [187,188] has demonstrated the safety of this agent and the efficacy of imaging for the detection of cardiac transplant rejection and acute myocardial infarction [189, 190].

Among patients with myocardial infarction, there is intense localization in the infarct region both in those with and in those without reperfusion [191]. These data suggest that a considerable number of cells in the infarct zone die by apoptosis. Although the most effective method to limit the zone of injury in areas of markedly decreased perfusion is restoration of blood flow, studies have demonstrated that reperfusion is a major stimulus for apoptosis in previously ischemic tissue, especially in nonsalvageable cells [185, 186]. A current concept is that apoptotic cell death occurs

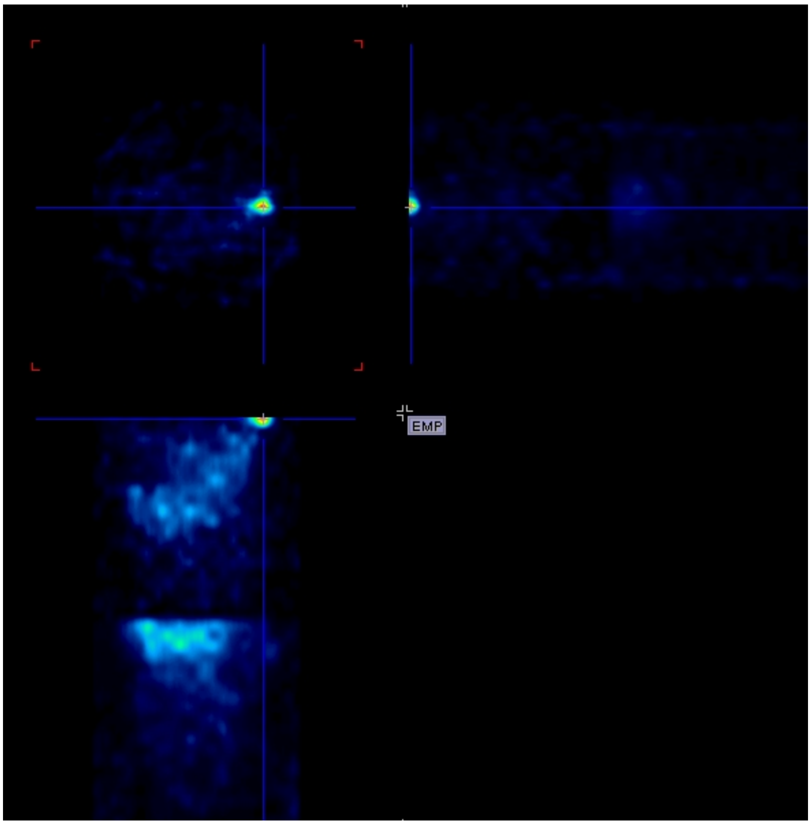

Figure 7.7: Transaxial (top left), coronal (bottom left) and sagittal (top right) section of RIII female mouse PET scans performed with ^{99m}Tc-Annexin V. The uptake in breast cancer sites highlighted by the blue cross-axises is located at the edge of the FOV. The images are displayed with Pmod software [109].

primarily at the periphery of the lesion, rather than in the center. However, the non-salvageable cells should be most abundant at the center of the lesion, where oxygen deprivation should be most prevalent [192].

Cardiovascular research in animals increasingly relies on small animals like rats and mice.

Phenotypic consequences on myocardial function, perfusion, and substrate metabolism in small animals can be evaluated with dedicated MR imaging, CT scan and radionuclide imaging systems.

Small animal emission tomography imaging systems allow noninvasive approach and provide high spatial resolution.

Examination of the heart remains challenging because of its small size, its thin wall, and motion and activity cross-contamination between blood and myocardium [193].

To determine the distribution of apoptosis in myocardial infarction, we performed PET and SPECT studies on rats using the tracer ^{99m}Tc-annexin V as a marker of apoptosis. These experiments were performed in collaboration with with the University of Pisa, Nuclear Medicine Department, group leader Prof. G. Mariani and with Scuola Superiore Sant'Anna, Institute of Clinical Physiology, C.N.R., Pisa, group leader F. Recchia. The evaluation of regional myocardial blood flow was performed with different tracers: ^{99m}Tc-Myoview, ^{99m}Tc-Sestamibi, ^{99m}Tc-Tetrofosmin or ^{13}N-Ammonia.

The ischemia reperfusion heart model was realized on male Sprague Dawley rats (10-12 weeks old). The animals were anesthetized with intraperitoneal injection of 50 mg/kg of sodium pentobarbital and artificially ventilated with room air by an animal respirator. Left thoracotomy at the fifth intercostal space and pericardiotomy were performed. A 6/0 braided silk suture was placed around the proximal portion of the left anterior descending coronary artery, and the coronary artery was occluded for 30 minutes by pulling on the suture. At 30 min after occlusion, the heart was reperfused by releasing the ligature, and the thoracotomy was closed. One hour later, the rats were injected via tail vein with a myocardial blood flow tracer and acquired in PET or SPECT modality according to the used tracer. Immediately after the perfusion acquisition, a tail vein injection of 300 MBq ($\sim$ 8 mCi) of ^{99m}Tc-Annexin V was performed. An acquisition of 1 hour and half was performed after 90 minutes of uptake. The images of blood flow and apoptsosis tracer were reconstructed and then fused in order to rightly localize the apoptosis signal.

Figures 7.8, 7.9, 7.10 show the three main heart axis images as obtained with blood flow tracer (^{99m}Tc-Myoview, ^{13}N-Ammonia or ^{99m}Tc-Tetrofosmin) and apoptosis tracer (first two rows) and the fusion (last row). The fused image allow to exactly localize the apoptosis signal on heart anatomy.

Other studies were performed on the same animal models. Glucose metabolism was evaluated with ^{18}F (see figure 7.11), while ^{99m}Tc-Glucarate was used to asses the presence of necrosis (see figure 7.12). As expected in the ischemia reperfusion model used no necrosis signal is present.

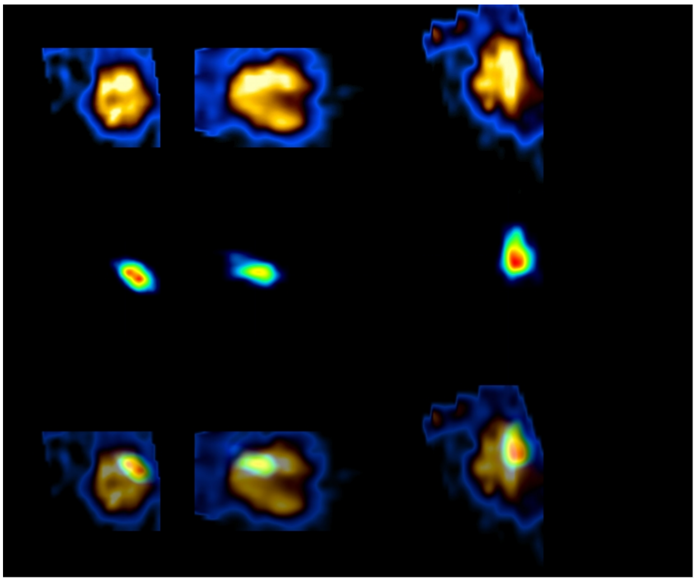

Figure 7.8: Short axis (left column), vertical long axis (center column) and horizontal long axis (right column) of the heart of a male Sprague Dawley rat. Top row: 300 MBq (8 mCi) of ^{99m}Tc-Myoview, uptake time time 180 minutes, acquisition 48 minutes, EM recostruction algorithm with 20 iterations. Central row: 300 MBq (8 mCi) of ^{99m}Tc-Annexin, uptake time 90 minutes, acquisition 1 hour and half, EM recostruction algorithm 20 iterationas. Bottom row: Fusion of the two previous images realized with Pmod software [109].

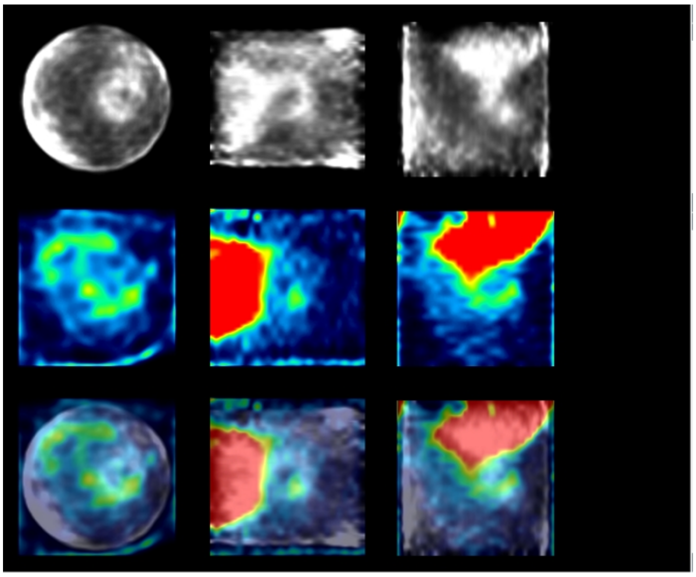

Figure 7.9: Short axis (left column), vertical long axis (center column) and horizontal long axis (right column) of the heart of a male Sprague Dawley rat. Top row: 111 MBq (3 mCi) of ^{13}N-Ammonia, no uptake time, acquisition 20 minutes, EM recostruction algorithm with 20 iterations. Central row: 300 MBq (8 mCi) of ^{99m}Tc-Annexin, uptake time 90 min, acquisition 1 hour and half, EM recostruction algorithm 20 iterationas. Bottom row: Fusion of the two previous images realized with Pmod software [109].

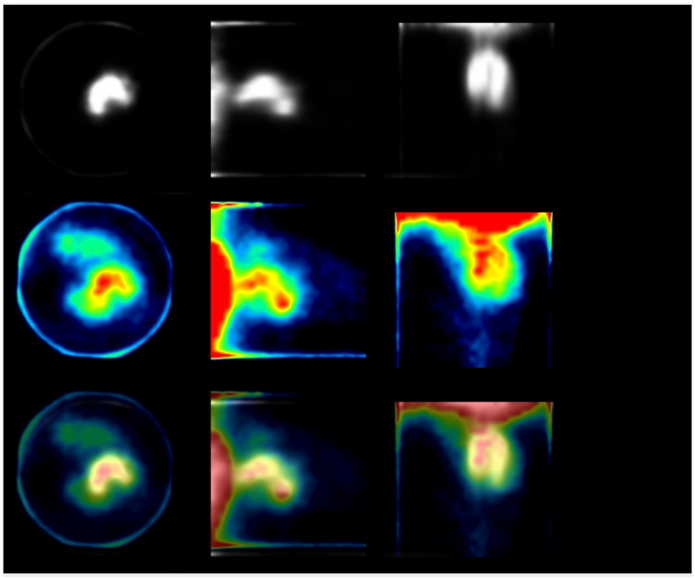

Figure 7.10: Short axis (left column), vertical long axis (center column) and horizontal long axis (right column) of the heart of a male Sprague Dawley rat. Top row: 300 MBq (8 mCi) of ^{99m}Tc-Tetrofosmin, uptake time time 180 minutes, acquisition 48 minutes, EM recostruction algorithm with 20 iterations. Central row: 300 MBq (8 mCi) of ^{99m}Tc-Annexin, uptake time 90 minutes, acquisition 1 hour and half, EM recostruction algorithm 20 iterationas. Bottom row: Fusion of the two previous images realized with Pmod software [109].

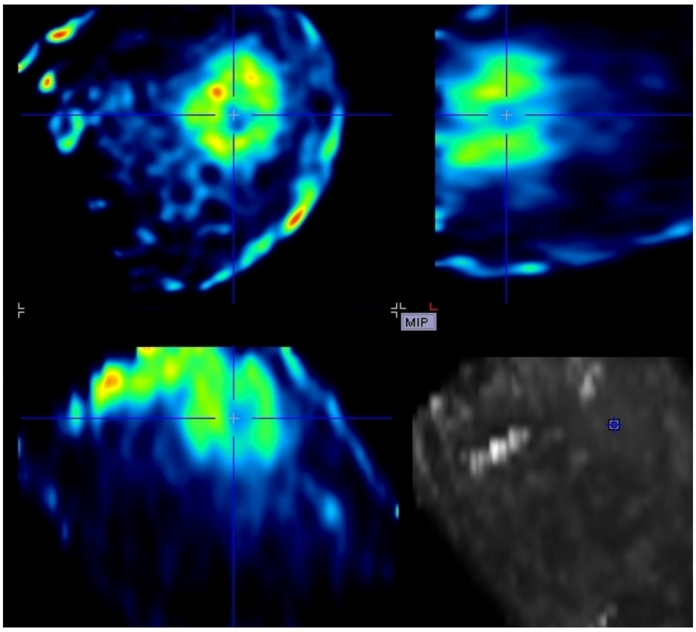

Figure 7.11: Short axis (top left), vertical long axis (bottom left) and horizontal long axis (top right) of the heart of a male Sprague Dawley rat. The uptake of ^{18}F-FDG is highlighted by the blue cross-axises. The images are visualized with Pmod software [109].

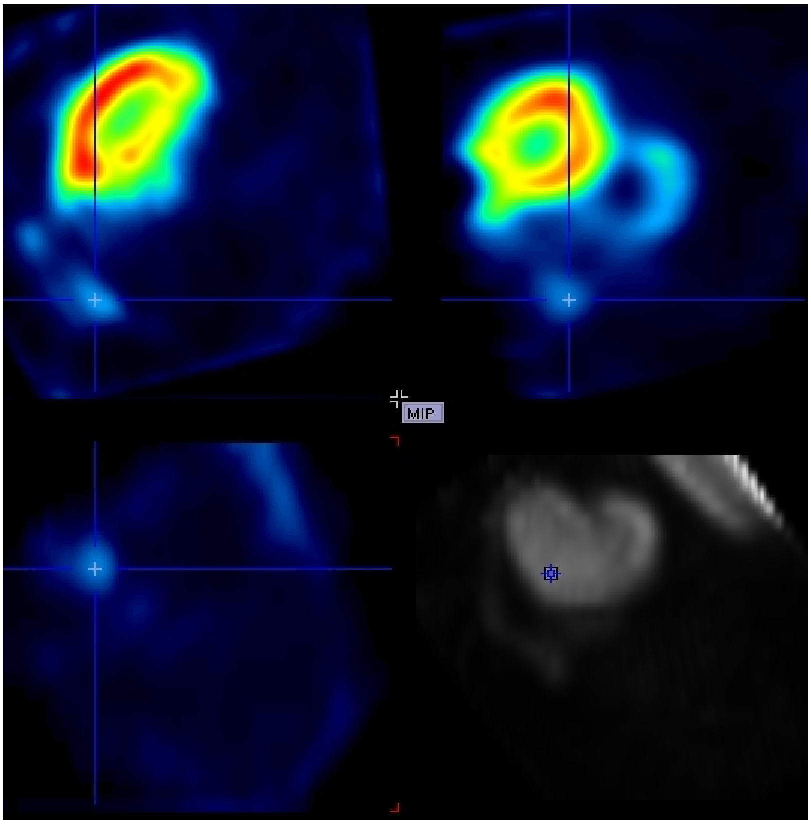

Figure 7.12: Short axis (top left), vertical long axis (bottom left) and horizontal long axis (top right) of the heart of a male Sprague Dawley rat. The uptake of ^{99m}Tc-Glucarate is the rat heart is nearly negligible (blue cross-axises). Clearly appreciable uptake comes from the kidneys, i. e., the execration organs. The images are visualized with Pmod software [109].

Chapter 8

Conclusion

The YAP-(S)PET is a small animal scanner that provide the capability of performing simultaneous PET and SPECT acquisitions on a single gantry [194, 195].

A new version of the scanner has been realized in the first half of 2006 within a collaboration between the Department of Physics of the University of Pisa and the small italian company I.S.E. Ingegneria dei Sistemi Elettronici s.r.l., Pisa, Italy [77]. The following improvements are included in this new version (in the thesis named "27 × 27" version):

- reduction of the YAP crystal pitch down from 2.0 to 1.5 mm to improve both PET and SPECT spatial resolution.
- faster ADCs in order to improve the count rate capabilities;
- a novel electronic pile-up rejection circuitry that allow to improve the image quality. (An application for patent has been filled for this circuit).
- more on-line counters in order to have a complete control of what is going on during the acquisition.

At present, there are only two "27 × 27" version units of the YAP-(S)PET scanner. The research unit is installed at the Institute of Clinical Physiology (IFC) of the National Research Council (C.N.R.) within a cooperative research agreement with the Center of Excellence AmbiSEN of the University of Pisa; while the commercial version has been delivered at the Scientific Institute H S. Raffaele in Milan, Italy, on July 2006.

During this thesis work, the research unit has been calibrated and the performance evaluation in both PET and SPECT modalities were evaluated at different head-to-head distances (100, 125 and 150 mm).

In PET mode the performance has been evaluated following the standards proposed by the PET NEMA task force for small animal scanners [124]. The performance evaluation regards spatial resolution, sensitivity, scatter fraction and count rate.

The spatial resolution was evaluated using a ^{22}Na point source positioned in different radial and axial positions within the FOV. Three components of the spatial resolution (FWHM) were measured for each position: the radial and tangential in the transaxial plane, and the axial component along the axis of the scanner. The radial spatial resolution shows a little improvement as the radial offset increases, while the tangential spatial resolution increases slowly approaching the edge of the FOV. The axial resolution degrades as the source radial offset exceeds 5 mm. The best volume resolution was obtained for 100 mm head-to-head distance and is about 8 μl. The

The maximum sensitivity was registered at the center of the FOV with a 50-850 keV energy window and with a ^{22}Na point source. As expected, the highest valued is reached at 100 mm head-to-head distance, about 3%. The system sensitivity was measured with a linear source of ^{18}F placed inside a metal tubes. The measurement was repeated five times with increasing wall thickness. This measurement confirmed that the sensitivity increases as the head-to-head distance is reduced.

The scatter fraction and NEC curve were evaluated using a mouse-like phantom filled with ^{18}F. Due to greater solid angle covered by the detectors, the scatter fraction is higher for closer head-to-head configuration (100 mm). The activity at which true and NEC count rate reach the peak increases with increasing head-to-head distance. This effect is mainly determined by the reduced sensitivity due to the reduced solid angle coverage with raising detectors separation. The peak NEC rate is about 38 kcps at an activity concentration in the FOV of about 370 kBq/ml. Derenzo, NEMA Image Quality and Defrise phantom were also performed. The NEMA Image Quality phantom was also used to evaluate partial volume effects. For a 4 mm rod, that is object size about $\simeq 2 \times$ FWHM the spatial resolution of the scanner, the activity concentration underestimation is about 20% for 100 head-to-head distances and less than 15% for 125 mm. The better quantification at wider detectors distance is due to lower acceptance angle, thus less parallax error and better spatial resolution.

The evaluation performance results and phantoms studies highlighted that the best compromise between spatial resolution and sensitivity is obtained whit a head-to-head distance of 100 cm.

Since the lack of small animal SPECT performance standardization, the SPECT performance of YAP-(S)PET scanner has been evaluated by rescaling the clinical SPECT NEMA reference standards NU1-1994 [116].

The spatial resolution and sensitivity measurements were evaluated with a glass capillar filled with ^{99m}Tc and positioned parallel to the FOV longitudinal axis with 1 cm radial offset. The radial and tangential resolutions highlighted the system performance degradation for wider detectors distances. This effect is due to collimator resolution R_{coll} dependence on source-to-collimator distance. The spatial resolution is about 2.8 mm at CFOV at 100 mm. The sensitivity is $3.7 \times 10^{-3}\%$ for 140-250 keV energy window.

Also in SPECT modality the best results are obtained for 100 mm head-to-head distance. Due to reduced working space at 100 mm, particularly highlighted in rats experiments, the best compromise between scanner performance and animal experiments is 125 mm for both PET and SPECT modality. On the contrary, mice experiments can better performed at 100 mm head-to-head distance.

Exploiting the YAP-(S)PET scanner intrinsic capability of both PET and SPECT imaging, we have implemented the simultaneous PET/SPECT dual imaging modality. The simultaneous PET/SPECT imaging modality was arranged by equipping two opposing heads the opposing heads 1 and 2 are equipped with the collimators and independently acquire single events (SPECT mode), while the other pair 3-4 detects coincident events (PET mode). In order to reduce the background produced by the Compton scattering of 511 keV gamma rays, each SPECT head (1 and 2) is set in anticoincidence with the opposing one. Since the thickness of the collimator is optimized to stop low energy photons, the crosstalk from 511 keV photons seriously impairs the single photon acquisition. The subtraction procedure we performed was based on a multi-energy window method. The phantoms and animal studies performed open the way to new and interesting protocols for the investigation of many biological phenomena, more effectively than with PET or SPECT modalities alone.

Different animal models and various isotopes and tracers have been used in the experiments performed in collaborations with the different research groups. The main medicine branch we investigated are: oncology, cardiology and neuroscience. PET receptors studies performed in collaborations with Vita-Salute San Raffaele University, Milan, group leader Dr. R. M. Moresco, was related to evaluation of certain areas of the brain degeneration as a consequence of Huntington's disease. The used radiotracer was ^{11}C-Raclopride and male rats were investigated at different time from disease starting.
The SPECT studies concerned the evaluation of Parkinson disease in a new mice model developed by a gene mutation. The ^{123}I-DaTSCAN was the used tracer, and the experiments were performed in collaboration with the Nuclear Medicine Department of the University of Pisa, group leader Prof. G. Mariani.

PET oncologic studies regarded a preclinical model for BNCT therapy and were realized within the collaboration project with Institute of Clinical Physiology of the C.N.R. in Pisa. F98 glioma cells were intracerebral implanted in Wistar male rats than were then subjected to ^{18}F-FDG scanner.
SPECT studies were performed on RIII female mice the represent a model of genetically induced breast cancer. The animals acquisistions were performed with ^{99m}Tc-Annexin V within a collaboration project with the Nuclear Medicine Department of the University of Pisa.

Cardiologic studies was related to a rat model of ischemia and reperfusion. To determine the distribution of apoptosis in myocardial infarction, we performed PET and SPECT studies on rats using the tracer ^{99m}Tc-annexin V as a marker of apoptosis. The evaluation of regional myocardial blood flow was performed with different tracers: ^{99m}Tc-Myoview, ^{99m}Tc-Sestamibi, ^{99m}Tc-Tetrofosmin or ^{13}N-Ammonia. The experiments were performed in collaboration with with the University of Pisa, Nuclear Medicine Department, group leader Prof. G. Mariani and with Scuola Superiore Sant'Anna, Institute of Clinical Physiology, C.N.R., Pisa, group leader F. Recchia.

8.1 Future challenges

8.1.1 Multimodality imaging

PET technology is rapidly advancing Among the most exciting developments is the emergence of combined PET and CT imaging devices The combination of molecular and anatomic imaging has several advantages.

- biologic and anatomic whole-body staging can be performed in one examination.
- because of limited patient motion due to the near simultaneous acquisition of PET and CT images, near ideal fusion of biologic and anatomic images can be achieved.
- anatomic landmarks provided by CT will greatly facilitate the assignment of biological abnormalities to anatomical structures in which disease exists.
- difficult-to-image regions of the body such as head and neck, mediastinum, and the postsurgical abdomen will be evaluated with a high diagnostic accuracy due to improved anatomical assignment of biologically identified disease.

The first commercial PET/CT devices became available for clinical testing in the later part of 2001 ([196]) and small animal imaging systems are now available [197,198].

A prototype of a high resolution CT scanner for small animals was built and tested in our laboratory, and it will be integrated in the YAP-(S)PET in order to realize a multimodal scanner [199]. In the current configuration, the main components of the prototype are: an X-ray source (Hamamatsu 60KVMFX) with tungsten anode, a peak voltage up to 60 kV with maximum power of 10 W, and a focal spot size of 20 μm, a flat panel detector (Radicon Rad-Eye 4) composed of a Ga_2O_2S:Tb layer directly coupled to a CMOS sensor. The active area of the detector is 10 $\times$5 cm^2. The obtained Field of View (FoV) is a cylinder of diameter 5 cm and height 4 cm, with a geometrical magnification varying in the range 1.2-2. Several phantoms and specimen of small animals were acquired in tomographic acquisition and the we are almost ready for the implentantion in the YAP-(S)PET scanner. In the meanwhile, we have performed a proof of principle of the fusion of the images, by acquiring a mice in both PET and CT modalities. The PET acquisition was performed by 30 minutes acquisitions of a healthly mouse inject with 4.6 MBq (about 125 μCi of ^{18}F realized wiht the YAP-(S)PET scanner. The The fusion realized with the PMOD software [109] is represented in figure 8.1.

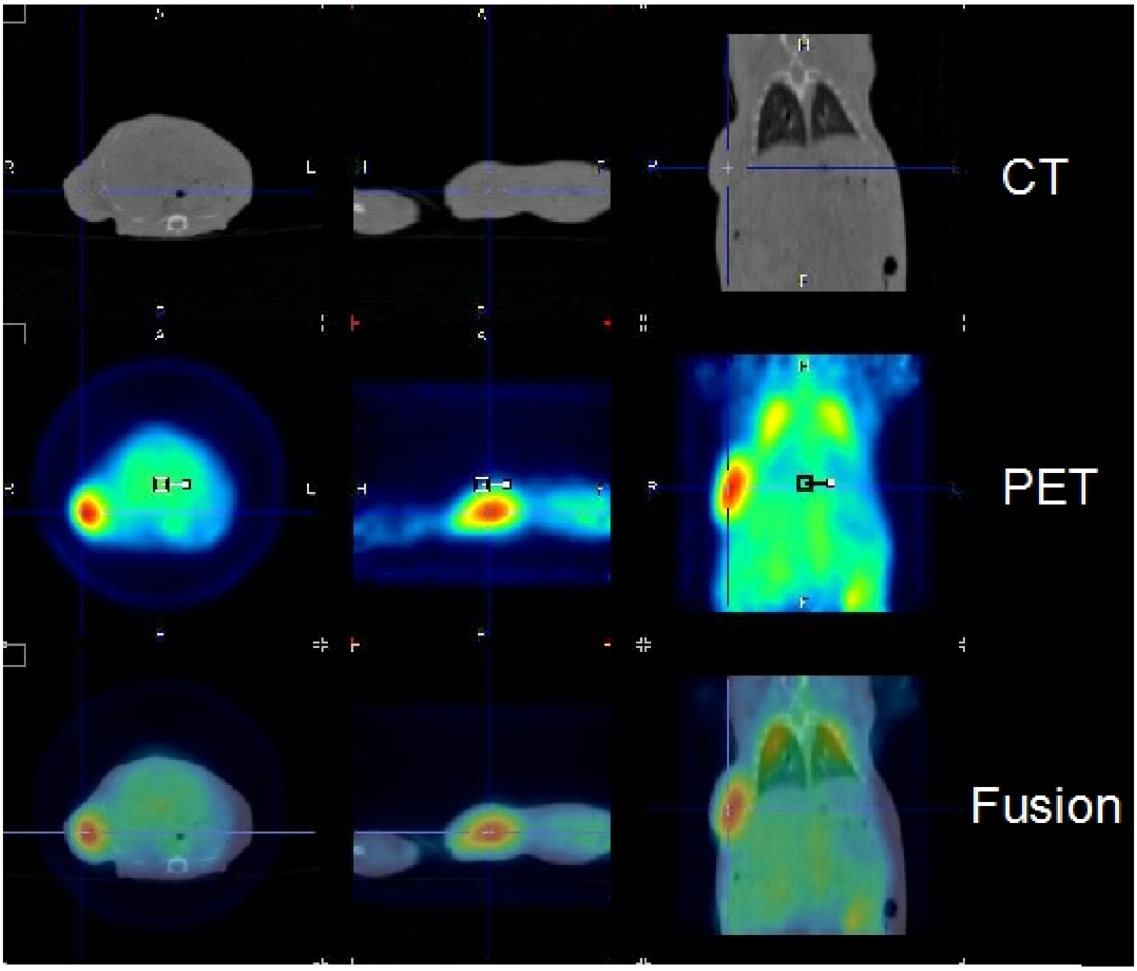

Figure 8.1: Transaxial (left column), sagittal (right column) and coronal (central column) section of a healthly mouse. Top row: CT study performed with a clinical PET/CT scanner (Gemini GXL, Philips). Acquisition time about 30 seconds. Central row: PET acquisition realized wiht the YAP-(S)PET scanner. 30 minutes acquisitions after an uptake time of 45 minutes by the injection of 4.6 MBq (about 125 μCi) of ^{18}F. EM reconstruction algorithm with 50 iterations. Bottom row: Fusion of the two previous images realized with Pmod software [109].

8.1.2 New photomultipliers

The development of novel photodetectors has a fundamental role for the future of nuclear imaging. The possible solutions proposed by various research groups have a two fold approach. On the one hand, systems overcoming the coding limitation have been introduced through APD based solutions (one-to-one coupling) [200]. On the other, detectors based on a scintillator block coupled to high granularity position-sensitive photodetectors (Anger camera principle) are under development [201]. In the latter case, the limitation introduced by the finite size of the crystal elements could be overcome by measuring, with high precision, the center of gravity of the light spot.

The Silicon Photomultiplier (SiPM) we are developing is a silicon diode detector that shows great promise as a photodetector for scintillators for both one-to-one or Anger camera approaches. The development of these devices started about 15 years ago at MEPHI (Moscow, Russia) [202] and has seen significant technological progress, in particularly in recent years. In summary, the SiPM is a densely packed matrix of small, Geiger-mode avalanche photodiode (GAPD) cells (typically 40 $\times 40$ mm^2), with individual quenching resistances for each cell. The Geiger-mode operation of each cell produces a large gain (of the order of 5 $\times 10^5$) at low bias voltage (50 V). All the cell outputs are then connected in parallel to produce the summed signal. This microcell structure of the SiPM gives a proportional output for moderate photon flux. The performance is in many ways comparable to that of a conventional PMT, but with the compactness and other benefits of a semiconductor detector. Such a compact silicon detector is well disposed for being developed into a close-packed array in order to have a position-sensitive detection surface, and this justifies the wide interest and the great efforts dedicated to the SiPM development. For example, a new camera design has been proposed by the Department of Physics, University of Pisa [203] . The proposed camera consists of a stack of three modular layers, each being relatively thin, continuous slab of LSO (or LYSO) scintillator viewed by an array of compact of 1mm^2 active area SiPM detector elements on a 1.5mm pitch. To provide sufficient detection efficiency as well as intrinsic DOI information, three of these modular layers are stacked together to form a single detector head. From Monte Carlo simulations the new detector heads is expected to show excellent performance in intrinsic spatial resolution (down to 0.5mm FWHM) [203].

Bibliography

[1] T. F.Massoud and S. S.Gambhir. “Molecular imaging in living subjects: seeing fundamental biological processes in a new light”. *Genes and development*, **17**, p. 545, 2003.

[2] S. R. Cherry, J. A. Sorenson, and M. E. Phelps. *Physics in Nuclear Medicine*. Saunders, Third edition, 2003.

[3] Meyers R. “ The biological application of small animal PET imaging”. *Nucl. Med. Biol.*, **28**, p. 585, 2000.

[4] M. E. Phelps. “PET: The Merging of Biology and Imaging into Molecular Imaging”. *J. Nucl. Med.*, **41**, p. 661, 2000.

[5] M. Rudin. *Molecular Imaging - Basic principles and applications in bionedical research*. Imperial College Press, 2005.

[6] S. R. Cherry. “In vivo molecular and genomic imaging: new challenges for imaging physics”. *Phys. Med. Biol.*, **49**, p. R13, 2004.

[7] D. Malakoff. “The rise of the mouse, biomedicine’s model mammal”. *Science*, **288**, p. 248, 2000.

[8] J. H. Nadeau et al. “Sequence interpretation: functional annotation of mouse genome sequences”. *Science*, **291**, p. 1251, 2001.

[9] E. Pennisi. “GENOMICS: Mouse Genome Added to Sequencing Effort”. *Science*, **286**, p. 210, 1999.

[10] A. F. Chatziioannou. “Molecular imaging of small animals with dedicated PET tomographs”. *Eur. J. Nucl. Med.*, **29**, p. 98, 2002.

[11] R. Weissleder and U. Mahmood. “Molecular Imaging”. *Radiology*, **219**, p. 316, 2001.

[12] V. Sossi and T. J. Ruth. “Micropet imaging: in vivo biochemistry in small animals”. *J. Neural Transm.*, **112**, p. 319, 2005.

[13] P. J. Early. “Use of diagnostic radionuclides in medicine”. *Health Phys.*, **69**, p. 649, 1995.

[14] M. J. Welch and C. S. Redvanly. *Handbook of Radiopharmaceuticals*. New York: Wiley, 2002.

[15] Y. Charon, P. Laniece, and H. Tricoire. “Radio-imaging for quantitative autoradiography in biology”. *Nucl. Med. Biol.*, **25**, p. 699, 1998.

[16] D. Weber and M. Ivanovic. “Ultra-high-resolution imaging of small animals: implications for preclinical and research studies”. *J. Nucl. Cardiol.*, **6**, p. 1999, 332.

[17] S.R. Cherry and S.S. Gambhir. “Use of Positron Emission Tomography in Animal Reserach”. *ILAR journal*, **42**, p. 219, 2001.

[18] B. Chance. “Near-infrared images using continuous, phase-modulated, and pulsed light with quantitation of blood and blood oxygenation”. *Ann. New York Acad. Sci.*, **838**, p. 29, 1998.

[19] B. W. Rice, M. D. Cable, and M. B. Nelson. “In vivo imaging of light-emitting probes”. *J. Biomed. Opt.*, **6**, p. 432, 2001.

[20] V. Ntziachristos, C. Bremer, and R. Weissleder. “Fluorescence imaging with near-infrared light: new technological advances that enable in vivo molecular imaging”. *Eur. Radiol.*, **13**, p. 195, 2003.

[21] C. H. Contag and M. H. Bachmann. “Advances in in vivo bioluminescence imaging of gene expression”. *Annu. Rev. Biomed. Eng.*, **4**, p. 235, 2002.

[22] M. Yang, Baranov. E., A. R. Moossa, S. Penman, and R. M. Hoffman. “Visualizing gene expression by whole-body fluorescence imaging”. *Proc. Nat. Acad. Sci. USA*, **97**, p. 12278, 2000.

[23] R. Y. Tsien. “The green fluorescent protein”. *Annu. Rev. Biochem.*, **67**, p. 509, 1998.

[24] M. V. Matz, A. F. Fradkov, Y. A. Labas, A. P. Savitsky, Zaraisky. A. G., M. L. Markelov, and S. A. Lukyanov. “Fluorescent proteins from nonbioluminescent anthozoa species”. *Nat. Biotechnol.*, **17**, p. 969, 1999.

[25] R. E. Campbell, O. Tour, A. E. Palmer, P. A. Steinbach, G. S. Baird, D. A. Zacharias, and R. Y. Tsien. “A monomeric red fluorescent protein”. *Proc. Nat. Acad. Sci. USA*, **99**, p. 7877, 2002.

[26] C. Bremer, V. Ntziachristos, and R. Weissleder. “Optical-based molecular imaging: contrast agents and potential medical applications”. *Eur. Radiol.*, **13**, p. 231, 2003.

[27] R. Weissleder, C H Tung, U Mahmood, and A. Bogdanov. “In vivo imaging of tumors with protease-activated near-infrared fluorescent probes”. *Nat. Biotechnol.*, **71**, p. 375, 1999.

[28] L. F. Greer and A. A. Szalay. “Imaging of light emission from the expression of luciferases in living cells and organisms: a review”. *Luminescence*, **17**, p. 43, 2002.

[29] P. R. Contag, I. N. Olomu, D. K. Stevenson, and C. H. Contag. “Bioluminescent indicators in living mammals”. *Nat. Med.*, **4**, p. 245, 1998.

[30] H. Benveniste and S. Blackband. “MR microscopy and high resolution small animal MRI: applications in neuroscience research”. *Prog. Neurobiol.*, **67**, p. 393, 2002.

[31] R. E. Jacobs and S. R. Cherry. “Complementary emerging techniques: high-resolution PET and MRI”. *Curr. Opin. Neurobiol.*, **11**, p. 621, 2001.

[32] R. E. Jacobs, E. T. Ahrens, T. J. Meade, and S. E. Fraser. “Looking deeper into vertebrate development”. *Trends Cell. Biol.*, **9**, p. 73, 1999.

[33] B. L. Beck and S. J. Blackband. “Phased array imaging on a 4.7 T/33 cm animal research system”. *Rev. Sci. Instrum.*, **72**, p. 4292, 2002.

[34] L. W. Hedlund, G. P. Cofer, S. J. Owen, and G. A. Johnson. “MR-compatible ventilator for small animals: computercontrolled ventilation for proton and noble gas imaging”. *Magn. Reson. Imaging*, **18**, p. 753, 2000.

[35] R. G. Pautler, A. C. Silva, and A. P. Koretsky. “In vivo neuronal tract tracing using manganese-enhanced magnetic resonance imaging”. *Magn. Reson. Med.*, **40**, p. 740, 1998.

[36] S. Aime, C. Cabella, S. Colombatto, S. G. Crich, E. Gianolio, and F. Maggioni. “Insights into the use of paramagnetic Gd(III) complexes in MR-molecular imaging investigations”. *J. Magn. Reson. Imaging*, **16**, p. 394, 2002.

[37] E. L. Ritman. “Molecular imaging in small animalsroles for micro-CT”. *J. Cell. Biochem.*, **87**, p. 116, 2002.

[38] M. J. Paulus, S. S. Gleason, S. J. Kennel, P. R. Hunsicker, and D. K. Johnson. “High resolution x-ray computed tomography: an emerging tool for small animal cancer research”. *Neoplasia*, **2**, p. 62, 2000.

[39] M. J. Paulus et al. “High-resolution X-ray CT screening of mutant mouse models”. *Optical Diagnostics of Living Cells III*, **(San Jose, CA: SPIE)**, p. 270, 2000.

[40] M. J. Flynn, S. M. Hames, D. A. Reimann, and S. J. Wilderman. “Microfocus x-ray sources for 3D microtomography”. *Nucl. Instr. and Meth. Phys. Res.*, **A 353**, p. 312, 1994.

[41] D. H. Turnbull. “In utero ultrasound backscatter microscopy of early stage mouse embryos”. *Comput. Cereb. Imag. Graph.*, **23**, p. 25, 1999.

[42] A. Stith, B. G. Zagar, R. Fournaris, and K. Ferrara. “3D ultrasonic mapping of the microvasculature”. *IEEE Ultrason Symp. Proc.*, **2**, p. 1473, 1996.

[43] G. M. Lanza and S. A. Wickline. “Targeted ultrasonic contrast agents for molecular imaging and therapy”. *Prog. Cardiovasc. Dis.*, **44**, p. 13, 2001.

[44] P. A. Dayton and K. W. Ferrara. “Targeted imaging using ultrasound”. *J. Magn. Reson. Imaging*, **16**, p. 362, 2002.

[45] F. S. Foster et al. “A new ultrasound instrument for in vivo microimaging of mice”. *Ultrasound Med. Biol.*, **28**, p. 1165, 2002.

[46] U. Mahmood and R. Weissleder. “Some tools for molecular imaging”. *Acad. Radiol.*, **9**, p. 629, 2002.

[47] B. J. Druker et al. “Effects of a selective inhibitor of the Abl tyrosine kinase on the growth of Bcr-Abl positive cells”. *Nat. Med.*, **2**, p. 561, 1996.

[48] H. I. Kornblum, Araujo D. M., A. J. Annala, K. J. Tatsukawa, ME Phelps, and S. R. Cherry. “In vivo imaging of neuronal activation and plasticity in the rat brain with microPET, a novel high-resolution positron emission tomograph”. *Nat. Biotechnol.*, **18**, p. 655, 2000.

[49] T. H. Moore, T. L. Osteen, T. F. Chatziioannou, D. A. Hovda, and S. R. Cherry. “Quantitative assessment of longitudinal metabolic changes in vivo after traumatic brain injury in the adult rat using FDG-microPET”. *J. Cereb. Blood Flow Metab.*, **20**, p. 1492, 2000.

[50] Y. Kuge, Y. Miyake, K. Minematsu, T. Yamaguchi, and Y. Hasegawa. “Effects of extracranial radioactivity on measurement of cerebral glucose metabolism by rat-PET with ^{18}F-2-fluoro-2-deoxy-D-glucose”. *J. Cereb. Blood Flow Metab.*, **[letter; comment]**, **17**, p. 1261, 1997.

[51] A. J. Morguet, A. F. Chatziioannou, S. R. Cherry, M. E. Phelps, and H. R. Schelbert. “Evaluation of a newly developed small-animal PET scanner in experimental myocardial infarction”. *J. Nucl. Med.*, **39**, p. 9P, 1998.

[52] T. Kudo, A. J. Annala, S. R. Cherry, M. E. Phelps, and H. R. Schelbert. “Measurement of myocardial blood flow during occlusion/reperfusion in rats with dynamic microPET imaging”. *J. Nucl. Med.*, **40**, p. 6P, 1999.

[53] M. D. Lapointe Bentourkia, J. Cadorette, S. Rodrique, R. Ouellet, F. Benard, J. E. Van Lier, and R. Lecomte. “High-resolution cardiac PET in rats”. *J. Nucl. Med.*, **40**, p. 185P, 1999.

[54] T. Higuchi, S. G. Nekolla, A. Jankaukas, A. W. Weber, M. C. Huisman, S. Reder, S. I. Ziegler, M. Schwaiger, and F. M. Bengel. “Characterization of Normal and Infarcted Rat Myocardium Using a Combination of Small-Animal PET and Clinical MRI”. *J. Nucl. Med.*, **48**, p. 288, 2007.

[55] S. P. Hume, A. A. Lammertsma, R. Myers, S. Rajeswaran, P. M. Bloomfield, S. Ashworth, R. A. Fricker, E. M. Torres, I. Watson, and T. Jones. “The potential of high-resolution positron emission tomography to monitor striatal dopaminergic function in rat models of disease.”. *J. Neurosci. Methods*, **67**, p. 103, 1996.

[56] S. P. Hume, J. Opacka-Juffry, R. Myers, R. G. Ahier, S. Ashworth, D. J. Brooks, and A. A. Lammertsma. “Effect of L-dopa and 6-hydroxydopamine lesioning on ^{11}C-raclopride binding in rat striatum, quantified using PET”. *Synapse*, **21**, p. 45, 1995.

[57] R. A. Fricker, E. M. Torres, S. P. Hume, R. Myers, J. Opacka-Juffrey, S. Ashworth, D. J. Brooks, and S. B. Dunnett. “The effects of donor stage on the survival and function of embryonic striatal grafts in the adult rat brain. II. Correlation between positron emission tomography and reaching behaviour”. *Neuroscience*, **79**, p. 711, 1997.

[58] A. L. Brownell, E. Livni, W. Galpern, and O. Isacson. “In vivo PET imaging in rat of dopamine terminals reveals functional neural transplants”. *Ann. Neurol.*, **43**, p. 387, 1998.

[59] E. M. Torres, R. A. Fricker, S. P. Hume, R. Myers, J. Opacka-Juffry, S. Ashworth, D. J. Brooks, and S. B. Dunnett. “Assessment of striatal graft viability in the rat in vivo using a small diameter PET scanner”. *Neuroreport*, **6**, p. 2017, 1995.

[60] H. Tsukada, J. Kreuter, C. E. Maggos, E. M. Unterwald, T. Kakiuchi, S. Nishiyama, M. Futatsubashi, and M. J. Kreek. “Effects of binge pattern cocaine administration on dopamine D1 and D2 receptors in the rat brain: an in vivo study using positron emission tomography”. *J. Neurosci.*, **16**, p. 7670, 1996.

[61] E. M. Unterwald, H. Tsukada, T. Kakiuchi, T. Kosugi, S. Nishiyama, and M. J. Kreek. “Use of positron emission tomography to measure the effects of nalmefene on D1 and D2 dopamine receptors in rat brain”. *Brain Res.*, **775**, p. 183, 1997.

[62] A. F. Shields, J. R. Grierson, B. M. Dohmen, H. J. Machulla, J. C. Stayanoff, J. M. Lawhorn-Crews, J. E. Obradovich, O. Muzik, and T. J. Mangner. “Imaging proliferation in vivo with [F-18]FLT and positron emission tomography”. *Nat. Med.*, **4**, p. 1334, 1998.

[63] A. M. Wu, P. J. Yazaki, S. Tsai, K. Nguyen, A. L. Anderson, D. W. McCarthy, M. J. Welch, J. E. Shively, L. E. Williams, A. A. Raubitschek, J. Y. Wong, T. Toyokuni, M. E. Phelps, and S. S. Gambhir. “High-resolution microPET imaging of carcinoembryonic antigen- positive xenografts by using a copper-64-labeled engineered antibody fragment”. *Proc. Nat. Acad. Sci. USA*, **97**, p. 8495, 2000.

[64] G. Sundaresan, P. J. Yazaki, J. E. Shively, T. Toyokuni, K. Nguyen, R. Finn, S. M. Larson, A. A. Raubitschek, S. S. Gambhir, and A. M. Wu. “I-124 radiolabeled genetically engineered anti-CEA antibody fragments for tumor imaging with microPET”. , page 42P, 2001.

[65] S. Dhandayuthapani, L. E. Via, C. A. Thomas, P. M. Horowitz, D. Deretic, and V. Deretic. “Green fluorescent protein as a marker for gene expression and cell biology of mycobacterial interactions with macrophages”. *Mol. Microbiol.*, **17**, p. 901, 1995.

[66] S. S. Gambhir, H. R. Herschman, S. R. Cherry, J. R. Barrio, N. Satyamurthy, T. Toyokuni, Phelps. M. E., S. M. Larson, J. Balatoni, R. Finn, M. Sadelain,

J. Tjuvajev, and R. Blasberg. “Imaging transgene expression with radionuclide imaging technologies”. *Neoplasia*, **2**, p. 118, 2000.

[67] S. S. Gambhir, J. R. Barrio, H. R. Herschman, and M. E. Phelps. “Imaging gene expression: principles and assays”. *J. Nucl. Cardiol.*, **6**, p. 219, 1999.

[68] S. S. Gambhir, J. R. Barrio, H. R. Herschman, and M. E. Phelps. “Assays for noninvasive imaging of reporter gene expression”. *Nucl. Med. Biol.*, **26**, p. 481, 1999.

[69] J. G. Tjuvajev, N. Avril, T. Oku, T. Sasajima, T. Miyagawa, R. Joshi, M. Safer, B. Beattie, G. DiResta, F. Daghighian, F. Augensen, J. Koutcher, J. Zweit, J. Humm, S. M. Larson, R. Finn, and R. Blasberg. “Imaging herpes virus thymidine kinase gene transfer and expression by positron emission tomography”. *Cancer. Res.*, **58**, p. 4333, 1998.

[70] D. C. MacLaren, S. S. Gambhir, N. Satyamurthy, J. R. Barrio, S. Sharfstein, T. Toyokuni, L. Wu, A. J. Berk, S. R. Cherry, M. E. Phelps, and H. R. Herschman. “Repetitive, non-invasive imaging of the dopamine D_2 receptor as a reporter gene in living animals”. *Gene Therapy*, **6**, p. 785, 1999.

[71] P. Ray, E. Bauer, M. Iyer, J. R. Barrio, N. Satyamurthy, M. E. Phelps, H. R. Herschman, and S. S. Gambhir. “Monitoring gene therapy with reporter gene imaging”. *Semin. Nucl. Med.*, **31**, p. 312, 2001.

[72] S. S. Gambhir, E. Bauer, M. E. Black, Q. Liang, M. S. Kokoris, J. R. Barrio, M. Iyer, M. Namavari, M. E. Phelps, and H. R. Herschman. “A mutant herpes simplex virus type 1 thymidine kinase reporter gene shows improved sensitivity for imaging reporter gene expression with positron emission tomography”. *Proc. Nat. Acad. Sci. USA*, **97**, p. 2785, 2000.

[73] L. A. Green, C. Yap, K. Nguyen, J. R. Barrio, M. Namavari, N. Satyamurthy, M. E. Phelps, E. P. Sandgren, H. R. Herschman, and S. S. Gambhir. “Indirect monitoring of endogenous gene expression by PET imaging of reporter gene expression in transgenic mice”. *Mol. Imaging. Biol.*, **4**, p. 71, 2002.

[74] M. Iyer, J. R. Barrio, M. Namavari, E. Bauer, N. Satyamurthy, K. Nguyen, T. Toyokuni, M. E. Phelps, H. R. Herschman, and S. S. Gambhir. "8-[^{18}F]Fluoropenciclovir: an improved reporter probe for imaging HSV1-tk reporter gene expression in vivo using PET". *J. Nucl. Med.*, **42**, p. 96, 2001.

[75] A. Del Guerra, G. Di Domenico, M. Scandola, and G. Zavattini. "High spatial resolution small animal YAP-PET". *Nucl. Instr. and Meth. Phys. Res.*, **A409**, p. 537, 1998.

[76] A. Del Guerra, C. Damiani, G. Di Domenico, A. Motta, M. Giganti, R. Marchesini, A. Piffanelli, N. Sabba, L. Sartori, and G. Zavattini. "An Integrated PET-SPECT Small Animal Imager: preliminary results". *IEEE Trans. Nucl. Sci.*, **47**, p. 1537, 2000.

[77] website, http://www.ise-srl.com/YAPPET/YAP-PET.htm.

[78] website, http://www.crytur.com.

[79] C.A. Burnham, D.E. Kaufman, D.A. Chesler, C.W. Stearns, J.A. Correia, and G.L. Brownell. "A low-Z PET detector". *IEEE Trans. Nucl. Sci.*, **37**, p. 832, 1990.

[80] P. Lecoq and M. Korzhik. "New inorganic scintillation materials development for medical imaging". *IEEE Trans. Nucl. Sci.*, **4**, p. 1651, 2002.

[81] S. I. Ziegler, J. G. Rogers, V. Selivanov, and I. Sinitzin. "Characteristics of the New YAl0,:Ce Compared with BGO and GSO". *IEEE Trans. Nucl. Sci.*, **40**, p. 194, 1993.

[82] J.A. MacIntyre. "Plastic Scintillation Detector for High Resolution Emission Computed Tomography". , page 351, 1980.

[83] S. Baccaro, K. Blazek, F. de Notaristefano, P. Maly, J.A. Mares, R. Pani, R. Pellegrini, and A. Soluri. "Scintillation properties of YAP:Ce". *Nucl. Instr. and Meth. Phys. Res.*, **A361**, p. 209, 1995.

[84] G. Zavattini, A. Del Guerra, N. Cesca, G. Di Domenico, M. Gambaccini, E. Moretti, and N. Sabba. “High Z and Medium Z Scintillators in Ultra High Resolution Small Animal PET”. *IEEE Trans. Nucl. Sci.*, **52**, p. 222, 2005.

[85] Angela Vaiano. . 2004. Speciality school of Medical Physics Thesis, University of Pisa, unpublished.

[86] G. Di Domenico, G. Zavattini, E. Moretti, A. Piffanelli, M. Giganti, A. Motta, N. Sabba, L. Uccelli, E. Benini, A. Duatti, C. Bolzati, A. Boschi, and A. Del Guerra. “YAP-(S)PET Small Animal Scanner: Quantitative Results”. *IEEE Trans. Nucl. Sci.*, **50**, p. 1351, 2003.

[87] H. Kume, S. Suzuki, J. Takeuchi, and K. Oba. “Newly developed photomultiplier tubes with position sensitivity capability”. *IEEE Trans. Nucl. Sci.*, **32**, p. 448, 1985.

[88] http://jp.hamamatsu.com/resources/products/etd/pdf/R2486_TPMH1206E02.pdf.

[89] L.H. Barone, K. Blazek, D. Bollini, A. Del Guerra, F. De Notaristefani, G. De Vincentis, G. Di Domenico, M. Galli, M. Giganti, P. Maly, R. Pani, A. Pellegrini, R. Pergola, A. Piffanelli, F. Scopinaro, A. Soluri, and F. Vittori. “Toward a nuclear medicine with sub-millimiter spatial resolution". *Nucl. Instr. and Meth. Phys. Res.*, **A360**, p. 302, 1995.

[90] A. Del Guerra. *Ionizing radiation detectors for medical imaging.* Chapter 10, World scientific, 2004.

[91] S. Webb. *The physics of medical imaging.* Chapter 6, Institute of Physics Publishing, 1988.

[92] P. E. Kinahan and J. G. Rogers. “Analytic 3D recosntruction using all detected events”. *IEEE Trans. Nucl. Sci.*, **36**, p. 964, 1989.

[93] M. Defrise, P. E. Kinahan, and D. W. Townsend. “Exact and Approximate Rebinning Algorithms for 3-D PET Data”. *IEEE Trans. Med. Imag.*, **16**, p. 145, 1997.

[94] M. E. Daube-Witherspoon and G. Muelhlehner. "Treatment of axial data in three-dimensional PET". *J. Nucl. Med.*, **28**, p. 1717, 1987.

[95] M.E. Phelps. *PET- Molecular imaging and its biological applications.* Springer, 2004.

[96] J.S. S. Matejy, Karp, R.M. Lewitt, and A. J. Becher. "Performance of the Fourier rebinning algorithm for PET with large acceptance angles". *Phys. Med. Biol.*, **43**, p. 787, 1998.

[97] G.N. Ramachandran and A.V. Lakshminarayanan. "Three dimensional reconstructions from radiographs and electron micrographs: Application of convolution transforms". *Proc. Nat. Acad. Sci. USA*, **68**, p. 2236, 1971.

[98] L.A. Shepp and B.F. Logan. "The Fourier reconstruction of a head section". *IEEE Trans. Nucl. Sci.*, **21**, p. 21, 1974.

[99] G. Di Domenico and G. Zavattini. .

[100] L. Shepp and Y. Vardi. "Maximum Likelihood Reconstruction for Emission Tomography". *IEEE Trans. Med. Imag.*, **16**, p. 113, 1982.

[101] C. A. Motta, Damiani, A. Del Guerra, G. Di Domenico, and G. Zavattini. "Use of a fast EM algorithm for 3D image reconstruction with the YAPPET tomograph". *Comput. Cereb. Imag. Graph.*, **26**, p. 293, 2002.

[102] A. Alessio and P. Kinahan. *PET Image Reconstruction, in Nuclear Medicine (2nd ed.). Henkin et al.* Eds., Philadelphia, Elsevier, 2006.

[103] H. M. Hudson and R. S. Larkin. "Accelerated image reconstruction using ordered subsets of projection data". *IEEE Trans. Med. Imag.*, **13**, p. 601, 1994.

[104] S. Moehrs, M. Defrise, N. Belcari, and A. Del Guerra. . Presented at 9th International Meeting on Fully Three-Dimensional Image Reconstruction in Radiology and Nuclear Medicine July 9 - 13, 2007, Lindau, Germany.

[105] M. P. Mildenberger, Eichelberg and E. Martin. "Introduction to the DICOM standard". *Eur. Radiol.*, **12**, p. 920, 2002.

[106] website, http://rsb.info.nih.gov/ij/index.html.

[107] website, http://www.nih.gov/.

[108] website, http://amide.sourceforge.net/.

[109] website, http://www.pmod.com/.

[110] P. H. Murphy. “Acceptance Testing and Quality Control of Gamma Cameras, Including SPECT”. *J. Nucl. Med.*, **28**, p. 1221, 1987.

[111] E. J. Hoffman, T. M. Guerrero, G. Germano, W. M. Digby, and M. Dalbom. “PET system calibrations and corrections for quantitative and spatially accurate iamges”. *IEEE Trans. Nucl. Sci.*, **36**, p. 1108, 1989.

[112] R. D. Badawi, M. A. Lodge, and P. K. Marsden. “Algorithms for calculating detector efficiency normalization coefficients for true coincidences in 3D PET”. *Phys. Med. Biol.*, **43**, p. 189, 1998.

[113] M. Defrise, D. W. Townsend, D. Bailey, A . Geissbuhler, C. Michell, and T. Jones. “A normalization technique for 3D PET data”. *Phys. Med. Biol.*, **36**, p. 939, 1991.

[114] National Electrical Manufactures Association. *NEMA Standards Publication NU2- 1994: Performance measurements of positron emission tomographs.* Washington, DC: National Electrical Manufactures Association, 1994.

[115] National Electrical Manufactures Association. *Standards Publication NU2-2001: Performance measurements of positron emission tomographs.* Rosslyn, VA: National Electrical Manufactures Association, 2001.

[116] National Electrical Manufactures Association. *NEMA Standards Publication NU1- 1994: Performance measurements of scintillation camera.* Washington, DC: National Electrical Manufactures Association, 1994.

[117] Y.Yang, Y.C. Tai, S. Siegel, D.F. Newport, B. Bai, Q. Li, R. M. Leahy, and S. R. Cherry. “Optimization and performance evaluation of the microPET II scanner for in vivo small-animal imaging”. *Phys. Med. Biol.*, **49**, p. 2527, 2004.

[118] K. P. Schaefers, A. J. Reader, M. Kriens1, Knoess. C., O. Schober, , and M. Schaefers. “Performance Evaluation of the 32-Module quadHIDAC Small-Animal PET Scanner”. *J. Nucl. Med.*, **46**, p. 996, 2005.

[119] Y. Wang, J. Seidel, B. M.W. Tsui, J.J. Vaquero, and M. G. Pomper. “Performance Evaluation of the GE Healthcare eXplore VISTA Dual-Ring Small-Animal PET Scanner”. *J. Nucl. Med.*, **47**, p. 1891, 2006.

[120] A. Del Guerra, A. Bartoli, N. Belcari, D.J. Herbert, A. Motta, A. Vaiano, G. Di Domenico, N. Sabba, E. Moretti, G. Zavattini, M. Lazzarotti, L. Sensi, M. Michele Larobina, and L. Uccelli. “Performance Evaluation of the Fully Engineered YAP-(S)PET Scanner for Small Animal Imaging”. *IEEE Trans. Nucl. Sci.*, **53**, p. 1078, 2006.

[121] A. E. Spinelli, D. D’Ambrosio, S. Pettinato, C. Trespidi, C. Nanni, V. Ambrosini, G. Baldazzi, C. Bergamini, and M. Marengo. “Performance evaluation of a small animal PET scanner. Spatial resolution characterization using 18F and 11C”. *Nucl. Instr. and Meth. Phys. Res.*, **A571**, p. 215, 2007.

[122] M. C. Huisman, S. Reder, A. W. Weber, S.I. Ziegler, and M. Schwaiger. “Performance evaluation of the Philips MOSAIC small animal PET scanner”. *Eur. J. Nucl. Med.*, **34**, p. 532, 2007.

[123] V. Spanoudaki, I. Torres-Espallardo, M. Rafecas, and S. Ziegler. “Performance evaluation of MADPET-II, a small animal dual layer LSO-APD PET scanner with individual detector read out and depth of interaction information”. *J. Nucl. Med.*, **48, (Supplement 2)**, p. 39P, 2007.

[124] website, http://hggm.es/animalpet/.

[125] website, http://hggm.es/animalpet/Sep_8th_2001_Workshop_Report.htm.

[126] website, http://hggm.es/animalpet/nema_small_animal_pet_all_sections_feb07.doc.

[127] N. Belcari, A. Del Guerra, A. Bartoli, G. Di Domenico, G. Zavattini, D. Bianchi, M. Lazzarotti, L. Sensi, M. Lecchi, and L. Menichetti. “Performance Evalua-

tion of the YAP-(S)PET Scanner with preliminary NEMA Standard for Small Animal PET systems". *J. Nucl. Med.*, **47, (Supplement 1)**, p. 396P, 2006.

[128] A. Bartoli, N. Belcari, S. Fabbri, S. Moehrs, and A. Del Guerra. "Characterization of the physical performance of the new PET/SPECT small animal scanner YAP-(S)PET II". *Eur. J. Nucl. Med.*, **Supplement 2**, p. S228, 2007.

[129] S. E. Derenzo, W. W. Moses, R. H. Huesman, and T. F. Budinger. *Critical instrumentation issues for <2 mm resolution, high sensitivity brain PET, in Quantification of Brain Function.* Amsterdam, The Netherlands: Elsevier Science Publishers, pp 25-37, 1993.

[130] C. S. Levin and E. J Hoffman. "Calculation of positron range and its effect on the fundamental limit of positron emission tomography system spatial resolution". *Phys. Med. Biol.*, **44**, p. 781, 1999.

[131] R. Lecomte. "Technology challenges in small animal PET imaging". *Nucl. Instr. and Meth. Phys. Res.*, **A527**, p. 157, 2004.

[132] A. Del Guerra, A. Bartoli, N. Belcari, G. Di Domenico, N. Cesca, E. Moretti, N. Sabba, G. Zavattini, M. Lazzarotti, and L. Sensi. "Latest mprovements of the YAP-(S)PET small animal scanner". *Eur. J. Nucl. Med.*, **Abstracts of the Annual Congress of the EANM, Istanbul, Turkey 2005, Supplement 1 / September**, 2005.

[133] D. L. Bailey, T. Jones, and T.J. Spinks. "Method for Measuring the Absolute Sensitivity of Positron Emission Tomographic Scanners". *Eur. J. Nucl. Med.*, **18**, p. 374, 1991.

[134] D. L. Bailey and S. R. Meikle. "A convolution-subtraction scatter correction method for 3D PET". *Phys. Med. Biol.*, **39**, p. 411, 1994.

[135] G. Di Domenico, A. Motta, G. Zavattini, A. Del Guerra, C. Damiani, V. Bettinardi, and M. C. Gilardi. "Characterization of the Ferrara animal PET scanner". **477**, p. 505, 2002.

[136] S.C. Strother, M.E. Casey, and E.J. Hoffman. “Measuring PET Scanner Sensitivity: Relating Countrates to Image Signal-to-Noise Ratios using Noise Equivalent Counts”. *IEEE Trans. Nucl. Sci.*, **37**, p. 783, 1990.

[137] E. J. Hoffman, S. C. Huang, and M. E. Phelps. “Quantitation in positron emission computed tomography: I. Effect of object size”. *J. Comput. Assist. Tomogr.*, **3**, p. 299, 1979.

[138] S. E. Derenzo, T. F. Budinger, J. L. Cahoon, Huesman R. H., and H. G. Jackson. “High resolution computed tomography of positron emitters.”. *IEEE Trans. Nucl. Sci.*, **24**, p. 544, 1977.

[139] L. S. Graham, F. H. Fahey, M. T. Madsen, A. Van Aswegen, and M. V. Yester. “Quantitation of SPECT performance: Report of Task Group 4, Nuclear Medicine Committee”. *Med. Phys.*, **22**, p. 401, 1995.

[140] G. T. Gullberg. “An analytical approach to quantify uniformity artifacts for circular and noncircular detector motion in single photon emission computed tomography imaging,”. *Med. Phys.*, **14**, p. 105, 1987.

[141] M. Dahlbom, L. R. MacDonald, M. Schmand, L. Eriksson, M. Andreaco, and C. Williams. “A YSO/LSO Phoswich Array Detector for Single and Coincidence Photon Imaging”. *IEEE Trans. Nucl. Sci.*, **45**, p. 1128, 1998.

[142] A. Saoudi and R. Lecomte. “A novel APD-based detector module for multimodality PET/SPECT/CT scanners”. *IEEE Trans. Nucl. Sci.*, **46**, p. 479, 1999.

[143] B. J. Pichler, T. Gremillion, V. Ermer, M. Schmand, B. Bendriem, M. Schwaiger, S. I. Ziegler, R. Nutt, and S. D. Miller. “Detector Characterization and Detector Setup of a NaI-LSO PET/SPECT Camera”. *IEEE Trans. Nucl. Sci.*, **50**, p. 1420, 2003.

[144] P. Guerra, J. L. Rubio, J. E. Ortuno, G. Kontaxakis, M. J. Ledesma, and A. Santos. “Performance analysis of a low-cost small animal PET/SPECT scanner”. *Nucl. Instr. and Meth. Phys. Res.*, **A57**, p. 98, 2007.

[145] G. F. Knoll. *Tracer Kinetics in Biomedical Research: From Data to Model.* Kluwer Academic/Plenum, London, 2001.

[146] A. Bartoli, N. Belcari, D. Stark, S. Hoehnemann, M. Piel, M. Jennewein, U. Schmitt, J. Tillmanns, O. Thews, C. Hiemke, F. Roesch, and A. Del Guerra. “Preliminary assessment of the imaging capability of the YAP-(S)PET small animal scanner in neuroscience”. *Nucl. Instr. and Meth. Phys. Res.*, **A569**, p. 488, 2006.

[147] P. Millet, M. Moulin, A. Bartoli, A. Del Guerra, N. Ginovart, L. Lemoucheux, S. Buono, D. Fagret, Y. Charnay, and V. Ibanez. . 2007. submitted to J. Cereb. Blood Flow Metab.

[148] M. E. Phelps, Mazziotta J. C., and H. R. Schelbert. *Positron Emission Tomography and Autoradiography.* New York: Raven., 1986.

[149] A. Bartoli, N. Belcari, A. Del Guerra, M. De Servi, M. Tonacchera, A. Pinchera, L. Menichetti, and P.A. Salvadori. Prelinimary evaluation of the YAP-(S)PET scanner for small animal imaging. In *Biomedizinische Technik*, page 891. Medical Physics vol. 2, suppl.vol.2, 2005.

[150] http://www.utexas.edu/research/asrec/dopamine.html.

[151] J. C. Mazziotta, M. E. Phelps, S. C. Haung, L. R. Baxter, W. H. Riege, Hoffman J. M., Kuhl D. E., Lanto A. B., J. A. Wapenski, et al. “Cerebral glucose utilization reductions in clinically asymptomatic subjects at risk of Huntigton’s disease”. *New Engl. J. Med.*, **316**, p. 357, 1987.

[152] M. F. Beal, N.W. Kowall, D.W. Ellison, M.F. Mazurek, K.J. Swartz, and J. B. Martin. “Replication of the neurochemical characteristics of Huntington’s disease by quinolinic acid”. *Nature*, **321**, p. 168, 1986.

[153] M. F. Beal, R.J. Ferrante, K.J. Swartz, and N. W. Kowall. “Chronic quinolinic acid lesions in rats closely resemble Huntington’s disease”. *J. Neurosci.*, **11**, p. 1649, 1991.

[154] A. R. Blight, T.I. Cohen, K. Saito, and M. P. Heyes. “Quinolinic acid accumulation and functional deficits following experimental spinal cord injury”. *Brain*, **118**, p. 735, 1995.

[155] M. P. Heyes, K. Saito, J.S. Crowley, L.E. Davis, M.A. Demitrack, M. Der, et al. “Quinolinic acid and Kynurenine pathway metabolism in inflammatory and non-inflammatory neurological disease”. *Brain*, **115**, p. 1249, 1992.

[156] Michela Lecchi. . 2006. Speciality school of Medical Physics Thesis, University of Milano, unpublished.

[157] G. Paxinos and C. Watson. *The Rat Brain in Stereotaxic Coordinates.* fourth ed. Academic Press, New York., 1998.

[158] S. Belloli, R. M. Moresco, M. Matarrese, G. Biella, F. Sanvito, P. Simonelli, E. Turolla, S. Olivieri, A. Cappelli, S. Vomero, M. Galli-Kienle, and F. Fazio. “Evaluation of three quinoline-carboxamide derivatives as potential radioligands for the in vivo pet imaging of neurodegeneration”. *Neurochem. Int.*, **44**, p. 433, 2004.

[159] T. Alexi, J.L. Venero, and F. Hefti. “Protective effect of neurotrophin-4/5 and transforming growth factor-alfa on striatal neuronal phenotypic degeneration after excitotoxic lesioning with quinolinic acid.”. *Neuroscience*, **78**, p. 73, 1997.

[160] T. Alexi, C.V. Borlongan, R.L.M. Faull, C.E. Williams, R.G. Clark, P.D. Gluckman, and P. E. Huges. “Neuroprotective strategies for basal ganglia degeneration: Parkinson’s and Huntington’s diseases”. *Prog. Neurobiol.*, **60**, p. 409, 2000.

[161] O. Warburg, K. Posener, and E. Negelein VIII. “The metabolism of cancer cells”. *Biochem. Zeitschr.*, **152**, p. 129, 1924.

[162] S. FLexner and S. Jobling. *Studies upon a transplantable rat tumor, Monographs on Medical and Allied Subjects.* Rockfeller Institute for Medical Resarch, New York, pp. 1-51, 1910.

[163] D. H. S. Silverman, C. K. Hoh, M. A. Seltzer, C. Schiepers, G. S. Cuan, S. S. Gambhir, L. Zheng, J. Czernin, and M. E. Phelps. “Evaluating Tumor Biology and Oncological Disease With Positron-Emission Tomography”. *Semin. Radiat. Oncol.*, **8**, p. 183, 1998.

[164] D. N. Louis, E. C. Holland, and J. G.Cairncross. “Glioma Classification: A Molecular Reappraisal”. *Am. J. Pathol.*, **159**, p. 779, 2001.

[165] W. H. Sweet. “The Use of Nuclear Desintegrations in the Diagnosis and Treatment of Brain Tumor”. *New Engl. J. Med.*, **245**, p. 875, 1951.

[166] L. E. Farr, W. H. Sweet, J. S. Robertson, S. G. Foster, H.B. Locksley, D.L. Sutherland, M.L. Mendelsohn, and E. E. Stickey. “Neutron Capture Therapy with Boron in the Treatment of Glioblastoma Multiforme”. *Am. J. Roentgenol.*, **71**, p. 279, 1954.

[167] J. T. Godwin, L. E. Farr, W. H. Sweet, and J. S. Robertson. “Pathological study of eight patients with glioblastoma multiforme treated with by neutron capture radiation using boron 10”. *Cancer*, **8**, p. 601, 1955.

[168] A. K. Asbury, R. G. Ojean, S. L. Nielsen, and W. H. Sweet. “Neuropathologic Study of Fourteen Cases of Malignant Brain Tumor Treated by Boron-10 Slow Neutron Capture.Therapy,”. *J. Neuropathol. Exp. Neurol.*, **31**, p. 278, 1972.

[169] H. Hatanaka. *Boron neutron capture therapy for brain tumors.* Karin ABMF, Laws E. Editor, Glioma, Springer-Verlag, 233-249, 1991.

[170] A. Z. Diaz. “ Assessment of the Results from the Phase I/II Boron Neutron Capture Therapy Trials at the Brookhaven National Laboratory from a Clinician’s Point of View”. *J. Neuro-Oncol.*, **62**, p. 101, 2003.

[171] I. Kato. “Effectiveness of BNCT for recurrent head and neck malignancies”. *Appl. Radiat. Isot.*, **61**, p. 1069, 2004.

[172] A. Wittig et al. *Current clinical results of the EORTC-study 11961, in Sauerwien W. Moss R. and Wittig A. Editors, Research and development in neutron capture therapy.* Bologna, Monduzzi Editore, 2002.

[173] J. Capala, B. H.-Stenstam, P. Skoeld, K.and Munck af Rosenschoeld, V. Giusti, C. Persson, E. Wallin, A. Brun, L. Franzen, J. Carlsson, L. Salford, C. Ceberg, B. Persson, L. Pellettieri, and R. Henriksson R. "Boron Neutron Capture Therapy for Glioblastoma Multiforme: Clinical Studies in Sweden". *J. Neuro-Oncol.*, **62**, p. 134, 2003.

[174] H. Joensuu, T. Kankaanranta L., Seppala, I. Auterinen, M. Kallio, M. Kulvik, Laakso J., J. J. Vahatalo, M. Kortesniemi, P. Kotiluoto, T. Seren, J. Karila, A. Brander, E. Jarviluoma, P. Ryynanen, A. Paetau, H. Ruokonen, I.and Minn, M. Tenhunen, J. Jaaskelainen, M. Farkkila, and S. Savolainen. "Boron neutron capture therapy of brain tumors: clinical trials at the Finnish facility using boronphenylalanine". *J. Neuro-Oncol.*, **62**, p. 123, 2003.

[175] R. F. Barth. "Rat brain tumor models in experimental neuro-oncology: the 9L, C6, T9, F98, RG2(D74) and CNS-1 gliomas". *J. Neuro-Oncol.*, **36**, p. 91, 1998.

[176] Luca Menichetti. . 2006. Disegno, Sviluppo e Biosperimentazione dei Farmaci PhD thesis, University of Pisa, unpublished.

[177] S. J. Martin, C. P. Reutelingsperger, A. J. McGahon, J. A. Rader, R. C. van Schie, D. M. LaFace, and D. R. Green. "Early redistribution of plasma membrane phosphatidylserine is a general feature of apoptosis regardless of the initiating stimulus: inihibition by overexpression". *Abl. J. Exp. Med.*, **182**, p. 1545, 1995.

[178] V. A. Fadok, D. R. Voelker, P. A. Campbell, J. J. Cohen, D. L. Bratton, and P. M. Henson. "Exposure of phosphatidylserine on the surface of apoptotic lymphocytes triggers specific recognition and removal by macrophages". *J. Immunol.*, **148**, p. 2207, 1992.

[179] V. A. Fadok, A. Cathelineau, D. L. Daleke, P. M. Henson, and D. L. Bratton. "Loss of phospholipid asymmetry and surface exposure of phosphatidylserine is required for phagocytosis of apoptotic cells by macrophages and fibroblasts". *J. Biol. Chem.*, **276**, p. 1071, 2001.

[180] G: Koopman, C. P. M. Reutelingsperger, G. A. M. Kuijten, R. M. J. Keehnen, S. T. Pals, and M. H. J. van Oers. “Annexin V for flow cytometric detection of phosphatidylserine expression on B cells undergoing apoptosis”. *Blood*, **84**, p. 1415, 1994.

[181] B. VerHoven, R. A. Schlegel, and P. Williamson. “Mechanics of phosphatidylserine exposure, a phagocyte recognition signal, on apoptotic T lymphocytes”. *J. Exp. Med.*, **182**, p. 1597, 1995.

[182] F. G. Blankenberg, P. D. Katsikis, J. F. Tait, R. E. Davis, L. maumovski, K. Otsuki, S. Kopiwoda, M. J. Abrams, Darkes. M., R. C. Robbins, H. T. Maecker, and H. W. Strauss. “In vivo detection and imaging of phosphatidylserine expression during programmed cell death”. *Proc. Nat. Acad. Sci. USA*, **95**, p. 6349, 1998.

[183] B. L. Wood, D. F. Gibson, and J. F. Tait. “Increased phosphatidylserine exposure in sickle cell disease: flow-cytometric measurement and clinical associations”. *Blood*, **88**, p. 1873, 1996.

[184] Chiara Manfredi. . 2007. Tesi di Laurea, University of Pisa, unpublished.

[185] H. Fliss and D. Gattinger. “Apoptosis in ischemic and reperfused rat myocardium”. *Circ. Res.*, **79**, p. 949, 1996.

[186] R. A. Gottlieb, K. O. Burleson, R. A. Kloner, et al. “Reperfusion injury induces apoptosis in rabbit cardiomyocytes”. *J. Clin. Invest.*, **94**, p. 1621, 1994.

[187] G. J. Kemerink, I. H. Liem, L. Hofstra, et al. “Patient dosimetry of intravenously administered ^{99m}Tc-annexin V”. *J. Nucl. Med.*, **42**, p. 382, 2001.

[188] G. J. Kemerink, Boersma H. H., P. W. Thimister, et al. “Biodistribution and dosimetry of ^{99m}Tc-BTAP-annexin-V in humans”. *Eur. J. Nucl. Med.*, **28**, p. 1373, 2001.

[189] L. Hofstra, I. H. Liem, E. A. Dumont, et al. “Visualisation of cell death in vivo in patients with acute myocardial infarction”. *Lancet*, **356**, p. 209, 2000.

[190] J. Narula, E. R. Acio, N. Narula, et al. “Annexin-V imaging for noninvasive detection of cardiac allograft rejection”. *Nat. Med.*, **7**, p. 1347, 2001.

[191] N. D. Steinmetz, R. Taillefer, R. C. Hendel, et al. “Molecular imaging of cardiac injury in patients with acute myocardial infarction using ^{99m}Tc-Rh-annexin V: results of a multicenter trial”. *Circulation*, **106, (Supplement II)**, p. 331P, 2002.

[192] J. Taki, T. Higuchi, A. Kawashima, J. F. Tait, S. Kinuya, A. Muramori, I. Matsunari, K. Nakajima, N. Tonami, and H. W. Strauss. “Detection of Cardiomyocyte Death in a Rat Model of Ischemia and Reperfusion Using ^{99m}Tc-Labeled Annexin V”. *J. Nucl. Med.*, **45**, p. 1536, 2004.

[193] T. Kudo, K. Fukuchi, A. J. Annala, A. F. Chatziioannou, V. Allada, M. Dahlbom, Y-C. Tai, M. Inubushi, S-C. Huang, S. C. Cherry, M. E. Phelps, and H. R. Schelbert. “Noninvasive Measurement of Myocardial Activity Concentrations and Perfusion Defect Sizes in Rats With a New Small-Animal Positron Emission Tomograph”. *Circulation*, **106**, p. 118, 2002.

[194] A. Del Guerra, G. Di Domenico, M. Moretti, E. Moretti, N. Sabba, and G. Zavattini. . Presented at the 2002 annual conference of the Academy of Molecular Imaging, October 23-27, 2002, San Diego, CA, (USA) (abstract).

[195] A. Bartoli, S. Fabbri, N. Belcari, and A. Del Guerra. . Presented at the 2007 annual conference of the IEEE Medical Imaging Conference (MIC), October 30 - November 3, 2007, Honolulu, HI, (USA).

[196] D. W. Townsend and T. Beyer. “A combined PET/CT scanner: the path to true image fusion”. *Br. J. Radiol.*, **75**, 2002.

[197] http://www.medical.siemens.com/webapp/wcs/stores/.

[198] http://www.gehealthcare.com/usen/fun_img/pcimaging/products/pcimg_prod.html.

[199] N. Belcari, M. G. Bisogni, C. Carpentieri, A. Del Guerra, P. Delogu, D. Panetta, M. Quattrocchi, V. Rosso, and a. Stefanini. “Preliminary characterization of a

single photon counting detection system for CT application". *Nucl. Instr. and Meth. Phys. Res.*, **A576**, p. 204, 2007.

[200] B. J. Pichler, J. Swann, B. K. Rochelle, R. E. Nutt, Cherry. S. R., , and S. B. Siegel. "Lutetium oxyorthosilicate block detector readout by avalanche photodiode arrays for high resolution animal PET". *Phys. Med. Biol.*, **49**, p. 4305, 2004.

[201] R. S. Miyaoka, S. G. Kohlmyer, J. Joung, and T. K. Lewellen. "Performance characteristics of a second generation micro crystal element (MiCE2) detector". *IEEE Trans. Nucl. Sci.*, **2**, p. 1124, 2001.

[202] V. Golovin and V. Saveliev. "Novel type of avalanche photodetector with Geiger mode operation". *Nucl. Instr. and Meth. Phys. Res.*, **A518**, p. 560, 2004.

[203] S. Moehrs, A. Del Guerra, D. J. Herbert, and M. A. Mandelkern. "A detector head design for small-animal PET with silicon photomultipliers (SiPM)". *Phys. Med. Biol.*, **51**, p. 1113, 2006.

List of acronyms and names

3-DMS	3-D Multi Slice
3-DRP	3-D Reprojection
ABL	Abelson
ADC	Analog to Digital Converter
Ambisen	Ambiente e Sistema Endocrino e Nervoso
AMIDE	Amide's a Medical Imaging Data Examiner
BCR	Breakpoint Cluster Region
BGO	Bismuth Ortho-Germanate
BNCT	Boron Neutron Capture Therapy
CCD	Charge Coupled Device
CFD	Constant Fraction Discriminator
CFOV	Center of the Field Of View
CNR	National Research Council
COR	Center of Rotation
CT	Computed Tomography
DICOM	Digital Imaging and Communication in Medicine
EM	Expectation Maximization
FAB	Fast Acquisition Board
FBP	Filtered Back Projection
FORE	Fourier Rebinning
FOV	Field Of View
FWHM	Full Width at Half Maximum
GBM	Glioblastoma Multiforme
GFP	Green Fluorescent Protein

GSO	Gadolinium Orthosilicate
HD	Huntington's Desease
HV	High Voltage
IFC	Institute of Clinical Physiology
IQ	Image Quality
ISE	Ingegneria dei Sistemi Elettronici
LOR	Line Of Response
LSF	Line Spread Function
LSO	Luthetium Orthosilicate
LUT	Look Up Table
ML-EM	Maximum Likelihood Expectation Maximization
MRI	Magnetic Resonance Imaging
MSRB	Multi Slice Rebinning
NCT	Neutron Capture Therapy
NEC	Noise Equivalent Count
NEMA	National Electric Manufacturers Association
NIH	National Institute of Health
OSEM	Ordered Subset Expectation Maximization
PET	Positron Emission Tomography
PMT	Photomultiplier Tube
PRG	PET Reporter Gene
PSF	Point Spread Function
PSPMT	Positron Sensitive Photomultiplier Tube
PVE	Partial Volume Effect
QA	Quinolinic Acid
RC	Recovery Coefficient
RF	
RNA	Ribonucleic acid

ROI	Region Of Interest
SF	Scatter Fraction
SNR	Signal-to-Noise Ratio
SPECT	Single Photon Emission Computed Tomography
SSRB	Single Slice Rebinning
VOI	Volume Of Interest
YAP	Yttrium Alluminium Perovskite